POLITECNICO DI MILANO

School of Industrial and Information Engineering

Master of Science in Space Engineering

DESIGN AND ANALYSIS OF A DAMPING SYSTEM FOR LANDING IN MICROGRAVITY

Supervisor: Prof. Mauro Massari

Co-Supervisor: Prof. Paolo Carlo Astori

Thesis by:

Luciano Oliva
841140

Jan Guil Park
835046

Academic Year 2016 – 2017

“Imagination will often carry us to worlds that never were, but without it we go nowhere”

Carl Sagan

Summary

Introduction

In the past space exploration missions, the development of a proper landing system was always a crucial aspect. The search for soft-landing devices for lunar and planetary probes was led by the need to preserve the internal payload from excessive decelerations during the touchdown and their application was usually though to be assisted by a retro-propulsion system and/or by the aerodynamic drag given by the parachutes for atmospheric probes. Since the targeted celestial bodies for the most of the landing missions were massive (Venus, Mars, Moons e t c), the issue regarding the escape velocity and the rebound weren't seriously considered. However, the recent attempt to land on a cometary surface of Rosetta/Philae Mission put in evidence all the difficulties associated to a landing on an almost zero-gravity body in a successful manner: the lander reached the comet surface with a velocity of 1 m/s and rebounded from it at 0.38 m/s before being arrested completely with an unpredicted attitude. The inability to dissipate in one time all the initial kinetic energy and the variability given by the ground properties, gravity field and the arrival velocity are the main problems related to this scenario. According to this premise, it's evident that a more performant landing system shall ensure high energy dissipation capability and adaptability, minimizing the bouncing velocity and the acceleration transmitted to the payload. Therefore, the purpose of this thesis is to search for an interesting technological solution starting from the already present ones, and to verify the feasibility in terms of efficiency, mass, volume, power and reliability through extensive numerical simulations, having in mind the complications related to the harsh space environment (vacuum, cryogenic temperatures and radiations) and keeping as reference the mentioned Rosetta/Philae Mission. With the intention of improving the performances and for the sake of robustness, the work is focused on the development of a device able to arrest a spacecraft with a mass similar to Philae's (about 100 kg) but falling at 2 m/s. A special attention is given to the modelling, simulation and sizing of a hybrid active-passive system, where an active piezoelectric frictional brake is combined with a

passive granular damper in order to achieve the wanted performances welding the good adaptability of the first one together with the high dissipation capability and reliability of the second one. The verification of the feasibility of a granular damper and its characterization is conducted through DEM (Discrete Element Method), which is based on a numerical approach of the granular mechanics, while the implementation of the combined active-passive system, the search for the best control law and the system robustness check (gravity, ground properties, control system noise and sampling frequency, mass and arrival velocities) are performed through Multibody simulations in MATLAB and Simulink environment. In both types of simulations, the search for the optimal parameters (dimensions, frictional coefficients and packings for the passive damper and force law coefficients for the active damper) is performed trying to reduce, again, the bouncing velocities and the transmitted forces. Finally, the definitive sizing based on the results obtained from the mentioned simulations is proposed, where the structural resistance and the required power/voltage are verified, and the masses, dimensions and geometry of the chosen configuration are illustrated.

1. State of Art

In order to understand better the goals of this work and to catch some possible useful similarities with past missions, a brief analysis of the state of art is presented.

1.1 Past Landing Missions in Low Gravity

1.1.1 Rosetta-Philae Lander Mission

Thanks to the similarities in the requirements, the environment, the objectives and especially for the final results observed, the mission which mostly inspired this work is the Rosetta-Philae Lander mission. Rosetta was a space probe built by the European Space Agency and launched on 2 March 2004. Along with Philae, its lander module, Rosetta performed a detailed study of the comet 67P/Churyumov-Gerasimenko. During its journey to the comet, the spacecraft flew by Mars and the asteroids 21 Lutetia and 2867 Steins. On 6 August 2014, the spacecraft reached the comet and on 12 November, its lander module Philae performed the first landing in human history on a comet. Due to diminishing solar power, the communication with the Lander was interrupted while the Rosetta spacecraft ended its mission on 30 September 2016 by hard-landing on the comet. Philae detached from Rosetta at a relative speed of about 1 m/s. Before stopping at the surface, it bounced twice. On the contact with the surface, two harpoons were to be fired into the comet to prevent the lander from bouncing off as the comet's escape velocity is only around 1 m/s. Analysis of telemetry indicated that the surface at the

initial touchdown site is relatively soft, covered with a layer of granular material and that the harpoons had not fired upon landing. Philae landed oddly, in the shadow of a nearby cliff and canted at an angle of around 30 degrees. This made it unable to adequately collect solar power, and it lost contact with Rosetta when its batteries ran out after two days, well before much of the planned science objectives could be attempted. However, the mission brought a big scientific return to the investigation of the comets, their relation with the terrestrial life and the origin of the Solar System. For example, thanks to the mission, scientists understood that the comets have no their own magnetic field and that the water present on them is different from the water present on the Earth. The box-shaped 100 kg Philae lander was carried on the side of the orbiter until it arrived at the comet. Once the orbiter was aligned correctly, the lander was commanded to self-eject from the main spacecraft and unfold its three legs, ready for the touchdown. On landing, the legs would have damped out the most of the kinetic energy to reduce the chance of bouncing. They could rotate, lift or tilt to return the lander to an upright position. The lander structure consisted of a baseplate, an instrument platform, and a polygonal sandwich construction, all made of carbon fiber. Some of the instruments and subsystems are beneath a hood that is covered with solar cells. Focusing more on the dissipation and stopping mechanisms, to land in the low gravity the lander was also equipped with ice screws that would automatically screw into the surface upon impact. As it was mentioned before, immediately after touchdown, harpoons were to be fired to anchor the lander to the ground and prevent it escaping from comet's extremely weak gravity. There was a damper between the main body of the lander and the landing feet, to decouple the rotation of the landing feet from the body. The lander also had one thruster to keep the vehicle on ground while firing the harpoons. In the end, the thruster, harpoons and ice screws failed to keep the lander on the surface. Philae inadvertently became the first hopper by bouncing at an estimated 0.4 m/s from the surface.

Figure 1 Philae Lander

1.1.2 Hayabusa

Japan's Space Agency (JAXA) launched the Hayabusa mission to return a sample from the Near Earth Asteroid 25143 Itokawa in 2003. The mission contained a mini-lander named Minerva. Minerva was designed to hop over the surface of Itokawa by using two reaction wheels. One would rotate the vehicle to the desired direction and the second would cause the vehicle to rotate around its base launching it off the surface onto a ballistic trajectory. Unfortunately, the part of the mission failed when the hopper was released from the orbiting spacecraft with the incorrect velocity. It never touched the surface of the asteroid and became solar satellite. As a consequence of this mission, several alternatives for the lander configuration were proposed. One of the most interesting alternative was a novel robot that could stick on the surface and move to desired direction on boulders and grooves. The conceptual design was named "Cliff Hanger, Rock Climber" robot. Differently from Minerva, which location when the bounds are finally damped out was very opportunistic and difficult to predict or control, this strategy enables the rover to walk on the surface like a rock climber, or an insect. The mission design actually considered two options of baseline mission scenarios. Scenario A is the option consisting of Orbiter and Rover. On the other hand, Scenario B is the option consisting of Orbiter, Lander, and Rover. Focusing on the Scenario A, the rover could be deployed from the mothership to touch down on a boulder. For soft touchdown, the deployment should be done not from a high altitude of orbit, but from

the mothership hovering at the height about 10-100 meters. Considering a Minerva-size rover, they estimated that the touchdown velocity could be 1-10 cm/s after the free fall. In this scenario, an effective shock absorber was required for the shock protection and quick stabilization. For this purpose, bead absorption technology developed for MUSES-C Target Markers was considered. The bead absorption has been proved highly effective to have smaller coefficient of restitution against landing impact. The rover could be covered by an insulator filled with a number of tiny beads. For the Scenario B, the lander must be anchored. As for the anchoring technology, penetration using the kinetic energy of hard landing could be applied. Technology for penetrators has been developed for Lunar-A and Deep Space 2 missions, where very high-G impact was a critical point in the design. On the other hand, technology for harpoons could be used for soft landing on a comet like in Rosetta mission. In the following, a conceptual picture of the climber is given.

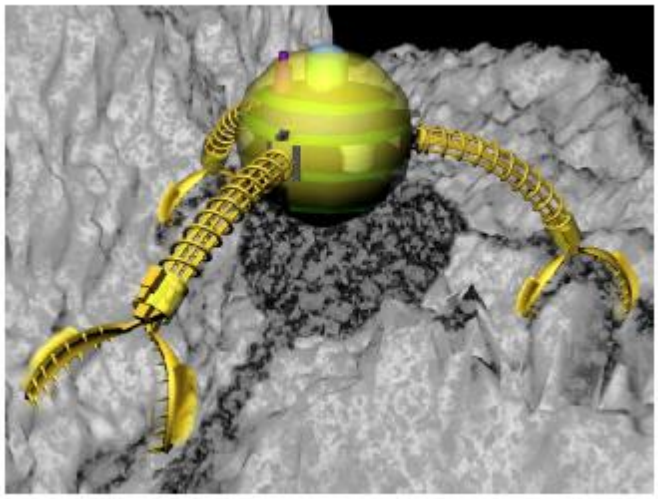

Figure 2 Conceptual alternative Hayabusa Lander

1.1.3 Phobos

In 1988 and 1989 the former Soviet Union launched the PHOBOS missions to study Mars and its moons. Phobos 2 had a hopper named Prop-f to explore Mars' moon

Phobos. The hopper was designed to launch itself in a particular direction using a compressed spring, then crash land and roll to a stop. Arms would extend to orient the hopper on its foot. Unfortunately the mission failed before the hopper could be deployed.

1.1.4 Other Missions

There were missions which dealt with a comet landing like the Deep Impact and the Near Shoemaker missions. The first one was a NASA space probe designed to study the interior composition of the comet Tempel 1, by releasing an impactor to a comet. It was the first mission to eject material from a comet's surface. The second one was another NASA mission designed to study the near-Earth asteroid Eros, from a close orbit, over a period of a year. The mission succeeded in closing in with asteroid and orbited it several times, finally terminating by touching down on the asteroid. However, even if both missions ended successfully, since the soft landing was not the main objective of these missions, they won't be described in detail. Indeed, in the Deep Impact's case, the impactor was designed to be completely destroyed at the impact while in the Near Shoemaker's case, the spacecraft wasn't designed as a lander and the soft touchdown occurred only in the decommissioning phase of the mission.

1.2 Past Landing Missions in High Gravity

1.2.1 Apollo

The impact energy absorption was a principal concern from the first human lander missions. The Apollo Lunar Module was equipped with a crushable aluminum honeycomb impact absorber. Because it takes a constant force to crush the honeycomb

through its entire stroke, the force displacement curve is a rectangular profile and it absorbs the maximum energy for a given stroke and maximum allowable decelerations. The landing data estimated that 60% of the landing energy was absorbed by the footpads compressing the regolith.

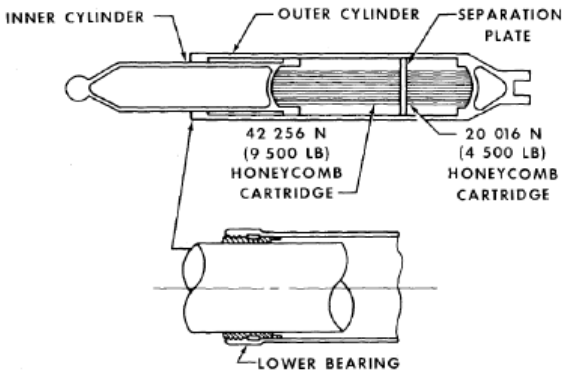

Figure 3 Apollo shock absorber

1.2.2 Schiaparelli EDM Lander

Schiaparelli EDM lander was the Entry, Descent and Landing Demonstrator Module (EDM) of the ExoMars program, a joint mission of the European Space Agency and the Russian space agency. It was intended to test technology for future soft landings on the surface of Mars. It also had a limited but focused science payload that would have measured atmospheric electricity on Mars and local meteorological conditions. The lander was designed to enter in the Mars' atmosphere and to be slowed down by a parachute then by its own hydrazine thrusters up to 2 meters above the surface from which it would have fallen freely. With a touchdown velocity of few meters per seconds, the final shock should have been cushioned by the crushable structure made of aluminum sandwich with Carbon fiber reinforce polymer. It was designed to limit the deceleration at landing to 40G in order to guarantee the survival of all components at the top of the surface platform. The expected impact velocity was 4 meters per second. This type impact attenuation system was chosen, for its design simplicity, as a passive system as opposed to controlled vented airbags or high fidelity sky crane system. Also,

it should have allowed the platform to land horizontally without necessitating protective covers which would be needed for a system relying on airbags for protection. This type of cushion should have permitted direct surface access to a rover, not requiring a complex delivery system with ramps or moving parts. Unfortunately, the braking thrusters didn't work properly during the descending phase and the lander impacted on the Martian surface at 540 km/h.

1.2.3 Huygens-Cassini Mission

Huygens was an atmospheric entry probe that landed successfully on Saturn's moon Titan in 2005. Built and operated by the European Space Agency, it was part of the Cassini-Huygens mission and became the first spacecraft ever to land on Titan and the furthest landing from Earth a spacecraft has ever made. The 318 kg probe itself consisted of the Entry Assembly and the Descending Module. The latter one comprised an aluminum shell and an inner structure containing all the payload. According to the recorded data, the lander impacted the Titan's surface at 5 m/s. The kinetic energy was absorbed by the honeycomb structure and the insulation foam. It is noticeable that Titan's gravity (1.35 m/s^2) is lower than Earth's of Mars' gravity. Moreover, in this mission a proper impact analysis was performed considering different properties of the surface which could be interesting for the purposes of this thesis.

2. Technology Selection and Preliminary Design

2.1 Environment

The analysis of the working environment is essential, in order to properly design a landing system capable to land safely on an unknown zero-gravity celestial body, and without bouncing away due to the lack of gravity. Since the gravity is absent, none kind of atmosphere could be present, temperature and pressure at the surface level are the same of deep space, and with no kind of shield against Sun radiations, solar wind and cosmic rays. Another critical aspect, especially for the purpose of this thesis, is the unknowing about properties of the soil, since every comets or asteroids could have different composition. Moreover, they have no magnetic field, because the movements of ferrous nucleus, surrounded by a liquid layer, have cooled down, with the consequent solidification of the nucleus and the demise of a magnetic field. So, with the absence also of the magnetic field, environmental context for the lander is the same of the deep space. In deep space, there is vacuum, so outgassing phenomenon shall be taken into account, avoiding volatile materials as polymers and elastomers. They, in fact, would be subjected to a degradation of their properties, but also of the other components of the spacecraft, which would be covered by the evaporated material amount. Let's think, for example, at a radiator or at a thermal blanket, where their functions is strictly related to their surface condition, and if evaporated materials lay down on them, the thermal control of the spacecraft would be compromised. For liquid fluids, vacuum is dangerous, causing their passage from liquid to gaseous state, modifying properties as volumetric compressibility and viscosity, that would be damaging for hydraulic

actuators, hydraulic shock absorbers or hydraulic command chains. Also for pneumatic systems vacuum is a problem, because they work always at high pressure, with the gas contained in the tank that would experience a pressure difference very large since the pressure outside is zero, and so heavy tanks would be required. For what regards radiations, without any kind of shield, they modify the structure of polymers and elastomers, changing completely their properties and compromising the mechanical behavior. Since the temperatures are very low, almost zero degrees Kelvin as in deep space, shall be used materials and technologies which can survive and work at these conditions. But also high temperatures could be a problem, in fact, usually, comets and asteroids pass very near to the sun, and in this period temperatures could increase of several hundreds of degrees Kelvin (400-500 K), depending on pericenter of the comets and asteroids orbit. For this reason, again, an accurate choice of working materials and technologies shall be performed. Polymers, elastomers and composite materials, for example, are very sensitive to temperature, both low and high, because in one case they become too brittle and in the other too soft, losing their mechanical properties. If fluid systems are employed, due to their large sensitivity to pressure and temperature, a strong system of pressurization and thermal control is required, but this results in too heavy and complex technologies for a small lander like the object of this thesis. Therefore, the general requirements derived from the environment analysis, in order to accomplish the goal of the thesis, consist in choosing materials and technologies able to survive and properly work at low and high temperature, in vacuum, and with the presence of sun radiations and cosmic rays.

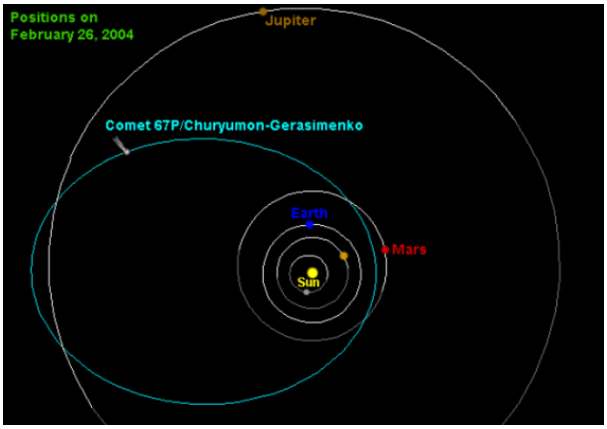

Figure 4 Orbit of Comet 67P/Churyumov-Gerasimenko

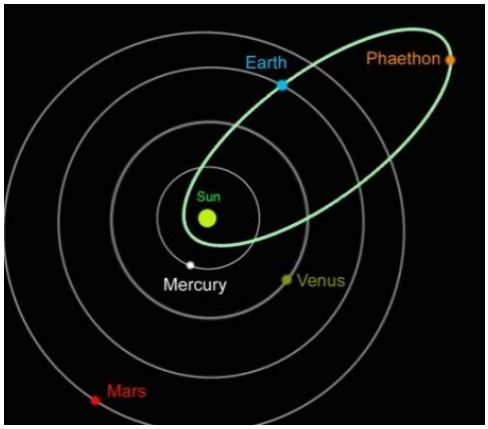

Figure 5 Orbit of Asteroid 3200 Phaeton

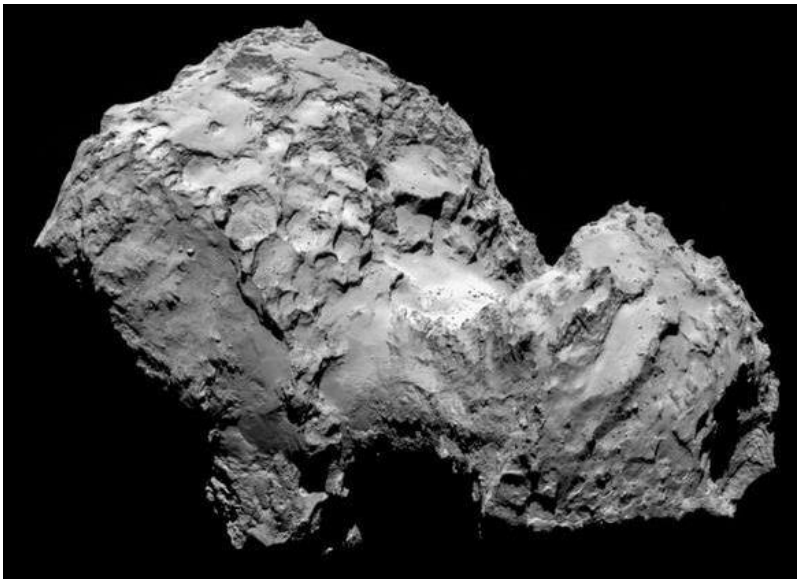

Figure 6 Pictures of Comet 67P/Churyumov-Gerasimenko, taken by ESA

2.2 Requirements

Hereafter, the requirements the landing system shall satisfy are presented. They are based on considerations about landing system perfomances and on environmental conditions it has to face with.

Design Requirements	ID
Landing system shall guarantee a safe landing	1
Landing system shall be non-destroyable, in order to stabilize the spacecraft during scientific operations performed on the ground	2
Landing system shall avoid bouncing away from the celestial body after the impact	3
Landing system shall absorb all the vertical kinetic energy of the spacecraft	4
Landing system shall guarantee the maximum load transmitted to spacecraft and payload stays under a certain value	5

Landing system shall have an actively controlled part, in order to be more robust against uncertainties	6
The active damper shall guarantee a deceleration lower than the one obtained with only passive device	7
The landing system shall be able to work and dissipate kinetic energy in nominal condition, even if active part doesn't work	8
Mass and volume of the landing system shall be limited under certain values	9
Power consumption of the landing system shall be limited under a certain value	10
Landing system shall be robust against uncertainties of arrival velocity, with values different from design condition	11
Landing system shall be robust against unknown ground properties	12
Landing system shall be robust against unknown gravity field	13
Landing system shall be capable of survive and work at deep space low temperature	14
Landing system shall be capable of survive and work at high temperature (400-500 K)	15
Landing system shall be capable of survive and work in vacuum	16
Landing system shall be capable of survive and work in presence of radiations	17

Table 1

2.3 Technology Research Summary

This section is deidicated to the illustrationtion of the available technologies devoted to the energy dissipation for an impact scenario. The following presented technology review is performed taking into account the applicability to the aim of this thesis, in terms of amount of energy to be dissipated, dimensions, mass, power required and space environment resistance.

2.3.1 Adaptive Pneumatic Absorber

This kind of device achieves the desired dissipation through the compression of an internally stored gas and regulates the generation of the force through piezoelectric valves which control the flow of the gas between two chambers. Differently from the traditional pneumatic absorbers used in the aeronautical field and in the food industries, where the dissipation efficiency does not exceed 40%, this adaptive absorber reaches an efficiency (80%) comparable to hydraulic devices. After an initial compression of the gas in the cylinder, the active valves release the gas to the second chamber. By this way the energy accumulated in the compressed gas is dissipated and the spring-back effect is diminished. In order to achieve this effect, a multilayered piezoelectric actuator is applied in a miniature valve positioned in the pneumatic cylinder piston. The physical phenomena involved in this case are the compressibility of the gas, internal friction, energy transfer by heat and non polytropic processes which are characterized by high nonlinearity and non-stationarity. They are principally utilized in suspension for vibration isolation, actuation in automatics and mechanical absorbers. Considering the phenomena in more detail, the dissipation process of the external mechanical energy by means of the absorber is conducted in three main phases. The first phase is the conversion of the mechanical energy into thermodynamic energy of the gas in the process of a simultaneous expansion and contraction of the media in the two internal volumes of the absorber. In the subsequent phase, in order to counteract the releasing of the accumulated energy via the spring-back effect, a flow through the piston is allowed in a controlled manner, which results in a spontaneous expansion of the gas within the cylinder volumes. The effect is a decrease of the pressure difference on the piston and a limitation of the reaction force generated by the absorber. The final dissipation phase is the cooling of the gas in the cylinder by the heat transfer to the sorroundings. The macroscopic effect which is observed is an elastoplastic-like response with a controllable level of plastic yielding. The flow process between the volumes is conducted within a period of several milliseconds for an impact velocity of 5 m/s. Employing a fast operating piezoelectric valve, it is possible to control the absorption process by adjusting the level of the mechanical energy dissipated by the system and

control the deceleration and forces acting on the protected objects. In the following, a schematic view of the device is given.

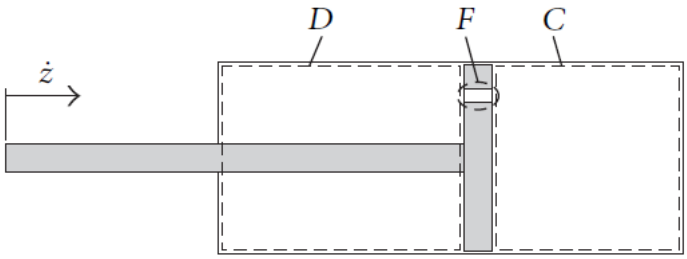

Figure 7 Schematic view of the pneumatic absorber

Regarding the control algorithm, the process can be based on three-stages operation. During the first stage, the energy of the moving object is estimated with a system of electronic non-contact sensors in a few milliseconds before the impact event. After the magnitude of the energy to be dissipated is determined, the mechanical energy of the object is converted into an increase of enthalpy of the gas in the absorber. In the third stage, an electronically controlled process of the accumulated energy dissipation is conducted via thermodynamically irreversible process of spontaneous gas expansion between the internal chamber of the absorber. This process is controlled by means of electronic pressure and temperature sensors positioned in the absorber cylinder. The piezoelectrically driven valve is used to adjust the process of the gas expansion and therefore to maintain the magnitude of the converted energy on the predefined level in accordance with the piston position. This configuration allows the generation of the reaction force on a desired level in dependence on the magnitude of the energy to be dissipated. Therefore, the device can be considered as adaptive. According to the studies related to the valves characterization, the piezo actuators seems to be suitable since they are characterized by good displacements, time resolution (high frequency) and high reliability. For this purpose, a multilayer piezo actuator is adopted since it needs low voltage and it's characterized by higher bandwidth, higher actuation force and shorter response. Because of the need of the high mass flow rate and high actuation frequency, a multiple metering holes-plates with piezoelectric actuator is developed. The chambers could be filled with an inert gas like the Nitrogen which is commonly used as pressurant

in the space propulsion system. One aspect to be considered is that, in the chocking condition, there is a maximum value of mass flow rate for given values of stagnation pressure and temperature, limiting the performances of the absorption process. One of the primary advantage of this kind of solution is the lightness. Indeed, it could be applied as the absorber of the landing gear of small Unmanned Aerial Vehicle (UAV). Another variant of this device are the Metal Bellows. In the following figure a schematic of the absorber is shown.

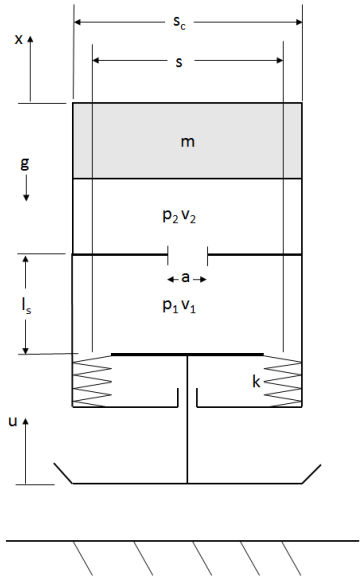

Figure 8 Metal bellows shock absorber

It consists on two chambers, one with a fixed volume and another with a variable volume which is a function of bellows position. The top of the bellows is connected to the landing pad with a rod. There are studies which deals with the conceptual design for a space application. The bellows are made of stamped diaphragms which are welded together. According to them, this device can operate at cryogenic temperatures and, since hermetically sealed, is not subjected (theoretically) to the leakage phenomenon and suitable for low gravity body landing. As in the previously discussed adaptive pneumatic absorber, the control strategies are based on check valves or control valves and varying the opening and the closing timing, it can achieve an optimal performance. Moreover, keeping closed the valve, at the impact, the metal bellows act like spring allowing consecutive hops. Therefore, it could be applied if an actuator able to operate

multiple times (as a hopper) is required. Another application of the pressurized air for the shock absorption is given by the Adaptive Inflatable Structures. They are structures filled with gas under appropriately adjusted changeable pressure. The idea of using compressed air and its controlled release makes pressurized structures easily adaptable for various impact forces and scenarios. The inflated structure can be rigid (as a cylinder enclosed by piston), it can be a thin walled structure undergoing plastic behaviour or it can be a completely deformable air-filled cushion. In these latter devices the deployment is planned only when the collision occurs. Pressure of the gas must be adjusted according to the velocity, mass and area of contact with the hitting surface. Fast reacting pyrotechnics systems based on the concept of micro explosions (similarly as in an airbag in a car) can be used for immediate gas pumping. Further improvement of this solution can be achieved by dividing the structure into several packages separated by flexible walls in which piezo valves allowing the flow of the gas are mounted. This method allows to adjust separately the level of the initial pressure in different parts of the structure. During the collision, the controlled released of the pressure is executed by opening exit piezo-valves. This way the stiffness of the pneumatic structure in the subsequent stages of the impact can be controlled and prevent excessive forces and accelerations to the system. Another purpose of applying a release of pressure is to control the dissipation of energy. An application considered for this device is the adaptive external airbag for helicopter. The system is designed for extremely severe, emergency landing. It consists of a multi-chamber air filled cushions attached to the helicopter undercarriage. Deployment of these cushions is executed just before the touchdown by means of pyrotechnic system. Distribution of pressure is adjusted to landing direction and velocity, which are identified by ultrasonic velocity sensors and pressure sensors inside the airbag. Release of pressure is due to fabric leakage and additional piezoelectric based controllable high speed and stroke valves. According to the considered gas-involving devices, the following considerations are done: they are characterized by the need of storing the pressurized gas inside them in order to achieve a correct energy dissipation. This aspect lowers dramatically the reliability of those solutions since in the vacuum environment of the space, notwithstanding an efficient sealing, the leakage phenomenon must be always carefully considered, especially when long time missions (more than 10 years) are planned.

Devices like the metal bellows allows to achieve a hopper-behavior which is out from the given requirements while an airbag-system could occupy a high volume after the inflation-deflation process reducing the available volume for the ground-related science activities. In the pyro-inflation or pumping cases the reliability of the system could also consider an eventual failure of the pyro devices. However, the low mass, the high efficiency and the controllability make them interesting for the purposes of this thesis.

2.3.2 Granular Shock Absorber

Everyone can easily understand that pushing something in a granular material (like the sand) creates a reaction force able to stop the motion. Moreover, this process occurs gradually, without involving excessive deceleration and preserving the integrity of the impacting object. Indeed, falling on a sandy beach is less painful than falling on the concrete. The energy dissipation occurs through the collision between the granules and the friction phenomenon. Some authors proposed the utilization of the granular material as noise reduction techniques at low frequencies (160 to 315 Hz) that are found in the revolution of motors and gears in the truck driving system. Experiments were performed using spherical and non-spherical granules of 1mm in diameter made of iron, plastic and lead. The tests involved both a vibrational case and an impact case. In the latter one, an unconstrained iron column was dropped onto a multiple lead granules validating the ability of the granular material to reduce significantly the impact force. Regarding the vibration isolation, some results showed that, increasing the mass, adopting a non-spherical geometry and increasing the exciting force, the damping effect is enforced. One of the simple ways using particles to damp vibration is a particle impact damper which comprises a container filled with granular particles. The particle impact dampers absorb kinetic energy through frictional collisions between particles and particles-wall of the container. Spherical solid particle assemblage can be used instead of working fluid of an oil damper, because a particle assemblage shows a fluid-like behaviour such as fluidity. High durable dampers can be obtained utilizing a particle assemblage having simple structures because they do not have fluid inside and oil seals are not required. In

order to change damping properties of the damper utilizing a particle assemblage, there are many physical conditions such as materials, size and shape of particles, shape of the cylinder and piston, installation angle of the damper, frequency of vibration and so on. Some experiments were done using beads made of soda glass with the average diameter of particles 1.16mm, 0.88mm and 0.56mm in the following configuration.

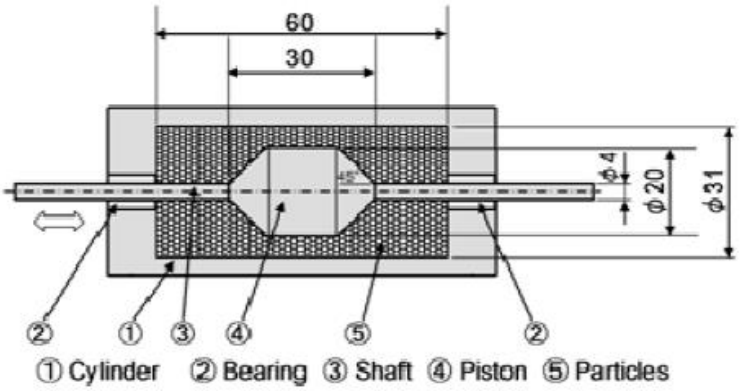

Figure 9 Granular damper

According to these experiments, it was observed a hardening property of the damping force which increases with the displacement. During the damping process, three different stages are identified. In the first stage, just after the piston passing through the dead centers, the damping force mainly comes from inertial force of the particles in the damper, because some space without particles exists in front of the piston in the direction of movement and the local packing fraction is smaller than the average value. In this stage, most of the particles pushed by the piston move into such space in front of the piston. After the first stage, the damping force increases due to compression of particles. The particles in front of the piston are compressed by the piston and the stress force of the particle increases. The piston moves furthermore, the damping force is almost constant (third stage), because the increase of stress force due to the compression of particles is balanced by the decrease of stress force due to the movement of particles to the opposite direction of motion of the piston. The mobility of particles is subject to several conditions such as distribution of diameters of particles, bulk density, number of particles, packing fraction, size of the orifice area, and shape of the piston. For example,

high packing fraction leads to low mobility of particles in the damper and produces stronger friction and stronger reactive force. Since the granular materials creates enormous friction through the interaction of their individual particles, they could be applied in the crashworthiness design in the automotive field using a tube containing granular material able to absorb the impact energy. Studies regarding this field revealed that the granular material filled tube is able to absorb much more crash energy than an empty tube and involved the calculation of the effective thickness of the tube which is the thickness of an empty tube with the same energy absorption capability of the granular material filled tube considering the axial, bending and mixed modes and assuming an elasto-plastic behaviour of the material. Recently, a considerable amount of research focused on the efficiency of granular dampers has been developed. In comparison with classical viscous dampers, the granular one exhibits several advantages for applications under extreme conditions: they are simple, easy to maintain, robust, very durable, insensitive to temperature and effective over a wide range of frequencies. It is only natural that these new dampers have a broad spectrum of applications (reducing vibrations in aerospace industry, sports, medical tools, oscillatory saws, dead-blow hammer, e t c). Through particle dynamic simulations, it has been found that the damping mechanism is mainly dominated by friction for small particles, but the collisions effect becomes important as the particle size increases. However, when the number of particles is large, the total energy dissipated (collisional and frictional) is independent of the friction and restitution characteristics of the particles. Moreover, the damping efficiency is related to the available space for the grains in the container of confinement. Too confined, the grains behave like a solid and the damping is weak. Too loose, the grains do not interact enough with the borders to damp the oscillations. An interesting variant of the application of the granular material for the vibration suppression are the Vacuum Packed Particles (VPP). They were studied especially for vehicle suspensions and allow to control actively their behaviour by controlling the underpressure resulting in various jamming mechanisms in the granular core. Actually, they belong to the class of the materials whose mechanical (rheological, dissipative) properties may be quickly changed by applying a partial vacuum inside the system. The discussed granular structures are conglomerates that consist of loose granular material placed in a soft and hermetic envelope. When exposed to a partial vacuum, the so called

"jamming mechanism" occurs and loose particles interact to form a solid-like structure that resists various types of deformations or flow. This change in the structure appears as a dramatic increase in apparent viscosity, and the "plastic" structure develops characteristics of a semisolid state. The magnitude of this transformation is controlled by the value of the partial vacuum and is immediately reversed upon removing the underpressure. The experimental tests of the VPP different materials for the grains were considered (PMMA, polypropylene, polystyrene, ABS) of same dimensions and shapes (cylindrical grains of 3mm length and 1mm in diameter) and various underpressure values. According to the results of such studies, an increase in the underpressure value results in an apparently larger force response. The force response can be 10 times greater than the nominal value for a relatively high value of underpressure. Therefore, the underpressure is a very convenient parameter for controlling the mechanical properties of vacuum packed particles. The force generated by the device can be modelled as a velocity proportional force where the linear damping coefficient depends on the value of the underpressure while another model underlines the dependency of the damping coefficient on the stroke, the wear of single grains caused by the intergranular friction phenomenon, rearrangement of the grains along the total path traveled and again, on the underpressure. The heart of the device is a granular core which is formed of a cylindrical envelope filled by loose grains and thanks to the special valve, it is possible to connect the core to a vacuum pump and generate the appropriate value of a partial vacuum inside the system. These studies which also involved vehicle simulations, demonstrated that it is possible to significantly reduce vertical accelerations using the controlled granular dampers and it may replace much more expensive and complex magnetorheological or electrorheological devices. Here a schematic view of such device is presented.

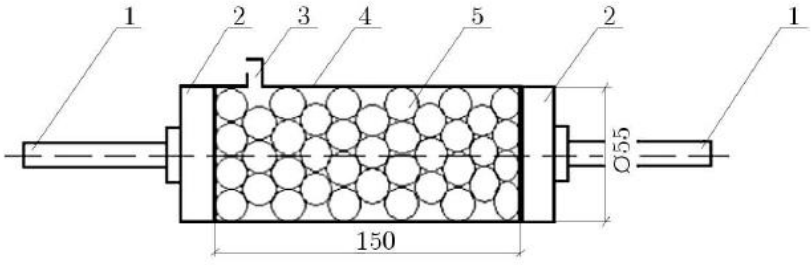

Figure 10 VPP damper

Considering the previously given requirements, the particle damping is an ideal technique for a space application because of the particular advantages such as temperature insensitivity, radiation resistance, long working life and reliability over other damping materials. Some studies concerning about the particle dynamic behaviour in 0g for the vibration suppression revealed that metal particles of high density, such as lead or tungsten steel, are the most common materials for better damping performance. According to them, because of the different particles dynamic behaviour induced by 0g, some of the conclusions and design guidelines obtained on the ground may no longer be applicable in space structures. Since it is impossible to do any 0g experiment on the ground it has hampered any attempt to establish an experiment-based benchmark that could be utilized to verify a theoretic model for predicting the particle damping property for orbital applications. The Discrete Element Method (DEM), pioneered by Cundall and Strack (1979) for the simulation of behaviour of granular particles, has been used to study particle damping, and shown a promising means for applications. The DEM simulations revealed that factors affecting 0g performance of a particle damper are the particle material, shape and size, the volumetric packing ratio, the restitution coefficient of particles and the friction coefficient between the particles. Anyway, considering all the discussions regarding the granular dampers, even if they were mentioned more in the vibration control attempts, their simplicity, reliability and the applicability in the space environment make them very interesting also for the impact mitigation in harsh environment which is the main purpose of this work.

2.3.3 Dry Frictional Damper

The damping mechanism of the friction is given by the slip force which may be constant or it may be an arbitrary function of the relative velocity. Constant or linear expressions of the slip force are used in models known as Coulomb friction law. The laws of the dry friction are usually different from static friction between surfaces which are not moving one in respect to the other and for kinetic friction (sometimes called sliding friction or dynamic friction) between surfaces with relative displacements. For the static friction,

the stick force is exerted in a direction that opposes potential moving (practically, it opposes to the resultant of forces). The static friction is a function of the external force and it exactly cancels it. When the other applied force overcomes this threshold value, the motion would commence. In the case of kinetic friction, the slip force opposes the relative movement between the contact points. Vehicles often uses friction elements because they are cheap and require only low maintenance. The dry friction dampers are much cheaper and more rugged than hydraulic dampers due to their mechanical simplicity. Moving towards the space application, NASA has developed a dry frictional shock absorber able to decelerate a vehicle as it impacts a surface. A dry frictional device was designed to afford minimum rebound and it is lightweight, compact, and needs no lubrication or hydraulic fluids. It offers a significant advantage over conventional hydraulic shock absorbing devices and can be used on vehicles operating in high vacuum and extreme temperature environments. Under such conditions, conventional devices eventually lose their lubricants and fluids. This device might be used also in such applications as aircraft landing gear and arresting devices, the bumper of motor vehicles and railroad cars, and artillery recoil mechanisms. It should be interesting for shock and energy absorbing devices requiring minimum rebound. It consists essentially of a cylindrical body, housing an internal expanding brake mechanism attached to the actuator rod, which is firmly attached to the vehicle body. The end of the cylindrical body is attached to a landing pad that impacts on a landing surface. In operation, the internal spring is compressed by the impact force and simultaneously expands radially forcing the peripheral surfaces of the cylinder which creates a frictional damping force. However, the presented solution remains a passive dissipation device since cannot be tuned according to the external parameters (like velocity and stroke). A damper able to overcome this issue is the semi-active piezoelectric based friction damper. It consists of an actuator, which is based on a piezoelectric stack with a mechanical amplifying mechanism that provides symmetric forces. The advantages of such an actuator are its high bandwidth, actuating response and its ability to operate in vacuum environment such as in space. Because the actuator only needs to change the normal force exerted onto the vibrating (or simply moving) element, it requires very little actuating displacement and mechanical power. The active element is not required to generate a displacement having the same order of motion as

the mounts. Therefore, the amount of work done by the control actuator is significantly smaller than that required of a purely active control actuator. Also, since the friction actuator only dissipates energy from the system, it cannot cause instabilities to occur. This notion of producing a damping force by controlling a secondary variable, is called semi-active control and is attributable to Karnopp and co-workers. This approach can effectively increase the damping which is the main motivation of this work. Furthermore, a controlled friction damper, which uses only local and instantaneous information, possesses advantages in terms of cost, ease of implementation and, in case of system with multiple dampers, tolerance of partial failure. Modern electromagnetic actuators are well suited to provide rotational motion (electric motors), however their use as linear actuators is limited. Although they are capable of generating sufficient force and displacement, the large size, weight, electrical demands and cost of these actuators makes them impractical. Because of their high force and bandwidth capability, piezoelectric actuators appear to be a natural candidate as friction dampers. These actuators has potential application to space environment in which other viscous dampers as well as electrorheological and magnetorheological dampers are not suitable. As it can be noticed from the following figure, the moving components consist of the outer housing and the air bearing. The outer housing also comes in contact with the friction pads as it vibrates. The normal force provided between the friction pads and the outer housing induces a frictional load which retards the motion of the outer housing.

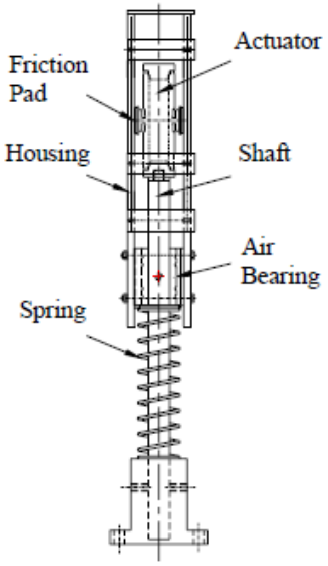

Figure 11 Frictional damper

Experimental studies were conducted with the discussed absorber. The friction pads were Kevlar bike disc brake pads and the housing were made of steel. According to their results, the frictional force of the actuator is essentially proportional to the voltage applied to the actuator. Different studies involving the frictional damper was performed, also using the Control Theory and more sophisticated models for the friction dynamic with the objective of maximizing the dissipated energy. Finally, considering that the modern piezoelectric stacks are characterized by high reliability in harsh environment (vacuum, cryogenic temperatures, radiations e t c) and a high actuation capability with a the minimum weight, volume and power, the just discussed damper seems to be one of the most interesting active solutions for the soft-landing purposes. A variant of this kind of damper is the pyrotecnically driven controllable linear brake which schematically is shown in the following figure. This solution consists of outer cylinder (1), which internal surface is a part of the brake's frictional pair and assembly module of the internal brake rod, built-in pre-stressing device and pyrotechnical control unit. The internal brake assembly module is composed of: conical pressing part (3) spreading the expandable spring collet becoming a second part of the frictional part of the brake (2). Also the pre-stressing coil spring (4), which tension is controlled via the pyrotechnical latching section are belonging to the internal brake assembly. A function of the pyrotechnical latching section is to reduce the spring pre-stress force after the operation of first pyrotechnic gas generator (5), whose chemical products of deflagration act with high pressure on internal surface of expandable latch sleeve, causing its expansion and allowing the piston insert (7) to move decreasing spring pre-stress force and lowering the same braking force of the system. After receiving the increase braking force signal, the second gas generator (8) chemical products of deflagration exert pressure on the piston insert, causing its movement to the previous position and pre-stressing again the coil spring to the initial value. When the piston insert translates to the suitable position, the expendable latch sleeve shrinks backs due to its elasticity, fixing the piston insert in the initial position. As a result, the breaking force is switched back to the initial value.

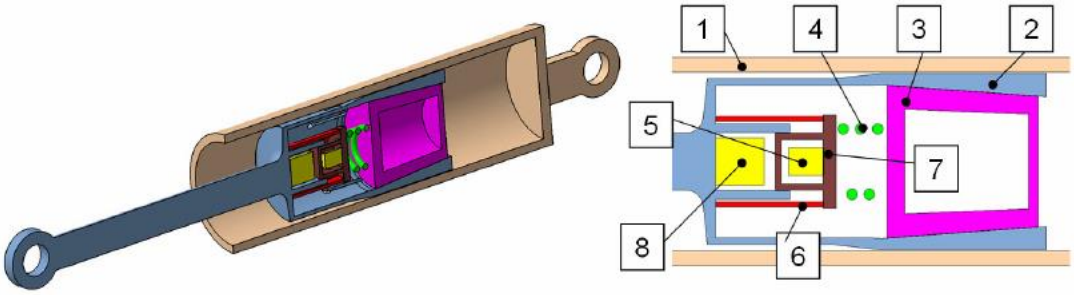

Figure 12 Pyro-friciotnal damper

The weakness of this device is that the control of the breaking force is limited to only two magnitudes of the force (high and low) and the reaction time depends strictly on the efficiency of the gas generation devices. In other words, it cannot give a continuous control during the dissipation process. Furthermore, its reliability depends on the pyro-devices which behaviour may be difficult to model and predict. For these reasons, this solution seems less interesting than the previously presented piezo-frictional damper. Another way to dissipate the kinetic energy through the friction is given by the elastomer piston head shock absorber. This damper has three primary components: the upper mounting plate, the lower mounting plate, and the elastomer puck or rubber disc which is sandwiched between them. The electric motor is connected via a shaft to the lower mounting plate and can move the plate axially up and down by means of a thread and nut connection. When the lower mounting plate is moved away from the upper mounting plate, the elastomer goes into a relaxed position for freer fluid flow around its outer surface and through its fluid channels. Conversely, when the lower mounting plate is moved toward the upper plate, the elastomer is compressed and its outer surface may contact the inner wall of the shock body, resulting in a sharp damping increase through Coulomb friction. In this way, the damper is able to change its damping ratio from low to high states and vice versa. Even if the original device requires the utilization of an internal fluid, the active impact damping and energy dissipation goals could be achieved also without the fluid. However, the elastomer, which is chiefly responsible for providing the semi-active damping functionality, is also the component most vulnerable to degradation, especially in the space environment. Cryogenic temperatures, the vacuum and subsequently the outgassing phenomenon together with the harsh radiation effects, could degrade dramatically the mechanical properties of the elastomeric

material. Moreover, the need of an electric motor to tune the compression/relaxation level of the elastomer, makes the entire device more cumbersome and less attractive. In the following figure a schematic view of the damper is given.

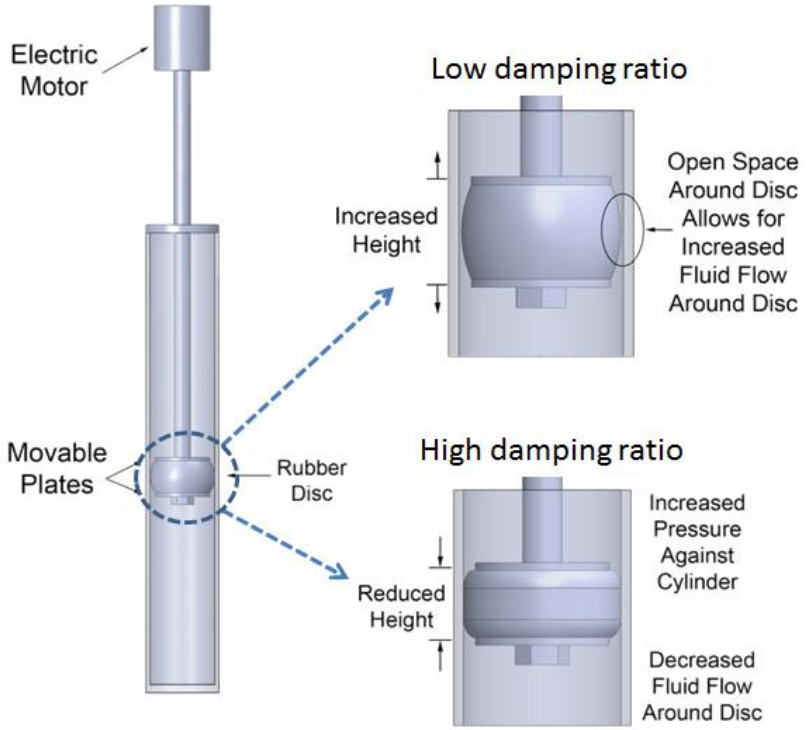

Figure 13 Elastomeric piston damper

2.3.4 Controlled Crushing Shock Absorbers

In the following part some solutions, which utilize the buckling and its adaptive control, will be presented. The first solution considered is the pressurized composite tube. Some experimental activities involving pressurized carbon-fiber/epoxy specimens shown that the crushing force can be controlled and so that pressurized composite elements can be fully expended under a range of crash scenarios demonstrating that an adaptive energy absorber can be designed using pressurized composite tubes in which the initial internal pressure and the release speed of the internally compressed gas are controlled. For this purpose, the laminated composite is chosen, because it offers vast potential for optimally tailoring a design to the applied loading, which in turn results in an energy

absorbing structure with increased strength and stiffness compared to the traditional metallic constructions. A circular shape is chosen since in general it provides the optimum geometrical form and it is easier to seal a circular section to maintain internal pressure. Typically, energy absorbers expend crash energy by crushing at a constant load over a variable stroke. The deceleration of the payload is therefore constant regardless of the crash velocity. The results is under-utilization of the crushing stroke if the crash speed is too low, leading to inefficient material usage and payloads experiencing unnecessarily high deceleration. Alternatively, if the crash speed is too high, the crushing stroke is exhausted and the tube "bottoms out", leading to very high peak loads experienced by the payload. With the variable load concept, the energy absorber is designed to crush with a variable load and constant stroke. In this case the payload never experiences unduly high decelerations because the energy absorber stroke is always optimally utilized, regardless of the crash scenario. In addition, the crushing can also be adjusted based on the payload mass. This can solve the issue that lower mass experiences higher acceleration for a constant force energy absorber. The thickness and the cross section must be chosen carefully in order to avoid a catastrophic global buckling of the axially compressed tube. In the following a view of the tubes is given.

Figure 14 Composite crushing tubes

The studies regarding this device revealed that high impact energy absorption can be achievable by increasing the internal pressure of the specimen. It has been observed that there are 60% and 55% of improvements, respectively for quasi-static and high speed tests, when compared to those tests without pressurization. Since only compressed air is added to the energy absorber, it indicates the potentially the crashworthy performance can be improved significantly without introducing any weight penalty. In order to improve the performance, a further work could be focused on the development of

practical energy absorbing structures which can automatically set energy under crash loading conditions. This could involve the development of suitable crushing system with a quick response pressure regulator, which is capable of releasing the compressed air rapidly under realistic impact loading. Other researches were focused on the development of the same type of solution using thin walled structures made of aluminum or steel where the energy absorption is given by the plastic folding. On those researches, the possibility to fill the thin walled structures with granular material is mentioned. Those devices could be combined with buckling initiators in order to reduce the initial peak crushing force. As in the previous case, it is focused on the concept of filling an axially loaded circular tubes with compressed gas in order to take advantage of the effect of the gas compression during impact and to affect the shape of deformation of the absorber. Moreover, this solution can improve the lateral load behaviour through the internal pressurization and the risk of explosion can be avoided through an active control (using automatic check valves). In operation, the inflation occurs before the impact after the energy detection. During the impact the gas release is controlled actively in order to ensure the optimal energy absorption. The adaptation to the actual loading results in favorable stress distribution, constant deceleration of the impacting object and desired final deformation. However, the need of a pressurization system for the correct working, makes this device complex, less reliable due to the gas leakage phenomenon and if composite tube is utilized, also susceptible to the material degradation in case of long travel in the harsh space environment. Another way to exploit the structural deformation energy in a controlled manner is given by pyro-adaptive impact absorber. It is a technique of controlling the energy dissipation density in lightweight thin walled structures by reducing the crushing stiffness during an impact process. This solution allows to decrease average crushing force when needed, by firing pyrotechnically actioned detachable connectors which release additional members of the absorber and lead to decrease of energy dissipation. In the following an illustrative figure of the device is presented.

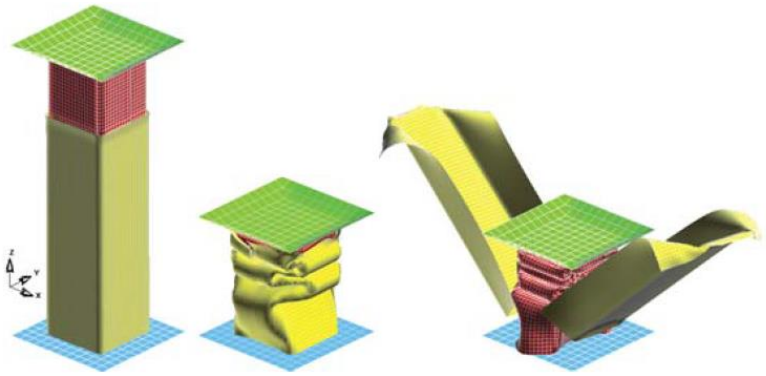

Figure 15 Pyro-controlled crushing structures

According to the experimental results obtained with this device, the active control of the pyro-connectors (where a photocell triggers the ignition time) lead to a lower value of the deceleration with respect to the passive case and the kinetic energy of the falling mass is dissipated through the plastic deformation of the absorber. Actually, the reduction of the stiffness is necessary to avoid the Euler buckling which can cause a reduction of the absorbed energy. Indeed, at the beginning of the deformation process, there is an axial crushing which may be followed by a global bending at low velocity if the stiffness is not reduced during the impact, while if the stiffness is low from the beginning, a progressive crushing is not observed. The reduction of the maximum deceleration can be achieved by a proper selection of the time instant to detach the stiffeners. The response of the device could be actually compromised by the delay of ignition of the pyro-connectors. The proposed solution adopts only two different levels of dissipation. Actually, even if the dissipation level could be more discretized adding multiple detachable layers, this could also increase the weight and the volume of the system and lead to a further complication due to layer interference during the detachment sequence. Another smarter way to control the buckling of the deformable structures in order to achieve an adaptive energy dissipation of the system is given by the studies related to the active buckling control of beams using piezoelectric actuators. The goal is to increase the beam buckling load by using piezoelectric actuators with an optimal feedback control. The tests were performed considering a simply supported beam with axial compression and z-polarized actuators. According to the results, in this way the beam was able to support a load up to the third critical load and revealed that the response depends also on the position of the actuators. The interesting aspect of this

device is that since the piezo-actuators can control the critical load of the beam, they could be tuned according to the energy that should be dissipated in order to achieve an optimal deformation/crushing behaviour during the impact. However, considering the preliminary status of the discussed device and the low capability to control the buckling (third critical load) with the unpredictable behaviour of the piezo-actuators during the deformation, it seems not to deserve a particular attention. The structural deformation control is exploited to obtain the impact energy dissipation also in the last following solution: adaptive truss structures. It consists of particular truss structure where the active energy absorption is obtained by the yield stress adjustment. It is based on advance impact detection and semi active dissipators called structural fuses which are shape memory alloy washers. The yield forces in the active elements depends on the friction force generated in the fuse by activating a different number of washers. It is able to provide a significant reduction of the acceleration level through a control which is formulated considering the number of active elements and trying to find the optimal distribution of the control yield stress which minimizes the acceleration. The impact detection may be provided by a set of sensors, which respond in advance in case of collision (e.g. radar, ultrasonic devices) or are embedded into the structure within a small passive crush zone (e.g. piezo-sensors). Estimation of the impact energy is then based on an inital deformation of the passive zone. In the following figure, a schematic view of the device is given.

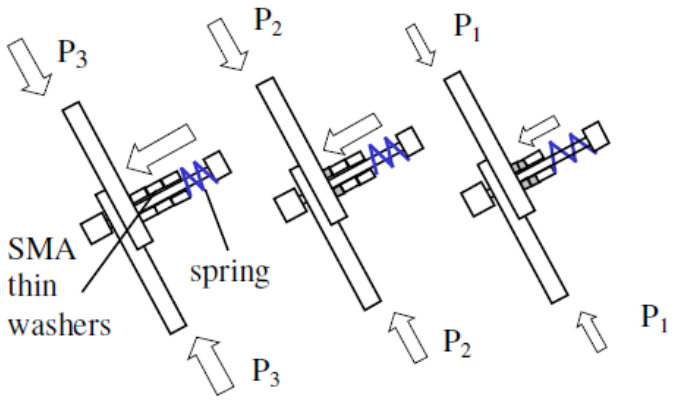

Figure 16 NiTiNOL fuses

This structure is able to operate both in semi-active and active modes. In the first strategy, yield stresses in structural members located in active zones remain unchanged

during an impact. In the second one, a possibility of real-time changes in control parameters is assumed. In this case, the semi-active strategy has a different meaning from what was discussed in the frictional absorber dedicated part. The yield stress level in active elements is adjusted according to the value of the kinetic energy of the impact. There are works which tried to demonstrate that adaptive impact absorption problem, with the adaptive truss structure, can be solved through the Particle Swarm Optimization both in the design and in the operational phase of the absorber. In any case, the elasto-plastic behavior for the fuses was assumed. The weakness of this last device is that the nitinol fuses needs a proper thermal control in order to be effective in the active or adaptive impact energy absorption. Considering the vacuum and cryogenic temperature of the space environment, this solution may create thermal/power issues which could be better to avoid.

2.3.5 Hydraulic, Magneto-Rheological and Elastomeric Shock Absorbers

Hydraulic systems and absorbers are often used in engineering application because they are able to dissipate a large quantity of kinetic energy. The mechanism of dispersion is obtained through a piston sliding in a viscous fluid cointained in a cylinder, where the friction of the fluid flowing across the orifices, dissipates kinetic energy into heat. The orifices and the dimensions of the chambers are the main parameters, because damping, pressure, and in general performances of the absorber, are very influenced by them. They are employed a lot, in aeronautic field, as landing gear for aircrafts, coupled with a tank of gas that, thanks to its elasticity, restores the initial stroke of the damper. Also in automotive sector they are employed a lot, with the same principles, but coupled to a real spring that has the same role of gas tank for aircrafts. Once the number, dimensions and geometry orifices are sized, defined characteristic dimensions and the pressures in chambers, performances of absorber are fixed.

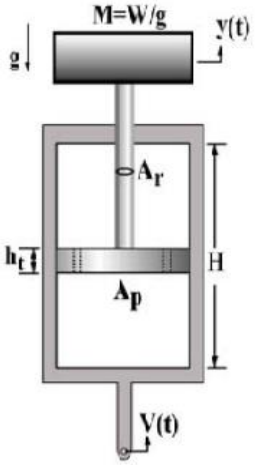

Figure 17 Schematic view of the liquid shock absorber

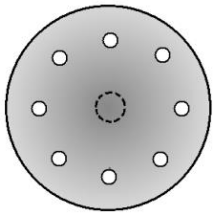

Figure 18 Top view of the orifices in the piston

This passive mechanism can become an active one, if coupled with a control system and an external source of energy. For example, adding an external reservoir containing fluid at a different pressure, and regulating in a proper way the separating valve, the pressure inside the main tank could be controlled. Obviously, weight and complexity of the system would increase, but for some application an active control may be useful. Another way to make the absorber active, is to regulate, while the dissipation is taking place, the dimension and geometry of the orifices in function of piston position with respect to the cylinder, for example through piezo-electric materials. The design shall take into account a lot of aspects, as operating pressure, temperatures and fluid dynamics, in order to avoid phenomena as flow choking, shock waves and cavitation. The kind of working fluid employed, afflicts the features of the shock absorber. Traditionally, the fluids employed are Newtonian, mainly air or oil, and are characterized by a linear relationship between stress and strain rate, where viscosity of the fluid is the constant of proportionality. But if it is required a force that varies with velocity, and so with strain-rate, a non-Newtonian fluid should be employed, choosing the one with the proper non-linear curve. The magnetorheological absorbers try to join the properties of Newtonian and non-Newtonian hydraulic absorber, modifying, through an applied magnetic field, the properties of the working fluid, especially viscosity and yield stress. Micron-sized magnetizable particles are suspended in a non-magnetic carrier fluid, such as mineral or silicon oil, whose rheological properties change rapidly and reversibly from liquid-like to solid-like depending on yield stress, under the

influence of an external controlled magnetic field acting orthogonally to fluid velocity. The controlled change of microstructure can guarantee a response for a different condition of yield stress, with a maximum limited by the saturation magnetization of the magnetic particles. Magnetorheological dampers are employed often in automotive sector. There is a version where the magnetic particles are suspended in a non-magnetic elastomer instead that in a carrier fluid, but applying an external magnetic field, it's possible to control the modulus. Although all the technologies presented above are interesting, they are not suitable for the purpose of this thesis because liquid fluids, in space, where there is vacuum, tend to evaporate, and so their properties would change drastically. Also elastomeric materials have a bad behavior in space, where they suffer from outgassing phenomenon due to vacuum, and, because of radiations and low temperatures, their micro-structure change damaging mechanical properties. Therefore, these types of possible technologies, have been rejected.

2.3.6 Electro-Magnetic Brakes

This kind of braking system exploits the relative motion between a magnet and a metal or alloy conductor, generating an eddy-current which induces a reverse magnetic field that opposes to the one of the magnet. The mathematical description of the induced eddy-current and of magnetic field is rather complicated, therefore designers make certain assumptions in order to describe the phenomenon, as constant magnetic field and an optimal magnetic field distribution. Magnets could be permanent, made of iron, aluminium, samarium and cobalt alloys, or electromagnets, where the magnetic field intensity depend on the feeding current. There are different applications of magnetic brakes, especially in railway and automotive sector (buses and tracks), where weight and power of the technologies adopted is not a so limiting requirement.

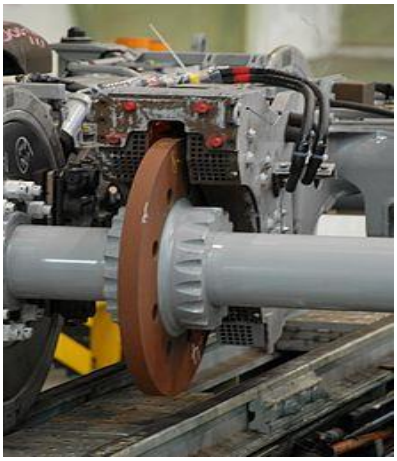

Figure 19 Rotating magnetic brake

Figure 20 Linear magnetic brake

Two different types of magnetic brakes are available, exploiting both the principle of eddy currents, one rotational and one translational. The first is used to brake trucks, cars or trains, and consists in a conductive disc in-built with the rotating wheel of means of transport, put between electromagnets, and when braking is required, the AC generator energizes them in order to produce a magnetic field. Also permanent magnets can be used, but the braking force can't be regulated. However, the disc, due to its rotation, sees a variable magnetic field in time, and according to Maxwell's equation, an electric field is created. So, in accord with Laplace's law (general case of Biot-Savart's law), an eddy-current is generated, heating the disc and dissipating in this way the kinetic energy. Eddy-currents produce a magnetic field that opposes the one produced by electromagnets, slowing down the disc and thus the wheel. The second type is based on linear motion, and it's used for trains or as shock absorber in aerospace and mechanical applications. It provides for a magnet moving in a tube made of conductive material, which sees a variable magnetic field in time and, again, according to Maxwell's equation, an electric field is produced and so eddy-currents are generated, causing a magnetic field which goes against the one of the magnet. In railway field the conductive plates may be rails, with magnets on board the train, or the magnets could be rails and conductive plates are assembled on board. An important parameter for electromagnetic brakes is the relative velocity, because the magnetic field produced by eddy-currents which opposes magnets magnetic fields, is strictly related to how fast the conductive materials meets the imposed magnetic field. Taking a conductive tube and a falling

magnet inside it, according to Lenz's law, the magnet is repelled by the lower section and attracted by the upper section, observing a damping force. The net force acting on the magnet is the sum of the forces generating by all sections, and it increases with magnet velocity. When the velocity reaches the value at which the magnetic force completely compensates for gravity, the acceleration will be zero, and the magnet will fall at constant terminal speed. For a sufficiently strong magnet, the terminal speed is reached very quickly. The magnetic brakes, both rotational and translational, if coupled with an electric motor and an energy source, could become actuators, accomplishing both functions of landing gear and leveling of lander attitude, allowing hopping mobility too. The European Space Agency is doing some tests and experiments about on these actuators for landing and leveling applications, but at the moment there are still problem related with the high power demand. So, summarizing, the main benefits achievable using magnetic brakes are: lack of wear due to the absence of friction, since the braking force is derived from the interaction of two magnetic fields, with the dissipation of the kinetic energy into heat, through eddy-currents generated in the conductor; reduction of sensitivity to high temperatures with respect to friction brakes, where friction coefficient is strictly related to temperature; controllability of the quantity of energy dissipated if electromagnets are used; possibility to brake efficiently also in wet conditions. But, on the other side, there are some drawbacks that limit the employment for space applications: permanent magnets for generate a significant magnetic field are heavy; if electromagnets are used for generating magnetic field, large power are required; a relative velocity between magnet and conductor is requested, and at low relative velocity the braking force is low; with electromagnets, lack of failure safety due to the fact that, if excitation current may not be available for any reason, the brake is totally useless. However, considering the high controllability and the possibility to be used as an actuator and the high environmental resistance of some magnets like the SmCo, this solution remains still interesting and deserves a further analysis.

$$\mathcal{E} = -\frac{\partial \Phi}{\partial t}$$ **Lenz's law**

$$\nabla \times \vec{E} = -\frac{\partial \vec{B}}{\partial t}$$ **First Maxwell equation**

$$\mathbf{B}(\mathbf{r}) = \frac{\mu_0 I}{4\pi} \int_\gamma \frac{\mathrm{d}\mathbf{l} \times (\mathbf{r} - \mathbf{r}')}{|\mathbf{r} - \mathbf{r}'|^3}$$ **Laplace's law**

2.3.7 Passive Deformation Shock Absorbers

Passive deformation shock absorbers are employed in situations where the contents of kinetic energy is rather high, and known a priori. In fact, they convert the mechanical energy in work of structural deformation, but for the process of deformation to be activated, a certain value of stress shall be overcome. A good design should dissipate gradually the total amount of energy, to have a small deceleration and without transmitting high forces to the pilot, or people on board of the means of transport. Indeed, their major applications are in aerospace, automotive, railway and car races sectors. Often sandwiches structures are used, and they are constituted by skins made of metallic or composite material and filled with polymeric, metallic or ceramic foam, typically aluminium. They are passive systems, where for a given impact loading conditions, an optimum density of foam may exist in order to absorb the maximum possible amount of energy. Aluminium foam is a lightweight material, with an excellent plastic energy absorption and environment resistant characteristics.

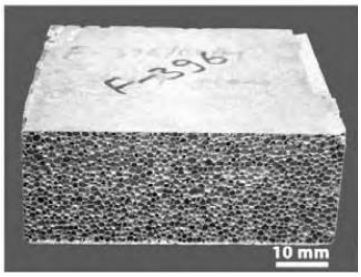

Figure 21 Aluminum-based foam plate product

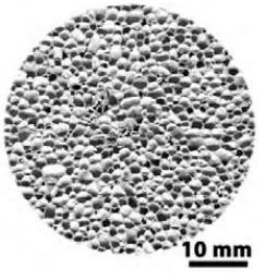

Figure 22 Cross-section of Aluminum-foam revealing cell structure

The metallic foams are obtained dispersing gas in a solid matrix, with a significant weight reduction and the improvement of some mechanical properties as bulk modulus. Polymer foams are used especially for insulation and packaging, but not for mechanical applications due to their low structural efficiency, whereas ceramic foams are used for insulation and structural implementation. Foams are commonly classified in two types: closed-pore foams and open-pore foams. Aluminium foam belongs to the first category,

which has a high compressive strength due to its structure. The open-foams are identical to the closed-cell ones except the membranes have been removed, producing large channels of interconnected cells and allowing liquids and gases to pass through. If the non-solid phases of the structure are non-random and in form of close-pores, the material is usually defined honeycomb structure. The dimensions of the pores can vary from several microns to several millimeters. There is a special class of closed-cell foams called syntactic foams. They are composite materials synthesized by filling metal, ceramic or polymer with hollow particles called micro balloons. The presence of hollow particles results in lower density, lower thermal expansion coefficient, plastic strength, permeability and, in some cases, radar or sonar transparency or electromagnetic waves shielding. A wide variety of micro balloons are available, including glass, carbon and polymer microspheres, and they influence the compressive properties, whereas the tensile ones are influenced by matrix. The design of the sandwiches structures is based on what written above, taking into account all aspects, skins, kind of material, constituent elements, type of foam, with the goal to reach an anisotropic behavior optimized for some load directions. When the shock absorber is subjected to the peak load, it will tend to destabilize on weakest or most stressed sections, forming some plastic hinges. The absorption of energy is due to the restricted plasticization on the hinges. Wall tracts between two hinges are almost not deformed, and the energy stored inside will be rather low. Carrying on the deformation, hinges close, and the linear tracts go to contact. The honeycomb structure included in these segments, works in compression along the cells axes, at the maximum of its capability. The target of sandwiches structures is to make work the honeycomb at its fullest capacity, so having the maximum absorption of energy with the minimum mass.

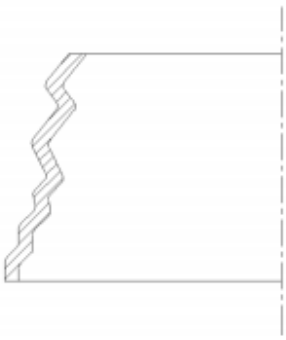

Figure 23 Wall instabilities

To reach the goal, it's needed to lead the structural deformation, in order to form a sufficient number of plastic hinges, but not too large otherwise the honeycomb wouldn't be exploited properly. Some triggers can be used to activate the dissipation mechanism, and once it's activated, it proceeds autonomously. The presented technologies is often employed for energy absorption application, but request to know the exact amount of energy to dissipate, and the mechanism is passive and no more controllable after the design. Therefore, it's discarded for this thesis, because an absorber able to dissipate kinetic energy also in condition different from the one of design is required, in order to be more robust since properties of the celestial body are not exactly known a priori.

2.3.8 Shape Memory Alloys Actuators

Shape memory alloys actuators are becoming increasingly popular for engineering applications, providing small dimensions and low weight, high work output and simplification of design. "Shape memory" effect describes the effect of restoring the original shape of a plastically deformed sample, by heating it. This phenomenon results from a crystalline phase change known as "thermo-elastic martensitic transformation", which is found only in a few alloy systems; the most important is the Nickel-Titanium alloy, but there are also shape memory alloys made of Copper-Zinc-Aluminum, Silver-Cadmium or Nickel-Aluminum. Nickel-Titanium shape memory alloy has been developed by Naval Ordinance Laboratory of U.S. Navy in 1959, and for this reason it is known as NiTiNOL. It owns good properties as high strength, high electrical resistivity, large recovery strains, easy workability and excellent corrosion resistance. Shape memory effect, thanks material properties, can be used to generate forces and actuation. At temperature below the transformation temperatures, these alloys are martensitic, and are very soft and can be deformed easily. Then, heating above the transformation temperature, recover the original shape and convert the material to, high strength, austenitic phase. Below, it is reported the diagram strain-stress of NiTiNOL alloys, in martensitic and austenitic conditions.

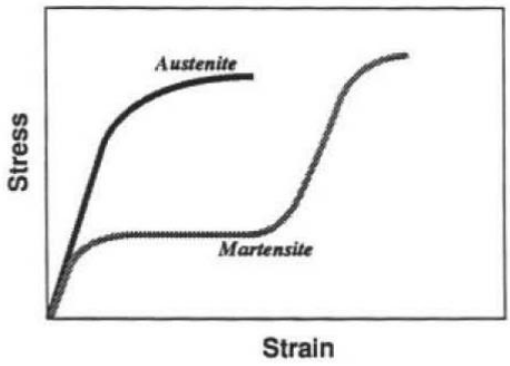

Figure 24 Stress-strain curve of SMA

Looking at the martensitic curve, it's clear that exceeding a first yield point, there is plateau region where, increasing the strain, the stress doesn't raise. This region can be thermally recovered. When deformation goes beyond the second yield point, it's no more recoverable, and the material it's deformed in a conventional way. The effect of actuation achievable could be linear, but in bending or torsional deformation mode too. NiTiNOL actuators resist for many thermal cycles, up to 100'000, and show excellent forces generated with just small deformations, for example 1000 N with a deformation of 0.5 mm for some valve used in automotive applications. Typical transformation temperatures are from -30 °C to +70 °C, but some binary and ternary alloy arrives to +150 °C (Shape Memory Actuators Improve Car Performance, Stoeckel). There are two main types of shape memory actuators, one thermal, which responds to a temperature variation of the system (for example valves), and one electrical, that applies a force when it is requested, by being electrically heated. NiTiNOL presents a high resistivity compared to common materials such as copper or aluminum, and this property is very useful because allows heating the material giving it an electric current, and being a metal alloy, it can conduct large currents. Another applications of shape memory alloys are in bio-medical field, thanks to its bio-compatibility and flexibility, or could be in suspension where controlling austenitic and martensitic phases it's possible to control damping and stiffness of the material, and so the buckling modes, but is still under study. It's this last application that has inspired a possible shock absorber for this thesis. The shock absorber would be an adaptive one, where, depending on arrival velocity of the spacecraft toward celestial body, the properties of the absorber would be properly changed, by electrically heating it and so controlling its microstructural composition,

stiffness and damping. But due to the thermal inertia of the process, the complicated thermal control system required to modify the temperature of the absorber, and the complicated modelling of the phenomena (being a structural deformation coupled with thermal phenomena), this kind of technology has been discarded.

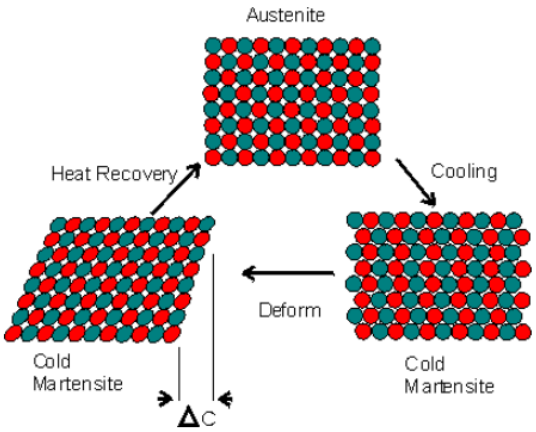

Figure 25 Example of NiTiNOL application: Thermostatic Governor Valve

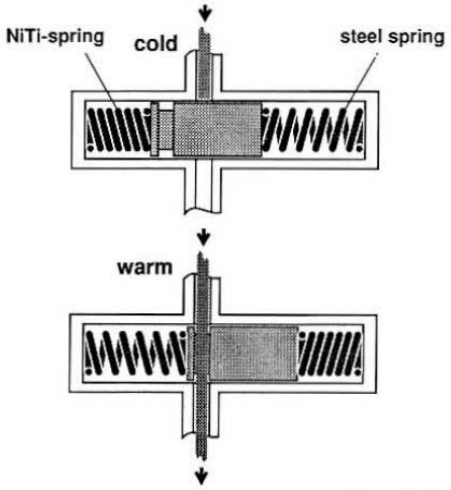

Figure 26 NiTiNOL operating principle

2.4 Preliminary Design and Configuration Selection

In the followings, the motivations which lead to the selection of the most suitable technologies will be described. According to the previous section about all the considered technologies, it is clear that passive, semi-active and active solutions are available. The passive solutions, which are preferred by the past missions because of their simplicity and reliability, cannot be tuned according to the mass, velocity and so the kinetic energy to be dissipated. Those parameters are not easily and exactly predictable in the design phase of the mission. A slight variation of the approaching velocity, of the mass (unpredicted maneuvers and so different fuel consumption), of the characteristics of the surface and of the gravitational field, could easily jeopardize the success of a landing mission. The fully passive solution like energy dissipation through

the structural deformation of foams, sandwich structures or polymeric absorbers, even if able to dissipate a high amount of energy, are too susceptible to external parameter variations. As it was presented before, there are solutions which can actively control the deformation process before and during the impact. Gas filled composite/metal cylinder, pyro-adaptive absorber or piezo-controlled buckling technique are some of them. Even if these solutions would increase the robustness of the system w.r.t the purely passive case, the need of a pressurization system easily susceptible to any leakage phenomenon in the first, the strict dependency on the reliability of the pyro-connectors (considering a 10 year long deep space mission) for the second and the low degree of controllability for the second (just 2 different stiffness') and for the third (capacity to control up to few critical loads) make them not so much appealing. Another smarter way to control the deformation can be achieved with the NiTiNOL absorbers. These temperature sensitive devices may need a complex dedicated thermal control system to work correctly and because of the thermal inertia of the material, the real-time active control may be very difficult to obtain. More traditional terrestrial solution like hydraulic dampers or more advanced magneto-rheologic dampers are not suitable for a long-term deep space application, like a comet landing, because they need a proper thermal control to maintain the fluid viscosity in an acceptable range in order to operate efficiently, which could be a concern for power, mass and complexity. Also the magneto-rheological elastomers could be subject to a degradation due to the harsh environment (cryogenic temperatures and radiations) which could make the material's behavior unpredictable. Solutions involving compressed gas like the piezoelectric pneumatic dampers and airbags, even if more light and simple than the hydraulic ones, have a big weak point which is given by the gas leakage susceptibility. Regarding the remaining solutions, the followings have been discussed. The piezoelectric frictional absorber is characterized by an intrinsic simplicity (it consists on just two sliding tubes which act as a brake), lightweight, reliability (modern piezoelectric stacks can operate in cryo-vacuum and high temperatures conditions, and are radiation resistant), fast response and low power consumption. Similarly to the last case, magnetic brakes or actuators are environmentally robust (Sm-Co magnets produces a magnetic field which is almost invariant to the radiation dose and temperature variation) and are highly controllable while the mass and the power consumption could be a concern. The granular damper

was presented as an active solution in the form of Vacuum Packet Particles (VPP). In this case, the active damping control should be given through the regulation of the internal gas pressure of the device. It would be subject to the leakage phenomenon which was the main weak point of the other gas involving solutions. However, even in a case of absence of the pressurizing gas because of the leakage, the granular material could be able to dissipate the impact anyway. Moreover, considering simply the granular material, its intrinsic simplicity, the absence of any fluid and gas, the environmental resistance (especially when metallic granules are used) and the ability to dissipate a huge amount of energy make this solution very interesting for an eventual active-passive hybrid configuration. In the following table, a more rigorous technology selection procedure is shown. The selection was done giving a score according to the level of the reliability, environmental robustness, efficiency, durability, controllability and to the mass and volume.

	A	B	C	D	E	F	G	H	y/n
Piezo-pneumatic	4	5	4	4	5	4	3	29	ok
Metallic VPP	5	5	4	4	4	4	5	31	ok
Polimeric VPP	5	3	4	3	4	4	5	28	no
MR	2	1	5	1	4	2	4	19	no
Elastomeric MR	3	2	3	2	5	3	2	20	no
Hydraulic	2	1	5	2	4	1	3	18	no
Crushing structure (metal)	5	5	5	5	0	3	4	27	no
Crushing structure (polymer)	5	2	5	2	0	4	3	21	no
NitiNOL	4	5	5	5	1	3	4	27	no
Magnetic brake	4	5	4	5	5	2	4	29	ok

Magnetic actuator	4	5	4	3	5	3	4	28	ok
Piezo-frictional	5	5	3	5	5	5	4	32	ok
Expandible elastomeric piston	3	2	2	2	4	3	3	19	no
Pyro-adaptive	4	5	5	5	1	2	3	25	no
Airbag	2	3	4	3	5	5	1	23	no
Controlled buckling	4	5	5	5	1	3	4	27	no
Gas filled cylinder (composite)	3	2	5	2	1	3	3	19	no
Gas filled cylinder (metal)	3	5	5	3	1	2	3	23	no

Table 2 Maximum possible score = 35. VPP = Vacuum Packet Particles. MR = magneto-rheological

A = Reliability. B = Environment. C= Efficiency. D = Durability.
E = Control. F = Mass. G = Volume. H = Score.

According to this preliminary selection, the most feasible solutions are the piezoelectric frictional damper, the magnetic damper and the granular damper. These technologies will be analyzed more in detail and subject to a further selection in a dedicated section.

2.4.1 Preliminary Design of Passive Granular Actuator

A preliminary design of the chosen possible technologies is performed in order to understand the feasibility of the actuators in terms of working, mass, power and dimensions. The design is based on the forces, stroke, sliding velocity and time obtained from multi-body simulations. Every actuator is sized to work singularly, with a prefixed stroke of **0.25 m**. For what regard the passive granular actuator, the multibody simulations have produced a maximum force of **1750 N**, a medium sliding velocity of

1.5 m/s and a medium sliding time of **0.6 s**. The model consists in two masses linked with a parallel spring-damper system, subjected to a gravitational field very low since the body on which the spacecraft is landing on is an asteroid or a comet, in the order of 1e-04 of terrestrial gravity. The mass of spacecraft plus the mass of the three actuators is concentrated in the upper part whereas the lower part represents the mass of three feet. It's chosen to consider three legs in terms of mass, but the multibody simulations and sizing are performed with just one spring-damper system in order to be more robust. The nominal landing velocity considered is **2 m/s**, the double of Philae landing velocity, used as basis of comparison since it is the only past mission of this type and it has failed the landing. Done these premises, the following part is focused now on the sizing process and criteria selected to accomplish the goal. The actuator is formed by a piston sliding in a cylinder containing granular metallic material. The piston is made of a cylindrical beam of **0.25 m** and variable radius plus a head consisting in a truncated cone intruder with height **0.05** m and variable radius. Internal cylinder height is **0.3 m**, since 0.25 m are necessary for stroke plus 0.05 m for include piston head and not permit to granular material to exit from the cylinder. The head is important because thanks to its geometry allows to the piston to slide more easily through granular material. Piston beam radius is computed taking the two times minimum value needed to not cause compressive buckling, whereas internal radius of the cylinder is chosen as two times piston beam radius. Below a general schematic view of the passive granular actuator is reported.

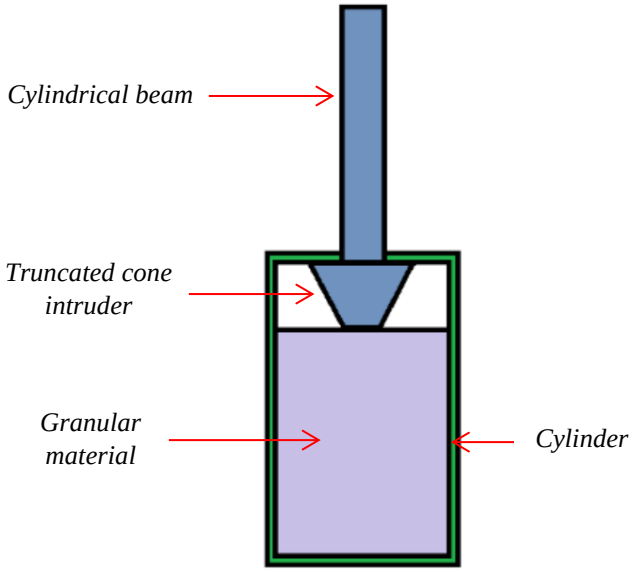

Figure 27 Schematic section view of passive granular actuator, where blue element is the *piston*, composed by cylindrical beam and truncated cone intruder, grey element represents the *granular material* and green element represents the *cylinder*

$$R_{cr} = \left(\frac{4Fh^2}{0.25\,E\,\pi^3}\right)^{0.25}$$

Equation to determine minimum radius of a beam for avoiding compressive buckling, where ***F*** is the acting force, ***h*** the piston beam height and ***E*** the Young modulus of material.

So, fixed internal cylinder radius, the radius of piston head is computed considering that the flow rate of granular material is its mass divided for sliding time and it is equal to the product of granular material density (800 Kg/m^3, since it isn't a continuum but it's in powder form), medium sliding velocity and the area of the orifice.

$$\dot{m} = \rho v A$$

Mass flow rate equation, where $\dot{m}$ is the mass flow rate, ρ is the material density, **v** the flow speed and **A** the cross section.

The orifice is the difference of cylinder internal section and major radius of truncated cone, and the minor radius of the truncated cone is take as proportion between a cone high 0.07 and major radius m and the truncated cone considered of height 0.05 m. The thickness of cylinder is selected considering the pressure acting on its wall, and results the minimum value required is in the order of 1e-05 m, therefore a thickness of **1e-03 m** is assigned.

$$th = \frac{PR}{\sigma^y}$$

Equation to determine the minimum thickness required of a pressurized cylinder, where ***P*** is the internal pressure, ***R*** is the cylinder radius and σ^y is yielding stress of material.

Granular material is always in Aluminium since its density is low while three different materials has been considered for piston and cylinder: Aluminium, Steel and Titanium. All these materials present good mechanical properties and especially a space environment resistance, which is essential for the application of this thesis. The sizing is performed considering piston and cylinder once made of Aluminium, then of Steel and finally of Titanium, but granular material always made of Aluminium since it has the lowest density among the selected materials. Below are reported some mechanical

properties of selected materials, actuator mass and dimensions, which are obtained using every material.

	Density [kg/m3]	Young Modulus [Gpa]	Yielding Stress [Mpa]
Aluminium Alloy Series 7075	2800	75	95
Steel 1018	7870	205	370
Titanium Alloy Ti6Al4V	4460	115	850

Table 3

Piston beam radius [m]	0,0105
Piston beam height [m]	0,0251
Piston beam mass [kg]	0,2434
Major truncated cone radius [m]	0,0178
Minor truncated cone radius [m]	0,051
Truncated cone height [m]	0,05
Truncated cone weight [kg]	0,0639
Internal cylinder radius [m]	0,021
Internal cylinder height [m]	0,3
Cylinder thickness [m]	0,001
Cylinder weight [kg]	0,121
Granular material volume [m3]	3,45E-04
Granular material weight [kg]	0,2442
Orifice Area [m2]	3,83E-04
Actuator deployed total length [m]	0,552
Single actuator total mass [kg]	0,6725
Three actuators total mass [kg]	2,0176

Table 4 Actuator made of Aluminium Alloy Series 7075

Piston beam radius [m]	0,0081
Piston beam height [m]	0,0251
Piston beam mass [kg]	0,4072
Major truncated cone radius [m]	0,0138
Minor truncated cone radius [m]	0,0039
Truncated cone height [m]	0,05
Truncated cone weight [kg]	0,1063
Internal cylinder radius [m]	0,0163
Internal cylinder height [m]	0,3
Cylinder thickness [m]	0,001
Cylinder weight [kg]	0,2607
Granular material volume [m$^{3]}$	3,45E-04
Granular material weight [kg]	0,1453
Orifice Area [m$^{2]}$	2,32E-04
Actuator deployed total length [m]	0,552
Single actuator total mass [kg]	0,9195
Three actuators total mass [kg]	2,7586

Table 5 Actuator made of Steel 1018

Piston beam radius [m]	0,0094
Piston beam height [m]	0,0251
Piston beam mass [kg]	0,3108
Major truncated cone radius [m]	0,016
Minor truncated cone radius [m]	0,046
Truncated cone height [m]	0,05
Truncated cone weight [kg]	0,0814
Internal cylinder radius [m]	0,021
Internal cylinder height [m]	0,3
Cylinder thickness [m]	0,001
Ø Cylinder weight [kg]	0,172
Granular material volume [m$^{3]}$	2,78E-04
Granular material weight [kg]	0,1957
Orifice Area [m$^{2]}$	3,09E-04

Actuator deployed total length [m]	0,552
Single actuator total mass [kg]	0,7599
Three actuators total mass [kg]	2,2796

Table 6 Actuator made of Titanium Alloy Ti6Al4V

2.4.2 Preliminary Design of Piezolectric Active Actuator

The parameters utilized to design this kind of actuator, as for the previous cases, come from multibody simulations where the model is two masses linked by a spring-damper system. The maximum force that the actuator has to generate is **1400 N**, the stroke is prefixed at **0.25 m** and the number of curved piezoelectric plates is chosen at **four**. Every piezoelectric plate has a height of **0.05 m**, a thickness of **0.001 m** and extends for an angle of **80°.** When a piezoelectric plate is perfectly constrained and so unable to move, and a difference of potential is given to it, it responds generating a force that in literature is known as Blocking Force. This force varies in dependence on the direction of applied electric potential, controllable simply positioning electrodes in the desired direction. There is an axial blocking force, which corresponds to electrodes positioned along a direction of the plate and the blocking force is along the same direction, and a transverse blocking force, where the electrodes are positioned along a direction of piezoelectric plate and the blocking force is along another direction. Below are reported the equation representing these two types of blocking forces.

$$F_b = \frac{d_{33} l w}{s_{33} h} U$$

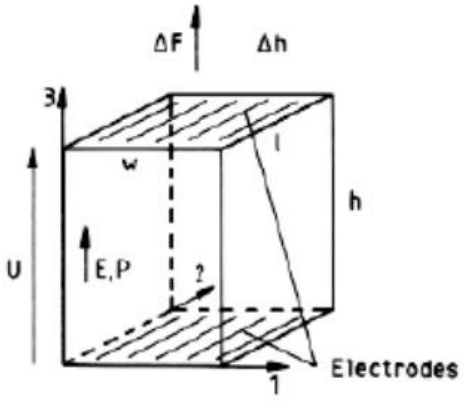

Figure 28 Equation of axial blocking force, where *l,w* and *h* are dimensions of piezoelectric, d_{33} and s_{33} are coefficients associated to direction 3, and *U* is the applied electric potential along direction 3. The Blocking Force is along the same direction of electric potential

$$F_b = \frac{d_{31}}{s_{11}} w U$$

Figure 29 Equation of transverse blocking force, where *w* is a piezoelectric dimension, d_{31} is the coupled coefficient between direction 3 and 1, s_{11} is the coefficient associated to direction 1, and *U* is the applied electric potential along direction 1. The Blocking Force is along direction 1

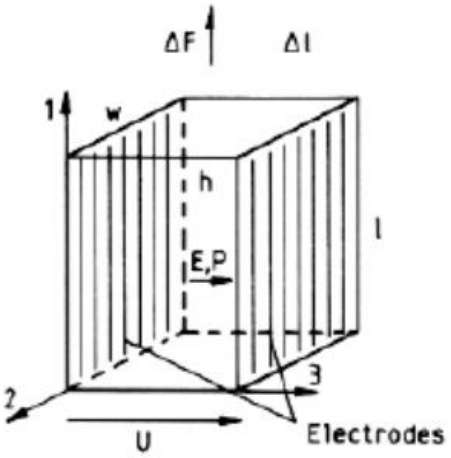

For the piezoelectric material PIC-151 (produced by PI Ceramic) the coefficients are:

d33 [m/V]	(500/3)E-12
s33 [(ms^2)/kg]	19 E-12
d31 [m/V]	(210/3)E-12
S11 [(ms^2)/kg]	1,50E-11

Table 7

Thin plates of Aluminium oxide are considered on the two sides of every piezoelectric plate, in order to electrically insulate the piezoelectric avoiding the dispersion of charges, but especially for increase friction coefficient between cylinder and piston. The piezoelectric plates in fact are in solid with the cylinder, and therefore a coating of Aluminium oxide is considered on piston, to increase the friction between cylinder block and piston during the sliding. The piezoelectric plates generate a force that depends on the applied potential, but the resulting braking force acting on the piston depends also on the dynamic friction coefficient existing between two surfaces. The braking force so is the force generated by piezoelectric plates multiplied by friction coefficient. Considering the friction between Aluminium oxide surfaces, and since the phenomena is occurring in vacuum, where there aren't impurities and contaminants present in atmosphere, with the consequent increase of friction, the friction coefficient is

about 0.98. The force acting on the piston so is more or less the same generated by piezoelectric plates. Both piston and cylinder are made of Aluminium. Finally, is considered a plate of steel between cylinder and external Aluminium oxide plate covering the piezoelectric one just in order to support the junction between them. Also steel and pure Aluminium have been considered as coating of piston and piezoelectric plates, but they don't have a so high dynamic friction coefficient.

Steel-Steel	0,57
Aluminium – Aluminium	0,34
Al_2O_3 - Al_2O_3	0,98

Table 8 Dynamic friction coefficients

To size the piston is considered again compressive buckling phenomenon, and for choosing minimum thickness of cylinder, the pressure acting on the interested internal wall cylinder area. Since a shear force is exchanged between piston and cylinder, it's also verified that the shear doesn't exceed the yielding shear stress. This last procedure is performed for all elements that exchange shear forces, piezoelectric plates, Aluminium oxide plates, steel plates, piston and cylinder. To make this step, it's used the Von Mises criterion, consisting in to identify shear yielding stress as axial yielding stress divided by square root of three, and verify if the shear stress present in the material is below Von Mises value.

$$\boldsymbol{\tau < \tau^y = \frac{\sigma^y}{\sqrt{3}}}$$

Von Mises criterion, where $\boldsymbol{\tau}$ is shear stress in the material and $\boldsymbol{\tau^y}$

A last data shall that be taken into account is the bandwidth of the piezoelectric actuator, that has to be greater of the frequency content of force the actuator shall provide. PIC piezoelectric actuators have bandwidth in the order of kHz, while the required force have a frequency content in the order of 1e+02 Hz. Here is reported the graph showing the frequency content of the required force.

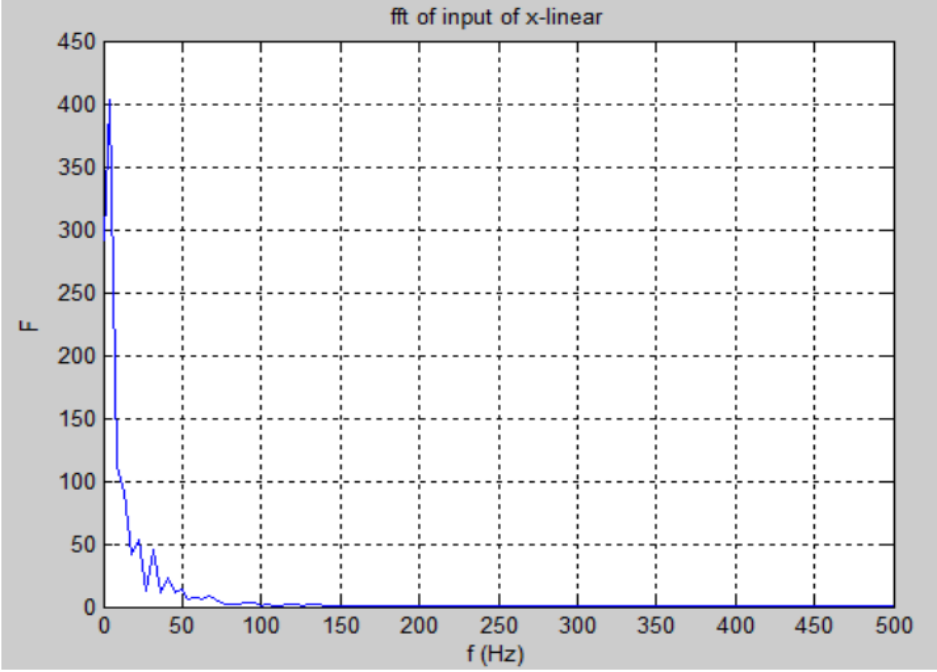

Figure 30 This graph has been obtained performing the Fourier Transform of the force the spacecraft is subjected to, and which landing system shall provide in order to decelerate the vehicle without transmitting it too high deceleration

A schematic view of the active piezoelectric actuator is reported below.

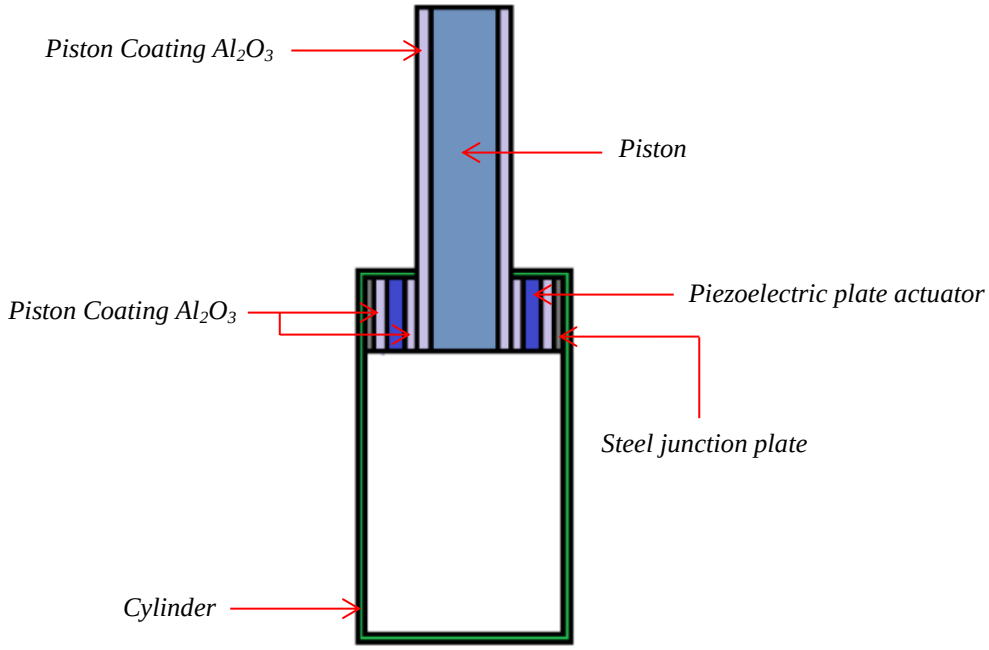

Figure 31 Schematic view of active piezoelectric actuator

Density Al_2O_3	3600
Density PIC piezoelectric [kg/m3]	7800
Density Aluminium Alloy Series 7075 [kg/m3]	2800
Density Steel 1018 [kg/m3]	7870
Yielding Stress Al_2O_3 [kg/m3]	330
Yielding Stress PIC piezoelectric [MPa]	76
Yielding Stress Aluminium [MPa]	96
Yielding Stress Steel 1018 [MPa]	370

Table 9 Material Data

Piston radius [m]	0,02
Piston Height [m]	0,3
Thickness Al_2O_3 piston coating [m]	0,001
Thickness cylinder [m]	0,001
Piezoelectric plate aperture [deg]	80
Height piezoelectric plate [m]	0,05
Thickness piezoelectric plate [m]	0,001
Al_2O_3 plate aperture [deg]	80
Height Al_2O_3 plate [m]	0,05
Thickness Al_2O_3 plate [m]	0,001
Steel 1018 plate aperture [deg]	80
Height Steel 1018 plate [m]	0,05
Thickness Steel 1018 plate [m]	0,001

Table 10 Active piezoelectric actuator dimensions

Cylinder mass [kg]	0,1426
Steel 1018 plates mass [kg]	0,0538
Al_2O_3 plates mass [kg]	0,0452
Piezoelectric plates mass [kg]	0,0490
Piston + Al_2O_3 coating mass [kg]	1,0591
Single active piezoelectric actuator total mass [kg]	1,4894
Three active piezoelectric actuators total mass [kg]	4,4681

Table 11 Masses

Axial case [V]	26,5
Transverse case [V]	830,4

Table 12 Voltage required for every piezoelectric plate

As it can be seen from the last data, the voltage for the axial case is not so far from the what was used on board the Philae lander and it is a value that can be easily achieved on the most common space systems. Together with its lightweight, simplicity and the good controllability, this aspect makes this device a feasible solution.

2.4.3 Preliminary Design of Active Magnetic Actuator

According to the previous selection of the technologies, this actuator deserves a more technical analysis. A preliminary sizing is performed using the force and stroke values obtained in multibody simulations in order to understand the feasibility of this electromagnetic device. The working principle of this actuator is given by the equation of the Lorentz force. The electromagnetic force is given by the cross product between the current and the magnetic field and it's perpendicular to them.

$$\vec{F} = k\vec{I} \times \vec{B}$$

I = current [A] k = wire length [m] B = magnetic field [T]

The actuator is sized as a hollow box containing the permanent magnets on two opposite sides with a piston which carries a head containing the electric wires. When the current flows through the wires, it interacts with the external magnetic field giving a force opposite to the piston motion according to the previous formula. The intensity of the force could be regulated controlling the current passing through the wires. In order to determine the magnetic field generated by the permanent magnets the following expression is adopted:

$$B = \frac{B_r}{\pi}\left[arctan\left(\frac{LW}{2z\sqrt{4z^2+L^2+W^2}}\right) - arctan\left(\frac{LW}{2(D+z)\sqrt{4(D+z)^2+L^2+W^2}}\right)\right]$$

The magnetic field depends on the geometry of the magnets and on the distance from the magnet and on its residual magnetic field Br [T]. The following figure illustrates better the meaning of the parameters present in the equation.

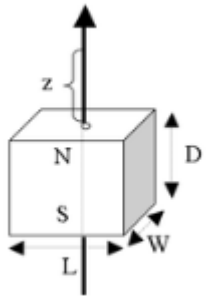

Figure 32 Example of magnet and its dimensions

During the sizing, the following constraints are considered:

Maximum force generated by the actuator [N]	1400
Maximum voltage required [V]	30
Electric wires length [m]	10
Maximum stroke [m]	0,25

Table 13

The previous value of the voltage is chosen as limit since it is similar to the one used on the Philae lander of the Rosetta mission. The material chosen for the permanent magnets is the Sm-Co (Samarium-Cobalt) because it is characterized by high reliability and durability in the harsh space environment as was mentioned in the section dedicated to the technology selection. The material considered for the piston and the box is the Aluminium because of its lightweight while the material for the piston head is the

copper because of its high electrical conductivity. Hereafter, the data of the materials used are given:

Density of magnets [kg/m3]	8400
Residual magnetic field of magnets (Br) [T]	1,15
Density of Aluminium [kg/m3]	2800
Density of Copper [kg/m3]	8920

Table 14

According to the stroke considered in the multibody simulations and a trial-and-error approach, the following dimensions and geometries are considered.

Magnets: they are box shaped elements attached to the walls of the external cage with the dimensions of **0.05 m** x **0.05 m** x **0.3 m** where the last value is the height. Obviously, in order to exploit all the available stroke (0.25 m) and to generate the maximum force from the beginning of the sliding, the magnets should have a total length equal to the available stroke summed with the length of the piston head.

Piston head: it carries the copper wires and generates the force during the sliding. For simplicity and to be mass-redundant, all copper-made head was considered. It has a box shaped geometry with the following dimensions: **0.05 m** x **0.04 m** x **0.05 m** where the last value is the height.

Piston rod: it has a cylindrical form with a radius of **0.01 m** and a height of **0.25 m**. The value of the radius was chosen higher than the critical radius which is defined by the material, maximum compression force and height to be robust against any buckling phenomenon.

External cage: it can be seen as an Aluminium shell which contains the magnets and the piston head. Its dimensions are **0.14 m** x **0.05 m** x **0.3 m** and the thickness is **0.001 m**.

The total extension of the actuator is **0.55 m**. The geometry of the actuator is schematized in the figure below.

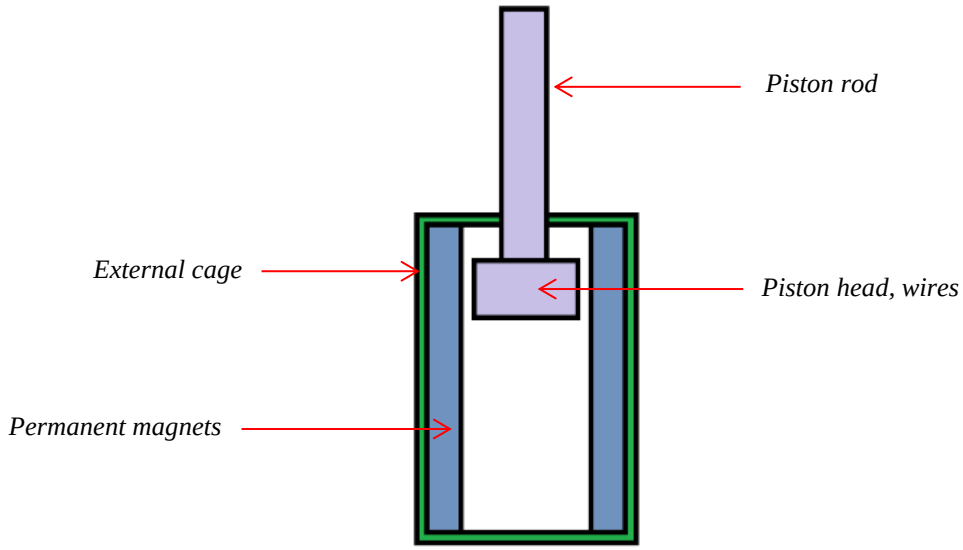

Figure 33 Schematic view of active magnetic actuator

According to the shown dimensions of the described components, their respective masses are calculated:

Single magnet mass [kg]	6,3
Total magnet mass (2) [kg]	12,6
Piston rod mass [kg]	0,2199
Piston head mass [kg]	0,892
External cage mass [kg]	0,363
Single actuator mass [kg]	14,0749
Total actuators mass (3) [kg]	42,2248

Table 15

Finally, the main outputs of this preliminary sizing are given:

Magnetic field generated by the permanent magnets [T]	0.2106
Power required to generate the desired force [W]	19938
Power required to generate 700 N [W]	9969
Power required to generate 233 N [W]	3323

Table 16

The last two data are related to the case where this actuator is used in series with a passive actuator of the same length (granular). The last value considers the case where the required force is distributed on 3 actuators. The magnetic field is calculated using the previous formula with the chosen geometry while the required power is found fixing the maximum voltage and using the current calculated from the equation of Lorentz force. These last results show that this kind of actuator cannot be used for the purposes of this thesis. Indeed, the required mass is too high considering that the payload mass (satellite/lander) is about 100 kg and a landing attenuation device which has a mass of about 40% of the payload mass seems to be nonsense. Moreover, the required power is much higher than the value of the power which can be supplied normally by the common satellites and landers. Also in the case where this actuator is used in series with a passive one and distributed through 3 legs, the value of the required power remains unfeasible. Even if interesting in terms of reliability and controllability, this solution is definitely discarded.

2.4.4 Preliminary Selection of Landing System Configuation

According to the description given in the previous paragraphs, the granular material has the capacity to dissipate a good amount of energy and, if metallic granular materials are considered, they are also highly robust against the effects of deep space environment. They are simple granules insensitive to the extreme temperature variations, the

radiations and the vacuum. Their working principle relays on the friction which usually in vacuum environment is enhanced. Of course, the simple granular damper cannot be considered as an active system since it isn’t able to adapt its behaviour according to the external parameters and a slight variation of the environmental conditions like the ground characteristics, the gravity or the touchdown velocity, which could compromise the success of the mission. In order to maintain the reliability of the granular damper without losing in terms of performance and controllability, a combined active and passive system is developed. The chosen active system is the frictional piezoelectric actuator which is connected in series with the granular damper. The active device is directly connected with the satellite body on its upper part and with the rod of the granular damper on its lower part. The passive granular damper is constrained directly with the landing pad. This configuration gives the possibility to lower the force transmitted to the satellite beside the capacity to adapt the dissipation phenomenon according to the initial conditions. In the selected configuration, the devices work simultaneously and the active damper could be able to dissipate the amount of energy that the passive damper wasn’t able to dissipate. The real advantage of this configuration will be fully justified through the results of the multibody simulations performed with the active damper calibrated according to the characterized model of the granular one. This configuration should be replicated on each leg of the lander in a more realistic model.

3. Multibody Simulations and Sensitivity Analysis

This chapter is dedicated to the explanation and the illustration of the methodologies, the procedures, the tools, physical and numerical issues which are involved in the Multibody Simulations. These simulations are useful to easily understand the behaviour of the system in terms of position, velocity and acceleration and allow to evaluate the performance of different types of actuators (or force laws) giving also the possibility to achieve the optimal solution. Moreover, the robustness of the chosen solutions can be tested varying the initial and environmental conditions (velocity, gravity and ground). In these simulations the entire system (satellite, actuators and landing pad) are schematized as concentrated masses and only the vertical 1D motion is allowed. These assumptions are reasonable for the purpose of this work since the main requirement is to dissipate the kinetic energy which is mainly given by the vertical motion in a typical landing scenario. Indeed, in the attempt to individuate the most suitable technological solution and force-laws, these assumptions are acceptable. The tool used to perform the multibody simulations was Simscape, which is embedded in the Matlab and Simulink coding program. This tool is characterized by an interactive interface which allow to build a simple multibody system using elementary mechanical schematic devices like masses, springs, dampers and hard stops and allow to impose external forces (like the gravity and the ground reactions) and initial conditions (velocity). In this way, there is no need of writing directly the equation of motion avoiding further complications and errors. The components of the model are directly interfaced with the traditional Simulink environment from which all the wanted data can be extracted (acceleration, velocities, strokes, dissipated energy e t c). The presence of the user defined blocks allows to test the performances of different types of actuators and force-laws and the possibility to parametrize the model (more specifically the force-laws) gives a tool able

to search for an optimal solution in a wide range of laws-coefficients. Moreover, when the parametrization is done on the external environmental conditions (ground properties and gravity) and on the initial condition (velocity), this tool allows to test the robustness of the model.

3.1 Elementary Multibody Simulations

These first simple simulations are done in order to understand the general behaviour of the system and its sensitivity to different types of actuators. The system was modelled as two concentrated masses (satellite and landing pad) which are connected through a hard-stop which constraints the relative motion within the allowed stroke defined by the user, a translational spring which creates on the both sides a force proportional to the relative displacement and a damper. The translational spring could be considered as a structural stiffness of the legs while the damper is a user defined function which represents the force-law of the chosen actuator. A generic force-law is a function which depends on the relative velocity and/or relative displacements of the masses. In this way, a feedback loop was created. Naturally, if this kind of loop regards an explicit active damper, the fundamental assumption is that there is an on-board sensor able to give the correct inputs (like the stroke or the velocity) to the actuation block. Usually, this kind of information can be obtained through the integration of the signal coming from an acceleration transducer. The ground reaction was modelled as a combination of a linear damper and spring which act on the landing pad mass when its position is equal or below the ground, and was embedded in a hard stop constrained to the origin of the frame. All the positions and velocities are evaluated with respect to a reference frame fixed on the ground. In order to have a physical meaning, all the force-laws were modelled in a way to create two opposite forces with same intensity on the both sides of the actuator and to be always opposite to the relative motion. At the beginning of the simulation, the entire system (satellite, actuators and landing pads) falls from a height of **5 m** with a velocity of $\mathbf{2\ \frac{m}{s}}$ and the gravity force is constantly applied on both the masses

during the entire simulation. Indeed, this is another assumption since the gravity of these celestial bodies is irregular and variable with high. However, keeping the gravity constant with its maximum intensity during the whole simulation seems to be a robust way to evaluate the performance of the actuator. Therefore, falling from such altitude, the actuators must dissipate also the work done by the gravity during the descent. Hereafter, the parameters used in these preliminary simulations are shown:

Satellite mass [kg]	90
Total actuators mass [kg]	10
Total landing pad mass [kg]	6
Total system mass [kg]	100
Initial velocity [m/s]	-2
Initial landing pad position [m]	5
Allowable maximum stroke [m]	0,25
Gravity [m/s^2]	0,0001
Ground stiffness [N/m]	1,00E+06
Ground damping [Ns/m]	0

Table 17

It is meaningful that the used mass is similar to the mass of the Philae lander while the considered touchdown velocity is two times the landing velocity registered in that mission. Regarding the ground damping, it is fixed to zero at the beginning in order to have a dissipation only from the actuators and to evaluate the performance of the chosen force-law without any other contribution. The gravity is chosen lower than the gravity registered in the Rosetta Mission because a higher value of the gravity could be beneficial in terms of bouncing velocity. Keeping it low, the real capacity of energy dissipation in an almost zero-g environment is tested. Regarding the choice of the masses some considerations about the configuration should be done. The mass of the actuators and the pads is related to the number of the considered legs which is three because it is the minimum number of legs required to have a stability during the impact and it is the same number of legs used in the Philae lander of the Rosetta Mission. However, this choice influences the multibody model only in the total mass of the

actuators and the landing pads because one of the primary objective is to develop a damper able to dissipate the entire energy alone, independently from the total number of legs/dampers. Indeed, only one actuator block is considered in the multibody problem but with the mass of three. In this way, the presence of additional dampers is already considered in term of mass but the dissipation is given by just one. Adding more actuator blocks could only improve the performances and lower the force that the single actuator must generate. In this simple model, the mass associated to all the actuators was 10 kg while for the pads was 6 kg. These values were considered reasonable taking into account that the real masses were not available during these preliminary simulations. Hereafter, a representative scheme of the Simulink model is illustrated.

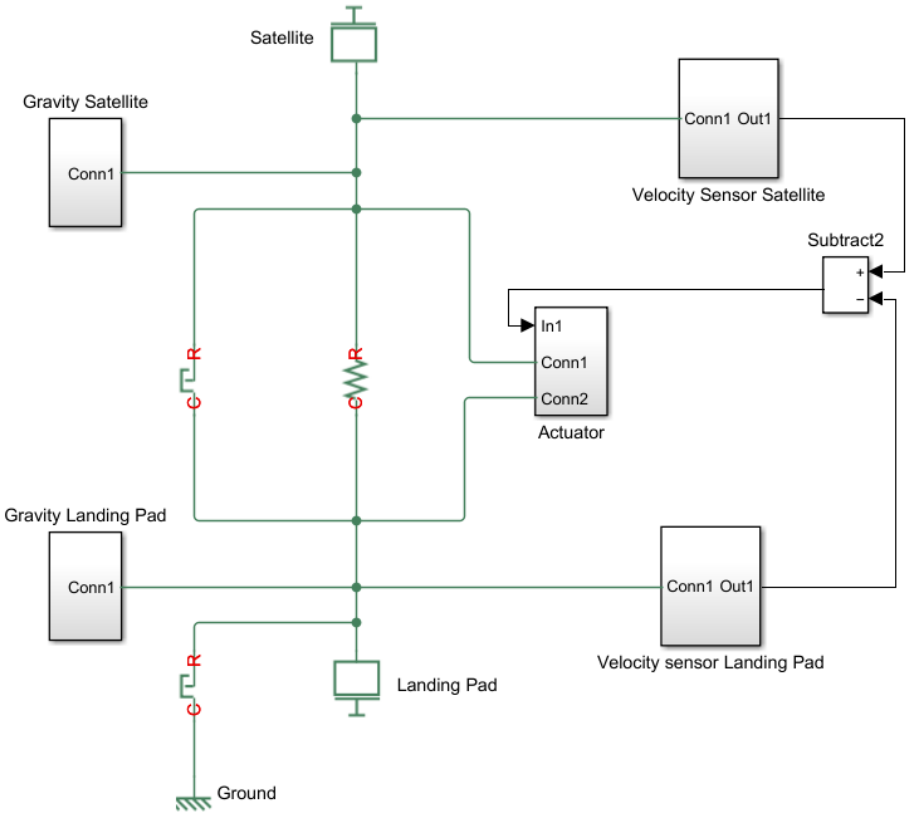

Figure 34 Simulink elementary two-masses model

The simulations are performed keeping the same schematic shown before but changing the force-law inside the actuator block. Different laws are tested starting from velocity dependent polynomial laws like the linear, quadratic and cubic cases to logarithmic, exponential and "bell-shaped" laws. Other laws which depend on the stroke and the

velocity are tested like the pneumatic case and the granular case. Here the expressions used for these laws are given:

➢ Linear:	$F_d = a\,v$	$F_e = kx$
➢ Quadratic:	$F_d = a\,v + bv^2$	$F_e = kx$
➢ Cubic:	$F_d = a\,v + bv^2 + cv^3$	$F_e = kx$
➢ Logarithmic:	$F_d = a * log(v\ +\ 1)$	$F_e = kx$
➢ Exponential:	$F_d = a * (e^v - 1)$	$F_e = kx$
➢ Pneumatic:	$F_d = av$	$F_e = \frac{k}{(c-x)}x$
➢ Granular:	$F_d = a * x * v$	$F_e = kx$
➢ Bell:	$F_d = -\frac{a}{b^2}(v-b)^2 + a$	$F_e = kx$

F_d = damper force, F_e = elastic force, v = relative velocity, x = stroke (initial position – relative displacement). As it can be noticed for all the considered laws, except from the pneumatic case, the elastic force of the translation spring has a linear behaviour with respect to the stroke. In the pneumatic case the elastic contribution given by the spring back effect was modelled as a force inversely proportional to the difference between the maximum allowable displacement c (maximum volume of the gas) and the current stroke and linearly proportional to the stroke, while the damping contribution was modelled as a viscous damper (linear). Even if the pneumatic actuator was previously discarded, the law associated to this device was tested anyway. The simple velocity linear law can be interpreted also as the law associated to the magnetic damper. As it was mentioned in the previous chapter, the granular actuator creates a force which depends also on the actual stroke. In this case, since the real stroke-dependence was still unknown, a simple linear behaviour was assumed. In the cases of the logarithmic and exponential laws, the expression was adapted in order to give a zero force when the relative velocity is zero. The same logic was used to define the last law which can be seen as an inverted parabolic law with respect to the velocity which actually has a shape of a bell. The parameter **b** defines the central position of the parabola on the velocity axis, and together with **a**, which is the maximum value of force which can be produced

by the law, defines the slope of the force with respect to the velocity. The idea behind this law is to have a good dissipation also when the velocity is low without exceeding in the transmitted force. In the subsequent phase of the work, these bell-shaped laws were slightly modified to make them provide a constant force when the relative velocity reaches the central position instead of a descending force as it would be in its original shape. Generally speaking, in order to univocally identify the single force-law, the coefficients present in the expressions must be fixed. The search of the optimal solution was done varying those coefficients in a wide range of values. This parameter-sensitivity analysis is done looking for the coefficients which minimized the bouncing velocity taking care of the force transmitted to the satellite. Moreover, the variation of the stiffness value **k** of the elastic contribution was considered with the aim to understand the influence of this parameter. Regarding the quadratic and the cubic cases, instead of considering a simultaneous variation of all the coefficients, only the linear term coefficient is varied, while the remaining ones were kept equal to the linear one but divided by 10 for the quadratic term and 100 for the cubic term. For the bell case, the central velocity b is kept fixed. Even if the logarithmic, exponential, bell laws seem to be unrealistic, they could be achievable by an active device able to modify its behaviour according to the given input like the active frictional piezoelectric actuator.

3.2 Multibody Simulations of combined Active-Passive System

In order to simulate the behaviour of the combined active-passive system, a new model with a slightly different mass distribution is developed. Three concentrated masses are considered, which are the satellite (upper mass), the total actuator mass which embedded both the active and passive devices (central mass) and the landing pad (lower mass). As it was said before, this assumption remains reasonable because in this 1-dimensional model the kinetic energy to be dissipated depends only on the value of the masses and not on their distribution (effects of moments of inertia and torques are

neglected). The upper satellite mass is attached to the central mass through the active damper and a spring which represents a residual structural stiffness of the actuator/leg, while the central mass is connected to the lower mass (landing pad) through the passive damper and with a spring which represents a stiffness related to the leg/actuator structure and/or the stiffness of the granules. Even if those stiffness' are not directly controlled and not well defined, the simulations are carried out considering the presence of those springs anyway. A residual spring-back effect could be always present on a complicated structure, and a performant damper (or dampers in this case) should work correctly also with these elastic effects. As in the elementary model, the gravity acts constantly on each mass during the whole simulation, the ground is modelled as a spring with a high stiffness (zero damping is maintained for the previously explained reasons) and the entire system falls from 5 m from the ground at 2 $\frac{m}{s}$. In the followings, the data of the used parameters are given:

Satellite mass [kg]	96
Total actuators mass [kg]	18
Landing pads mass [kg]	6
Total system mass [kg]	120
Gravity [m/s^2]	0,0001
Ground stiffness [N/m]	1,00E+08
Ground damping [Ns/m]	0
Initial velocity [m/s]	-2

Table 18

The first Multibody Simulations performed with the presented configuration don't involve the real masses of the actuators since they aren't still exactly defined. The values of masses and dimensions obtained in the preliminary sizing of the previous chapter are not definitive but they were calculated to have a rough idea of the actuator masses with the purpose of selecting the most feasible solution. In order to perform simulations robust against a further mass variation of the system, the following incremented masses are used. Indeed, 3 kg of mass are associated to each actuator and,

considering that there are three legs (three granular dampers and three active piezo dampers), the total actuator mass is fixed to 18 kg. These values are higher than the values obtained in the preliminary sizing. Hereafter, a schematic view of the implemented model is reported.

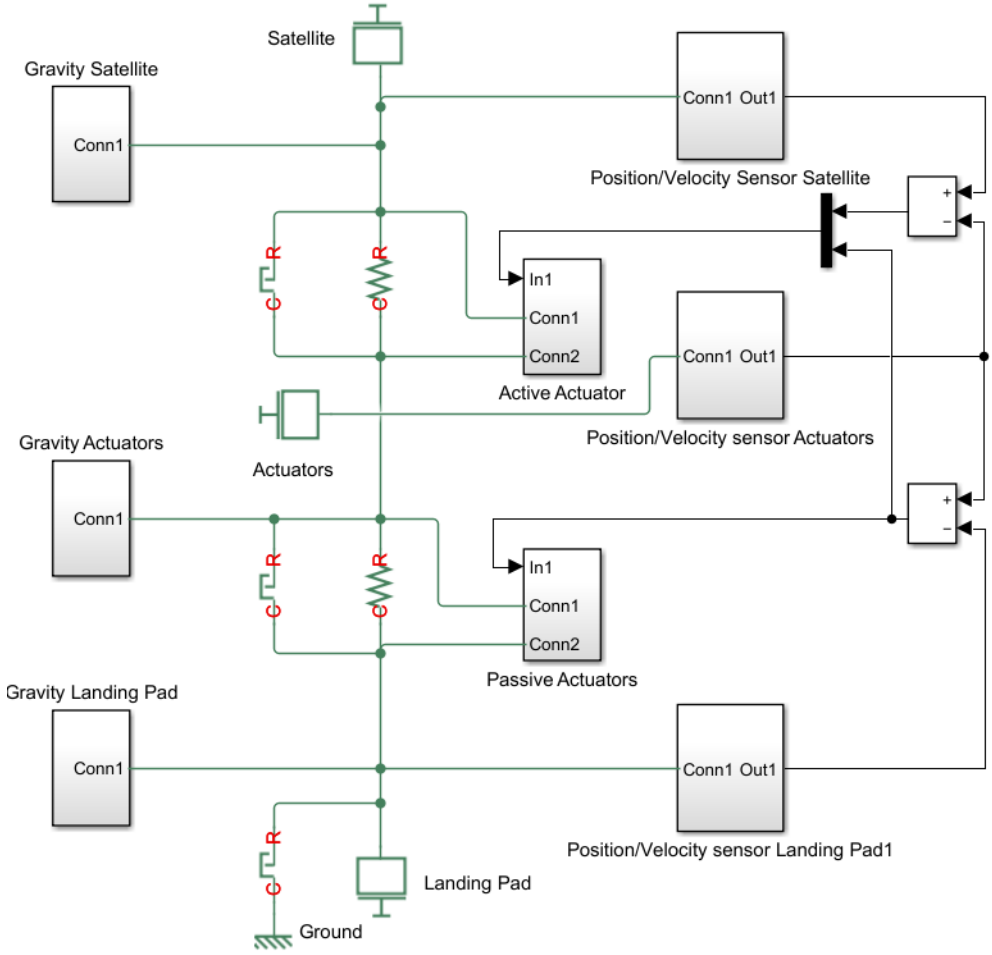

Figure 35 Simulink three-masses model, with active and passive actuator

The previously discussed elementary models were done with the willing to understand the behaviour of the multibody model and the selected force-laws. In this stage of the work, the main objective is to identify the most suitable and performant force-law for the selected configuration, where the active and passive devices are connected in series and work together. Indeed, as it is said before, the principal duty of the active damper is to dissipate the amount of energy which the passive damper doesn't dissipate. From this point of view, it seemed to be quite reasonable to make the force law of the active

damper dependent on the parameters of the passive damper like the stroke and the velocity. In this way, the active damper could be "aware" of the status of the passive device and adapts itself in order to mitigate the lack of performance of the passive damper. Obviously, the implementation of this kind of laws assumes that the active damper receives the signals coming from the sensors which measure the parameters of the passive damper as can be seen in the previous scheme. The tested force laws for the active damper can be divided in 6 groups:

1. Force linear with active velocity and passive stroke dependent coefficients:

   - $F_{active} = a * x_{passive} v_{active}$
   - $F_{active} = (a {x_{passive}}^2 + b x_{passive}) v_{active}$
   - $F_{active} = (a {x_{passive}}^3 + b {x_{passive}}^2 + c x_{passive}) v_{active}$
   - $F_{active} = (-\frac{a}{b^2}(x_{passive} - b)^2 + a) v_{active}$
   - $F_{active} = (\log(x_{passive} + 1)) v_{active}$
   - $F_{active} = (\sqrt[2]{x_{passive}}) v_{active}$

2. Force linear with active velocity and passive velocity dependent coefficients:

   - $F_{active} = a * v_{passive} v_{active}$
   - $F_{active} = (a {v_{passive}}^2 + b v_{passive}) v_{active}$
   - $F_{active} = (a {v_{passive}}^3 + b {v_{passive}}^2 + c v_{passive}) v_{active}$
   - $F_{active} = (-\frac{a}{b^2}(v_{passive} - b)^2 + a) v_{active}$
   - $F_{active} = (\log(v_{passive} + 1)) v_{active}$
   - $F_{active} = (\sqrt[2]{v_{passive}}) v_{active}$
   - $F_{active} = (5 - v_{passive}) v_{active}$

3. Force linear with the complementary value of the passive velocity and active velocity dependent coefficients:

   - $F_{active} = (a{v_{active}}^2 + bv_{active})(5 - v_{passive})$
   - $F_{active} = (a{v_{active}}^3 + b{v_{active}}^2 + cv_{active})(5 - v_{passive})$
   - $F_{active} = (-\frac{a}{b^2}(v_{active} - b)^2 + a)(5 - v_{passive})$
   - $F_{active} = (\log(v_{active} + 1))(5 - v_{passive})$
   - $F_{active} = (\sqrt[2]{abs(v_{active})})(5 - v_{passive})$

4. Force linear with the passive stroke and active velocity dependent coefficients:

   - $F_{active} = a * v_{active}x_{passive}$
   - $F_{active} = (a{v_{active}}^2 + bv_{active})x_{passive}$
   - $F_{active} = (a{v_{active}}^3 + b{v_{active}}^2 + cv_{active})x_{passive}$
   - $F_{active} = (-\frac{a}{b^2}(v_{active} - b)^2 + a)x_{passive}$
   - $F_{active} = (\log(v_{active} + 1))x_{passive}$
   - $F_{active} = (\sqrt[2]{v_{active}})x_{passive}$

5. Force linear with the passive velocity and active velocity dependent coefficients:

   - $F_{active} = a * v_{active}v_{passive}$
   - $F_{active} = (a{v_{active}}^2 + bv_{active})v_{passive}$
   - $F_{active} = (a{v_{active}}^3 + b{v_{active}}^2 + cv_{active})v_{passive}$
   - $F_{active} = (-\frac{a}{b^2}(v_{active} - b)^2 + a)v_{passive}$
   - $F_{active} = (\log(v_{active} + 1))v_{passive}$
   - $F_{active} = (\sqrt[2]{v_{active}})v_{passive}$

6. Force linear with the complementary passive stroke and active velocity dependent coefficients:

   - $F_{active} = a * v_{active}(0.3 - x_{passive})$
   - $F_{active} = (a{v_{active}}^2 + bv_{active})(0.3 - x_{passive})$
   - $F_{active} = (a{v_{active}}^3 + b{v_{active}}^2 + cv_{active})(0.3 - x_{passive})$
   - $F_{active} = (-\frac{a}{b^2}(v_{active} - b)^2 + a)(0.3 - x_{passive})$
   - $F_{active} = (\log(v_{active} + 1))(0.3 - x_{passive})$
   - $F_{active} = (\sqrt[2]{v_{active}})(0.3 - x_{passive})$

x represents the stroke and v represents the relative velocity between the two extremities of the actuators. All the presented force-laws work simultaneously in series with the lower passive actuator which acts with the previously mentioned law: $F_{passive} = a * x * v$. A single passive simulation is firstly performed and once the optimal value of the coefficient is found, it is kept fixed for all the active-passive combined simulations. Both active and passive dampers work in parallel with their springs, which give an elastic contribution in the form $F_e = k * x$. As it can be noticed, some laws used in the elementary simulations are tested again in this new configuration, but in different forms. The linear, quadratic, cubic, logarithmic and bell expressions (a new square-root law was introduced) are combined with a linear term of velocity, stroke and the complementary value of them. A square-root form is tested because, according to the value given to the coefficient, it is able to generate a high force at low velocity thanks to its high slope and a quite constant force at high velocities, like the bell-shaped force law. This behaviour could give a benefit in term of bouncing velocity because it can "stop" the spacecraft when it is bouncing upward with a relative velocity far lower than the velocity experienced during the descending phase. As it can be seen in the previous expressions, the complementary terms are given by the difference between a constant value and the relative velocity or the stroke of the passive damper. The constant values are chosen in order to be always higher than the variable. For example, the stroke cannot be higher than 0.3 m since the hard stop was fixed at 0.25 m and the relative

velocity of the passive damper cannot be higher than 5 because even if the landing pad rebounds with the same velocity of the touchdown velocity ($2\ \frac{m}{s}$, perfectly elastic ground case), the maximum relative velocity cannot be higher than $4\ \frac{m}{s}$. The constant values in the complementary expression are kept slightly higher than the maximum values of the variables, in order to avoid a zero force when the active relative velocity is still different from zero. The expressions with the complementary terms increase the active actuator force when the passive velocity and stroke are low. If the passive velocity is low, this condition could be interpreted as a signal of the "end" of the passive dissipation phenomena which must be replaced subsequently by the active device, while if the passive stroke is low, this could be the signal of the "lack" of dissipation of the passive actuator because it has a too stiff behavior during the impact. Other expressions without the complementary terms are considered interesting to be tested since they carry the information of the passive device in different forms. These expressions increase the active damping force when the passive stroke and relative velocities increase. If the lower stroke or relative velocity are high, it could be interpreted as a sort of a difficulty of the passive device to stop properly the falling mass, leaving it to hit violently the lower bound of the hard stop. The increment of the dissipation from the active device in this scenario could avoid that issue. All the presented considerations are just hypotheses that lead the creation and the selection of the force-laws to be tested, but the most important aspect of these laws is that they carry somehow both the information of the passive and active devices, leaving the possibility to obtain benefits in terms of transmitted force and bouncing velocity in an unexpected way. Indeed, the real behaviour of them can be understood only from the results of the proposed simulations. As it has been done for the elementary simulations, a parametric sensitivity analysis for each force-law is performed for a wide range of the values of coefficients and elastic stiffness', trying to identify the most performant solution. Actually, the search for the most performant law, in terms of rebound velocity and transmitted force, induces to a further consideration in this phase of the work: it is observed that leaving the possibility to change the force-law between the compression and the extension (rebound) phase, it is possible to optimize the system separately for the minimum deceleration and the minimum rebound velocity. Indeed, leaving the stroke to be exploited almost completely during the compression, it is possible to diminish the maximum

deceleration, while keeping a high force during the extension phase, it is possible to "stop" properly the ascending payload mass achieving a lower bouncing velocity. This target is achieved just imposing different values of the coefficient to the same force-law according to the sign of the relative velocity. For these simulations, the value of the stiffness of the translational spring is kept fixed and the force-laws coefficients (both for the ascending and the descending phases) are varied. The coefficient for the descending phase is chosen in order to have the minimum force while the coefficient for the ascending phase is chosen in order to have the minimum rebound velocity. A proper attention is given in the selection of the descending coefficient range in order to avoid the bottom-impact that is mentioned before. Looking for the coefficients which allows the exploitation of all the stroke, the risk to have the impact with the bottom is high. Therefore, a lower boundary for these coefficients is found for each one of the presented laws.

3.3 Robustness Analysis of preliminary Models of Landing System

An analysis of the system with respect to the variations of arrival velocity and ground properties from nominal condition is performed, in order to study system robustness. This is important because the arrival velocity of the lander can be affected by uncertainties during the deployment from the orbiter, and this becomes a problem if landing system isn't able to work with a different landing speed since could cause possible damages to the vehicles or its rebound. The analysis of stability is also very important considering different ground parameters with respect to the ones used to size the landing system, because the properties of the celestial body the spacecraft is achieving are not known, and so a certain robustness against these parameters is required. Therefore, numerical simulations are done, using the same model previously

presented, of the landing system where arrival velocity is changed in a range of ± 2 $\frac{m}{s}$ with respect to the nominal condition of 2 $\frac{m}{s}$. So as maximum value is taken **4** $\boldsymbol{\frac{m}{s}}$, as minimum **0.2** $\boldsymbol{\frac{m}{s}}$ (not truly 0 m/s because obviously the vehicles wouldn't reach the ground), and all values with a discretization step of 0.2 $\frac{m}{s}$, included between maximum and minimum, are analyzed in the multibody simulations. The coefficients of the active force-laws are optimized according to the mentioned velocity range. For what regard the ground parameters, the model used to describe ground behaviour inspires to BIMPAM model (Boulder IMPAct Model - Calvetti, Di Prisco, Geotechnique, 2006), but without considering plastic and visco-plastic blocks. This model was developed to study the structural response of artificial tunnels, where the solicitations transmitted to the ground derive from a circular surface foundation, and consists in a concentrated spherical mass, one plastic friction block, one visco-plastic friction block, one viscous damper and one elastic spring.

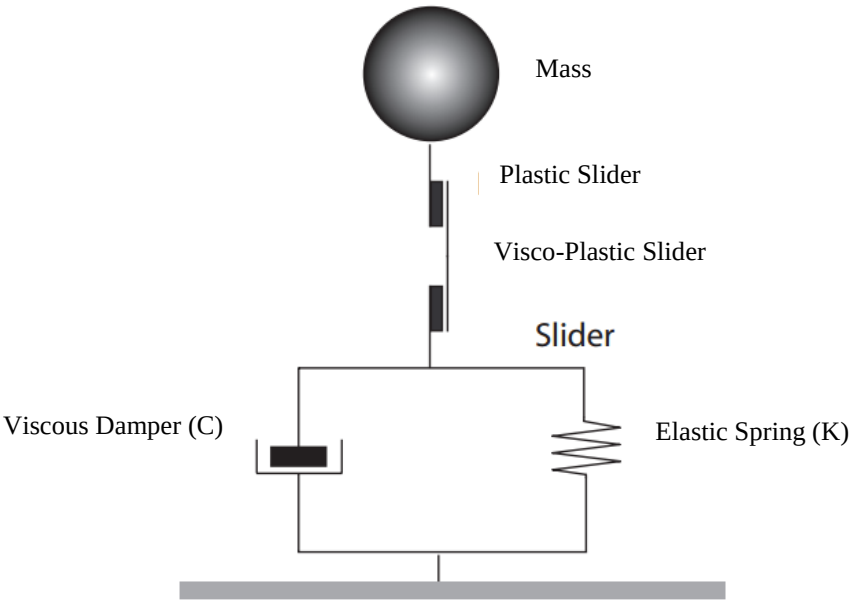

Figure 36 BIMPAM Model

Since it is complex to properly model the plastic and viscous-plastic blocks, the model adopted for ground is simpler than BIMPAM and neglects these two blocks. This

hypothesis is acceptable and more robust since, so doing, the ground dissipates less lander kinetic energy and this amount of energy shall be dissipated by the landing system. Moreover, also for Cassini-Huygens mission designed by NASA and ESA, where Cassini is the orbiter and Huygens the lander grounding Saturn satellite Titan, the model utilized for describing the ground was something like BIMPAM, but without plastic and visco-plastic blocks. The model adopted for ground in this thesis so is the following.

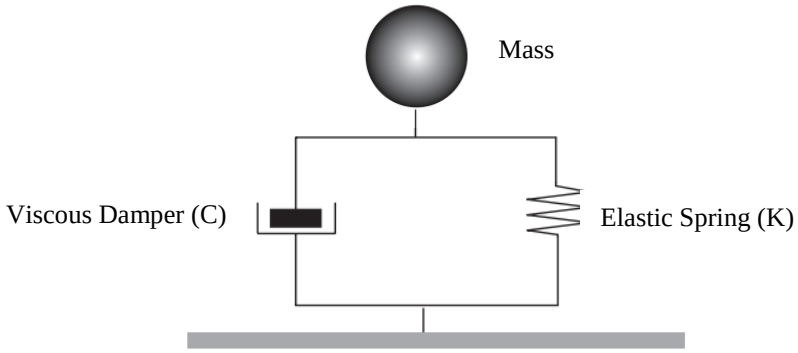

Figure 37 Ground model adopted in this thesis

The constant **K** of the elastic spring and **C** of the viscous damper are computed according to these equations:

- $\boldsymbol{K = \frac{4GR}{1-v}}$
- $\boldsymbol{G = \frac{E}{2(1+v)}}$
- $\boldsymbol{C = K \frac{R}{V_S}\ \eta_N}$

$\boldsymbol{G}$ is the tangential elastic modulus of the ground, $\boldsymbol{R}$ is the radius of the concentrated mass, $\boldsymbol{E}$ is the Young modulus of the ground, $\boldsymbol{v}$ is the Poisson coefficient of the ground, $\boldsymbol{Vs = \sqrt{\frac{G}{\rho}}}$ where $\boldsymbol{\rho}$ is ground density, and $\boldsymbol{\eta_N}$ is friction coefficient in normal direction

fixed to $\boldsymbol{\eta_N}$ = 0.85. As radius of the concentrated mass is considered the dimension of the foot, **0.05 m**. Below are reported, in a table, different ground materials with their own properties. A wide selection is performed in order to consider different types of ground and analyze the behaviour of the landing systems in conditions relatively far from each other.

	K [N/m]	C [Ns/m]
Clay	6,67E+06	9,81E+04
Sand	8,90E+06	8,57E+04
Basalt	1,02E+10	3,69E+06
Granite	7,32E+09	3,11E+06
Dolomite	4,54E+09	2,42E+06
Schistous Rock	4,15E+09	3,02E+06
Gneiss	6,28E+09	3,01E+06
Soft Regolith	1,02E+07	8,39E+04
Compact Regolith	1,74E+07	1,26E+05
Quartz	1,06E+10	3,52E+06
Iron	1,94E+07	2,76E+05
Nickel	2,45E+10	1,10E+07
Zinc	7,98E+09	5,63E+06
Magnesium	4,79E+09	4,36E+06
Copper	1,54E+10	8,73E+06
Ice	1,01E+06	2,23E+04
Titanium	1,25E+10	5,60E+06

Table 19

Once stiffness and damping are computed for every selected material, an interpolation is performed between maximum and minimum values of stiffness and their associated damping coefficients, and multibody simulations are run for every couple of stiffness-damping coefficient in order to study and analyze the sensitivity of the landing system with respect to ground parameters. Below it is reported the link between stiffness and damping of the ground.

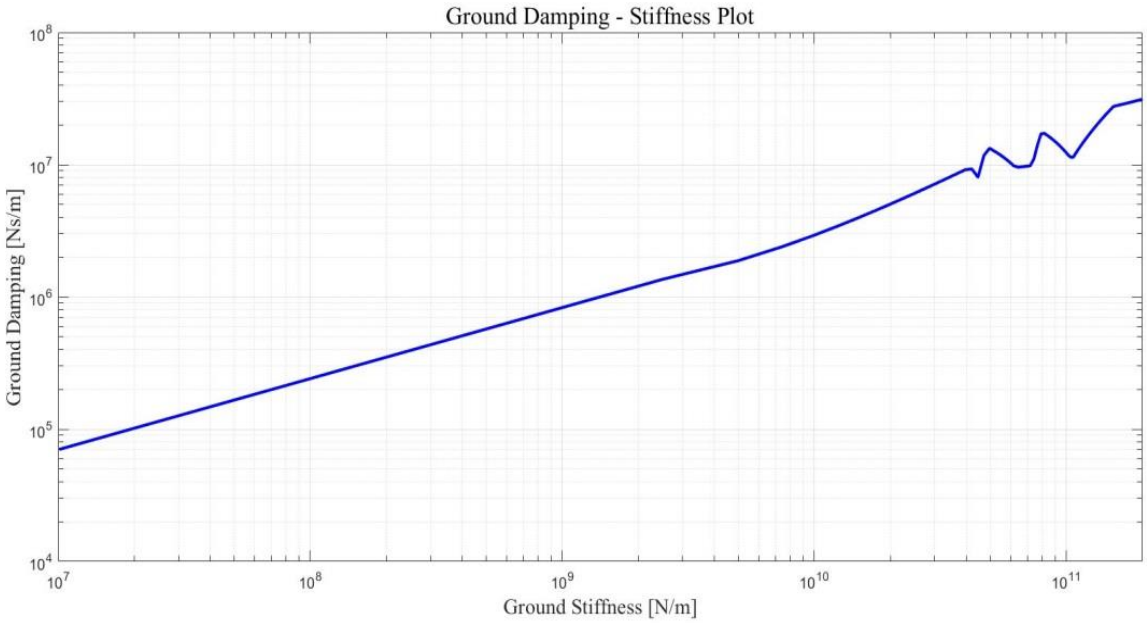

Figure 38 Ground stiffness - Ground damping link

The multibody simulations are run keeping the nominal arrival velocity (2 $\frac{m}{s}$) and varying ground parameters, while when the arrival velocity is changed the ground parameters are kept nominal (K = 1e+08 $\frac{N}{m}$, C=0 $\frac{Ns}{m}$). The idea is to check if landing system is able dissipate the kinetic energy of the spacecraft, verifying if the rebound speed is sufficiently low (in the order of 1e-03 $\frac{m}{s}$), and if the vehicle acceleration is limited under a critical value (typically the value observed during launch, 8-10 g). So, for every touchdown velocity, it's found the damping coefficient which allows to exploit all the stroke of the active actuator, while its stiffness is constant and not controllable. Whereas regarding the sensitivity to the ground properties, the stiffness and the damping coefficients are kept fixed. The Passive actuator properties are constant, therefore the robustness against uncertainties depends only on active part. An analysis of stability and robustness is made for two types of the landing systems, one with just one passive actuator and one for a system formed by one passive actuator and one active actuator linked in series. The comparison is meaningful since the choice to select an active-passive landing system respect to an only passive one is based on better results in terms of spacecraft acceleration and bouncing velocity in nominal conditions, but as well on the superior robustness against the presented uncertainties. The study of system robustness is very important because, for these missions which last years and

happens in very unpredictable environmental conditions, being robust against these sorts of uncertainties is an essential feature that can reduce margin of error and the probabilities of failure.

3.4 Feasibility Study – Results

Hereafter, the figures and the numerical results of the performed simulations are illustrated. Because of the high amount of the obtained data, presenting all of them is impossible. Therefore, only the most meaningful results are chosen, with the aim of giving to the Lector the essential information about the work according to the scheme presented in the previous section.

3.4.1 Elementary Simulations – Results

The following 3D figures show the results obtained from the parametric analysis with the first elementary Multibody simulations. As it can be seen directly on the velocity figures, the color is associated to the maximum force registered in the simulations.

Linear Damping

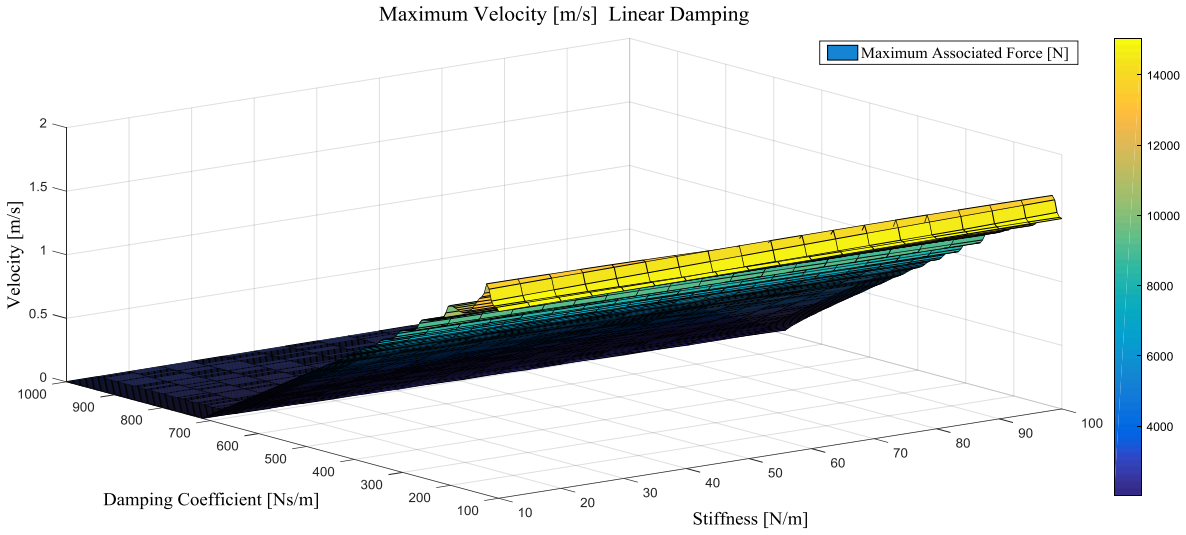

Figure 39

Granular Damping

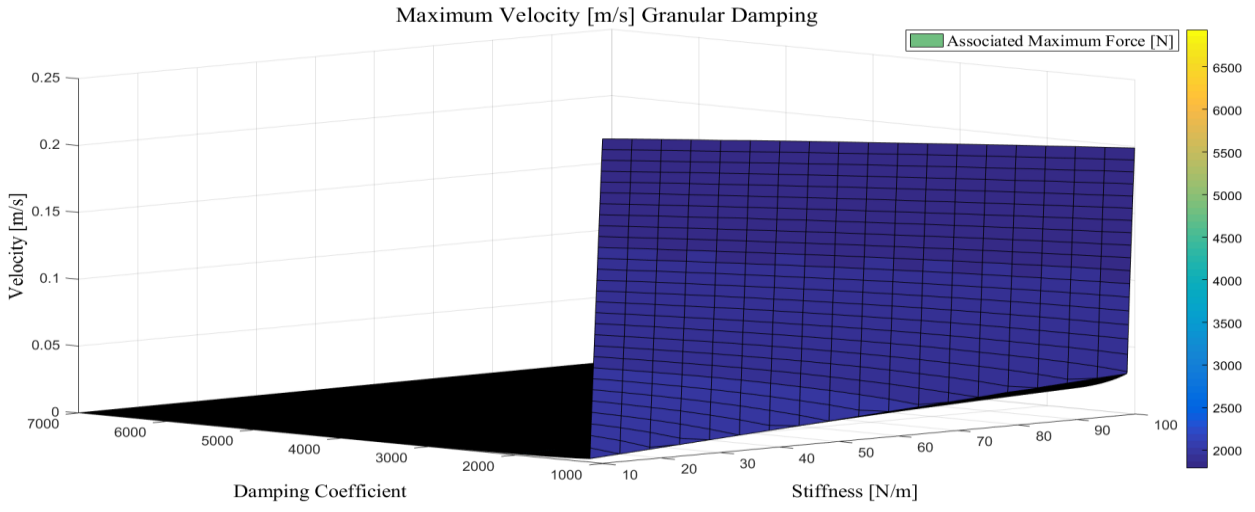

Figure 40

Logarithmic Damping

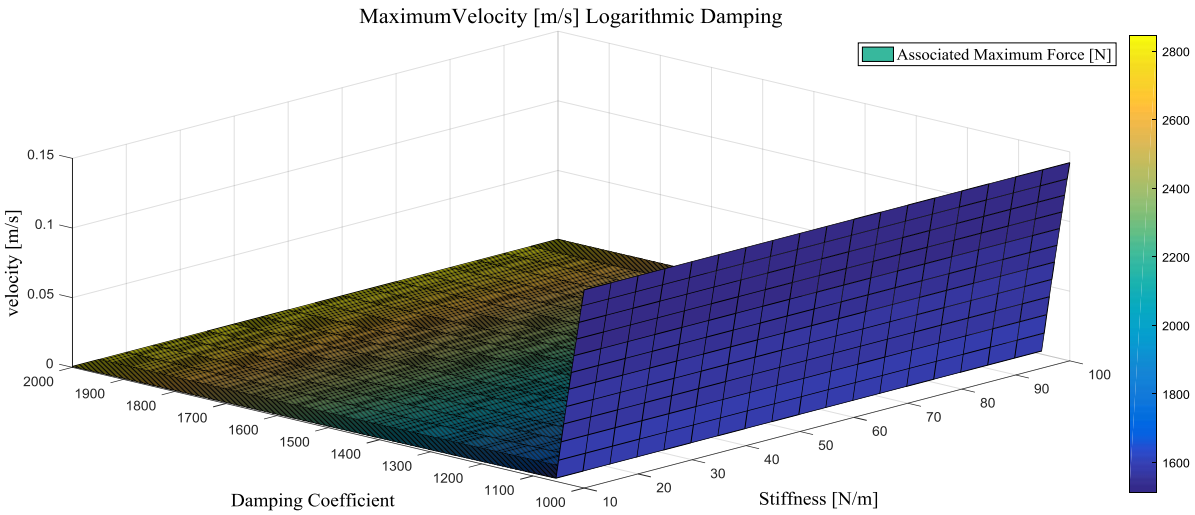

Figure 41

Exponential Damping

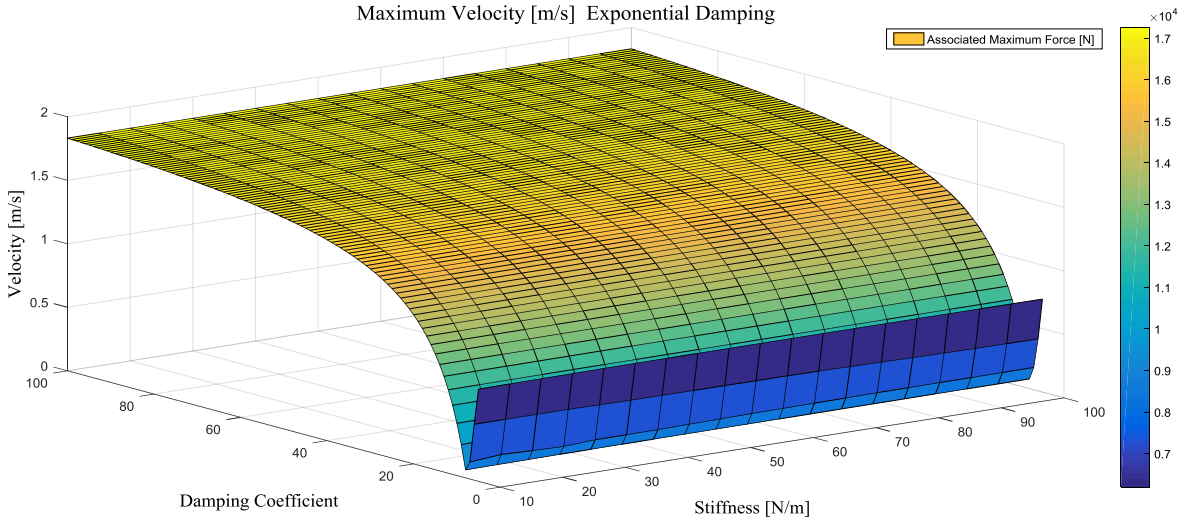

Figure 42

Pneumatic Damping

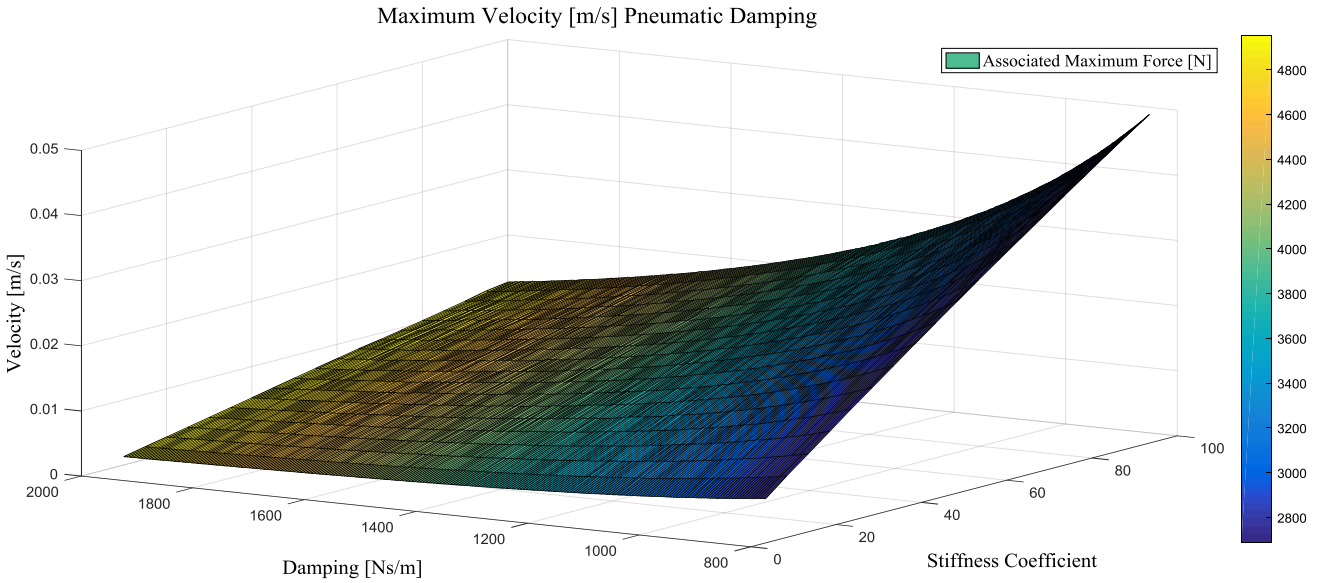

Figure 43

Bell Damping

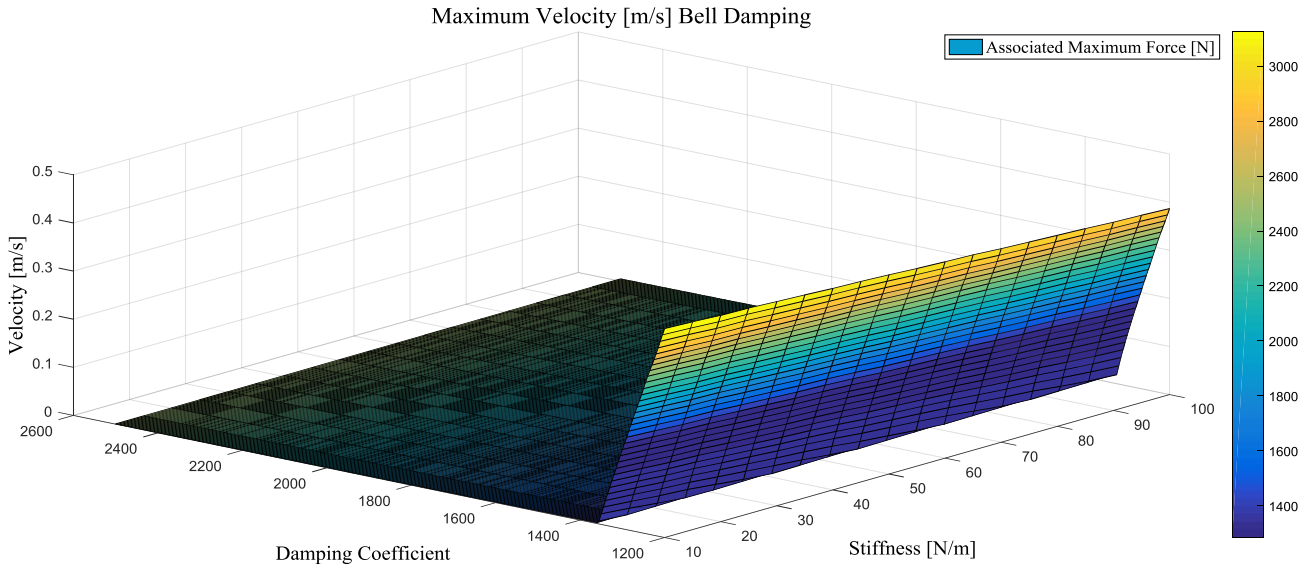

Figure 44

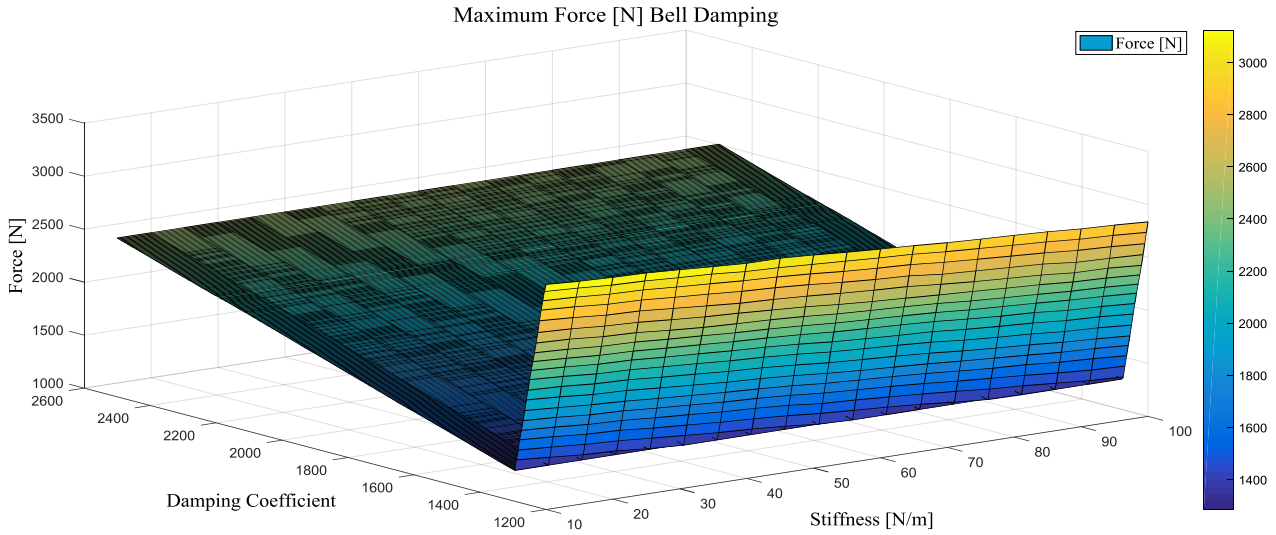

Figure 45

In the most of the presented velocity plots, a sort of knee-trend can be observed. This behavior is associated to the shock with the bottom part of the actuator and can be evidenced also in the last force figure. It is noticeable the obtained results are not sensible to the variation of the stiffness value but highly damping dependent.

Optimal Results

The following chart shows the optimal results in terms of the fundamental parameters (force, velocity and stroke) and the associated optimal coefficients with their test ranges.

	Damping Range	Stiffness Range [N/m]	Maximum Velocity [m/s]	Maximum Force [N]	Maximum Stroke [m]	Optimal Damping	Optimal Stiffness [N/m]
Linear	100_5_1000	10_5_100	0,0017	3100	0,18	1000	10
Quadratic	100_5_1000	10_5_100	0,0041	5200	0,12	494,5	35
Cubic	1_0,05_50	10_5_100	0,0034	5500	0,11	46,5	30
Granular	1000_5_7000	10_5_100	4,2297E-04	7000	0,06	6990	35

Logarithmic	1000_5_2000	10_5_100	6,1999E-04	2847	0,13	2000	10
Exponential	5_1_100	10_5_100	0,0622	9500	0,17	10	8
Bell	1200_5_2500	10_5_100	4,7693E-04	2473	0,13	2475	10
Pneumatic	850_5_2000	10_5_100	0,0013	4945	0,09	2000	10

Table 20

It can be seen that the optimal values of the stiffness are quite low. It's obvious that a low spring back effect is beneficial to reduce the maximum velocity.

3.4.2 Multibody Simulations with combined Active and Passive System – Results

As was done for the elementary simulations, only the most meaningful data are presented. In this case, 4 linear laws are chosen where the relative velocity of the active damper is multiplied by the stroke, the complementary value of the stroke, the relative velocity and the complementary value of the relative velocity of the passive damper. These laws can represent all the 6 groups of laws which were illustrated in the dedicated chapter. However, the optimal results are given for all the considered laws. It's important to underline that the parameters of the passive damper are kept fixed to their optimal values (c = 7300 and k = 10).

Linear Passive Delta X with Linear Active Delta V Force Law

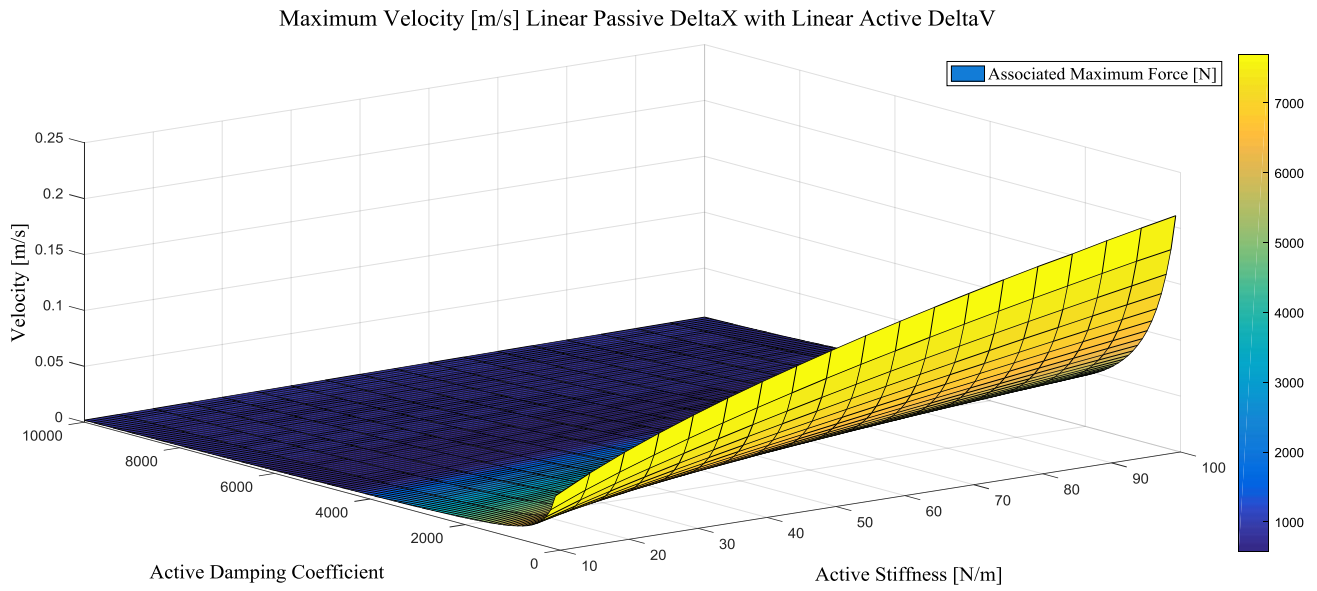

Figure 46

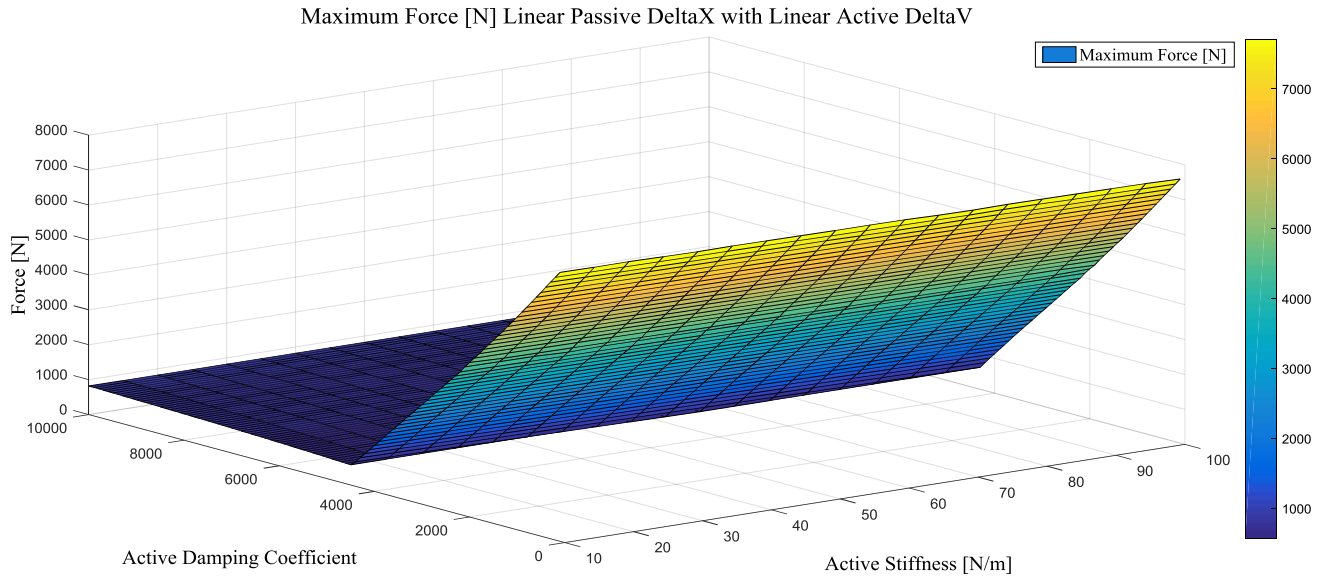

Figure 47

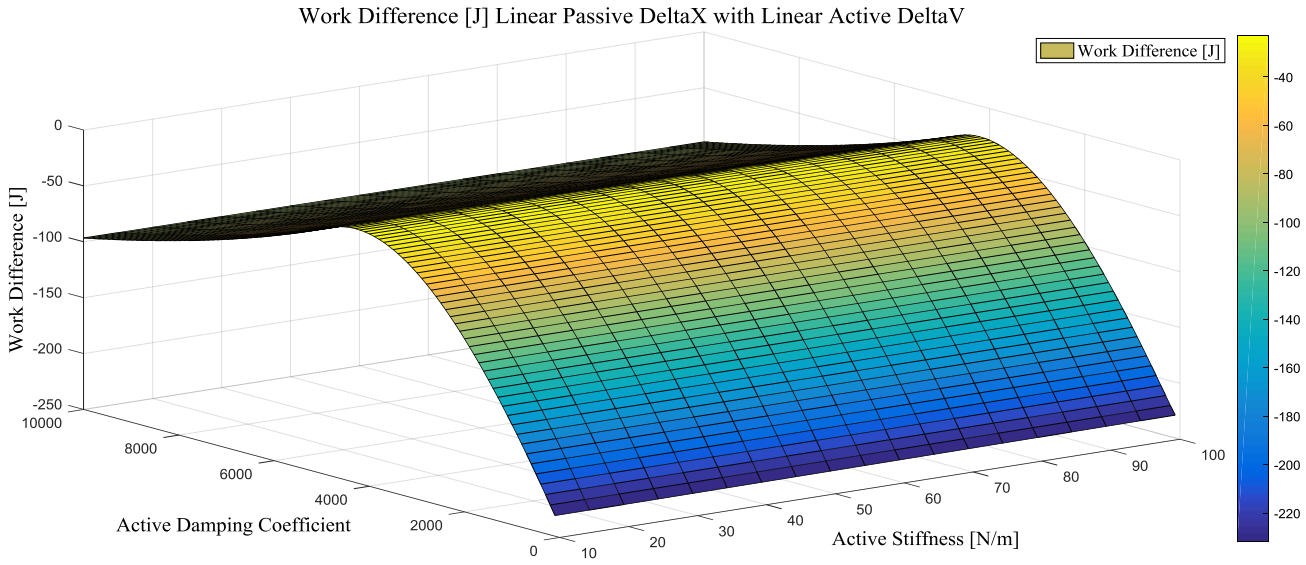

Figure 48

The last figure represents the difference between the active and passive dampers' works. It can be observed that it remains negative in all the considered ranges (the passive damper is giving the biggest damping contribution). Moreover, it can be seen that increasing up to certain level the active damping coefficient, the active work slightly decreases. It occurs because the damper becomes rigid and the sliding is limited.

Linear Passive Delta V with Linear Active Delta V Force Law

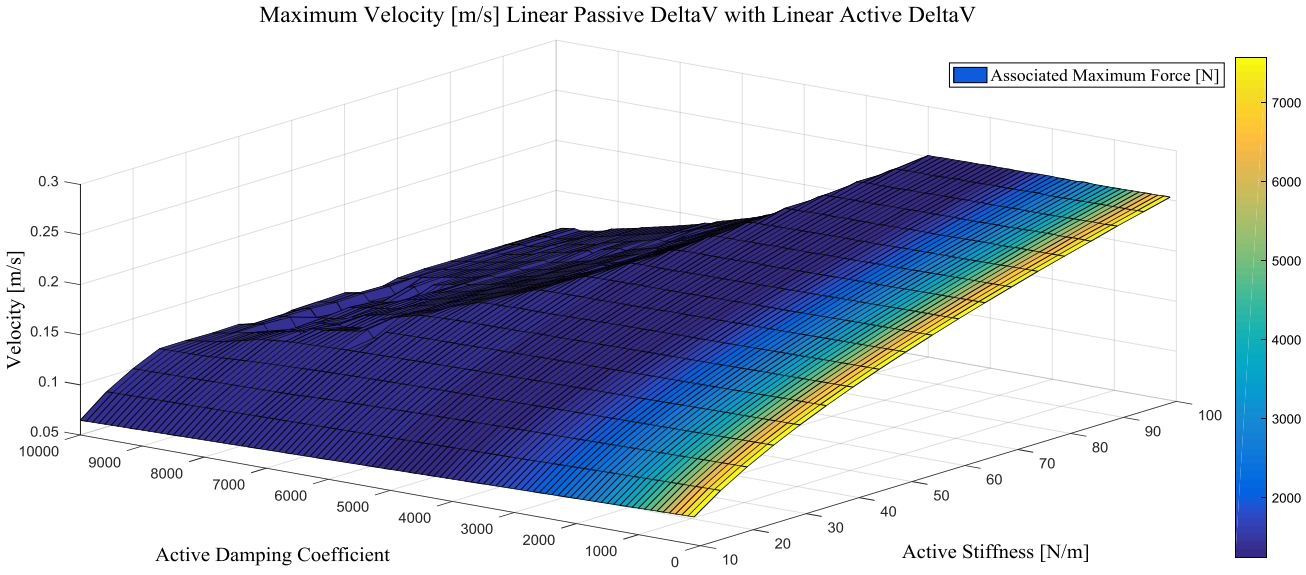

Figure 49

This law is one of the worst solution among those analyzed. The velocity remains always above the cm/s and the transmitted forces are quite high. The low performance of this solution is caused by the “shift” between the passive damper velocity peak and the active one. When the active damper is still sliding, the velocity of the passive tends to zero making the active force low and unable to stop properly the falling mass. The “low” velocity zone corresponding to high values of damping and stiffness is caused probably by the fact that a too rigid damper doesn’t allow a high compression of the spring lowering in this way the spring back effect and so the maximum velocity.

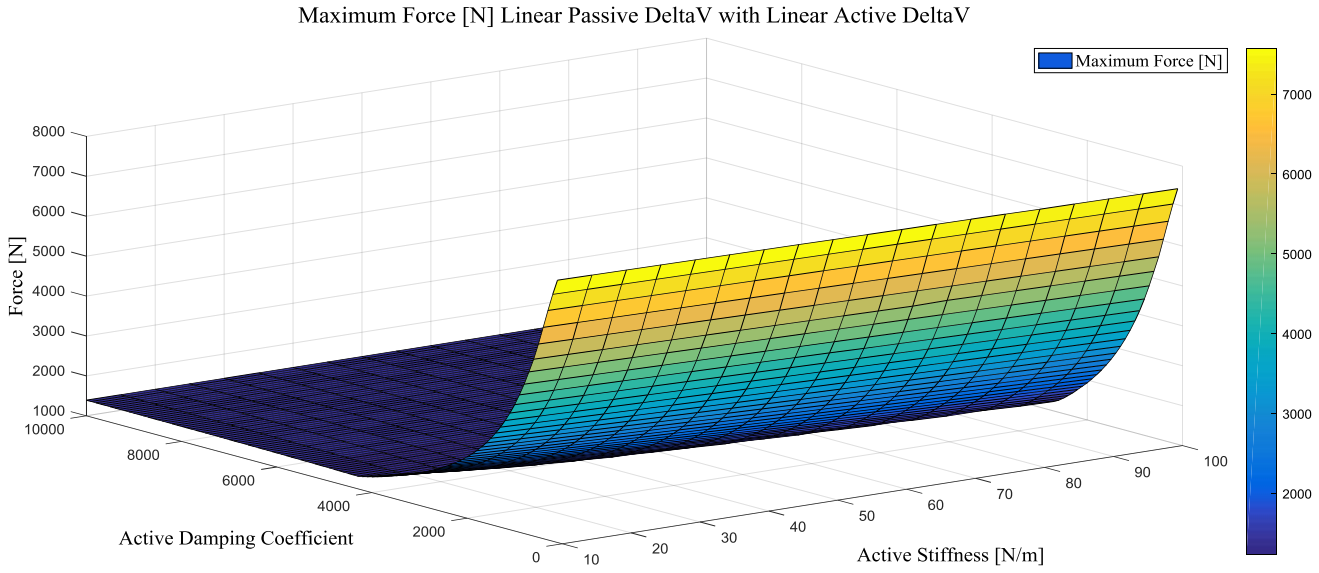

Figure 50

Linear Passive Complementary Delta X with Linear Active Delta V Force Law

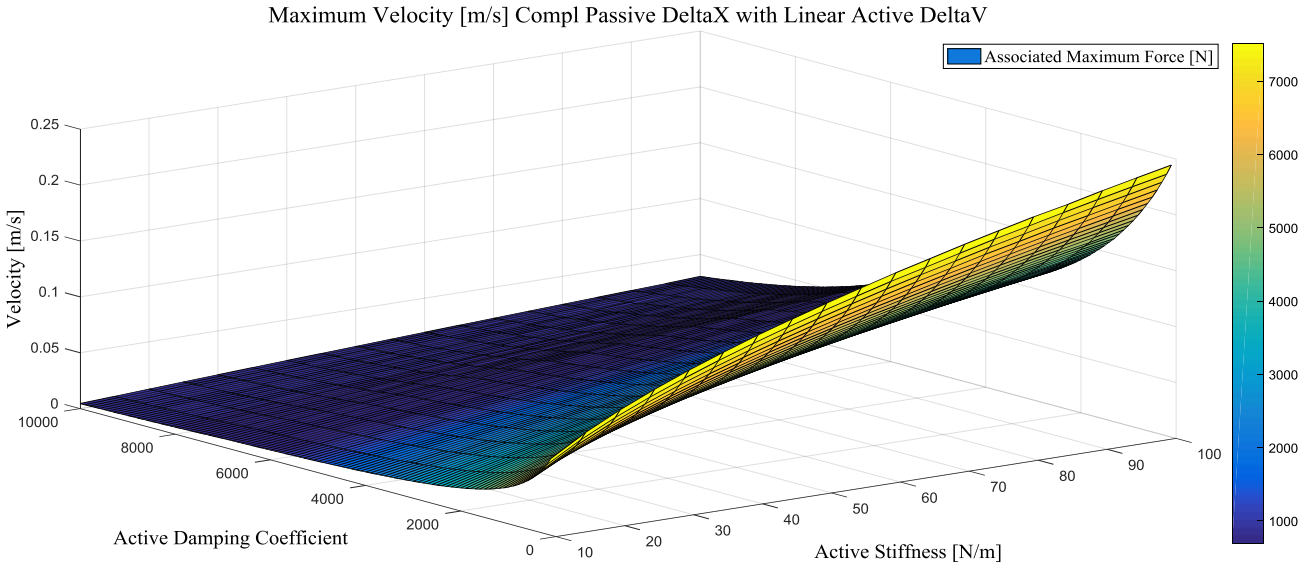

Figure 51

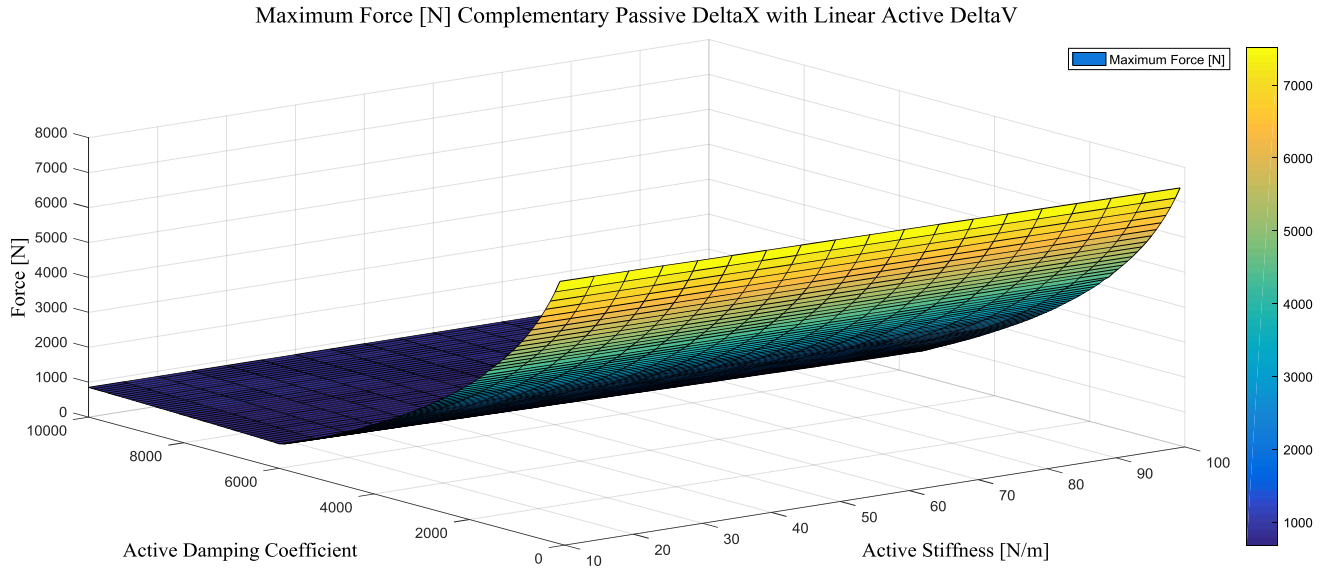

Figure 52

Linear Complementary Passive Delta V with Linear Active Delta V Force Law

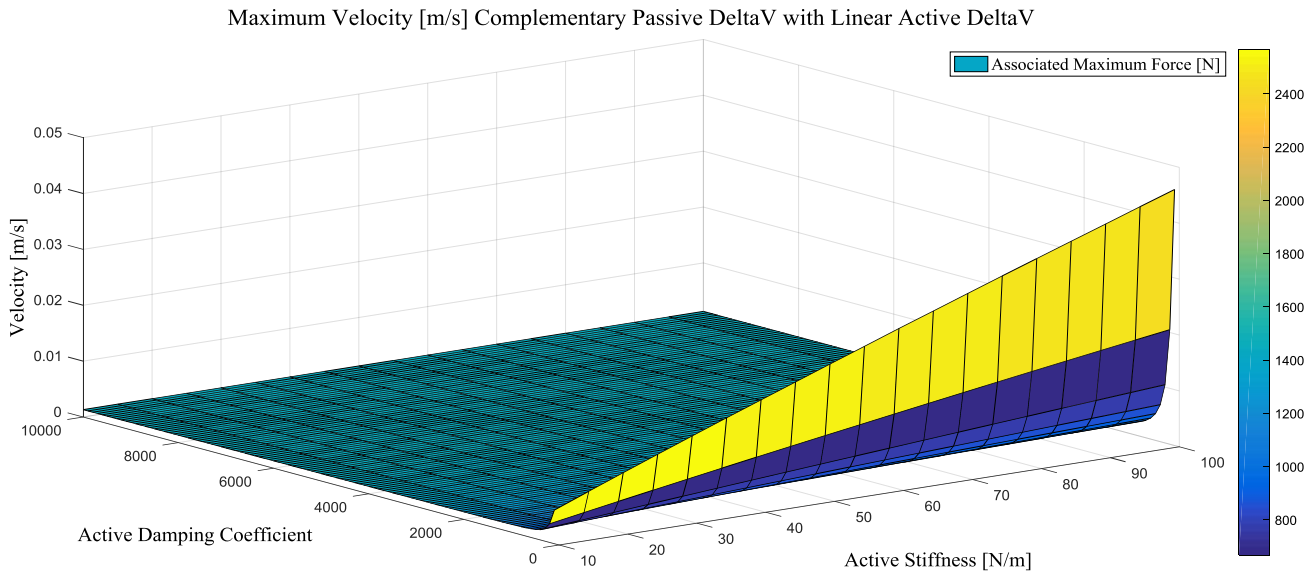

Figure 53

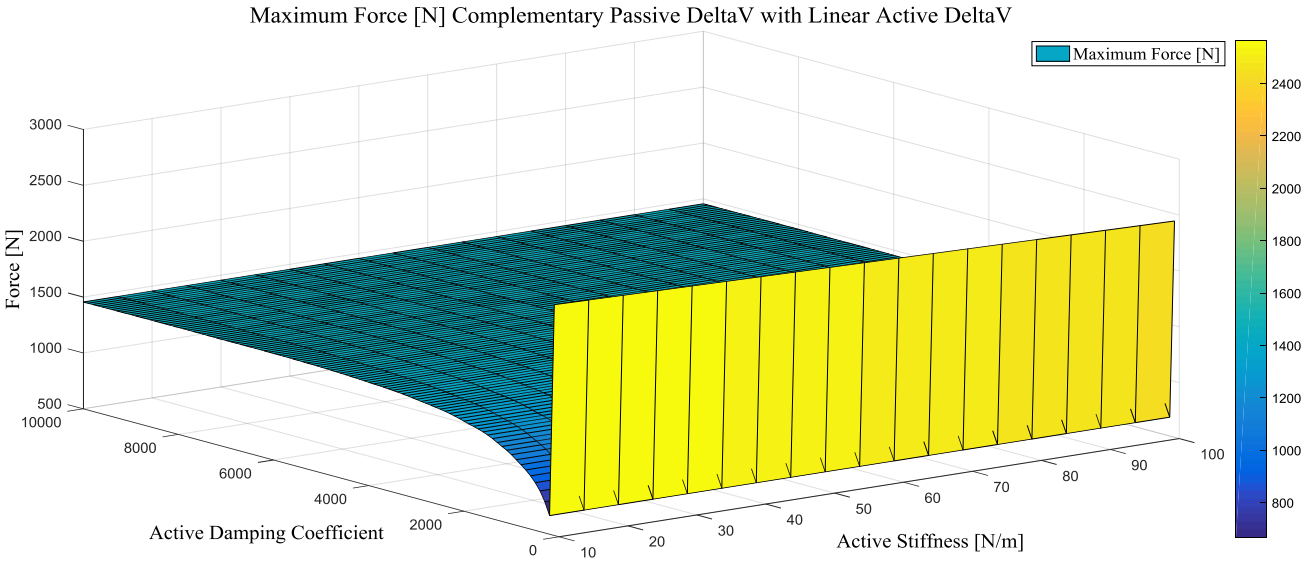

Figure 54

Optimal Results

The charts show the refined optimal solutions obtained through the simulations.

Force Laws Linear with Active V and Passive X Dependent Coefficient					
	Maximum Velocity [m/s]	**Maximum Force [N]**	**Maximum Active Stroke [m]**	**Maximum Passive Stroke [m]**	**Work Difference [J]**
Linear	0,0019	788,24	0,1393	0,2493	-87,03
Quadratic	0,0048	3332	0,2533	0,2494	-60,33
Cubic	0,0034	581,65	0,2504	0,2494	-24,15
Bell	0,0064	3392	0,2534	0,2494	-60,19
Logarithmic	0,0041	1995	0,252	0,2494	-31,2
Square Root	0,003	664,5	0,2073	0,2491	-52,8

Table 21

The following chart shows the optimal coefficients and their ranges of the force laws presented in the previous char.

	Damping Range	**Stiffness Range [N/m]**	**Optimal Damping**	**Optimal Stiffness [N/m]**
Linear	1000_10_4500	10_1_20	4500	10
Quadratic	2550_1_2650	10_1_20	2650	10
Cubic	4400_1_4500	10_1_20	4500	10
Bell	360_1_460	10_1_20	460	10
Logarithmic	3715_1_3815	10_1_20	3815	10
Square Root	2200_1_2300	10_1_20	2299	10

Table 22

Force Laws Linear with Active V and Passive V Dependent Coefficient					
	Maximum Velocity [m/s]	**Maximum Force [N]**	**Maximum Active Stroke [m]**	**Maximum Passive Stroke [m]**	**Work Difference [J]**
Linear	0,0646	1391	0,2505	0,2477	-204,95
Quadratic	0,0646	1399	0,2505	0,2476	-207,52
Cubic	0,0646	1400	0,2505	0,2476	-207,77
Bell	0,0646	1316	0,2505	0,2477	-194,7
Logarithmic	0,0646	1320	0,2505	0,2478	-193,01
Square Root	0,002	1358	0,0344	0,2488	-209,03

Table 23

	Damping Range	**Stiffness Range [N/m]**	**Optimal Damping**	**Optimal Stiffness [N/m]**
Linear	9000_10_10000	10_1_20	9990	10
Quadratic	9000_10_10000	10_1_20	10000	10
Cubic	9000_10_10000	10_1_20	10000	10
Bell	9000_10_10000	10_1_20	9990	10
Logarithmic	9000_10_10000	10_1_20	10000	10
Square Root	9000_10_10000	10_1_20	10000	10

Table 24

Force Laws Linear with Comp Passive V and Active V Dependent Coefficient					
	Maximum Velocity [m/s]	**Maximum Force [N]**	**Maximum Active Stroke [m]**	**Maximum Passive Stroke [m]**	**Work Difference [J]**
Linear	0,0014	1255	0,0302	0,2495	-194,02
Quadratic	0,0013	1209	0,0358	0,2495	-186,84
Cubic	0,0013	1253	0,031	0,2495	-193,12
Bell	0,0014	1063	0,0502	0,2494	-170,14
Logarithmic	0,0017	859	0,1039	0,2493	-116,86
Square Root	0,0015	7095	0,2558	0,2494	-189,67

Table 25

	Damping Range	Stiffness Range [N/m]	Optimal Damping	Optimal Stiffness [N/m]
Linear	200_10_1600	20_1_30	1600	20
Quadratic	100_10_1400	10_1_20	1320	10
Cubic	200_10_1600	10_1_20	1540	10
Bell	100_2_500	10_1_20	494	10
Logarithmic	100_2_500	10_1_20	500	10
Square Root	13_0,1_26	10_1_20	25,8	10

Table 26

The linear cases of the following charts are omitted because they were already embedded in the previous charts.

Force Laws Linear with Passive X and Active V Dependent Coefficient					
	Maximum Velocity [m/s]	**Maximum Force [N]**	**Maximum Active Stroke [m]**	**Maximum Passive Stroke [m]**	**Work Difference [J]**
Quadratic	0,0104	5838,7624	0,2558	0,2495	-176,5328
Cubic	0,0104	5862,9908	0,2559	0,2495	-177,1539
Bell	0,0104	5496,3537	0,2555	0,2495	-167,9871
Logarithmic	0,0104	6817,9276	0,2568	0,2495	-203,4527
Square Root	0,0014	657,5863	0,2506	0,2495	-11,6948

Table 27

	Damping Range	Stiffness Range [N/m]	Optimal Damping	Optimal Stiffness [N/m]
Quadratic	990_0,1_1010	10_0,1_12	1010	10
Cubic	990_0,1_1010	10_0,1_12	1010	10
Bell	990_0,1_1010	10_0,1_12	1010	10
Logarithmic	990_0,1_1010	10_0,1_12	1010	10
Square Root	990_0,1_1010	10_0,1_12	1010	10

Table 28

Force Laws Linear with Passive V and Active V Dependent Coefficient					
	Maximum Velocity [m/s]	**Maximum Force [N]**	**Maximum Active Stroke [m]**	**Maximum Passive Stroke [m]**	**Work Difference [J]**
Quadratic	0,0646	1391,7425	0,2505	0,2477	-38,8924
Cubic	0,0646	1391,7300	0,2505	0,2477	-38,8937
Bell	0,0648	1392,4459	0,2505	0,2476	-38,8629
Logarithmic	0,0650	1389,3208	0,2506	0,2478	-39,0616
Square Root	0,0187	1450,3006	0,0903	0,2473	-29,7427

Table 29

	Damping Range	Stiffness Range [N/m]	Optimal Damping	Optimal Stiffness [N/m]
Quadratic	9970_0,1_9990	10_0,1_12	9989	10
Cubic	9975_0,1_9995	10_0,1_12	9994	10
Bell	9970_0,1_9990	10_0,1_12	9980	10
Logarithmic	9985_0,1_10000	10_0,1_12	10000	10
Square Root	8125_0,1_8145	10_0,1_12	8127	10

Table 30

Force Laws Linear with Comp Passive X and Active V Dependent Coefficient					
	Maximum Velocity [m/s]	**Maximum Force [N]**	**Maximum Active Stroke [m]**	**Maximum Passive Stroke [m]**	**Work Difference [J]**
Linear	0,0121	2014,6012	0,2520	0,2494	-65,6894
Quadratic	0,0142	1817,6250	0,2518	0,2493	-62,6882
Cubic	0,0120	1838,1653	0,2518	0,2493	-62,9502
Bell	0,0121	1567,1250	0,2516	0,2493	-59,3499
Logarithmic	0,0121	2934,1106	0,2529	0,2494	-83,7764
Square Root	0,0089	1911,2690	0,2502	0,2494	-0,9134

Table 31

	Damping Range	**Stiffness Range [N/m]**	**Optimal Damping**	**Optimal Stiffness [N/m]**
Linear	3990_0,1_4000	10_0,1_12	4000	10
Quadratic	3990_0,1_4000	10_0,1_12	3999	12
Cubic	3990_0,1_4000	10_0,1_12	4000	10
Bell	3990_0,1_4000	10_0,1_12	4000	10
Logarithmic	3990_0,1_4000	10_0,1_12	3999	10
Square Root	490_0,1_500	10_0,1_12	500	10

Table 32

The previous values were obtained trying to minimize the bouncing velocities. In some cases, the maximum forces are quite high because the stroke is not completely exploited or because the impact with the bottom is reached. From these results was evident that another approach of optimization was necessary.

3.4.3 Combined Active and Passives system Sensitivity Simulations – Results

\The following figures show the trend of the fundamental parameters with respect to the arrival velocity and the ground stiffness. As in the previous cases, the results of the 4 principal linear cases are given with an exception for the arrival velocity sensitivity analysis.

3.4.3.1 Arrival Velocity Sensitivity Analysis– Results

Linear Passive Delta X with Linear Active Delta V Force Law

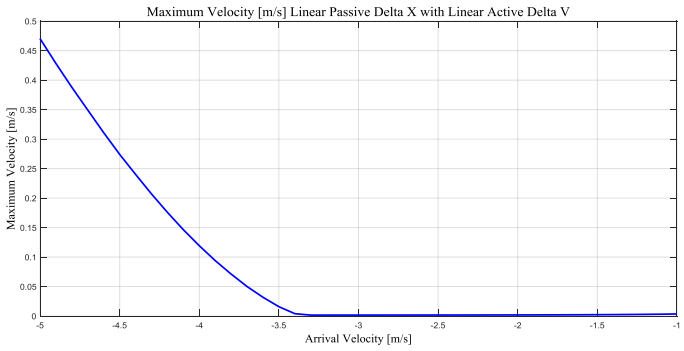

Figure 55

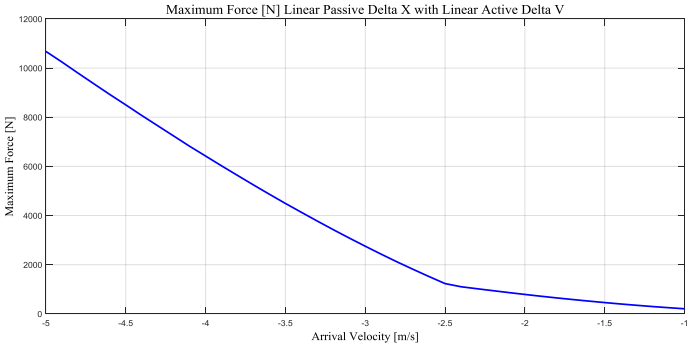

Figure 56

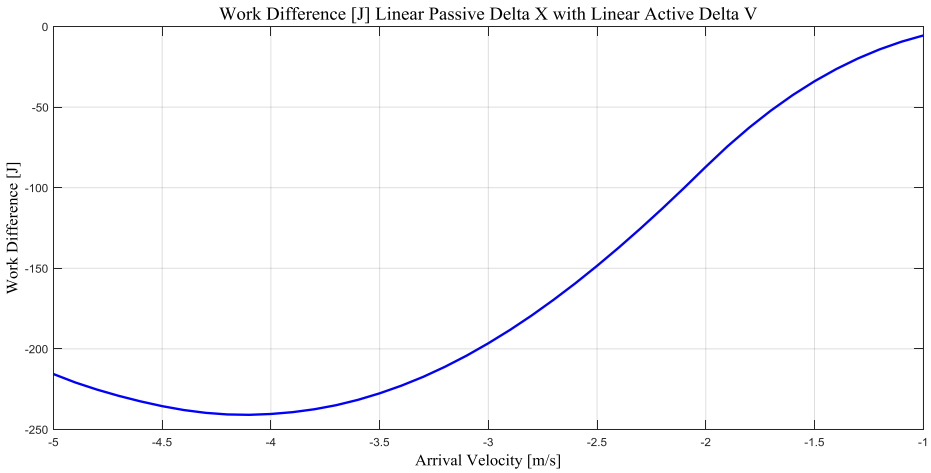

Figure 57

It can be observed that the work difference becomes more negative for higher velocities. Indeed, this means that the passive damper has a predominant role also for other velocities.

Linear Passive Delta V with Linear Active Delta V Force Law

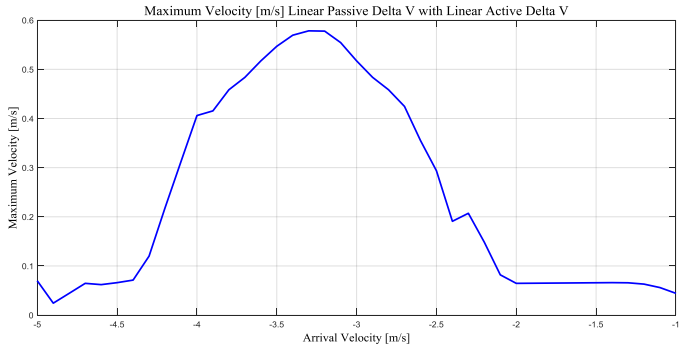

Figure 58

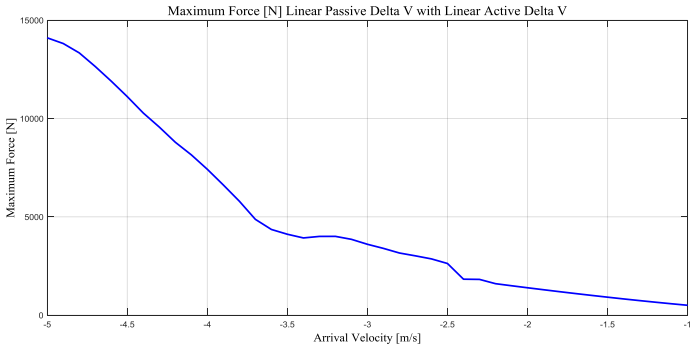

Figure 59

Linear Complementary Passive Delta X with Linear Active Delta V Force Law

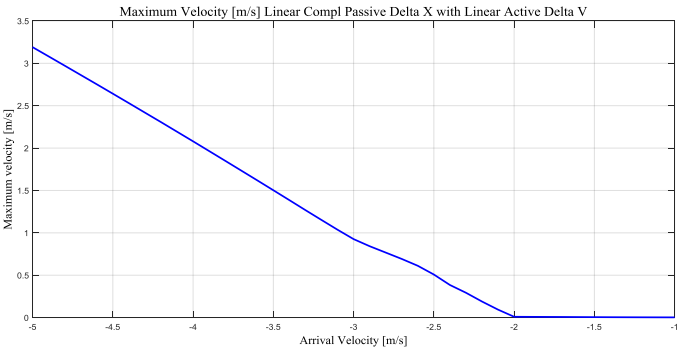

Figure 60

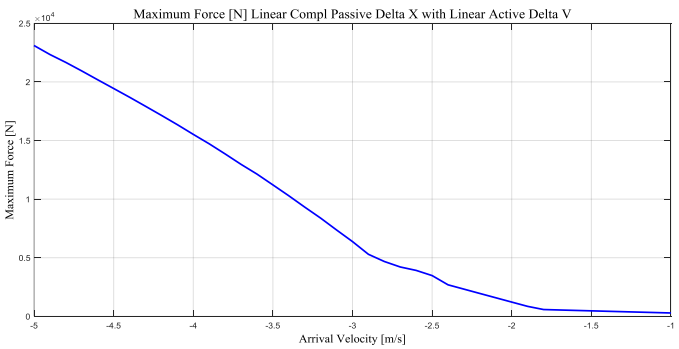

Figure 61

Linear Complementary Passive Delta V with Linear Active Delta v Force Law

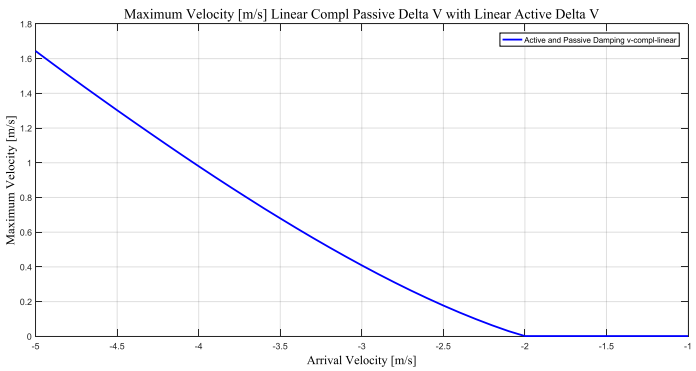

Figure 62

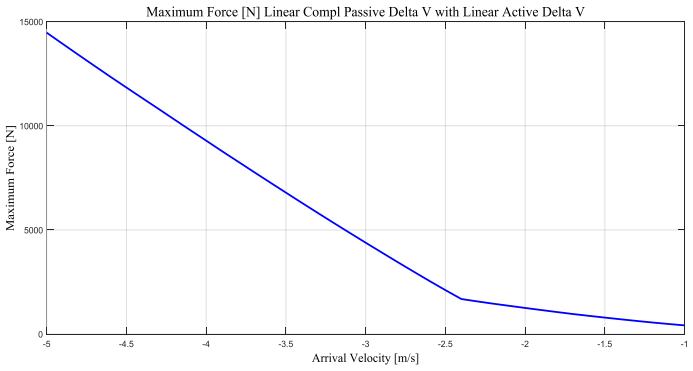

Figure 63

Linear Complementary Passive Delta V with Bell Active Delta V Force Law

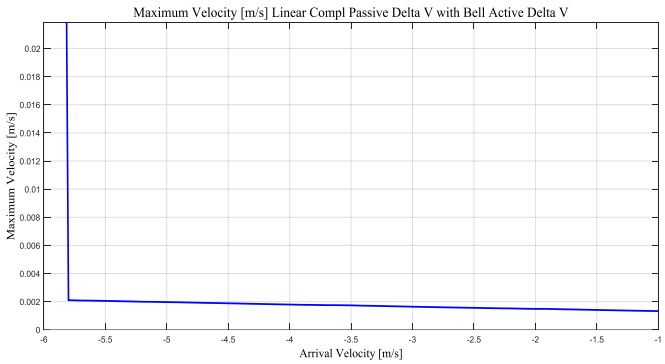

Figure 64

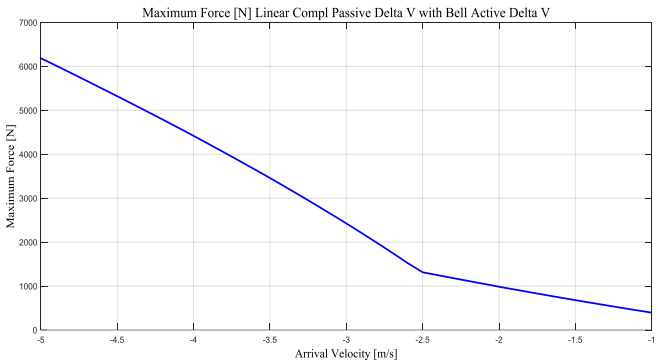

Figure 65

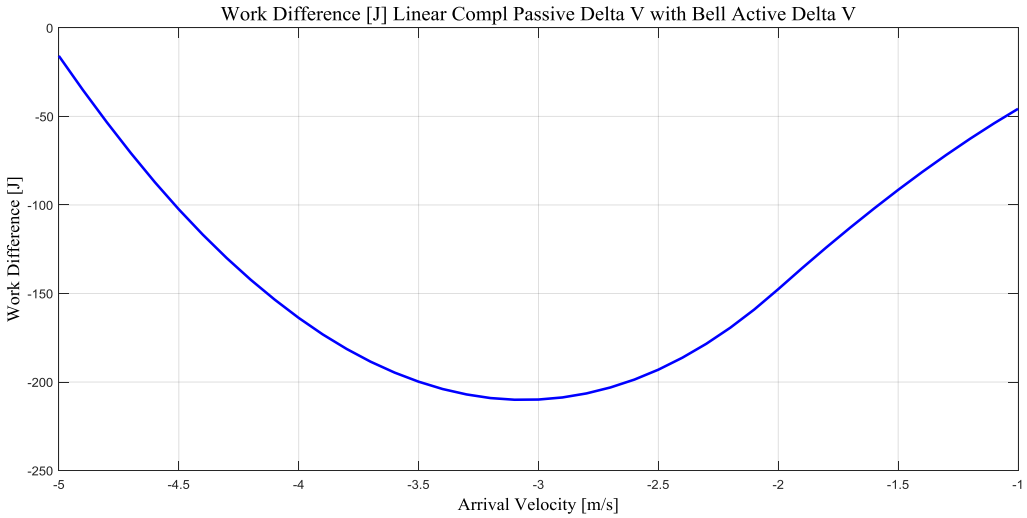

Figure 66

The last case shows the best result among all the considered cases. The high performance of this solution is given by its adaptability. Indeed, the central position of the bell is let to change according the arrival velocity while for other laws all the coefficients are kept fixed. Thanks to this consideration, it is understood that an adaptive solution is strictly necessary to achieve an acceptable behavior for higher velocities. Below, the figures of the only-passive case are given. It is quite obvious that the passive solution (which has no adaptive capability) cannot be apply alone for velocities higher than 2 m/s.

Passive Granular

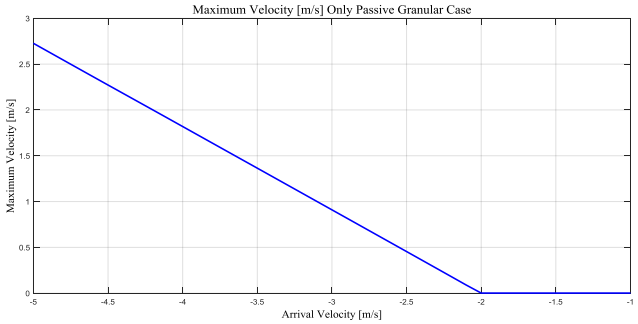

Figure 67

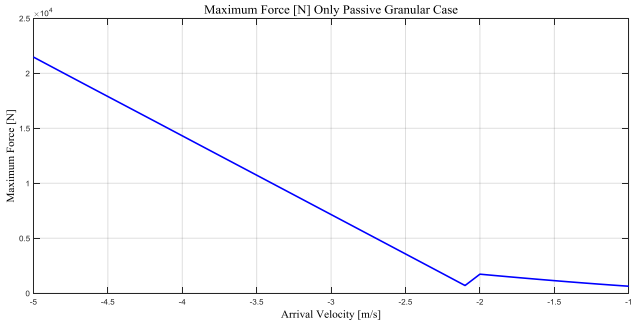

Figure 68

3.4.3.2 Ground Properties Sensibility Analysis – Results

The following figures shows the trend of the force and velocity of the usual 4 linear cases with respect to the ground stiffness. Actually, to each value of the stiffness, a damping value is associated. The ground damping – stiffness trend was already presented in the section dedicated to the first sensitivity analysis. The logarithmic scale is used for the stiffness axis to have a better view of the used range.

Linear Passive Delta X with Linear Active Delta V Force Law

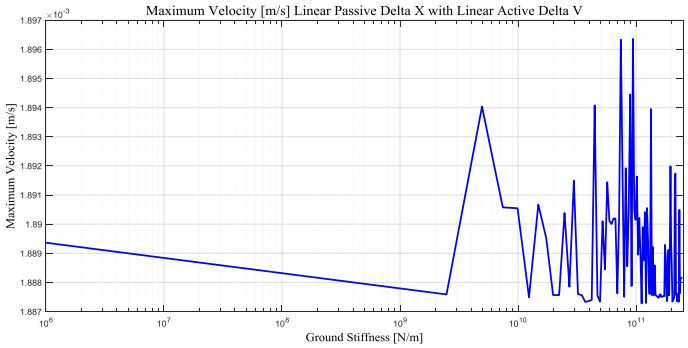

Figure 69

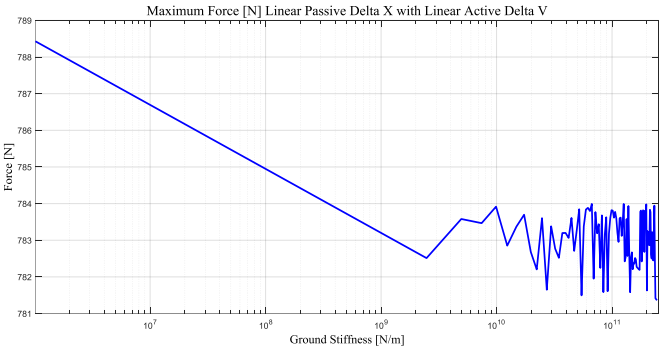

Figure 70

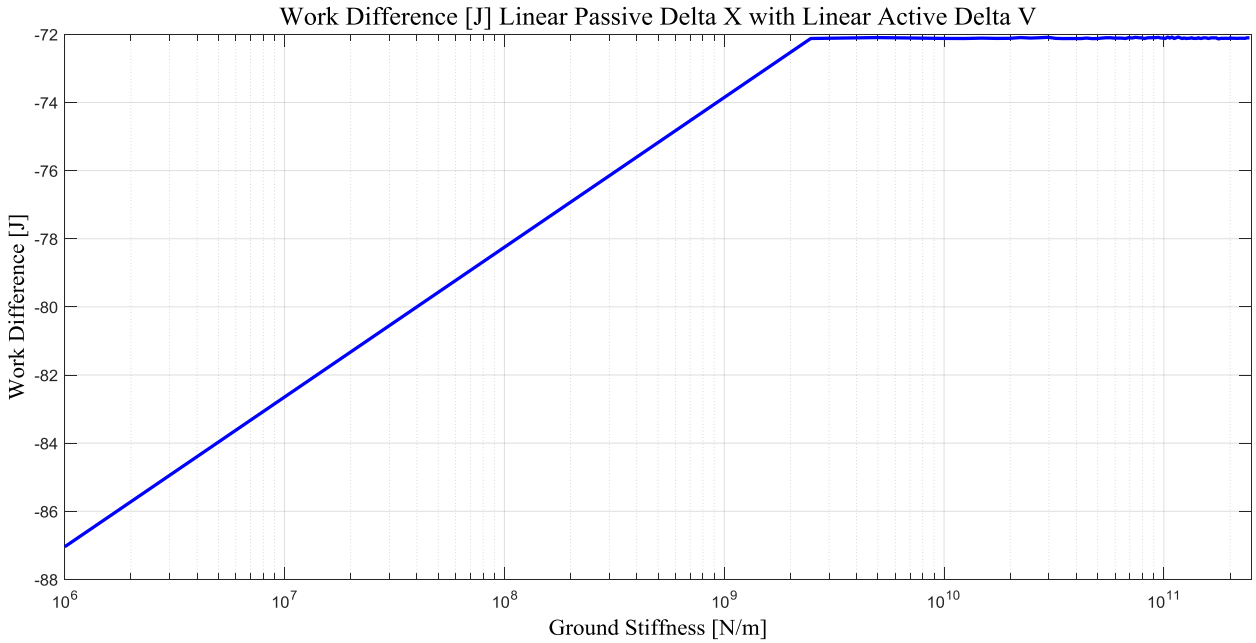

Figure 71

Linear Passive Delta V with Linear Active Delta V Force Law

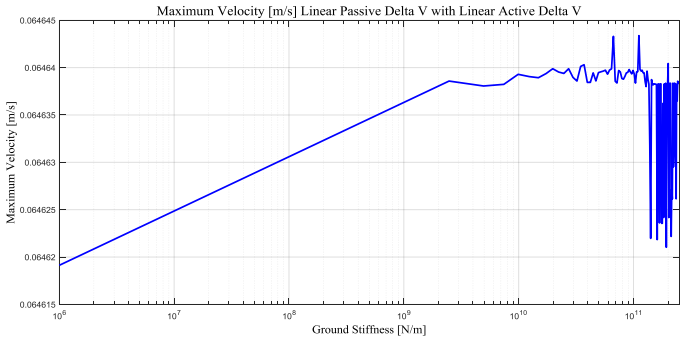

Figure 72

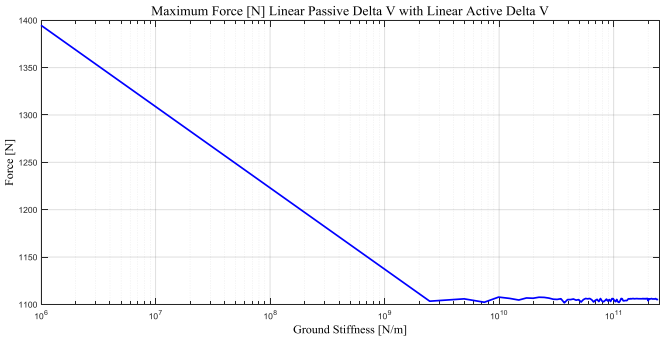

Figure 73

Linear Complementary Passive Delta X with Linear Active Delta V Force Law

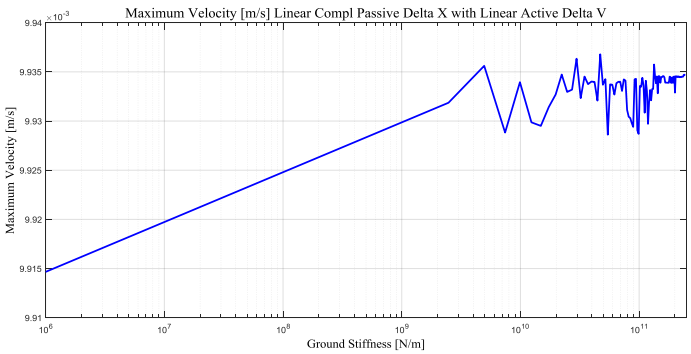

Figure 74

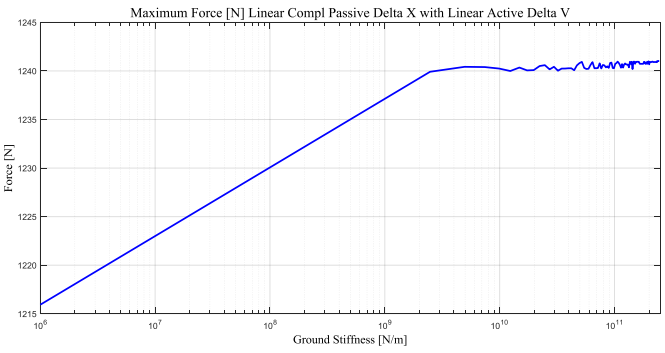

Figure 75

Linear Complementary Passive Delta V with Linear Active Delta V Force Law

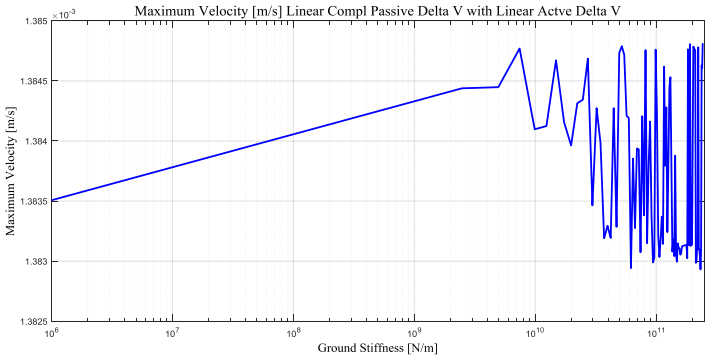

Figure 76

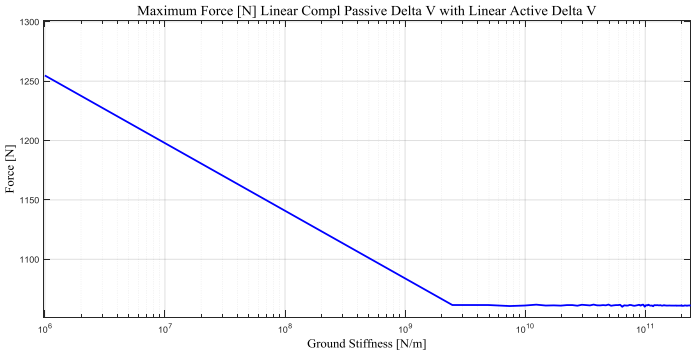

Figure 77

Passive Granular

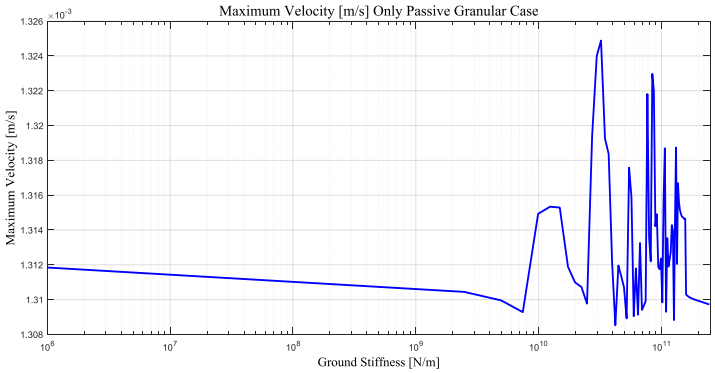

Figure 78

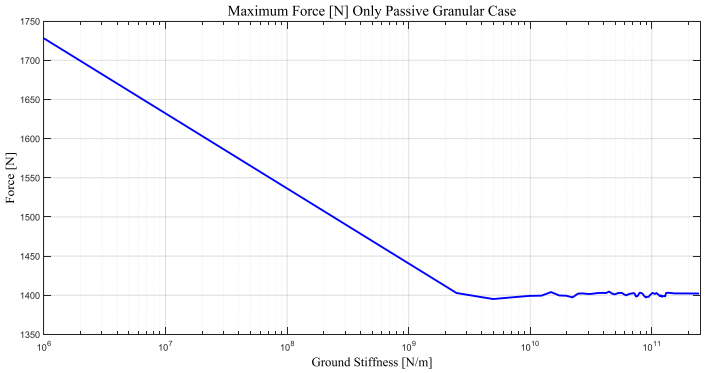

Figure 79

Looking on the previous figures, the velocities remain in their optimal values ranges and the forces show a descending trend except for the X-complementary case. This last consideration is related to the fact that for higher stiffness', higher damping values are associated which make the relative velocity of the passive damper to be lower and so the force produce by it (look the last figure). Indeed, lower passive force could reduce also the maximum force transmitted by the active one. Only in the X-complementary case the trend is reversed since the stroke of the passive device is reduced and so the complementary value of it is increased. Anyway, it is noticeable that also the passive device has a quite robust behaviour against the variation of the ground properties.

3.4.4 Simulations with Different Laws for Ascent and Descent Phases – Results

In these simulations, the parameters which are varied are the damping coefficients for the descent and the ascent phases. During the descent, the active damper has a linear behavior while for the ascending phase, different laws are considered. Since these simulations were done only with the aim to investigate the feasibility of this configuration, the 3D plot of only one linear case is given and the coarse data are presented in the optimal data table.

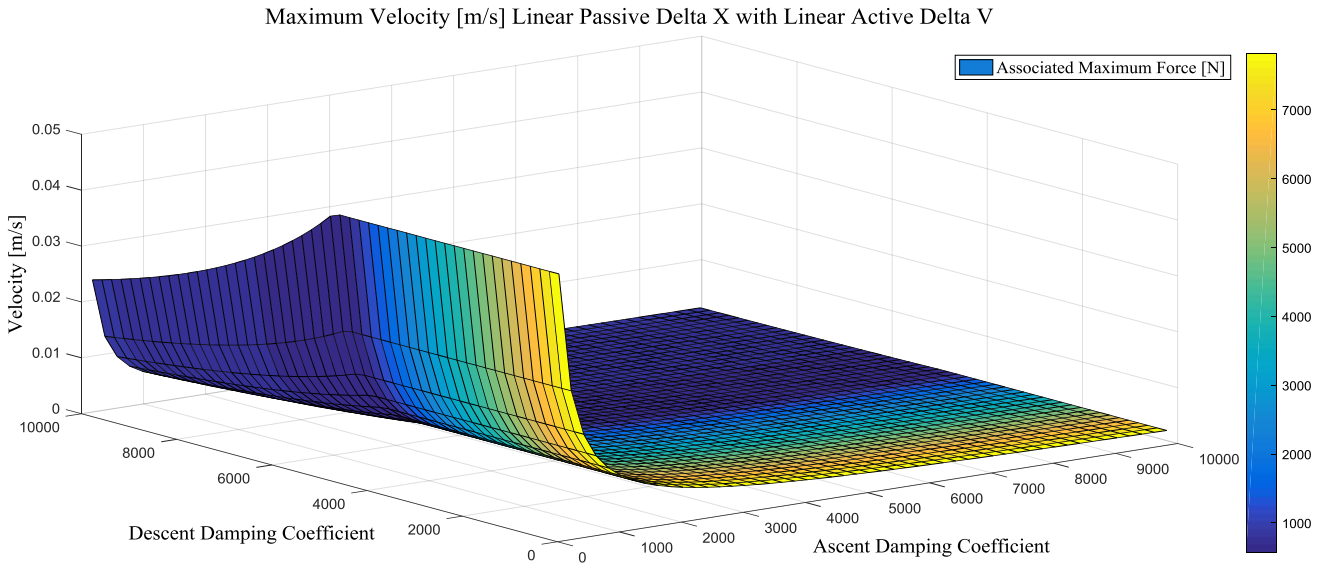

Figure 80

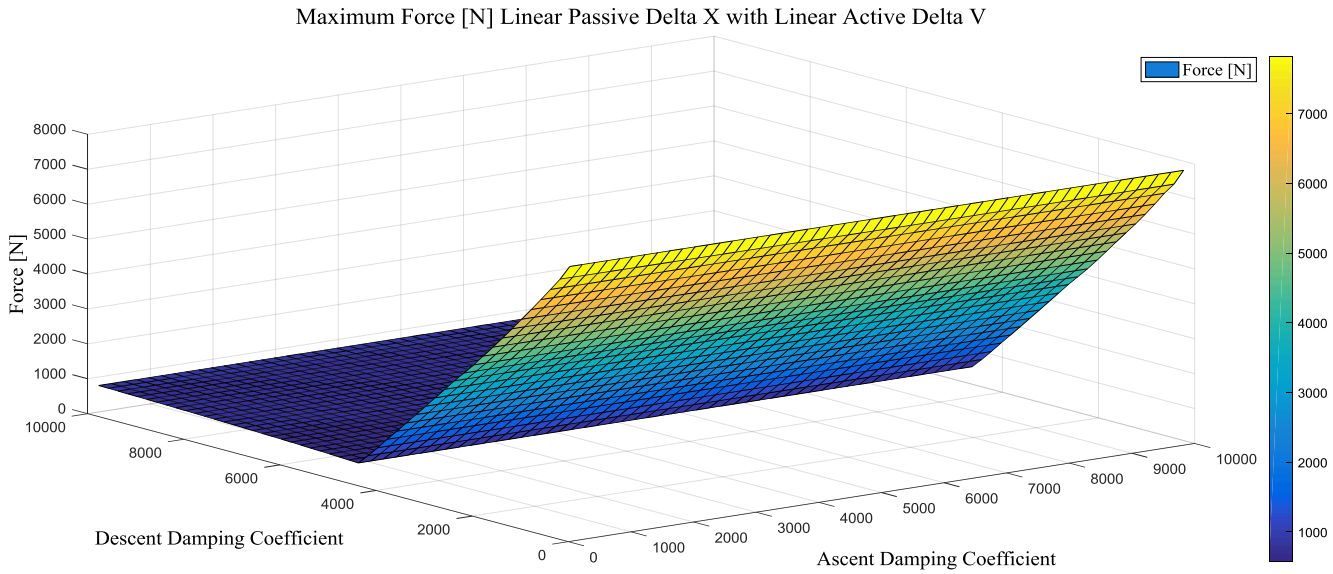

Figure 81

It is noticeable that the velocity trend depends mainly on the coefficient of the ascent while the force on the descent's one. As in the previous cases, the "knee" of the force trend is related to the bottom shock of the active damper.

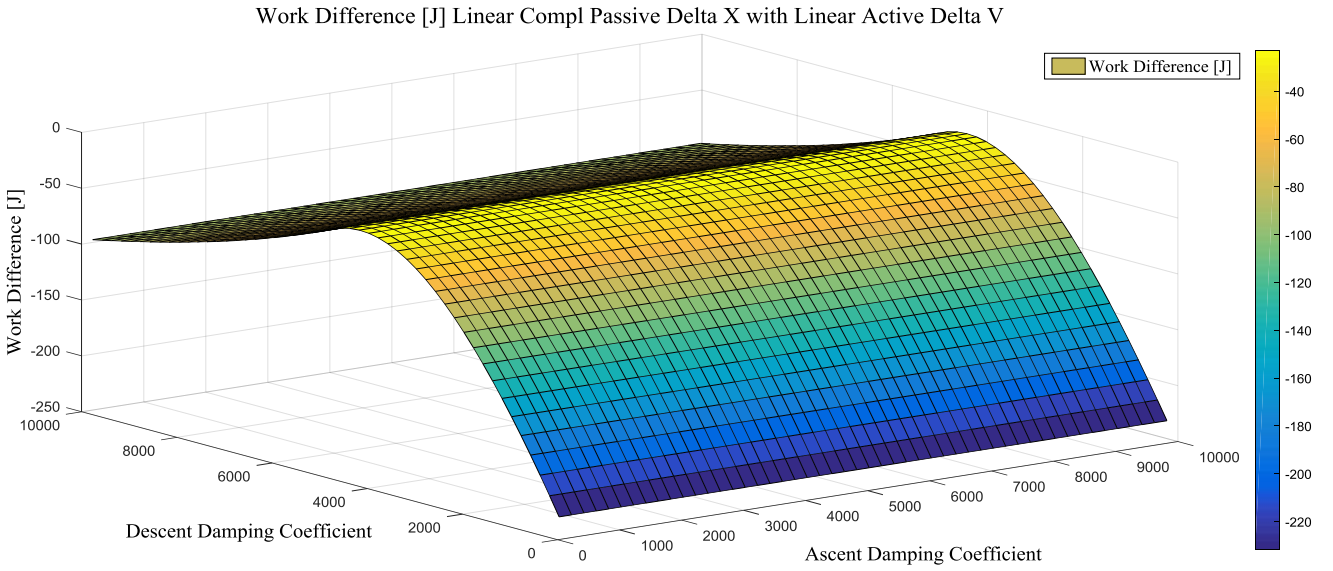

Figure 82

Optimal Results

In this case, the force laws which depend directly on the passive delta V were not considered since they were characterized by the worst results in terms of rebound velocity and force.

Force Laws Linear with Active V and Passive X Dependent Coefficient					
	Maximum Velocity [m/s]	**Maximum Force [N]**	**Maximum Active Stroke [m]**	**Maximum Passive Stroke [m]**	**Work Difference [J]**
Linear	0,0023	577	0,2505	0,2494	-23
Quadratic	0,0023	577	0,2505	0,2494	-23
Cubic	0,0023	577	0,2505	0,2494	-23
Bell	0,0016	577	0,2505	0,2494	-23
Logarithmic	0,0024	577	0,2505	0,2494	-23
Square Root	0,0018	577	0,2505	0,2494	-23

Table 33

	Descent Damping Range	**Ascent Damping Range**	**Optimal Descent Damping**	**Optimal Ascent Damping**
Linear	100_200_10000	100_200_10000	4500	9900
Quadratic	100_200_10000	100_200_10000	4500	9900
Cubic	100_200_10000	100_200_10000	4500	9900
Bell	100_200_10000	100_200_10000	4500	9900
Logarithmic	100_200_10000	100_200_10000	4500	9900
Square Root	100_200_10000	100_200_10000	4500	9900

Table 34

Force Laws Linear with Compl Passive V and Active V Dependent Coefficient					
	Maximum Velocity [m/s]	**Maximum Force [N]**	**Maximum Active Stroke [m]**	**Maximum Passive Stroke [m]**	**Work Difference [J]**

Linear	0,0015	779	0,1464	0,2494	-89
Quadratic	0,0015	779	0,1464	0,2494	-89
Cubic	0,0015	779	0,1464	0,2494	-89
Bell	0,0015	779	0,1464	0,2494	-89
Logarithmic	0,0014	594,9	0,2505	0,2493	-33,08
Square Root	0,0014	594,9	0,2505	0,2493	-33,08

Table 35

	Descent Damping Range	**Ascent Damping Range**	**Optimal Descent Damping**	**Optimal Ascent Damping**
Linear	100_200_10000	100_200_10000	300	1700
Quadratic	100_200_10000	100_200_10000	300	1700
Cubic	100_200_10000	100_200_10000	300	1700
Bell	100_200_10000	100_200_10000	300	1900
Logarithmic	100_5_200	8100_10_10000	155	9160
Square Root	100_5_300	1_1_50	155	49

Table 36

Force Laws Linear with Passive X and Active V Dependent Coefficient					
	Maximum Velocity [m/s]	**Maximum Force [N]**	**Maximum Active Stroke [m]**	**Maximum Passive Stroke [m]**	**Work Difference [J]**
Quadratic	0,0025	576,773	2,51E-01	2,49E-01	-52,3208
Cubic	0,0025	576,773	2,51E-01	2,49E-01	-52,3208
Bell	0,0025	576,773	2,51E-01	2,49E-01	-52,3219
Logarithmic	0,0025	576,7715	2,51E-01	2,49E-01	-52,326
Square Root	0,0032	609,4983	0,2418	0,249	-50,7401

Table 37

	Descent Damping Range	**Ascent Damping Range**	**Optimal Descent Damping**	**Optimal Ascent Damping**
Quadratic	3000_500_8000	100_200_8000	4500	7900
Cubic	3000_500_8000	100_200_8000	4500	7900

Bell	3000_500_8000	100_200_8000	4500	7900
Logarithmic	3000_500_8000	100_200_8000	4500	7900
Square Root	3500_500_5500	1000_500_1500	5000	1200

Table 38

Force Laws Linear with Compl Passive X and Active V Dependent Coefficient					
	Maximum Velocity [m/s]	**Maximum Force [N]**	**Maximum Active Stroke [m]**	**Maximum Passive Stroke [m]**	**Work Difference [J]**
Linear	0,0070	703,8150	0,2507	0,2492	-51,1208
Quadratic	0,0025	576,7730	0,2505	0,2494	-52,3208
Cubic	0,0070	703,8150	0,2507	0,2492	-51,1201
Bell	0,0025	576,7730	0,2505	0,2494	-52,3219
Logarithmic	0,0070	703,8153	0,2507	0,2492	-51,1251
Square Root	0,0024	727,1399	0,2504	0,2491	-49,8310

Table 39

	Descent Damping Range	**Ascent Damping Range**	**Optimal Descent Damping**	**Optimal Ascent Damping**
Linear	3000_500_8000	100_200_8000	6000	7900
Quadratic	3000_500_8000	100_200_8000	4500	7900
Cubic	3000_500_8000	100_200_8000	6000	7900
Bell	3000_500_8000	100_200_8000	4500	7900
Logarithmic	3000_500_8000	100_200_8000	6000	2500
Square Root	3000_500_7500	100_100_2500	6500	7900

Table 40

Thanks to this analysis, it was evident that an approach based on the separation of between the ascent and descent phases is able to ensure lower forces and bouncing velocities.

4. Granular Damper Characterization and Active System Calibration

4.1 About DEM Analysis

4.1.1 Premise

As it was said in the chapter dedicated to the State of Art, granular materials (like sand, powder and small spheres) have the capability to dissipate a huge amount of kinetic energy during an impact scenario. The momentum is transferred to the granules and the energy is subsequently dissipated through the collisions and the frictional interactions between the granules. This distinctive feature of the granular material lead to a preliminary sizing of a granular damper composed by a cylinder containing the granules and by an intruder which penetrates in the granules during the landing. This damper is characterized by an intrinsic simplicity, high efficiency and high reliability in the space environment, especially if only metallic granules are used. In the first multibody simulations, the behaviour of this damper was modelled as a force proportional to the penetration velocity with a coefficient which varies linearly with the stroke. This simple assumption was done because some authors refer to a stroke-velocity dependent granular-force without specifying the type of this dependency precisely but, in the aim of identifying the general response of the system with different configurations and active laws, this simplification was acceptable. However, the need of a more detailed

comprehension of the granular material and the need of verifying the feasibility of this damper, require a more sophisticated tool of analysis. An experimental approach would be too onerous and unable to reproduce a real comet-landing scenario while the search or the determination of an analytical solution would be too difficult considering that the granular mechanic is still in the field of research for this kind of space application. The most suitable solution for this work is given by a numerical approach and the DEM (Discrete Element Method) offers the possibility to model and to simulate the granular behaviour numerically. The DEM software used for this purpose is YADE and the following sections will be dedicated to the explanation of the physic of the problem, the logic of the software, the modelling, the performed simulations, the problems faced and the analysis of the obtained data.

4.1.2 Description of the DEM Software

YADE is an open-source framework for Discrete Element Method written in C++ language and allows the implementation of the models, the creation of scenarios and the control of simulations and calculated data through Python. The main elements of the DEM model are the particles (spheres) which are defined by the material (Young modulus, Poisson coefficient, friction angle, density) and the radius. The particles can interact one with another and with other elements like walls, boxes, cylinders and polyhedrons. The mutual configuration of two particles has 6 degrees of freedom like a beam in 3D space because both particles have 6 DOFs each, but the interaction itself is free to move and rotate in space having 6 DOFs itself (12 - 6). The algorithm defines the interaction between the particles (or more generally between the bodies) through the detection of the collisions and then creating the interactions and determining its properties like the stiffness. Once all the interactions are defined, the algorithm performs the strain evaluation, the stress computation based on strains and the application of the forces. The detection of the collisions is done in two steps where in the first step a fast collision detection in an approximated way is performed while in the

second step a selection (or filtering) is done in order to calculate more accurate collisions. The collision detection is based on the interaction between the **AABB**s (axis aligned bounding boxes) which is the imaginary box-shaped boundary defined for each particle and the internal algorithms (which won't be explained in this work) verify if these boundaries overlaps and so if the collisions can really occur. Hereafter, a scheme of the mentioned sphere-boundary is given.

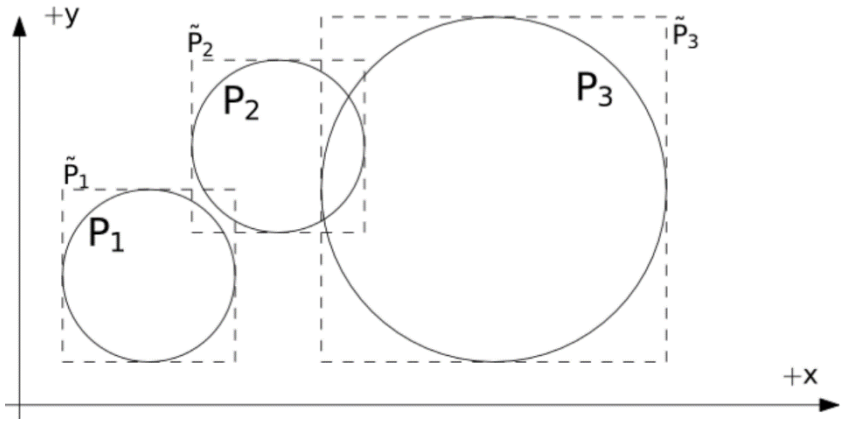

Figure 83 Illustration of the axis aligned boundary boxes

This stage is followed, as said before, by the creation of interactions between the particles where the physical properties instead of the geometrical properties are involved. The basic DEM interaction defines two stiffness's: the normal and the shear stiffness's. The normal stiffness is directly related to the Young's modulus of the material while the ratio between the normal and the shear stiffness's is related to the Poisson's coefficient. In the stage devoted to the determination of the interactions between the particles, YADE computes the normal interaction stiffness as the stiffness of the springs in series each one with lengths equal to the sphere radii. The calculation of this equivalent normal stiffness considers that each particle generates a force which is proportional to the variation of its radius and a stiffness constant which depends on the material property. The value of the obtained interaction normal stiffness depends only on the materials' properties and particle dimensions. The following step is the strain evaluation. In this stage, constant geometrical quantities are calculated (like the initial

distance and the contact area) useful to define the strain and subsequently the stress. As the particles undergo motion during the simulation, the normal and shear displacements and so the respective strains are calculated. Once strain on a contact is computed, it can be used to compute stresses/forces acting on both particles. This process depends on the nature of the material being modeled and requires a constitutive law. The most usual constitutive law in DEM formulation is the simple non-cohesive elastic case with dry friction, which was proposed by Cundall. At each step, given normal and shear displacements, normal and shear forces are computed as the products between the previously mentioned interaction stiffness's and their respective displacements as in the following expressions.

$$\boldsymbol{F}_{\mathrm{N}} = \mathrm{K}_{\mathrm{N}} u_{\mathrm{N}} \boldsymbol{n},$$
$$\boldsymbol{F}_{\mathrm{T}}^{\mathrm{t}} = \mathrm{K}_{\mathrm{T}} \boldsymbol{u}_{\mathrm{T}}$$

The letter **n** in the first expression denotes the normal direction vector while the apex **t** in the second expression indicates that the shear force is a trial force. In the simple case of the frictional material constitutive law (which is the case considered in this work), a simple non-associated stress return algorithm is applied for the final shear force calculation:

$$\boldsymbol{F}_{\mathrm{T}} = \begin{cases} \boldsymbol{F}_{\mathrm{T}}^{\mathrm{t}} \frac{|\boldsymbol{F}_{\mathrm{N}}| \tan \varphi}{\boldsymbol{F}_{\mathrm{T}}^{\mathrm{t}}} & \text{if } |\boldsymbol{F}_{\mathrm{T}}| > |\boldsymbol{F}_{\mathrm{N}}| \tan \varphi, \\ \boldsymbol{F}_{\mathrm{T}}^{\mathrm{t}} & \text{otherwise.} \end{cases}$$

In this expression, **ϕ** represents the friction angle (in radians) and it is calculated as the arctangent of the frictional coefficient of the considered material. This algorithm relays on the fact that, if the tangential force reaches the static frictional limit, it cannot exceed this value during the simulation. Indeed, if the frictional force between two surfaces exceeds the static frictional limit, they would start to slide and the frictional force becomes dynamic and diminishes. Actually, YADE considers only the static friction because it treats the problem as a quasi-static phenomenon for each time instant of

integration. It's important to underline that in DEM generally, some constitutive laws are expressed using strains and stresses while others prefer displacements and forces like in this latter case. Anyway, the sum of both the forces are applied on the particles and each particle accumulates forces, during the time step, acting on it. Actually, since the computed forces act on a contact point which is different from the center of the sphere, the torques generated by the force are considered. Finally, the equation of motion for each particle is integrated using the already mentioned forces and torques. In this phase, the algorithm determines the position and the orientation of the particles in the next timestep from the integration of the current linear acceleration and angular acceleration respectively. Beside the previously mentioned body elements (spheres, boxes e t c), YADE allows to work with rigid aggregates of elements which are called Clumps. They are very useful because they give the possibility to model objects with complex shapes (like the intruder, the piston rod e t c) that must interact with the granular material. They can be composed of many spheres or other elements like boxes and polyhedrons and their dynamic properties are computed as properties of their members. Each element of the Clump is treated separately for the collision detection and contact resolution but during the integration, the entire Clump is treated as a unique body. Indeed, instead of integrating each element separately, forces and torques acting on each element are converted to forces and torques on the Clump itself and the relative positions of Clump members are kept fixed, resulting in a behavior of a rigid aggregate. As it was said before, YADE considers the problem as a quasi-static phenomenon. However, in order to include the dissipation of kinetic energy of the particles in the simulation, velocity-based damping should be introduced. This feature is not included in most of the constitutive laws and so YADE considers the artificial numerical damping. The basic idea is to decrease forces which increase the particle velocities and vice versa. YADE adopts this strategy which, even if not physical, is easy to compute. The damping is defined by a damping coefficient which is embedded in the integrator-engine. For what regards the computational aspects, DEM simulations use implicit integration schemes because they demand a lower number of step during the simulation compared to the explicit schemes. The total computational time for a single simulation depends on the number of time steps, the number of particles and the number of the computational cores. It can be demonstrated that an estimation of the simulation time

can be obtained as the inverse of fourth power of the radius of the spheres. Generally speaking, the simulation time per particle and per time step is about 10e-06 s for current machines. It's interesting to underline that DEM simulations are characterized by the results indeterminism which is caused by the fact that the interactions between the particles are treated in an arbitrary order. All these explanations are given with the intention to give a rough view of the used tool but for a more detailed information about DEM and the software, the reader is recommended to consult the YADE Documentation.

4.2 Scenario Modelling and Simulation Issues

4.2.1 Scenario Presentation and Granular Material Definition

As it was said in the previous section, the principal objective of DEM simulations is to understand the behaviour of the granular material and the feasibility of this solution. To achieve this goal, it is not strictly necessary to reproduce the properties of the ground (in terms of stiffness and damping) and to include the contribution of the upper active damper. This consideration lead to the construction of a simpler scenario where an intruder with an equivalent satellite mass is left to fall through the granular material which fills a container rigidly constrained to the ground. Indeed, the kinetic energy involved in this simplified scenario is almost the same to that considered in the multibody simulations (where the landing pad attached to the granular container is free to move) and ignoring the contribution of the active device, DEM simulations are able to demonstrate the real capacity of the granular damper to dissipate the kinetic energy when it's used alone. As it was mentioned before, YADE offers the possibility to model the problem using some elementary bodies like spheres, boxes, walls, polyhedrons and

so on. The elements considered to model the granular material are obviously spheres which are characterized by the chosen material and radius. YADE allows to create a single sphere separately or to create a group of multiple spheres through the packing algorithms. Once the geometry of the packing is defined (called also predicate), YADE is able to fill the defined volume with spheres using different packing strategies like the orthogonal, hexagonal and random-dense packings. In the first two cases, the spheres are packed according to the given packing geometry and gap trying, to fill the available volume without being compressed but in the last case, the algorithm performs a sort of pre-simulation where the spheres are compressed up to a certain limit allowing the best exploitation of the given volume. This latter case is the most computationally onerous case because it involves a higher number of spheres and gives a packing where the spheres are pre-stressed from the beginning of the simulation and are randomly distributed. Regarding the packing volumes, the software gives the possibility to create simple packing geometries like spheres, cylinders and boxes but it also allows to import particular geometries or distributions from external sources. As it can be imagined, the packing of the granular material has a noticeable impact on the simulation results and so a more detailed discussion about this issue will be given in a dedicated section.

4.2.2 Container Modelling

After the definition of the granular material, the attention is focused on the modelling of the container. Usually, in most of DEM simulations, the "boundary" or the container is modelled using elements called facets. They are geometrical zero-thickness elements defined by the coordinates of three points (vertices) which interact with the spheres. YADE allows to build containers with different geometries (boxes, cylinders) as a composition of multiple facets. However, the principal problem related to the facet-made containers is that, because of its zero-thickness, the spheres tend to exit freely from the container walls when the random-dense packing is used or when the spheres are subjected to a high compression during the simulation (for example when the

intruder penetrates through the granular material). For these reasons, the idea of the facet-made container is discarded and another approach is used. Boxes are YADE elements able to interact with the spheres (but not with another boxes) and are defined by dimensions, position of the centroid and material. A container made of boxes (as walls with a certain thickness) would avoid the spheres to exit from the container, guaranteeing a realistic simulation. Obviously, this approach doesn't allow to model a cylindrical container as was proposed in the previous chapters (to do this, only the facet-made cylinders can be used), but in the aim of identifying the behaviour of the granular material, the geometry of the container would not have a too high impact on the results. Indeed, these DEM simulations are done as a sort of numerical "experiment" to verify if the kinetic energy of the intruder falling through a pool of granular material can be effectively dissipated.

4.2.3 Falling Body Assembly Modelling

Once the sphere packing and the container are defined, the attention is focused on the modelling of the falling body, which is composed by the intruder (made of a rod and a head) and the equivalent satellite mass. Differently from the container, the geometry of the intruder head would have a non-negligible influence on the dissipation phenomenon and so it's important to be able to model properly the shape of this device. The intruder head is considered with a conical shape with a cylindrical base, similarly to what was done in the preliminary sizing. Unfortunately, a conical element doesn't belong to the catalogue of the elementary bodies of YADE and a more complicated procedure must be used to achieve this geometry. The cone can be modelled as a composition of facets but, as was mentioned before, the pure geometrical nature of this element (zero-thickness) doesn't allow it to withstand high values of stresses. Moreover, it is observed that the dynamic interaction between the facets and the spheres is only one-directional: when the spheres interact with the facet, they "feel" the presence of this boundary and respond modifying their trajectory after the contact, while this doesn't occur for the

facets because they are dynamically inert. For the given values of the initial states (position and velocity), they maintain these conditions during the whole simulation. In other words, they can move the spheres, but they cannot be moved by them. This feature of the facet makes impossible to build an intruder made of facets. Using these elements, the intruder would penetrate in the granular material without being stopped and the simulation would be nonsense. A solution for this issue would be given by the possibility of YADE to build complex shapes using the Clump function. As it was said before, this function can build rigid aggregates from elementary elements like the spheres. The idea is to model the intruder as a Clump of small spheres constrained each one to another and able to behave as a rigid body. In this way, a correct dynamical interaction between the intruder and the granular material would be ensured because only a sphere-to-sphere interaction would be involved. Actually, this strategy could be used also for the modelling of the container with a cylindrical geometry (as a difference of cylindrical predicates), giving also the possibility to have a container able to interact dynamically with the ground and so able to reproduce the bouncing behaviour. Indeed, YADE allows to model the ground as a rigid wall which can be positioned on the origin of the reference frame and only the spheres can interact with it. In a model where also the granular container falls together with the intruder, rod and satellite mass, the previously mentioned box-made container would freely pass the ground wall but with a container made of rigid aggregates of spheres this doesn't occur. Even if the observation of the bouncing behaviour is not the main objective of these simulations, the possibility to have it would be quite interesting. However, the number of particles involved in a scenario where the intruder and the container are modelled as Clumps of spheres would be excessive, increasing dramatically the computational time. This consideration is related to the fact that to have a regular shape for the conical intruder head and the cylindrical container, the radius of the spheres used to create the Clumps would be quite small increasing the number of the needed spheres. For this reason, the presented strategy is discarded. The solution to obtain a dynamically interacting intruder is definitely given by the Polyhedra functions. These functions allows to build facet-like elements that are able to interact with the spheres in "two" directional ways. In other words, they can move the spheres and they can be moved by the spheres. This feature, together with their geometrical flexibility, make them the perfect candidate to be used

for the intruder modelling. They are polyhedral shape elements which are defined by the coordinates of the vertices and by the material. The conical part of the intruder head is modelled as a Clump of different 4-points polyhedrons (more specifically tetrahedrons) disposed circularly around the intruder vertical axis having as common points the vertex of the cone and the projection of this point on the base of the cone. A discretization of 30 elements is used to have a quite regular shape. The same approach is used for the cylindrical part of the intruder head where 6-points polyhedrons are used with the same disposition and discretization of the conical part. In this case, the polyhedrons have in common the centers of the upper and lower bases of the cylinder. At this point, the remaining parts are the piston rod and the equivalent satellite mass. Regarding the rod, it has the main task of transmitting the damping force from the intruder to the satellite. Since the shape of this component wouldn't have a huge impact during the dissipation phenomenon (which actually occurs mainly between the intruder and the granules), it is modelled as a simple 0.25 m long box element with a quadratic base with a side dimension equal to the diameter of the rod determined in the preliminary sizing of the granular damper. Once the rod is defined, it is attached to the equivalent satellite mass. In the DEM scenario, the satellite is modelled as a box (more specifically as a cube) which should have the same mass of the satellite. The dimensions of this equivalent cube can be obtained knowing the mass, the density and so the volume. The value of the mass associated to the cube in this model is **105 kg**. Actually, this value embeds the masses of the satellite (**96 kg**) plus the mass associated to the active dampers (**3x3 kg**). As it was done for the combined active-passive multibody simulations, the mass of the active devices is taken higher than the values obtained in the preliminary sizing in order to leave a mass margin for a further eventual variation. The idea is to include in the cube all the system masses but those associated to the granular dampers and the landing pads. In this way, even if the simulation is devoted to the verification of the efficiency of the granular damper when it is used alone, the presence of the active damper is considered in terms of mass and so in terms of the kinetic energy to be dissipated. All these last elements (conical and the cylindrical parts of the intruder head, the intruder rod and the satellite mass) must behave as a unique rigid body during the simulation. This condition is achieved using the already mentioned Clump function of YADE. For all the

mentioned elements, the material considered as reference is the Aluminium, with the following properties:

Density [kg/m3]	2800
Young Modulus [Gpa]	80
Poisson Coefficient	0,33
Friction Angle [rad]	0,87

Table 41

All the simulations are performed with the same values of density, Young modulus and Poisson coefficient, while for some models the friction angle is modified. The motivations that lead to the simulations with different friction angle will be explained in the dedicated section.

4.2.4 Other Modelling Issues

The scenario is almost complete but a brief explanation about the dimensions of the used container should be still done. According to the preliminary sizing, the height of the container should be **0.3 m** leaving in this way, **0.25 m** to the granular material and **0.05 m** to the intruder head. As it was said before, the container is modelled as an assembly of 6 boxes where each box represents a wall of the container. Considering that a box element cannot interact with another box or with a polyhedron element, the assembly of intruder head and intruder rod, made of polyhedrons and box respectively, would penetrate and bounce into and from the granular material without interacting with the top of the container. However, if at least one sphere is interposed between the upper cylindrical face of the intruder and the top box (or wall) of the container during the simulation, this would block the intruder during the bouncing phase (since the container is rigidly attached to the ground) and, subsequently, it may cause a cyclical motion of

the intruder (up and down) and so a dissipation higher than what could be obtained in a real scenario. In order to avoid this issue, the top of the container should be removed or more easily, since the used YADE function builds automatically the container with 6 boxes, the height of the container can be increased in order to have the top of the container very far from where the dissipation occurs. It is observed that increasing the height of **1 m**, the previously described issue doesn't occur within the simulated time. Another issue related to the container geometry is here explained: according to the described model, during the penetration, some spheres should pass through the gap between the intruder and the container, then they should be free to move upward since the top of the container is very far from it (indeed, the situation is mostly the same of the case where the top of the container is completely removed) while in a more realistic scenario, the spheres which have passed through the gap, should be constrained to move within the container of the original dimensions and should give a dissipating contribution in the bouncing phase of the intruder. In the chosen configuration (with the long container), since the spheres are free to move away, this further dissipation is difficult to achieve. However, the optimal solution obtained with this model, should be robust in term of dissipation capability because it would mean that the damper is able to dissipate the initial kinetic energy in just one "shot" during the penetration phase. Regarding the values of stroke obtained from the simulations, the following consideration is done. The stroke is calculated as the difference between the initial position (fixed) and the actual position of the satellite. If the granular material is not able to stop or to pull up the intruder within the allowed stroke (**0.25 m**), it would touch the bottom of the container. However, as it was said before, the polyhedrons, which are elements that the intruder is made of, and the boxes (which compose the container) cannot interact and so if the intruder moves downward with a negative velocity at the end of stroke, it would pass freely through the bottom of the container. Actually, since the aim of these simulations is to find a configuration able to stop the intruder within 0.25 m of stroke, what occurs after this value is out of interest. The search for the optimal solution will discard any result which exceeds the allowed stroke value. Hereafter, the views of the complete model and a zoom on the intruder are given.

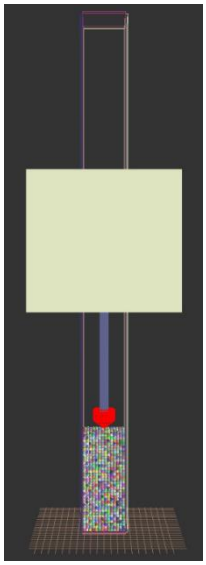

Figure 84 Complete model of the passive actuator adopted in DEM simulations

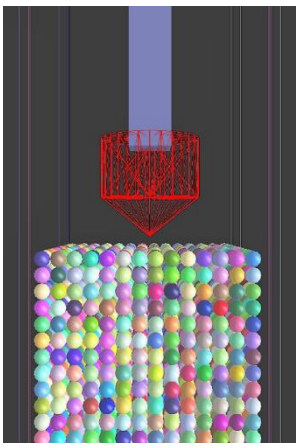

Figure 85 Zoom of intruder head

In the presented model, the regular orthogonal packing is used (as said before, different packings are considered).

4.2.5 Simulation Features and Outputs

As it was done for the multibody simulations, the dynamics of the satellite involves only 1 degree of freedom (the vertical one) but the spheres of the granular material are obviously let free to move and rotate in the space. This can be done in YADE, blocking selectively the degrees of freedom for each body and clump. A body can be completely constrained to remain in a fixed position even if it interacts with other bodies or is subjected to external forces (which is actually the case of the ground-fixed granular container), or to have a dynamic interaction in a just single direction (which is the case of the intruder-rod-satellite assembly). The simulated time is fixed to **4 s** (with slight variations according to the model) because it is a time interval sufficiently long to observe the dissipation phenomenon and an eventual rebounding without requiring a too excessive computational time. The integration timestep is let according to YADE default value (about **1e-07 s**). At the beginning of the simulation (t = 0 s), the assembly

of intruder head, intruder rod and satellite is positioned above the granular material and let fall with an initial velocity of $\mathbf{-2}\ \frac{\boldsymbol{m}}{\boldsymbol{s}}$. The container is fixed to the ground and the granular material is arranged according to the chosen packing in the container and still. All the elements of the built scenario are subjected to a constant gravity acceleration of **-1e-04** $\frac{\boldsymbol{m}}{\boldsymbol{s^2}}$ during the whole simulation, coherently with what was done in the multibody simulations. The main outputs which are extracted from the simulations are the simulated time, the stroke and the satellite velocity. These vectors are discretized according to the simulated time interval (4 s) and the integration timestep. The time vector is required to calculate the acceleration (and so the transmitted force) as the derivation of the velocity. This procedure is necessary because it is impossible to obtain the force transmitted to the satellite directly from the simulation. YADE doesn't output the forces or torques which are acting on a Clump (like the intruder-satellite assembly) and for a single body (only the satellite mass for example) it gives as output the contact (or surface) forces and it is not able to measure inertial forces. In the described model, the intruder rod is clumped with the satellite and a small penetration gap of 5 mm is let between the two bodies. Asking directly the forces acting on the satellite, the obtained values include also the pre-stress caused by the rod making impossible to measure the real damping force generated during the dissipation. Even if the clumping would be made without this common gap between the bodies, the problem would still remain since the force output wouldn't measure the acceleration of the satellite mass. For these reasons, the velocity-derivation strategy is adopted. In this way, only the inertial force acting on the satellite would be measured which is mainly equal to the damping force generated by the granular material (the contribute of the gravity is included hear but is negligible w.r.t the damping forces). The velocity-derivation strategy is a reliable solution but it has one issue: looking the acceleration data obtained in this way, it can be observed that the trend is quite irregular. The figure is characterized by a high single peak with a lot of smaller peaks distributed around it. This behaviour is caused by the numerical derivation of the velocity which transforms also a small amplitude variation (in the velocity) in a huge irregularity in the acceleration data. In order to have acceptable data, a filtering process is necessary. The filter should discard any high frequency content of the signal making the acceleration/force trend smoother. Before filtering the signal, it is necessary to determine the bandwidth of the signal in order to

not cancel those frequency contents which the phenomenon is characterized of. Looking on the FFT (Fast Fourier Transform) of the force signal, it is observed that the fundamental frequencies are far below **1 Hz** and applying a filter with a cutoff frequency of **60 Hz** (which is a value mostly used in the dynamic tests), the wanted trend of the force is obtained. In order to verify the correctness of this process (so to verify if any significant data is deleted), an inverse-check is done, where the velocity is obtained as the integration of the filtered acceleration. As it can be seen in the result section, the velocity trend obtained in this way is quite similar to the original one. Anyway, from those three vectors obtained from the simulations (time, stroke and velocity) is possible to plot the velocity, stroke and force trends w.r.t the time or to plot the force trend w.r.t the stroke and the velocity, or, moreover, it's possible to obtain the work computed by the damper as the integral of the force w.r.t the stroke.

4.2.6 Plots about filtering of Simulations Data

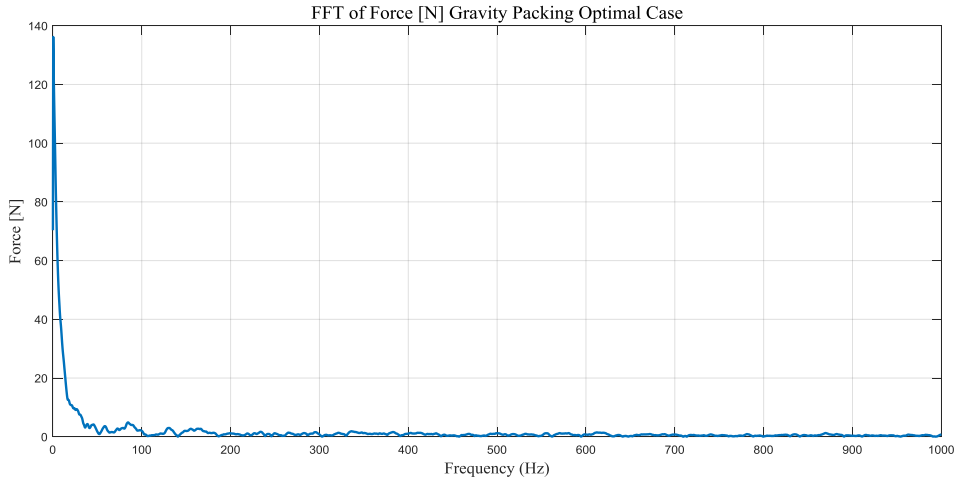

Figure 86

It can be seen that the fundamental frequency of the signal is located at very low frequencies and, even if some oscillations are present up to 200 Hz, the filtering was done at 60 Hz since the real purpose of this process was to make smoother the original signal without losing the main frequency content.

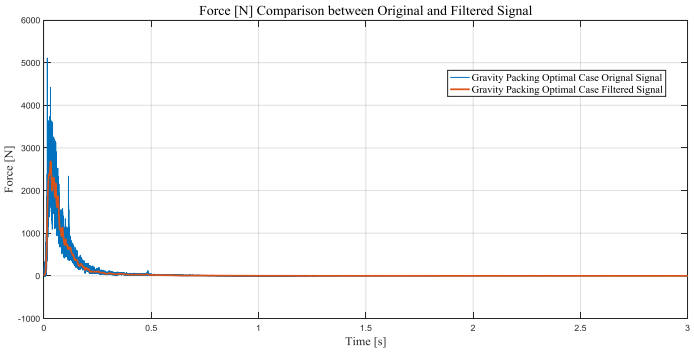

Figure 87

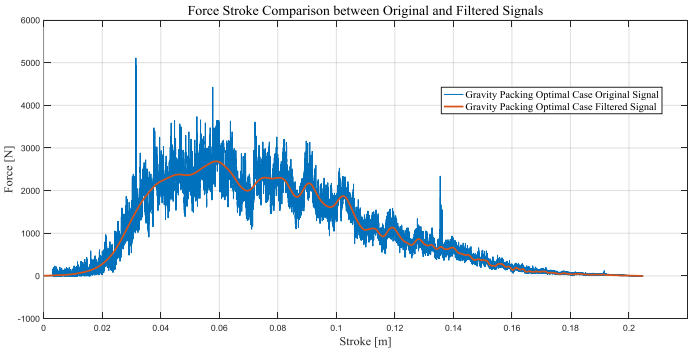

Figure 88

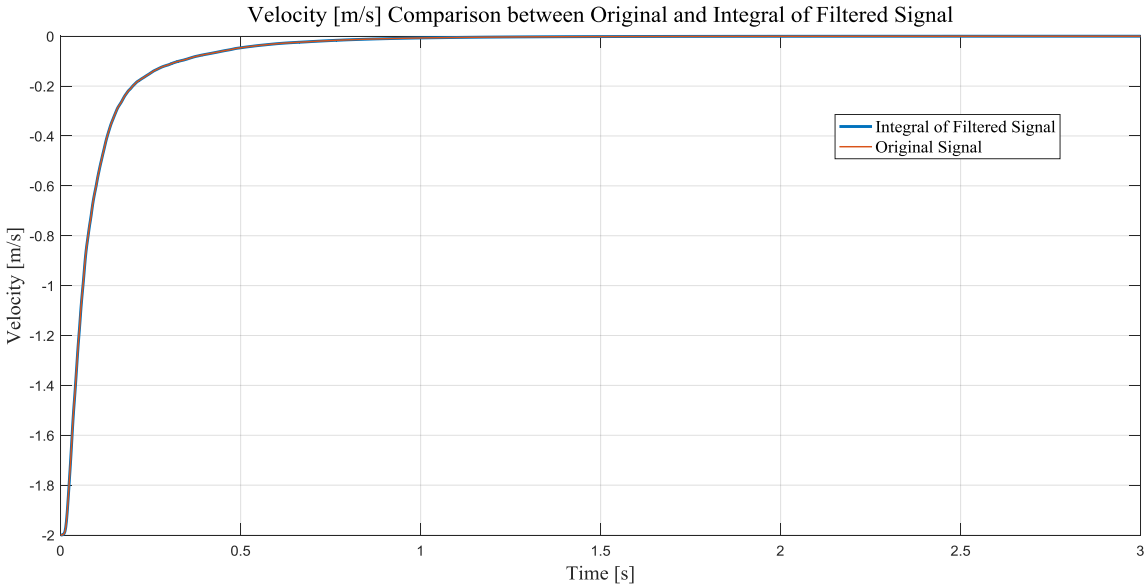

Figure 89

Indeed, in this last figure, it can be noticed that the original velocity signal is almost equal to the one obtained through the integration of filtered acceleration signal.

4.2.7 Computational Issues

The DEM simulations performed with the previously described model are characterized by issues related to the computational time. As it was said in the previous section, the computational time depends mostly on the number and the dimensions of the particles. In the aim of identifying the optimal configuration (in terms of geometry, packings and

so on), multiple simulations with different numbers and radii of particles must be performed and especially for small values of radius, the required computational efforts are excessive for the common personal computers. In order to perform faster multiple simulations, it is necessary to have multiple cores able to work parallelly. The simulations are run using the calculator of the Department of Aerospace Engineering of Politecnico di Milano, where 32 cores are involved. Both the simulations and the data were managed remotely. To each simulation 4 cores are associated and 8 simulations are run parallelly each time. The maximum number of cores involved in the single simulation is fixed to 4 because, according to the YADE documentation, a further increment of the cores' number doesn't bring an improvement of the computational efficiency. Moreover, a too high number of cores can cause also a worsening of the performances. This issue occurs because, since the cores are working parallelly, they must "share" the data during the calculation and this process lead to a decrement of the computational speed. Notwithstanding the availability of these cores, the simulations required a lot of time and a proper control and data management are needed. Indeed, for models with the sphere radius of **4-5 mm**, the simulations last approximately **3-4 hours** while for models with smaller sphere radius (**2-2.5 mm**), they last **3-4 days** and up to **7 days** for radius of **1 mm,** and could vary with the dimension chosen for the container. For this reason, it is difficult to obtain data about models with too small sphere radius.

4.3 DEM Simulations for the Identification of the Damper Characteristics

4.3.1 Granular Damper Dimensional Sensitivity Analysis

The first YADE simulations are done with the aim of understanding the granular damper sensitivity to the variation of the geometrical parameters. The most significant

dimensions of the previously explained model are the granular radius, the container side length, the intruder head radius and the height of the cone. These dimensions can influence the results in terms of velocity, stroke and force. For example, a too small container with large spheres and large intruder head could determine high friction forces while a large container with small spheres and a relatively small intruder head could cause a too "soft" behaviour compromising the efficiency of the damper. However, because of the unpredictable behaviour of the granular material, these hypotheses can be only verified through DEM simulations. This investigation can be done running different simulations, each one with a different combination of values for the previously mentioned dimensions. Since 4 dimensions are involved, trying all the possible combinations in a certain range for each of them is computationally too onerous. Therefore, the following strategy is adopted: a set of different granular radius is chosen (from **3 mm** to **5.5 mm** with a discretization of **0.5 mm**) and three different values of the cone height are defined (**0.5 cm**, **2 cm** and **4 cm**). In this way, a good range of the granular radius is used without requiring too long simulations, while regarding the cone height, it is possible to understand what happens when the cone is almost flat or when it has a medium or very sharp dimension. Once these ranges are defined, the following cases are considered: for a fixed value of the granular radius, the previous three different cone heights are considered. For each one of this three combinations, five cases are defined: the first three cases are obtained fixing the dimension of the container to its maximum value (**10 cm**) and putting the intruder head radius equal to its minimum value (**1.05 cm** which is the radius obtained from the preliminary sizing with the buckling robust criterion), a medium value (**2.5 cm**) then to a value which corresponds to the interference condition which depends on the chosen granular radius. While the last two cases are obtained fixing the intruder head radius to the minimum and putting the container side dimension equal to a medium value (**5 cm**) and again to the value which corresponds to the interference condition. In this way, it is possible to observe the behaviour of the granular damper when the piston is subjected to interference or when it is relatively free to move in different manners. As it was said before, the five cases are repeated for each combination of granular radius and cone height. For some values of granular radius, the already mentioned intruder head and container dimensions are slightly modified in order to fill properly the container space with the granules without

leaving free gaps (when the container dimension is not a multiple of the diameter of the spheres, YADE leaves a row without spheres) and to obtain a correct interference. All these simulations are run with the same material-parameters showed in the previous section. Once the simulation data are obtained, in order to find the optimal solution, a pareto-front plot is created. This figure plots on the abscissa the maximum velocity while on the ordinate the maximum transmitted force. Each simulation (characterized by a set of 4 dimensions) is represented as a single point on this figure. It's important to underline that the velocity value is always kept with its own sign as it was done for the multibody simulations. Other similar figures, like force-stroke and force-work plots, are created to understand if there are any relation between these parameters. The search for the optimal solution simply consists in the calculation of the distance of each of those points from the origin of the F-V figure and in the individuation of the parameters (dimensions) which corresponds to the minimum distance. However, even if the search of the optimal solution is important, considering that the phenomenon depends also on other parameters like the material properties and the packing, this first set of simulations has to be considered more as a dimensional-sensitivity analysis than an optimization, because it has the task of helping to understand the feasibility and to give a rough idea of the dimensions which should be involved in a further analysis. According to this consideration, an additional analysis is performed with the data obtained from these simulations. Because of the previously mentioned computational reasons, it is impossible to perform simulations for all the possible combination of the dimension values. In order to overcome to this lack of data, an interpolation is performed to estimate the behavior of the granular damper for those combinations of geometrical parameters that haven't been tested in DEM simulations. The MATLAB interpolation tool for scattered data (which corresponds to this case), allows to perform interpolations up to three dimensions. Since the variable parameters in this problem are four, the interpolation can be performed only if at least one parameter is kept fixed. The adopted strategy consists in performing three different groups of interpolations each one with a fixed value of cone height. A query-point range for each of the variables is created between the minimum and maximum values used in the real simulations with a discretization of **1 mm**, except for the granular radius which is discretized with a step of **0.1 mm**. Once the interpolation is performed, all the obtained data for all the groups are

plotted in the pareto-front plot and the optimal solution is identified. Actually, it is observed that a lot of the obtained data are unrealistic (negative force, for example), and even if the nonsense data are filtered, the identified optimal solution remains still too far from the real DEM simulations data, making them unreliable. This issue is strictly related to the pure mathematical nature of the interpolation which ignores the physical aspect of the problem and to the low amount of the data obtained from the simulations.

4.3.2 Friction Coefficient Sensitivity Analysis

As it can be seen in more detail in the result section, the previous dimensional analysis demonstrates that a granular damper with feasible dimensions can effectively dissipate a good amount of kinetic energy but also that the transmitted force is still high and the available stroke is still not efficiently exploited. Actually, the mentioned simulations have been performed imposing a friction angle for the granules, intruder and container equal to **0.87,** which corresponds to a frictional coefficient of **1.19**. According to the data obtained from the literature, the static frictional coefficient in vacuum between pure Aluminium-made surfaces can oscillate from **1.05** to **1.35** and for the previous simulations a mean value was taken. Initially, this high value of frictional coefficient has been used because it is the real friction coefficient of the Alluminium (which is the material considered in the preliminary sizing) and because the main idea was to have a good dissipation capability through a high frictional coefficient. However, as said before, this choice lead to excessive values of deceleration. Therefore, the subsequent step is to understand how the frictional coefficient can influence the behaviour of the granular material trying to achieve an improvement especially in term of the transmitted deceleration. This process is done running simulations with different pairs of frictional coefficients (one between the granules and one between the granules and the intruder/container) for different values of granular radius. The dimensions of the intruder head radius, the container side length and the cone height are kept fixed. This choice is done because in this way, it is possible to focus only on the effect of the

variation of the tribological properties of the materials and the granulometry, without considering other geometrical parameters of the damper. The values of the intruder head diameter, the container side length and the cone height used for these simulations are respectively **5** cm, **10** cm and **2** cm. These values are not so far from what was determined as optimal solution in the previous DEM simulations, except for the cone height which was **4** cm. The choice of using a so different cone height relays on the fact that the value obtained in the first simulations corresponds to the optimal case where the frictional coefficient was quite high (**1.19**), while in the following simulations where lower values of frictional coefficient are considered, this too sharp intruder could lead to an excessive penetration and a too low dissipation. The idea is to use dimensions which are "standard" and not too much related to the friction value which was used in the first simulations. Indeed, it should be quite wrong to assume that the dimensions identified with a previous frictional coefficient must be still the optimal ones for a scenario with different material property and granular radius. It is quite important to underline that in this analysis, the material considered for the density, Young modulus and Poisson coefficient for all the bodies involved in the simulations is the Aluminium, while for the frictional coefficient not. This assumption is based on the possibility of modifying the tribological properties of a material through technological solutions like the electrochemical deposition of nanoparticles or the PE-CVD (Plasma Enhanced Chemical Vapor Deposition) which are able to modulate the frictional coefficients of the treated surfaces. For example, studies revealed that the deposition of nanocomposite of TiN/a-SiN through the last technique can reach friction coefficient values of 0.32. Moreover, some researches demonstrated that frictional coefficient of the stainless still against itself in cryogenic and vacuum environment can drop up to 0.3 and this material can be deposited on a metallic substrate thanks techniques like the Cold Spray deposition. Since the thickness of the deposited layer through the mentioned technologies is very small (generally in the order of nm or μm), the simulations can be run using the properties of the bulk material (Aluminium). The couples of the tested frictional coefficients are hereafter presented. The first value (μ_1) corresponds to the frictional coefficient of the granular material while the second value (μ_2) corresponds to the frictional coefficient of the material considered for the intruder and the container.

- $\mu_1 = 0.3$, $\mu_2 = 0.3$
- $\mu_1 = 0.3$, $\mu_2 = 0.6$
- $\mu_1 = 0.6$, $\mu_2 = 0.6$
- $\mu_1 = 0.6$, $\mu_2 = 0.3$
- $\mu_1 = 0.2$, $\mu_2 = 0.2$
- $\mu_1 = 0.2$, $\mu_2 = 0.45$
- $\mu_1 = 0.45$, $\mu_2 = 0.45$
- $\mu_1 = 0.45$, $\mu_2 = 0.2$
- $\mu_1 = 1.19$, $\mu_2 = 1.19$

The last couple corresponds to the values used in the first simulations and it is taken as a term of comparison for the data obtained with the new coefficients. Initially, for each one of the presented couples, simulations are run using different values of granular radius (from **3 mm** to **6 mm** discretized with **0.5 mm**). The granular radius is kept in this range in order to perform multiple simulations in an acceptable time. According to this strategy, it is possible to obtain the multiple trends of the maximum velocity, transmitted force, maximum stroke and dissipated energy w.r.t the granular radius where the curves are parametrized according to the used couple of frictional coefficients. Thanks to these simulations, it is observed that the maximum forces and velocities associated to the models with different frictional coefficients are lower than those obtained in the first simulations. Especially, this occurs for low values of friction coefficients and low values of granular radius. Thanks to these second groups of simulations, it is evident that a general performance improvement can be achieved modifying these parameters. Notwithstanding these improvements, the results obtained from these simulations open a new issue. It is observed that the maximum velocity curves associated to some couples of frictional coefficients show high irregularities for certain values of the granular radius (**4.5 mm**, **5 mm** and **5.5 mm**). In those points, the curves show high peaks with unacceptable values (up to 30 cm/s) while on the other points the behaviour remains quite regular and acceptable (around mm/s). In order to understand if these cases are isolated irregularities caused by numerical issues, further

simulations are run using a range for the granular radius with a major discretization around the anomaly points with the same couples of frictional coefficients of the curves that manifest the irregularities. The interval of granular radius from **4.5 mm** to **5.5 mm** is discretized with a step of **0.1 mm**. The same type of figure as before is obtained but denser in the range where the anomalies are observed. Moreover, a new pareto-front plot is created involving all the simulations where the granular radius and the frictional coefficients are varied. According to the results, it is observed that, for some couple of frictional coefficients, the previous irregularities remain isolated, while for another couple new irregularities are created. These results demonstrate that these irregularities are not related only to a numerical issue but that they could have a physical explanation related to the built model. All the mentioned simulations, (both the first and the second groups), have been run using a model where the packing for the granular material was orthogonal (more specifically called regular-ortho packing). As it can be seen in the imagine of the final model showed in the previous section, this packing algorithm puts the spheres regularly and orthogonally one respect to the others. In other words, all the centers of the spheres are perfectly aligned in both the vertical and horizontal directions. Since there are not misalignments in the arrangement, when the intruder penetrates into the granular mean, this crystal-like perfect packing may cause a too rigid behaviour of the granular material or it may induce resonance phenomena which could be responsible of some of the unacceptable results obtained in the last simulations. For what regards the resonance hypothesis, it is noticeable that the irregularities are present around the granular radius values (**4 - 5.5 mm**) which are near to the submultiples of dimensions of the intruder head (**5 cm**) and the container (**10 cm**). Obviously, verifying if this kind of resonance phenomena is really occurring is not a trivial task and it cannot be given in this work. However, thanks to this intuition, it is possible to choose a direction to proceed: in order to avoid the mentioned irregularities, a small offset between the container and the intruder could be introduced or different types of packings could be considered.

4.3.3 Simulations with Intruder Offset and Different Packings

In all the models used up to now, the intruder is exactly positioned above the granular material and the center of the container. One way to "break" the high regularity given by the orthogonal packing, is to impose a small offset between the centers of the container (so of the granular arrangement) and the intruder. In this way, the peak of the intruder's head cone may penetrate through the granules without causing the previously mentioned resonance phenomena. The original model is slightly modified translating the centers of the container and the granular packing with an offset of **- 0.5 mm** both in X and Y directions (this is easier to do than changing the centers of all the bodies which compose the falling mass assembly) and simulations are run for the values of granular radius and frictional coefficients which caused the previous irregularities. The original regular-ortho packings is maintained. The usual plots are created (velocity, force, stroke and energy) with the granular radius on the abscissa where the friction-parametrized multiple curves are superposed. In this case, the previous anomaly points are substituted with the new data obtained with the offset. According to the obtained results, it is evident that some irregularities are highly reduced or almost disappeared with this strategy. As it was said before, another way to improve the behaviour of the damper is to try with other types of packing. Beside the orthogonal one, YADE allows by default to create sphere arrangements according to the hexagonal packing and the random-dense packing. The first one is similar to the orthogonal packing but the spheres are distributed in a hexagonal shape while in the second one, the distribution is fully random and it's obtained through a pre-compression of the spheres in the available volume and so they are pre-stressed from the beginning of the simulation. Firstly, the attention is focused on the hexagonal packing and simulations are run using the original model (without the offset) for those combinations of granular radius and friction coefficients corresponding to the initial irregularities. Same plots of the previous case are created where the anomaly points, in this case, are substituted by those obtained with the hexagonal packing. As it can be seen in the result section, a simple modification of the packing can bring to a remarkable improvement in terms of rebound

velocity, eliminating completely the initial irregular points. Hereafter, a view of the model with hexagonal packing is given.

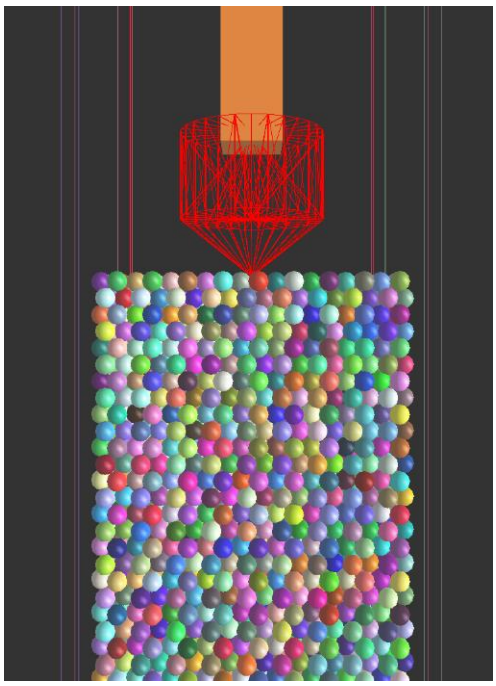

Figure 90 View of the model with hexagonal packing

However, both the used packings (regular-ortho and regular-hexa) cannot be considered as realistic packings. Indeed, the manufacturing of a damper with these types of sphere arrangements (considering the high number of spheres) could be too onerous and costly and maintaining the original distribution up to the real landing scenario could be unfeasible. Moreover, there are no significant reasons to justify such technologically complicated arrangements, considering that for example, the orthogonal one is characterized by non-negligible irregularities. The most realistic packing is obviously the random packing. However, the already mentioned random-dense packing cannot be used because the spheres are pre-compressed and when the simulation starts, they start to move in the given volume before the intruder enters into contact with them. Obviously, this is a highly unrealistic scenario. The strategy adopted to create an acceptable random packing is the gravity deposition. This strategy consists in to let falling the spheres under the Earth gravity field making them to lay in the empty

container randomly. First of all, a simple model only with the empty container is considered and an orthogonal packing of spheres with the same volume of the original packing is created (actually the height is increased and the width reduced in order to avoid any interference with the lateral walls before the touchdown) and positioned with a certain height from the bottom of the container. The gravity is applied (**-9.81** $\frac{m}{s^2}$) and the simulation is run for **4 seconds**. This time interval is sufficiently long to have the total deposition of the granules in the container. At the end, the spheres are all still and randomly distributed. The position of each one of the involved spheres are saved and are used to create the same random packing in the original model (with the intruder and low gravity). This procedure is repeated for each combination of sphere radius and friction coefficient that is necessary to test. Of course, the explained strategy increases the time needed to obtain the final results because, before running the real simulations, it is necessary to perform those ones that simulate the gravity deposition in order to obtain the respective packings. However, this is the unique method available to obtain a realistic sphere arrangement and once the packing is saved, it can be always reused for other simulations for given values of granular radius and friction coefficients. A view of the model with the gravity-deposition packing is shown below.

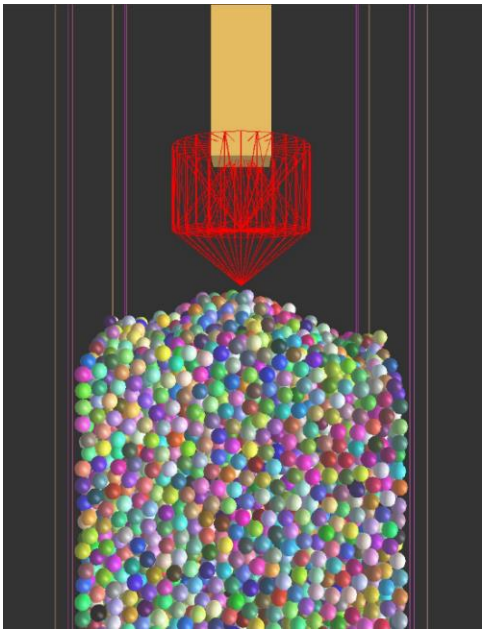

Figure 91 View of the model with gravity-deposition packing

As it can be noticed from the previous figure, the upper boundary of the sphere packing is now irregular and an exact value of its height (**0.25 m**) cannot be more guaranteed. However, it is verified for all the used gravity-deposited packings that the maximum vertical position of the spheres doesn't oscillate excessively (generally, **± 3 cm** around the reference height). Once all these variations are identified, the initial vertical position of the intruder is incremented in order to have realistic simulations. Indeed, if the intruder is let at its original position, the simulation starts with intruder already immerse in granular material, and excessive repulsive forces are created making the force results nonsense. This issue occurs because the gravity deposition simulations for the packing is performed without the intruder-satellite assembly and the spheres are free to lay in the available volume of the container. It is also true that, through this strategy, the maximum available stroke is potentially increased. However, since in the optimal solution selection procedure all those simulations which exceeds the stroke of **0.25 m** are discarded, the mentioned issue is not considered. The number of simulations performed with this packing is different from the previous ones. First of all, the already mentioned anomaly points are considered as has been done for the offset and hexagonal cases but having in mind that obtained packing is the most realistic one, a further step is performed with the aim to identifying an acceptable solution with this kind of packing. Since running simulations with all the previous couples of frictional coefficients and granular radius could employ a lot of time, the best solution among those obtained through the orthogonal packing is taken ($\boldsymbol{\mu_1}$ **= 0.45**, $\boldsymbol{\mu_1}$ **= 0.2** and granular radius of **4 mm**) because at this point, a relatively high number of simulations with the orthogonal configurations have been already performed and so the obtained optimal solution can be taken with good fidelity. However, even if the optimal solution is associated to a granular radius of **4 mm**, it should be interesting to investigate the behaviour of the damper for lower values of radius with this new random packing. Therefore, additional simulations with smaller radius are run (**2.5 mm**, **3 mm**, **3.5 mm**, **4 mm**) with the same couple of friction coefficients. Moreover, in order to have at least two groups of simulations to compare, another friction couple is chosen ($\boldsymbol{\mu_1}$ **= 0.3**, $\boldsymbol{\mu_2}$ **= 0.3**) and simulations are run with the same range of granular radius used for the first couple. This last friction couple is chosen because it is a relatively low value (w.r.t the pure Aluminium case) which can be easily achieved technologically (indeed, the value

corresponds to the Titanium) and, considering that a simulation with gravity-deposited packing has been already done for the radius of **4.5 mm** for anomaly points analysis, this choice can be useful to obtain a trend of the velocity, force, stroke and work in a signficant range of granular radius values (from **2.5** up to **4.5 mm**) at least for this friction couple. The same types of figures are created (different curves parametrized with the friction coefficients) replacing the old values (like the previous irregular points and others like those which correspond to radius of **3 mm** and **4 mm** with $\mu_1 = \mu_1 = 0.3$ and $\mu_1 = 0.2, \mu_2 = 0.45$) and adding new ones (like points corresponding to the radius of **2.5 mm** with the already mentioned coefficient couples). In this way, it is possible to observe if this new packing is able to remove the irregularities obtained with the orthogonal packing and to identify the trend w.r.t the smaller granular radius. As it was done for previous cases, a pareto-front plot is created in order to search the optimal configuration among the simulations obtained with the gravity-deposited packing. According to this procedure, the solution which minimizes the velocity and the transmitted force is hereafter given:

- granular radius: 2.5 mm
- frictional coefficient of the granular material: 0.3
- frictional coefficient of the intruder/case material: 0.3
- intruder head diameter: 5 cm
- head cone height: 2 cm
- container side dimension: 10 cm

These friction coefficient values correspond to a friction angle of **0.2915 rad** (actually, this is the real input that the model receives). The last three parameters are kept constant in this last analysis as it has been explained before.

4.4 DEM Results

This section is dedicated to the illustration of the results obtained from DEM simulations performed focusing mainly on the effects of the characteristic parameters, which could influence the behaviour of the granular damper, and looking for those values able to enure a feasible solution.

4.4.1 Simulations with High Friction and different Characteristic Dimensions – Results

Hereafter, Pareto front, the force-stroke and force-work of DEM simulations where the characteristic dimensions (cylinder, intruder and granular radii) were varied, are presented.

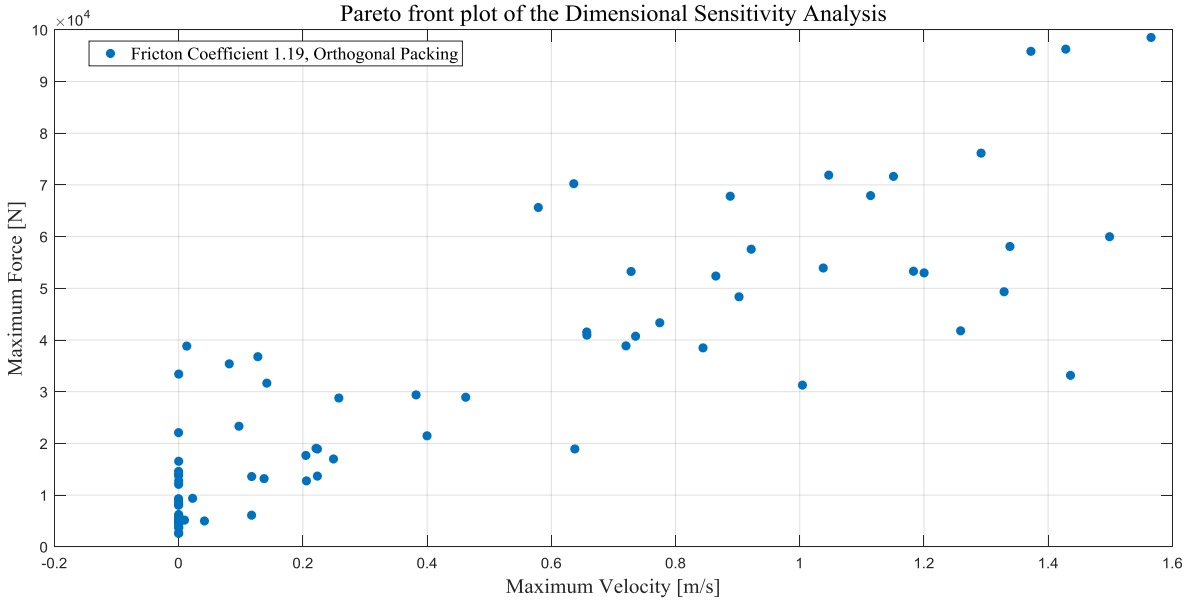

Figure 92

This plot was used to determine the optimal solution (which minimizes the distance from the origin without exceeding the maximum stroke value).

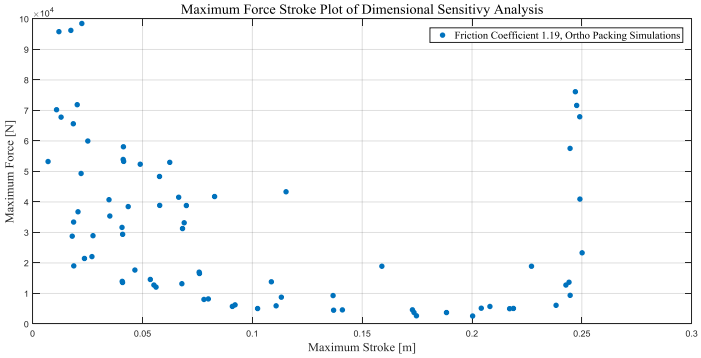

Figure 93

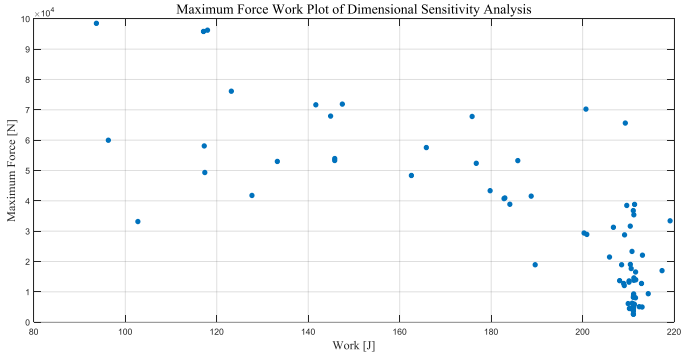

Figure 94

It is noticeable that for low values of strokes and works the transmitted forces are high.

4.4.2 Simulations with Different Frictions Coefficients and Granular Radius – Results

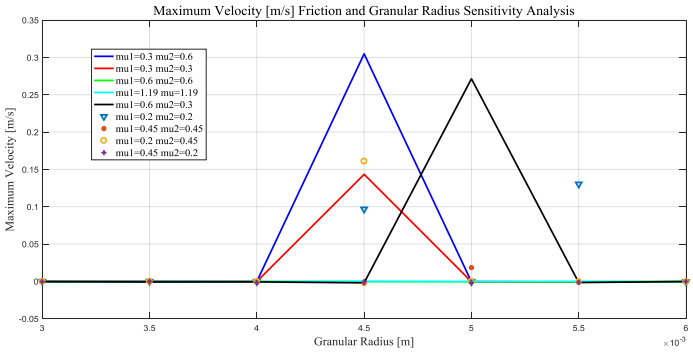

Figure 95

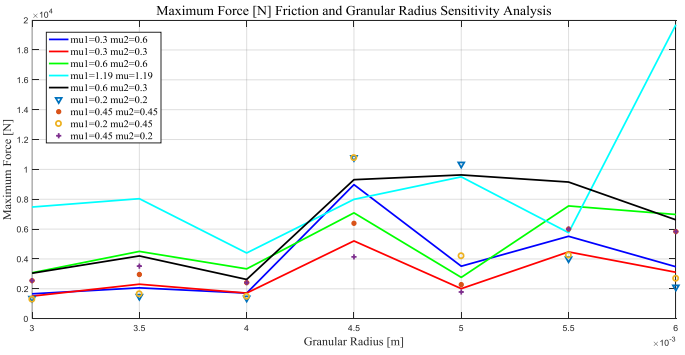

Figure 96

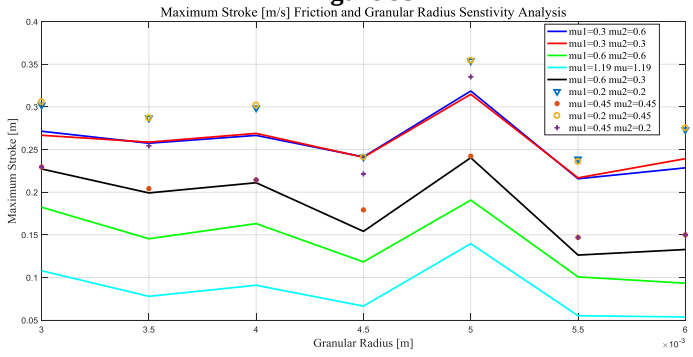

Figure 97

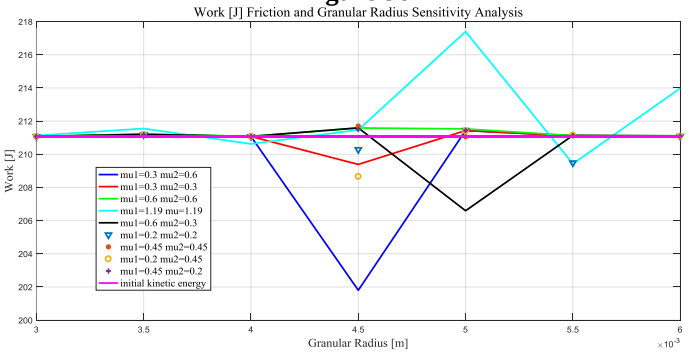

Figure 98

In the velocity plot, it is possible to observe the anomaly points (6) that were discussed in the dedicated section. It can be observed that the simulations with the highest friction coefficient value show more or less the highest forces and the lowest strokes evidencing the advantage of using different (and lower) friction coefficients. The trend of the stroke w.r.t the granular radius has an unpredicted shape while in the plot of the energy some values higher than the initial kinetic energy are present. Even if unphysical, the error is relatively low and is caused mainly by numerical issues regarding the derivation of the velocity and the subsequent integration w.r.t the stroke.

4.4.3 More detailed Analysis around the Anomaly Points – Results

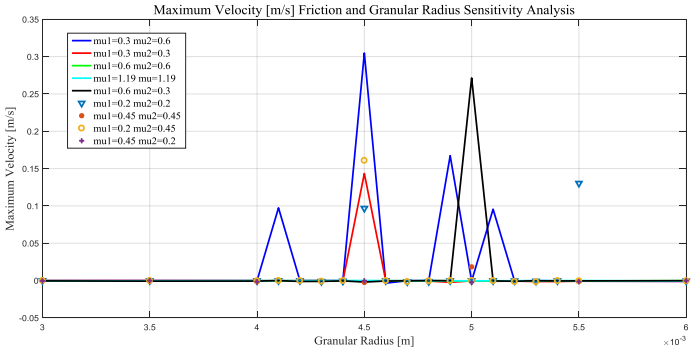

Figure 99

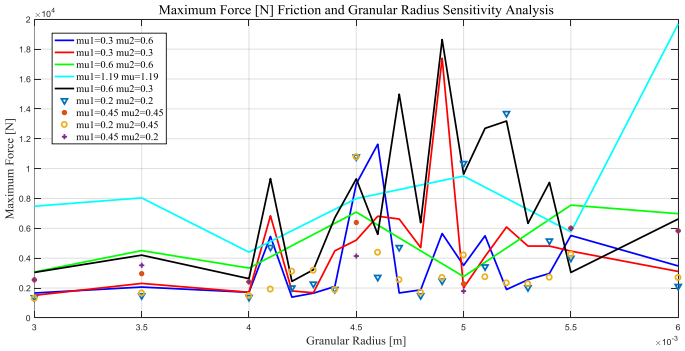

Figure 100

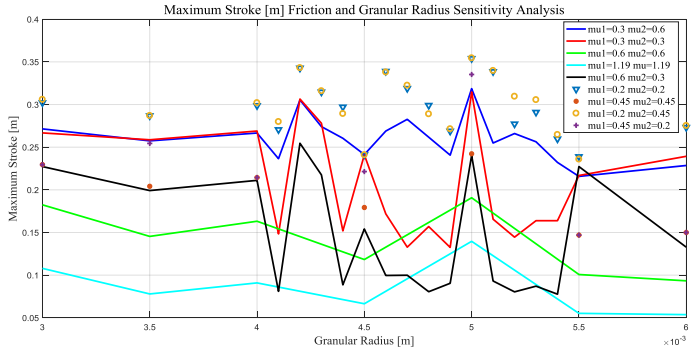

Figure 101

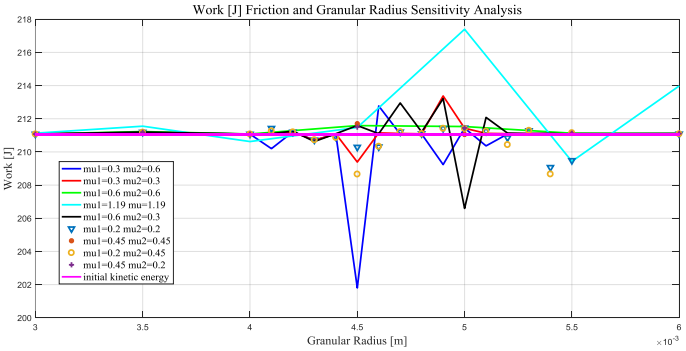

Figure 102

Thanks to this analysis, it can be noticed that the force and the stroke trends w.r.t the granular radius is not quite trivial and that the previous anomaly points are not

completely isolated. The big amount of data obtained from this analysis gives the possibility to look for an optimal solution though a Pareto plot as before.

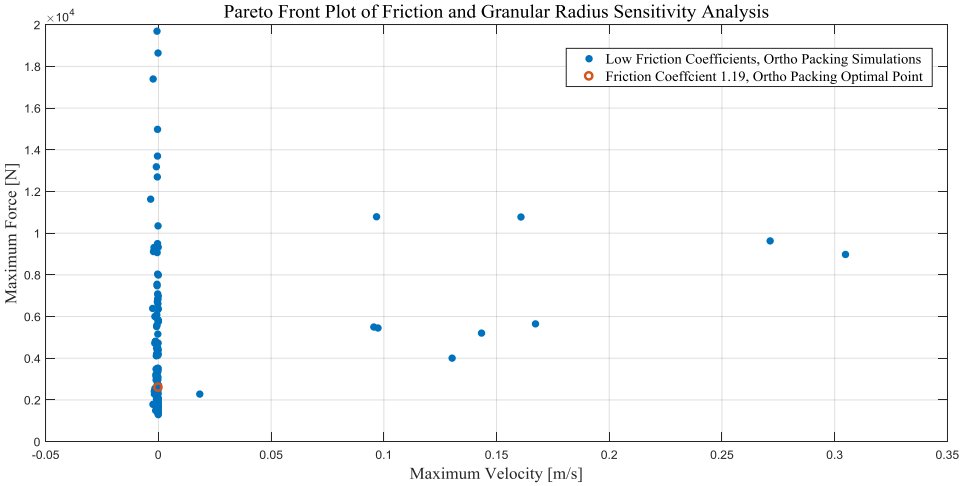

Figure 103

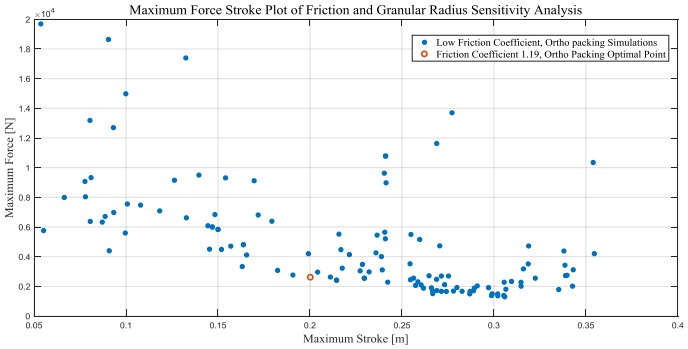

Figure 104

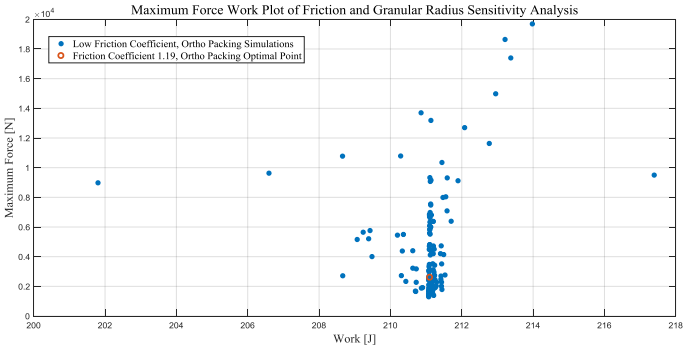

Figure 105

4.4.4 Simulations with Offset

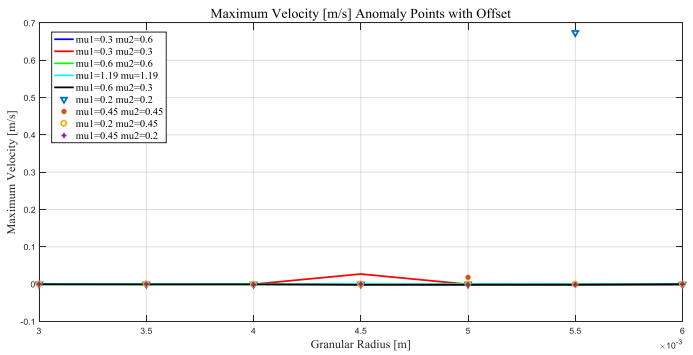

Figure 106

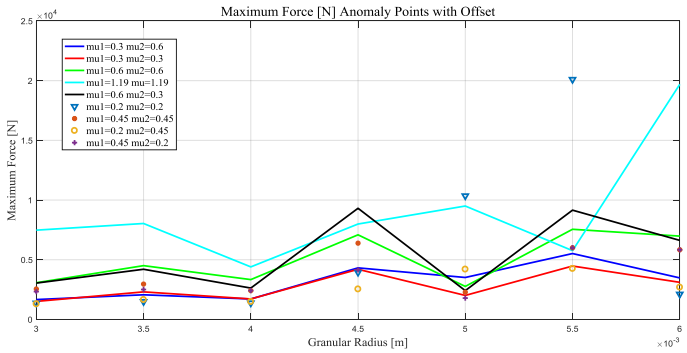

Figure 107

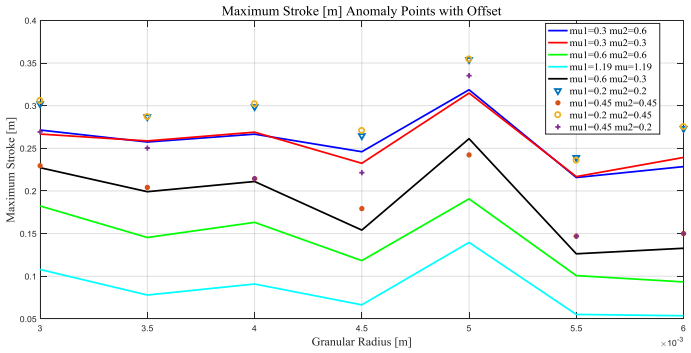

Figure 108

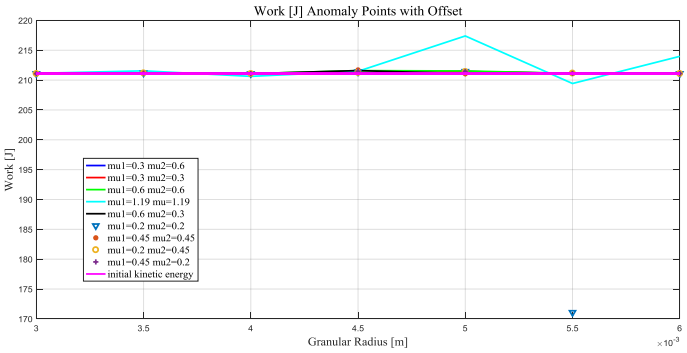

Figure 109

Focusing on the velocity plot, it can be observed that there is a partial improvement w.r.t the previous cases.

4.4.5 Simulations with Hexagonal Packing

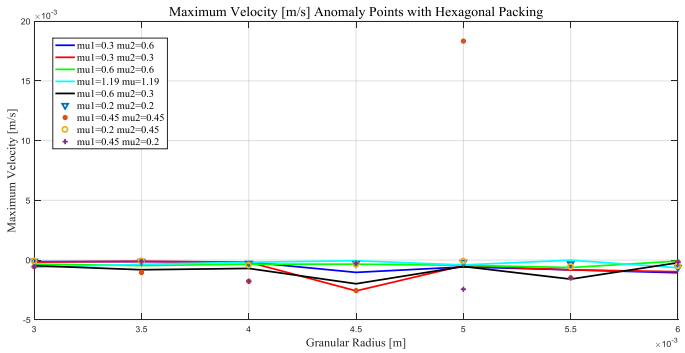

Figure 110

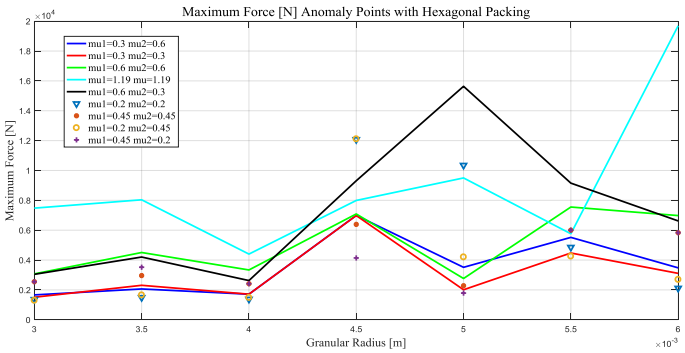

Figure 111

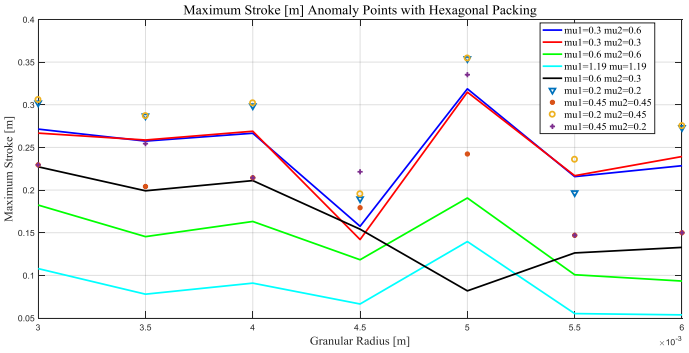

Figure 112

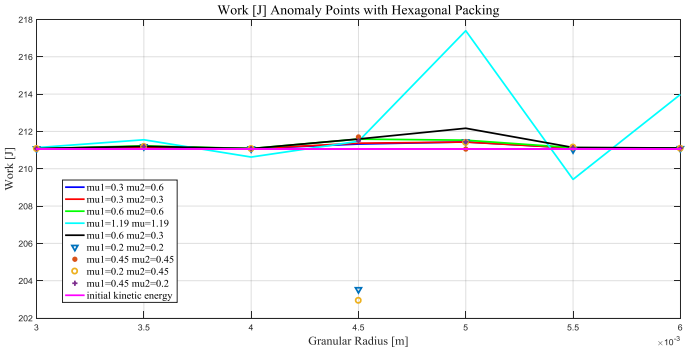

Figure 113

Differently from the previous case with the offset, the improvement in term of the velocity is total since no anomalies are observed.

4.4.6 Simulations with Gravity Packing

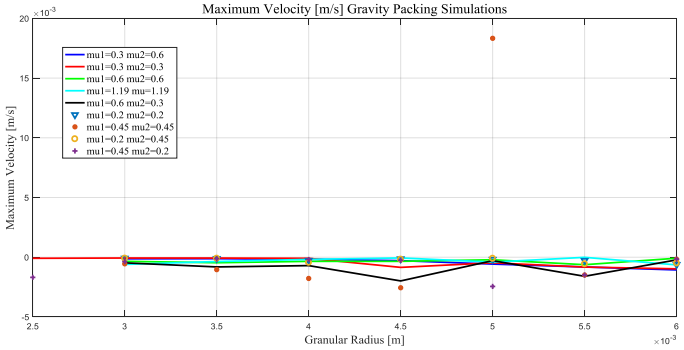

Figure 114

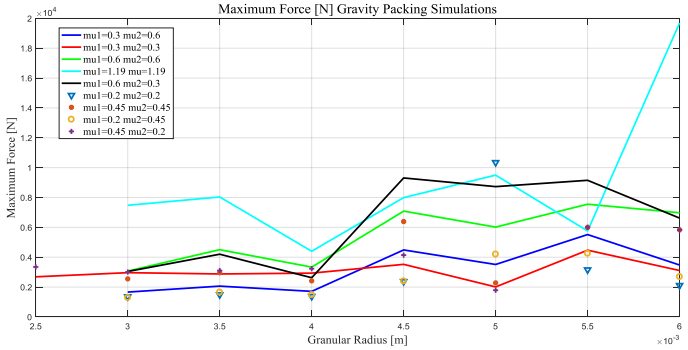

Figure 115

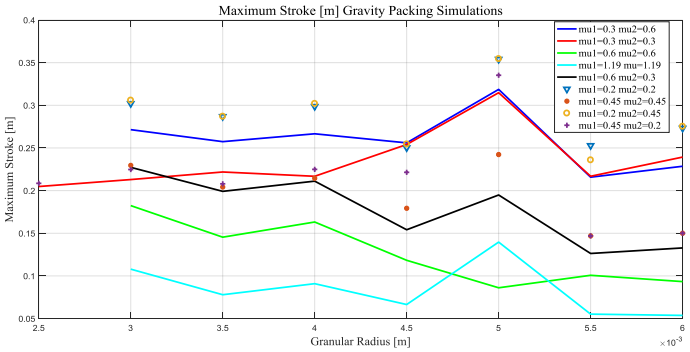

Figure 116

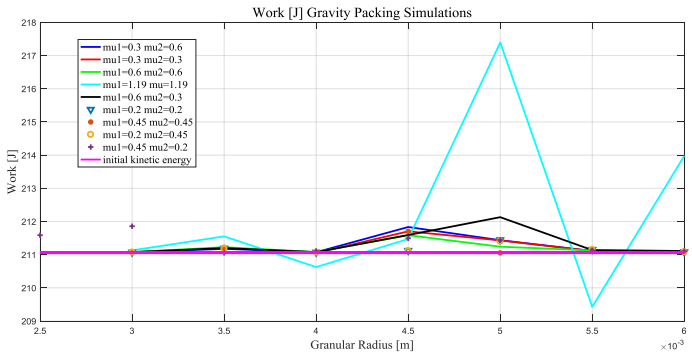

Figure 117

These plots are obtained substituting the anomaly points with the those obtained with the gravity packing and adding new ones as explained in the dedicated section. The improvement in term of velocity is again total as in the hexagonal case but with lower forces. The red curve has the largest granular radius range with gravity packing and includes the optimal solution which was determined with the following Pareto plot.

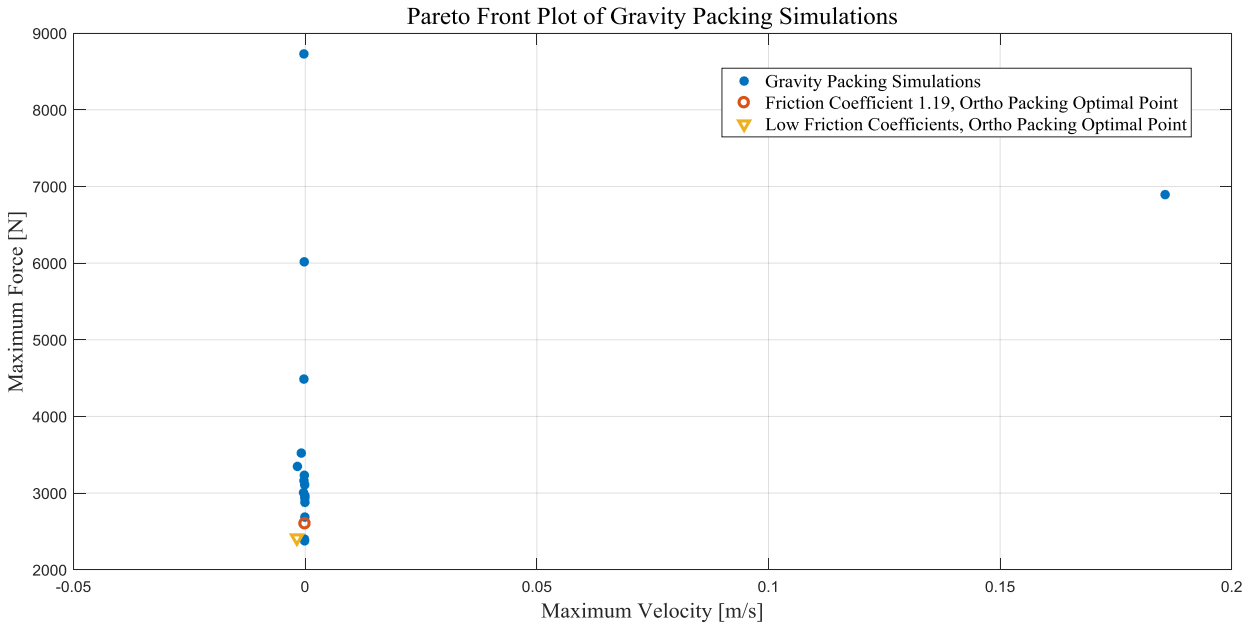

Figure 118

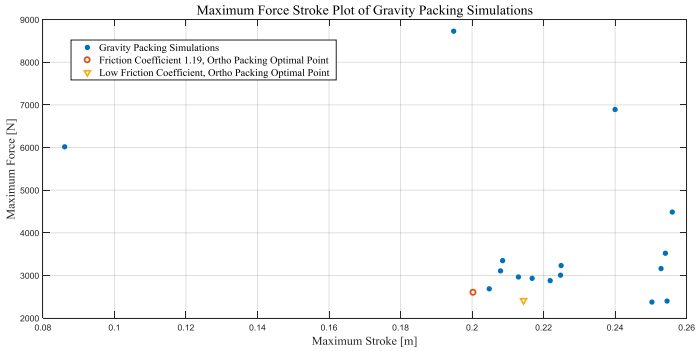

Figure 119

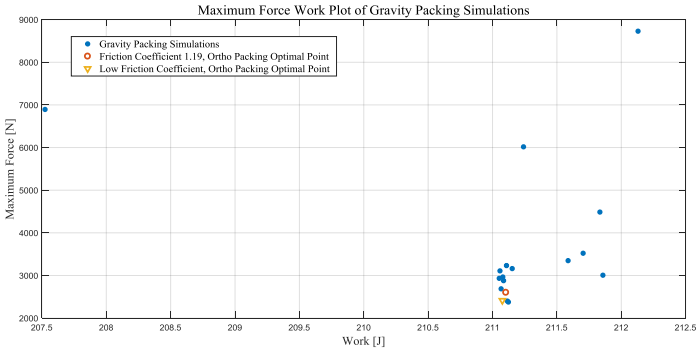

Figure 120

4.4.7 Different Configurations Comparison Plots

Hereafter, some plots which put in evidence the different behavior in term of velocity, force and stroke between different configuration (offset, orthogonal, hexagonal and gravity packing) are given.

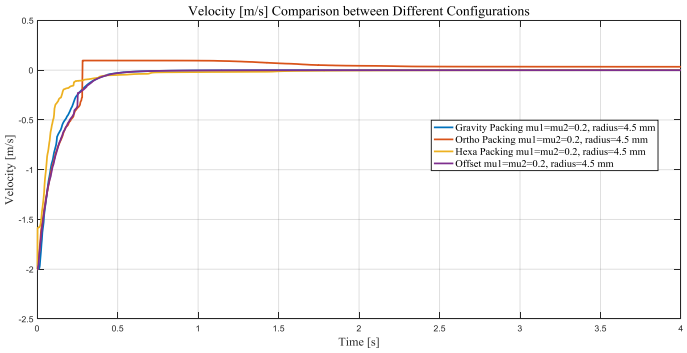

Figure 121

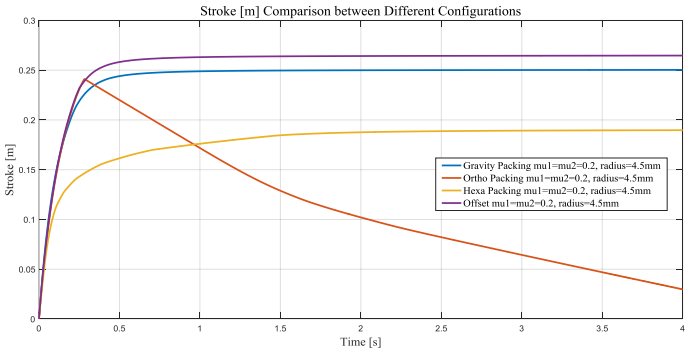

Figure 122

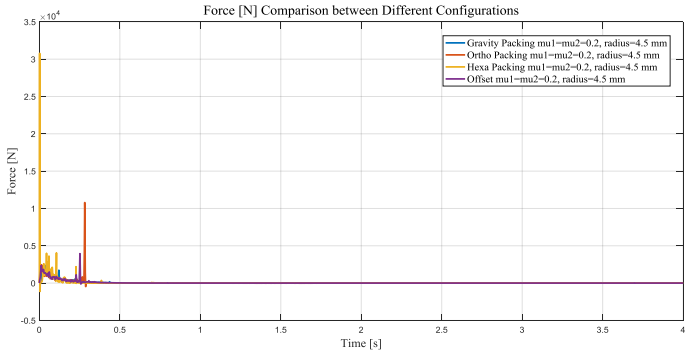

Figure 123

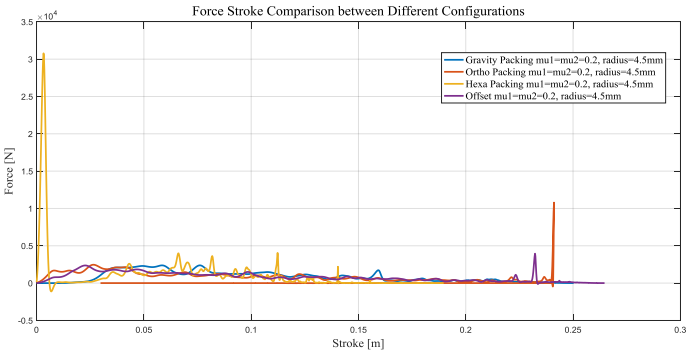

Figure 124

It can be observed that the gravity packing shows the smoothest velocity trend while other configurations (like the orthogonal one) are characterized by sharp trends which are responsible of higher forces. Looking on the force-stroke trends, it is noticeable that some of them are characterized by high peaks (someone at the beginning and someone at the end) while the gravity packing case doesn't shows these kinds of anomalies.

4.5 Granular Model Characterization and Multibody Simulations for the final Calibration of the Active System

4.5.1 Granular Model Characterization

The previous multibody simulations with combined active and passive system were carried out considering a very simple force-law for the passive-granular damper.

According to the first bibliographical research, the force produced by a granular material is proportional to the velocity of the intruder with a linear coefficient which depends on the penetration (or stroke). This dependence is not better specified and so a simple linear behavior was assumed. These simulations produced interesting results both in the nominal conditions and in the sensitivity analysis, and increased the comprehension of the behavior of the combined active and passive system. However, these results cannot be considered reliable because the law used for the granular damper was still too simple, hypothetic and unable to represent correctly the behaviour of the granular material. The primary objective of Multibody Simulations performed after the presented DEM analysis is to calibrate properly the active damper with respect to a more detailed and realistic model of the granular damper. In order to achieve this objective the results obtained from the DEM analysis, in terms of force w r t the stroke and velocity, are fit with a polynomial surface. A proper fitting process is necessary because the dynamics of tests simulated in the DEM environment are different from what has been simulated in the Multibody analysis. Indeed, in DEM simulations, the upper active device effects are neglected and the ground, which the granular container is constrained to, is considered infinitely stiff. This simple scenario is adopted in the DEM simulations because the main objective of these simulations is to characterize the energy dissipation capability of the granular material and not to simulate a real condition. In a more realistic scenario, the bounce of the landing pad (which here is rigidly attached to the granular damper) and the simultaneous dissipation of the upper active damper would change the history of the stroke and relative velocity of the granular damper with respect to what is observed in DEM scenario, where the value of generated force is defined, for a given value of touchdown velocity, for a certain value of relative velocity or stroke. Indeed, the results of a single DEM simulation can be seen as a single curve on the stroke-velocity plane. For the combinations of stroke and velocity different from those where this curve is defined, no force is available. In order to overcome this issue, it is strictly necessary to find an analytical expression of a surface able to define univocally the damping force for given values of stroke and velocity. The determination of this analytical expression would bring the possibility to characterize the behaviour of granular material, the possibility to perform Multibody simulations with different configurations and dynamics from what is tested in DEM environment and to avoid

further numerical complication (indeed, performing DEM analysis parallelly with the Multibody simulations would have been practically unfeasible). The method to obtain a reliable analytical surface consists in performing multiple DEM simulations with the optimal parameters (geometry, frictional coefficients e t c) at different touchdown velocities. In this way, multiple curves of damping force on the stroke-velocity plane are obtained. These 3-D curves are fit through the Matlab fitting tool with the Linear and Nonlinear Least Square Methods. The first method is related to the fitting expressions which are linear with fitting coefficients, while the second one is related to those expressions which are nonlinear with the coefficients. Indeed, different types of functions are tested, looking for those which minimized the error (between the fitting surface and the DEM data) without complicating furtherly the model. The fitting is done using polynomial expressions with different orders, logarithmic, exponential, square root expressions and mixed functions. Since trying with all the existing functions is obviously impossible, these "elementary" functions are chosen. Hereafter, the expressions used in the fitting problem are presented.

- $F_{fit} = a * x * v$
- $F_{fit} = a * \sqrt{|x|} * \sqrt{|v|}$
- $F_{fit} = a * \sqrt{|x + v + b|}$
- $F_{fit} = a * \log(|x + b|) * \log(|v + c|) + d$
- $F_{fit} = a * \log(|x + v + b|) + c$
- $F_{fit} = a * \exp(x) * \exp(v) + b$
- $F_{fit} = a * \exp(x + v) + b$
- $F_{fit} = p_{00} + p_{10}x + p_{01}v + p_{20}x^2 + p_{11}xv + p_{02}v^2$ (2^{nd} order polynomial)

- $F_{fit} = p_{00} + p_{10}x + p_{01}v + p_{20}x^2 + p_{11}xv + p_{02}v^2 + p_{30}x^3 + p_{21}x^2v + p_{12}xv^2 + p_{30}v^3 + p_{40}x^4 + p_{31}x^3v + p_{22}x^2v^2 + p_{13}xv^3 + p_{04}v^4$ (4^{th} order polynomial)

- $F_{fit} = p_{00} + p_{10}x + p_{01}v + p_{20}x^2 + p_{11}xv + p_{02}v^2 + p_{30}x^3 + p_{21}x^2v + p_{12}xv^2 + p_{30}v^3 + p_{40}x^4 + p_{31}x^3v + p_{22}x^2v^2 + p_{13}xv^3 + p_{04}v^4 + p_{50}x^5 + p_{41}x^4v + p_{32}x^3v^2 + p_{23}x^2v^3 + p_{14}xv^4 + p_{05}v^5$ (5^{th} order polynomial)

- $F_{fit} = |p_{00} + p_{10}x + p_{01}v + p_{20}x^2 + p_{11}xv + p_{02}v^2 + p_{30}x^3 + p_{21}x^2v + p_{12}xv^2 + p_{30}v^3 + p_{40}x^4 + p_{31}x^3v + p_{22}x^2v^2 + p_{13}xv^3 + p_{04}v^4 + p_{50}x^5 + p_{41}x^4v + p_{32}x^3v^2 + p_{23}x^2v^3 + p_{14}xv^4 + p_{05}v^5|$ (5^{th} order polynomial with absolute value)

- $F_{fit} = x * |p_{00} + p_{10}x + p_{01}v + p_{20}x^2 + p_{11}xv + p_{02}v^2 + p_{30}x^3 + p_{21}x^2v + p_{12}xv^2 + p_{30}v^3 + p_{40}x^4 + p_{31}x^3v + p_{22}x^2v^2 + p_{13}xv^3 + p_{04}v^4 + p_{50}x^5 + p_{41}x^4v + p_{32}x^3v^2 + p_{23}x^2v^3 + p_{14}xv^4 + p_{05}v^5|$ (5^{th} order polynomial with absolute value and x)

- $F_{fit} = |v| * x * |p_{00} + p_{10}x + p_{01}v + p_{20}x^2 + p_{11}xv + p_{02}v^2 + p_{30}x^3 + p_{21}x^2v + p_{12}xv^2 + p_{30}v^3 + p_{40}x^4 + p_{31}x^3v + p_{22}x^2v^2 + p_{13}xv^3 + p_{04}v^4 + p_{50}x^5 + p_{41}x^4v + p_{32}x^3v^2 + p_{23}x^2v^3 + p_{14}xv^4 + p_{05}v^5|$ (5^{th} order polynomial with absolute value and x, v)

The first expression is tested since it represents the force-law which is associated to the granular damper in the first multibody simulations. However, it is not able to fit correctly the real behaviour of the granular material as it will can be seen in the results section. Indeed, the force dependence on the stroke and velocity is more complicated, and so more sophisticated functions are necessary. Increasing the number of the coefficients, the error (called also residual) shows a tendency to decrease but the fitting calculations become heavier and longer. Some coefficients are mathematically necessary, like in the logarithmic expressions, to avoid singularities. As it can be noticed from the polynomial expressions, some of them carry the absolute value and are multiplied by the stroke and/or the velocity. The choice of putting the absolute value is

given by nature of the DEM data, where the forces are always positive (indeed, since it is obtained as the derivation of the velocity of the falling intruder, the deceleration is always upward or positive according to the ground-fixed reference frame). Moreover, a negative force couldn't be realistic and would bring numerical issues. The multiplication of the expression by the stroke, the velocity or with both of them, are justified by the need of having a fitting curve able to give a zero force when the stroke and/or the velocity are zero according to the DEM data. Indeed, when the stroke is zero, it means that the intruder is still above the granular material while when the velocity is zero, it means that the dissipation process is quite over. In this way, the fitting process is "helped" in the task to minimize the error and to achieve an expression with a physical meaning. Eliminating the constant value of the polynomial, it wouldn't give the same results since in the original polynomial expression there are isolated velocity and stroke terms (indeed, at the end of compression phase, the non-zero stroke dependent terms would pull up the upper mass also at zero relative velocity). This analysis demonstrates that the best solution in terms of error is the absolute value of 5^{th} order polynomial surface multiplied by absolute value of the velocity (the absolute value is taken because the velocity used in DEM and in the fitting are mostly negative) and the stroke. As it can be seen in the result section, the increment of the polynomial order doesn't improve the error and would complicate uselessly the model. The search is done up to the 8^{th} order polynomials. During the fitting process with the presented expressions some numerical issues are faced. Indeed, the amount of data of DEM simulations that the fitting tool has to manage is excessive with respect to the assigned memory capacity of the software. In order to perform the fitting, a decimation process of DEM data is necessary. It is similar to a filtering process where the sampling rate of the data is reduced by a factor defined by the user. The decimation of the data is done preserving the significant values of the force vector which are the initial, maximum and the final values. It was quite important to preserve especially the maximum value of the force because it was one of the main parameter in the evaluation of the damper performance. From the results, it will be observable that the difference between the original and the decimated curves is negligible. Regarding the number of curves that are used to build the fitting surface (each one associated to a single simulation with a different touchdown velocity), the following considerations are done: since in the nominal

condition the touchdown velocity is nearly 2 $\frac{m}{s}$, in the multibody scenario where the elasticity of the ground is considered, the landing pad rebounds almost at the same velocity at which it falls on the ground making the instantaneous relative velocity of the granular damper double (4 $\frac{m}{s}$). This means that the fitting surface should guarantee a reliable result at least in a velocity range from zero (nearly) and 4 (actually up to 5 $\frac{m}{s}$ to be more robust). Having good results in this region (of velocity and stroke) is very important because it represents the dynamics of the nominal condition which strongly influences the sizing of both passive and active dampers. However, since one of the primary objectives is to test the sensitivity of the system at different velocities (at least up to 4 $\frac{m}{s}$ which means 8 $\frac{m}{s}$ of relative velocity), the fitting process is done considering also the data of DEM simulations performed at higher velocities. Since this velocity region doesn't represent the sizing condition, a lower number of curves are used. Indeed, it is observed that a higher number of curves in this region has a negative effect in the quality of the fitting in the sizing region. Obviously, having a good result in this latter region would have meant to obtain a reliable fitting surface also for the multibody sensitivity simulation with velocities lower than the nominal condition. For these reasons, force curves from v = 0.2 $\frac{m}{s}$ to 5 $\frac{m}{s}$ are taken with a discretization of 0.2 $\frac{m}{s}$ while the curves from 5 $\frac{m}{s}$ to 8 $\frac{m}{s}$ are taken with 1 $\frac{m}{s}$ of separation. In order to test the quality of the results of the fitting, a single multibody simulation which reproduces the same configuration of the DEM simulation is performed. Comparing the force-stroke trends obtained with DEM simulation and this latter multibody simulation, it is observed that the fitting polynomial is able to follow DEM behaviour with a good approximation. In this validating simulation, the granular damper case is fixed to the ground neglecting any ground elasticity and the force is applied only on the falling satellite mass exactly as it's done in DEM simulations. The fitting polynomial is inserted in a Matlab function block which receives as inputs the stroke and the relative velocity (in this case equal to the velocity of the satellite). According to the shape of the selected polynomial, the granular damper exerts initially, a zero force for zero stroke and subsequently, increases the damping force for different values of stroke and velocity. The mass associated to the landing pad is removed and single mass (105 kg) dynamics is considered as in the following figure.

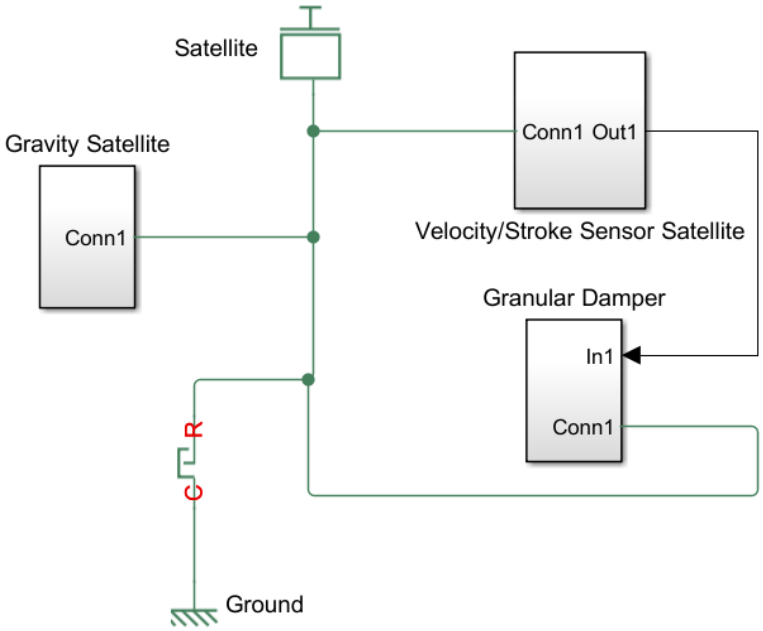

Figure 125 DEM imitation multi-body model

Also in this case, a hard stop is added to prevent a stroke value higher than the maximum allowed value (0.25 m), but it doesn't represent the stiffness and the damping of the ground. Differently from the previous models, the translational spring is removed because the Granular Damper Block, which embeds the fitting polynomial, represents both "elastic" and damping contribution of the granular material. An additional stiffness would have made the model different from what was tested in the DEM simulation.

4.5.2 Granular Model Characterization – Results

As it was done in the previous results presentations, also for the plots regarding the fitting process, only the most meaningful ones will be shown.

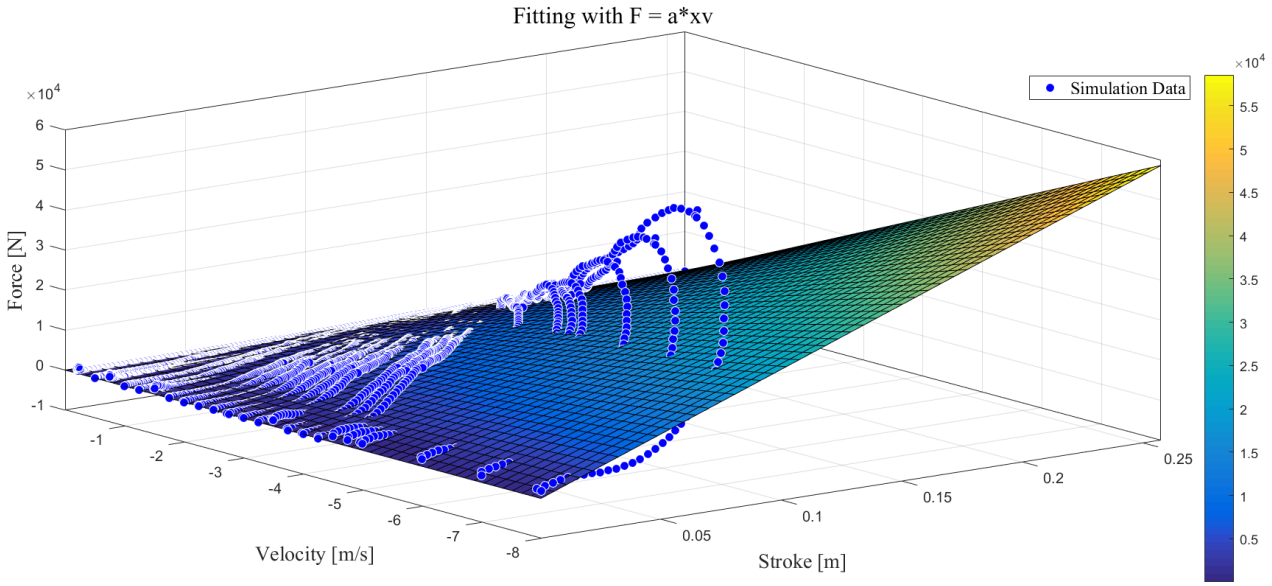

Figure 126

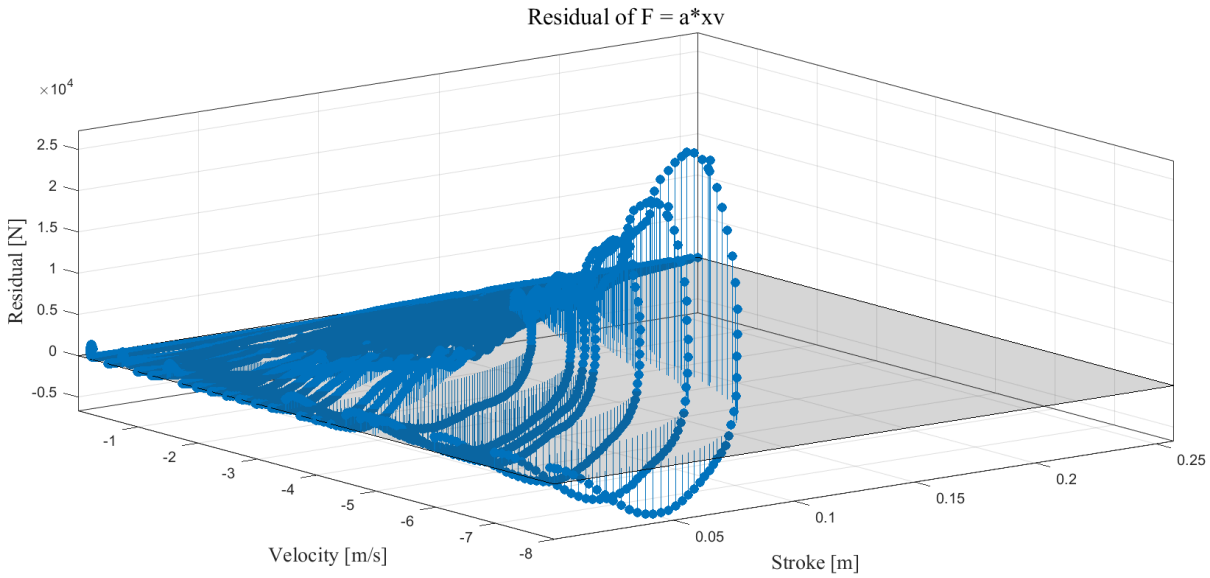

Figure 127

The last two figures represent the fitting surface (together with DEM data) and the associated residual respectively. These results are meaningful since they are related to the model of the granular damper used before DEM analysis.

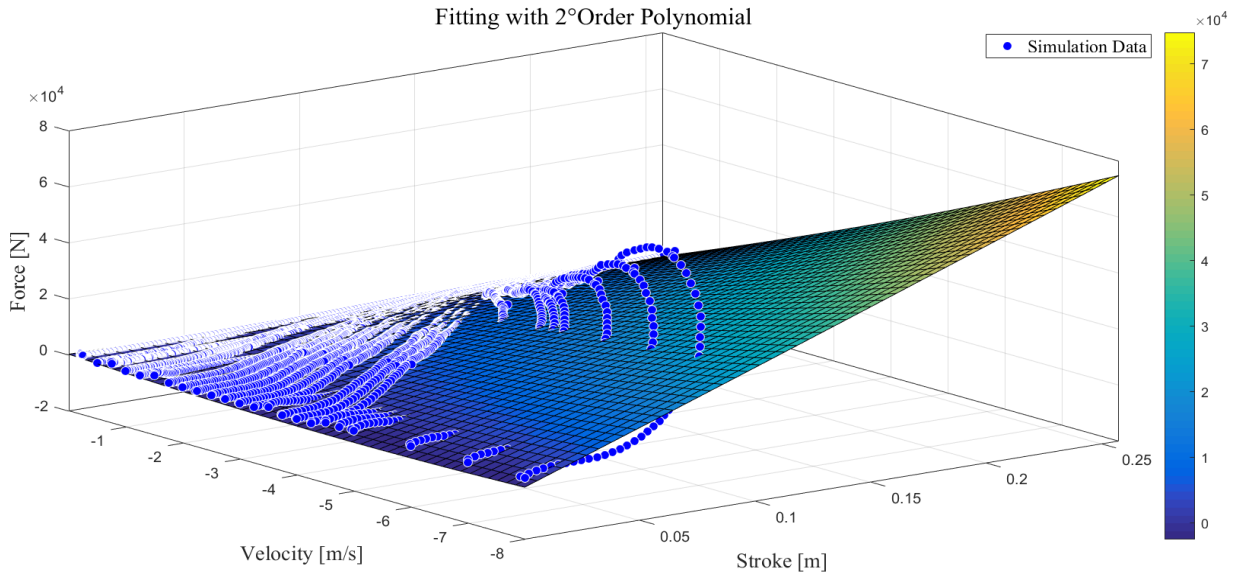

Figure 128

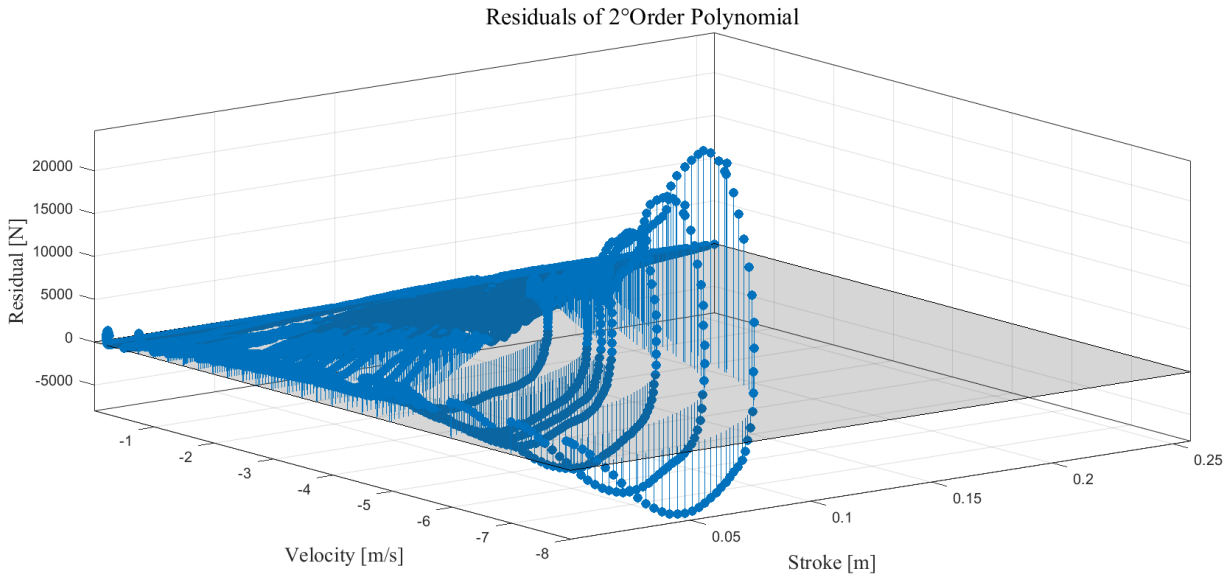

Figure 129

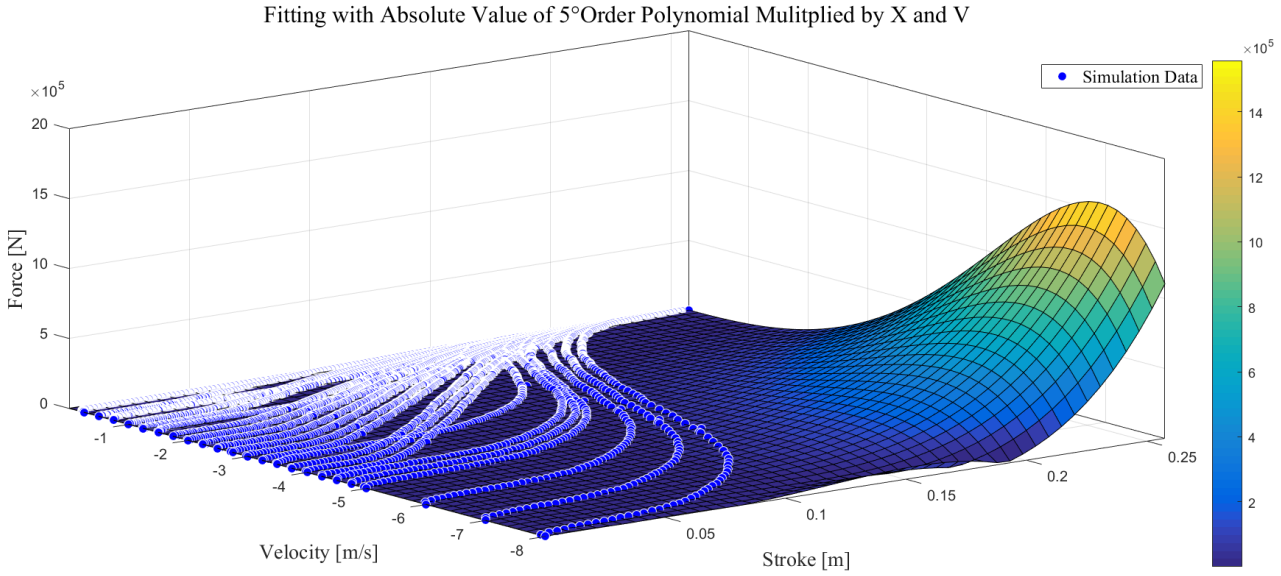

Figure 130

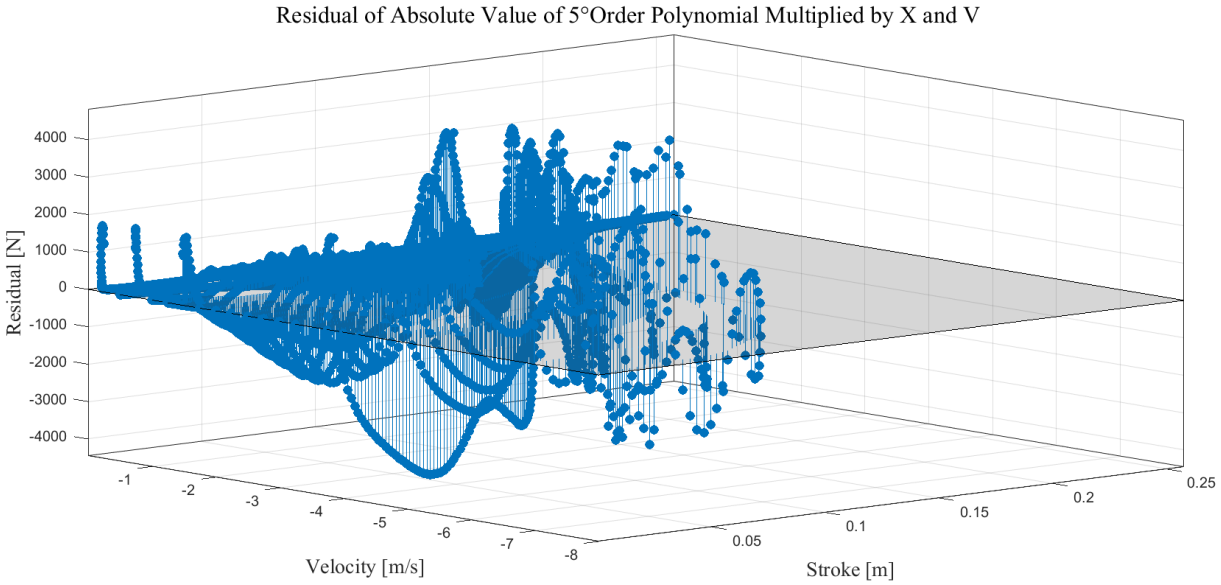

Figure 131

The last two figures are related to polynomial fitting which was effectively used for all the subsequent Multibody simulations. As it was mentioned in the dedicated section, for zero velocity and strokes the forces obtained in DEM are zero in most of the cases and therefore, in order to obtain a fitting polynomial coherent with these data, the original 5°order polynomial was multiplied by X and V (stroke and velocity respectively).

Moreover, in this way, when the polynomial is used in the Multibody simulations, it doesn't generate forces before that the impact occurs.

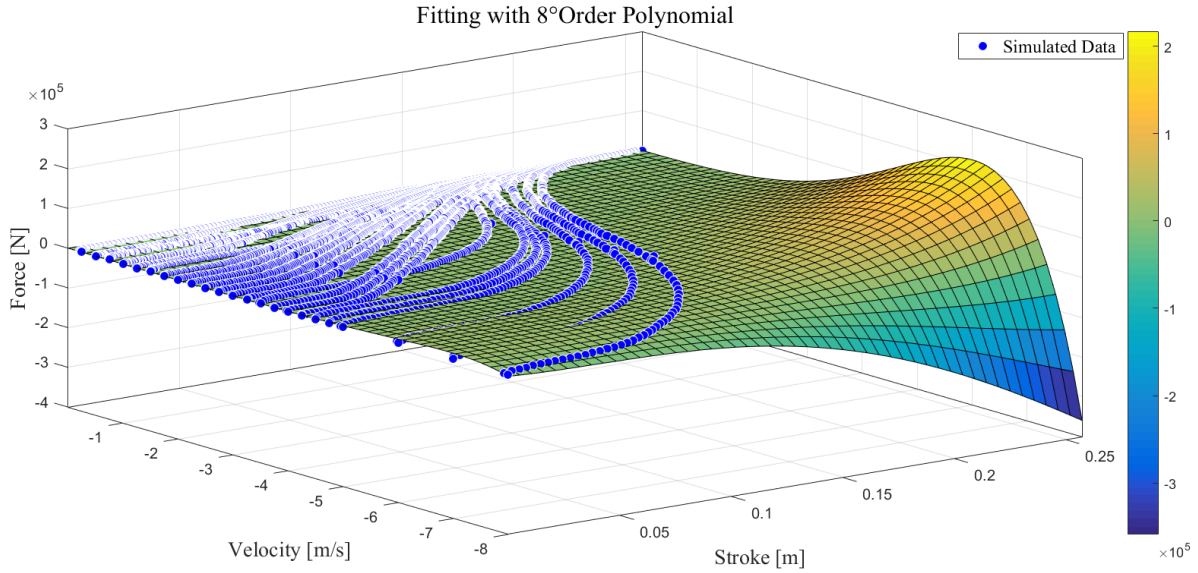

Figure 132

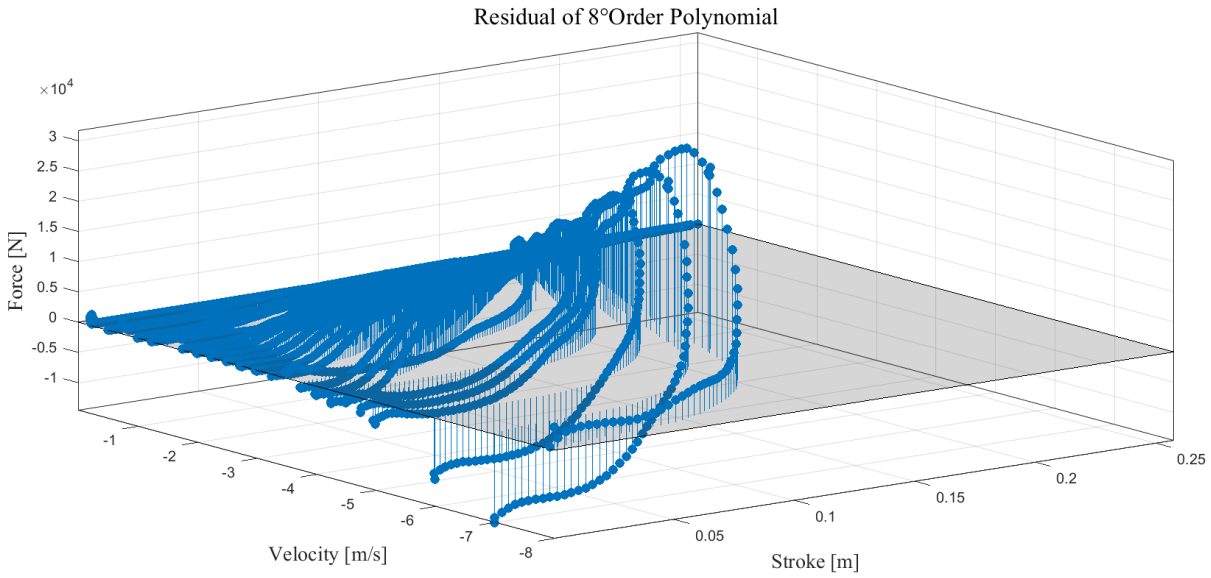

Figure 133

According to these last two figures, increasing the order of the fitting polynomial, the error (or residual) is worsened.

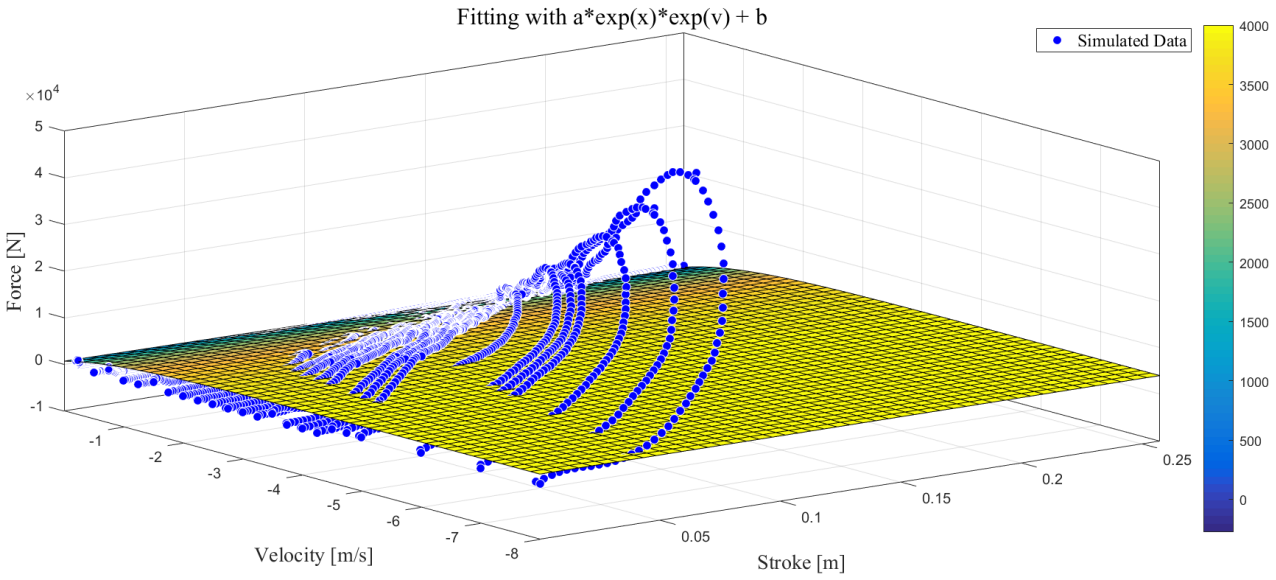

Figure 134

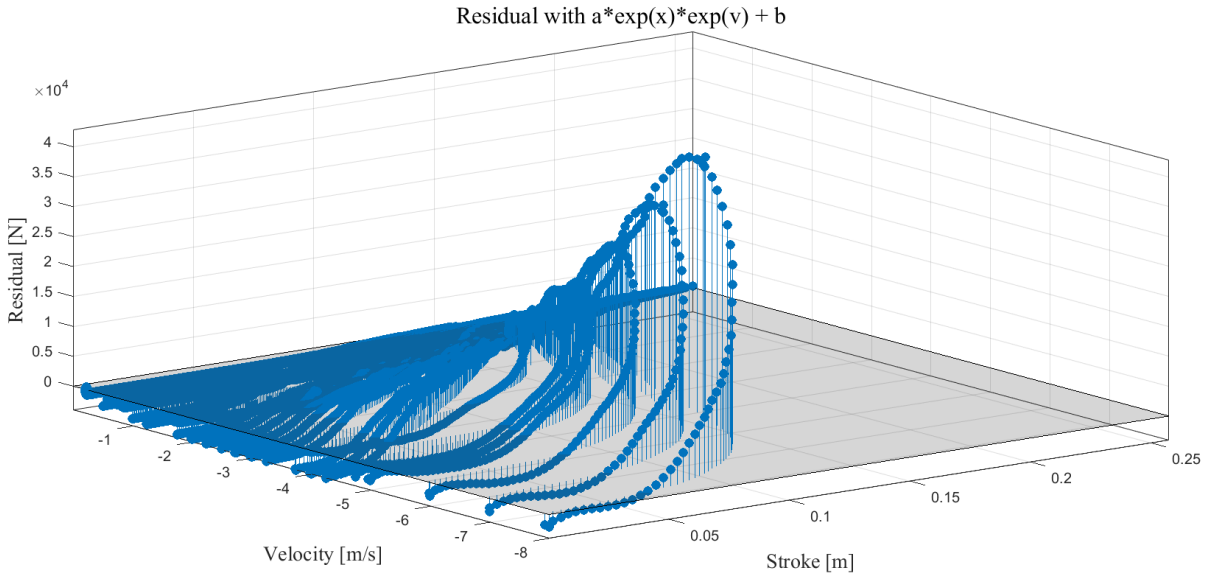

Figure 135

As it can be noticed, a non-polynomial model (like the exponential one) is not able to give an improvement in the fitting process.

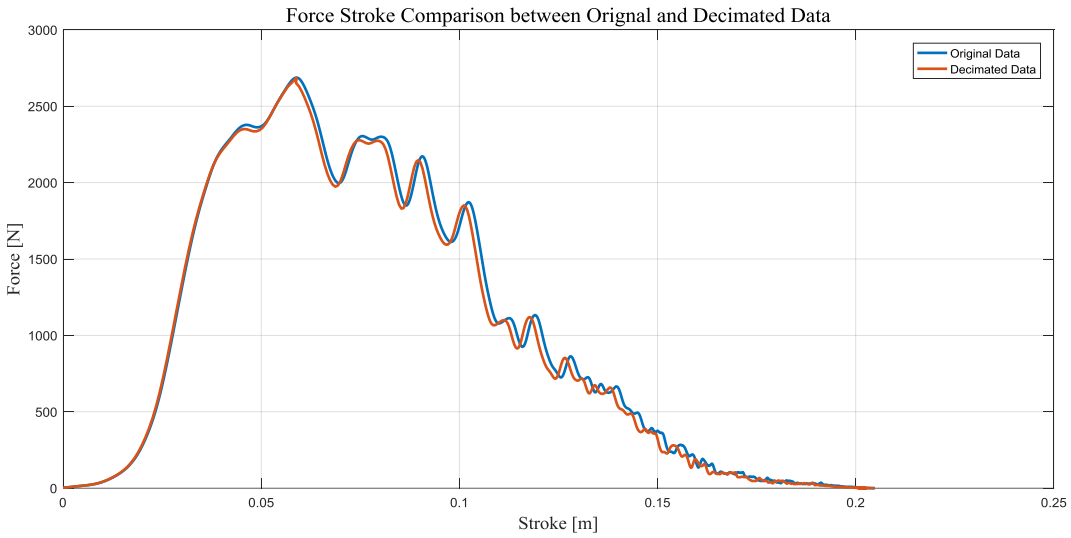

Figure 136

As it was mentioned in the dedicated section, the fitting tests were done after a decimation of the data obtained from DEM. In the last figure can be verified that the trends of the original and the decimated signals are quite similar. Finally, the comparison between the DEM and the fitting polynomial forces is given.

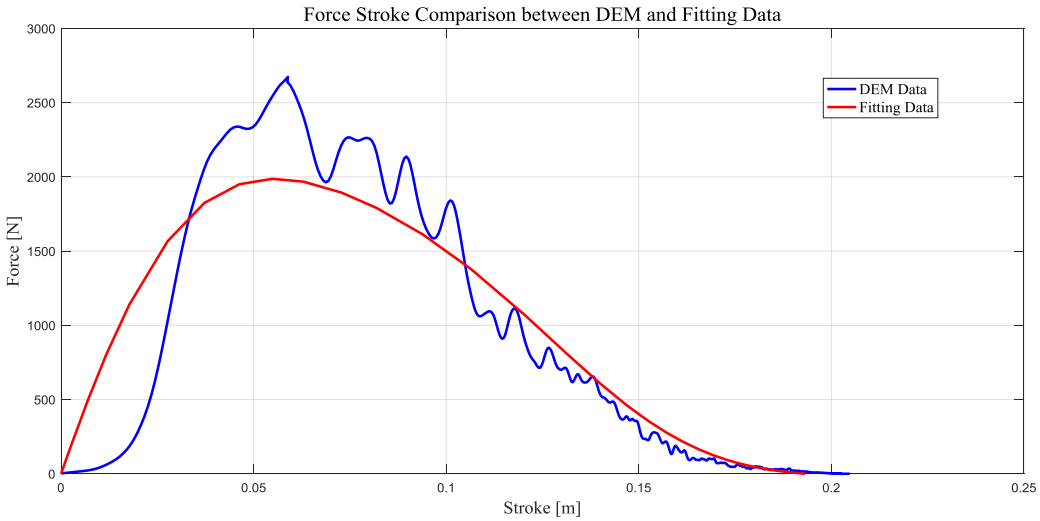

Figure 137

In the last figure, the fitting data is obtained through a Multibody simulation which reproduces exactly the DEM scenario. The difference between the curves is given by the error (residual) of the fitting.

4.5.3 Multibody Simulations for the final Calibration of the Active System

After the proper characterization and the validation of the granular model, a more realistic multibody model, only with the passive damper, is firstly implemented. In this scenario, the landing pad mass is introduced again together with the properties associated to the ground. The aim of this model is to test the performances of the passive device when it is used alone (both in nominal and different conditions), in order to have a comparison term for the calibrated active system and to understand the behaviour of the fitting polynomial when involved in different dynamics. Thanks to the results obtained in this simulation, a significant consideration about the implementation of the fitting polynomial is done: because of the difference between DEM data and the fitting surface (given by the error or residual) and the different dynamics, the dissipation processes are different. It is observed that, when the velocity of the spacecraft becomes positive (during the rebound), the multibody simulation diverges causing numerical issues. This occurred because the fitting polynomial gives always a positive value of force as explained before and, when the spacecraft is rebounding, it applies a force which has the same direction of the velocity, pulling up the mass causing unphysical solution (and subsequently numerical issues). In order to avoid it, a zero force for positive velocity is imposed in the granular damper block. Actually, this condition is not so far from what could happen for an intruder that penetrates in the granular material and rebounds from it. The dissipation occurring in the extension phase should be much smaller than what occurs in the compression phase of the damper. In this way, the multibody simulation neglects a small dissipating contribution looking for a more robust and performant active solution in the calibration phase. The scheme adopted for these

multibody simulations is similar to the those used in the first preliminary simulations. Two concentrated masses are attached together through a hard stop and the actuator block. The spring is removed for the already explained reasons and the ground acts on the landing pad mass with elastic and damping contributions. According to the granular damper's mass estimation, directly obtained from DEM, and the active damper's mass, obtained from the preliminary sizing, a slightly different mass distribution is chosen. The satellite mass was kept 96 kg, while the mass associated to the sum of all the actuators (of the three legs) is fixed to 20 kg. During this phase, a rough calculation demonstrates that the granular damper mass should be 4.6 kg while the active one 1.48 kg. Multiplying by three the sum of the masses of both actuators, 18.24 kg is obtained. Since these numbers will be furtherly modified in the definitive sizing phase, some margin is taken, fixing the total mass of the actuators to 20 kg. The landing pad mass is kept equal to the previous simulations (6 kg). In the multibody scheme only with the characterized passive granular device, the upper mass embedded both the satellite mass and the actuators' mass (116 kg) while the lower mass is left 6 kg. Thanks to this simulation, it is observed that the force generated by the fitting polynomial is quite different from what is observed in the fitting-validating simple model (without landing pad). The force obtained in the first case is higher than the second case. This occurs because the dynamics involved in those simulations are different. In the first case the elasticity of the ground makes the relative velocity to be higher than the second case (almost double). Falling at 2 $\frac{\mathrm{m}}{\mathrm{s}}$, the instantaneous relative velocity becomes 4 $\frac{\mathrm{m}}{\mathrm{s}}$ and the fitting surface give a force value which is near to that obtained from the DEM simulation falling a 4 $\frac{\mathrm{m}}{\mathrm{s}}$. Obviously, in the remaining part of the dissipation, the force-velocity-stroke path would be different from the DEM-curve obtained falling at 4 $\frac{\mathrm{m}}{\mathrm{s}}$, since the kinetic energy involved in the phenomenon is different. As it is said from the beginning of this section, one of the main purpose of the fitting is to open the possibility to calibrate the active damper according to a more accurate granular model. The multibody schemes created to achieve this goal has the same configuration of those used in the first combined active and passive simulations. A maximum allowable stroke of 0.25 m is given to both the dampers, while the only difference is given by a different mass value associated to the dampers block (20 kg) and the absence of the translational

spring between the central and the lower masses. The same force-laws of the previous cases are used (proportional to passive stroke, velocity and the complementary value of them) and again a wide range of the values of coefficients are used to determine the optimal solution for each one of the considered force-laws. In the selection of the range for the coefficients, it is important to fix a lower boundary for those values in order to avoid the "shock" against the bottom of the damper, which would cause an excessive deceleration to the payload mass. Moreover, considering that the passive damper (defined by the fitting polynomial) isn't able to generate a reaction force during an eventual bouncing, it is important to tune coefficient of the active damper in order to avoid the bottom "shock" also for the passive damper, which would cause a rebound of the system. Anyway, thanks to these simulations, it is possible to calibrate the active force-laws and to test their ability to "cooperate" together with the granular damper achieving interesting results. The previous simulations demonstrates that the fitting model of DEM data is reliable and that an active system with different force-laws can be implemented and tuned according to a more sophisticated granular law. However, these simulations cannot fully justify the adoption of a combined active and passive system. As it is said before, the real need for an active system is to reduce the force transmitted to the payload and to increment the robustness of the system against the variation of the external parameters and initial conditions. Regarding the first issue, it is obvious that adding a 0.25m long active damper on a passive damper of the same length (or allowable stroke), the performance in terms of deceleration would be better than an only-passive system with a 0.25 m of stroke. A more logical comparison would involve a passive device and a combined active and passive device with the same total strokes. The willing of creating a more compact damping system and the availability of DEM simulation with 0.25 m as maximum stroke, lead to the multibody simulations where the maximum strokes, both for the active and passive dampers in the combines case, are reduced to 0.125 m. In this way, the entire system would have a more feasible dimension and DEM data and the respective fitting model (since defined up to 0.25 m) would be used with good reliability. The implementation of the active-passive device would be really justified only if in this latter configuration the level of deceleration would be lower than what is obtained in the only-passive model of same total stroke. Actually, this significant change of the configuration have brought a different evaluation

of most of the previously discussed force-laws. According to the results of this last multibody simulations, the only force-law able to ensure a deceleration far lower than the single passive system is a "bell" shaped active-velocity function multiplied by the complementary term of the passive velocity. The good results obtained with this law encouraged the individuation, the test and the calibration of another similar law where the "bell" function was multiplied by the relative displacement between the central and the lower mass. The peculiarities of these laws are the possibility to change both the slope of the force changing the central position of the bell and the maximum value changing the vertex of this inverted parabola. As it is mentioned in the previous section, these "bell" laws are integrated with a switch block that keeps constant the force value when the velocity exceeds the central velocity. It is observed that the benefits in terms of deceleration are obtained changing this central position of the bell function. Indeed, moving the central position towards v = 0 $\frac{m}{s}$ (so increasing its slope), it was possible to lower the maximum value (the vertex) and so the maximum deceleration. It could be interpreted as a way to have a better exploitation of the force-velocity curve (having an adequate force value in the velocity range where the phenomenon is occurring) or as an increment of the dissipated power (increasing the slope also the integral of the force with respect to the velocity increases). Differently from what has been done in the previous simulations (where the central position was kept fixed), in this case the attention is focused on the research of both the maximum value (vertex) and the central position of these bell-laws, which are able to give the optimal performances both for the compression and the extension phases. Hereafter, the final expressions of the selected force-laws are given:

- $F_{active} = (-\frac{a}{b^2}(v_{active} - b)^2 + a)(5 - v_{passive})$
- $F_{active} = (-\frac{a}{b^2}(v_{active} - b)^2 + a)(p_{central} - p_{lower})$

Coefficient **b** represents the central position while **a** represents the maximum value (vertex). **v** is equivalent to the relative velocity. In the last expression **p** represents the position of the respective masses in the absolute reference frame. The search of the central position and the maximum value of these laws look for those values which

minimize the transmitted force in the compression case and for those which minimize the rebound velocity for the extension phase.

4.5.4 Active Damper Calibration with Long Stroke (0.25 m) – Results

The following results are related to the first calibration process of the active damper with the characterized granular damper. Since the considered stroke (0.25 m) is different from the definitive configuration (0.125 m), only the linear ones are presented (also for optimal results table). Indeed, these simulations were done more as a sort of first calibration "test" than a final optimization of the active damper. For the same reason only the coarse data are presented.

Linear Passive Delta X with Linear Active Delta V Force Law

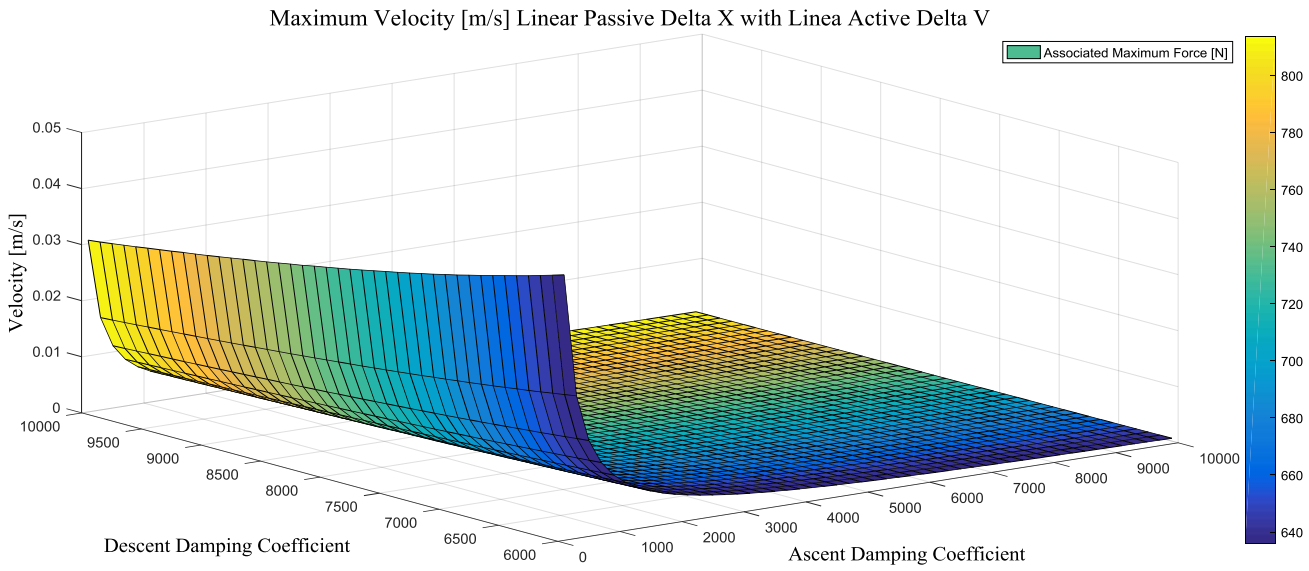

Figure 138

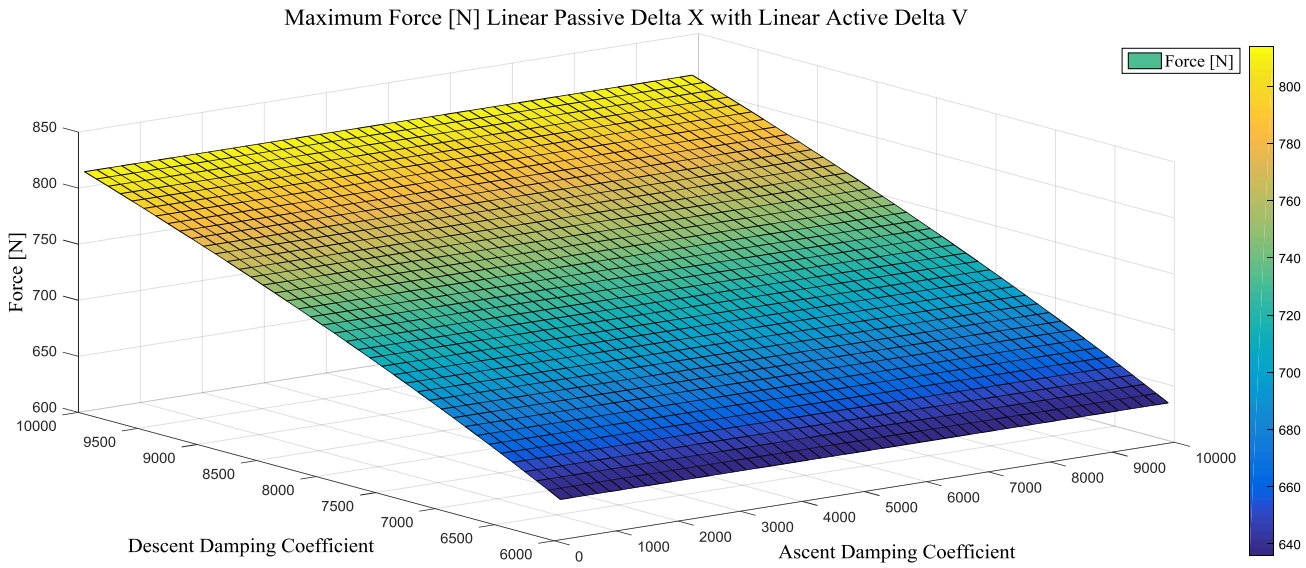

Figure 139

Linear Passive Delta V with Linear Active Delta V Force Law

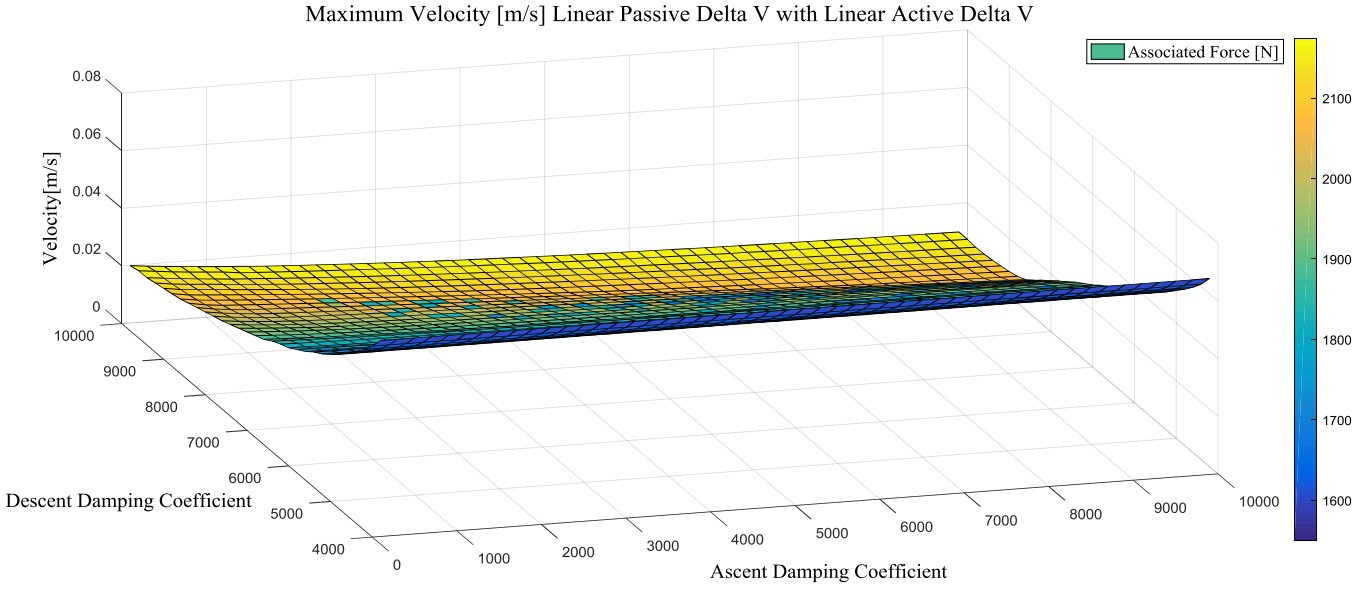

Figure 140

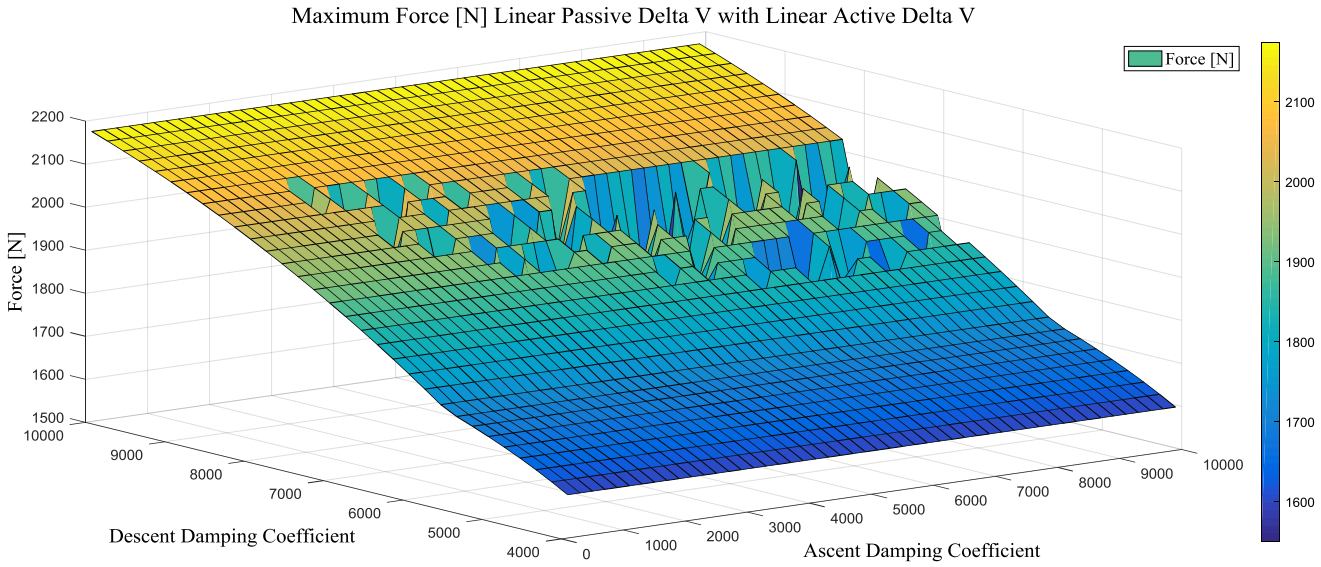

Figure 141

Linear Complementary Passive Delta V with Linear Active Delta V Force Law

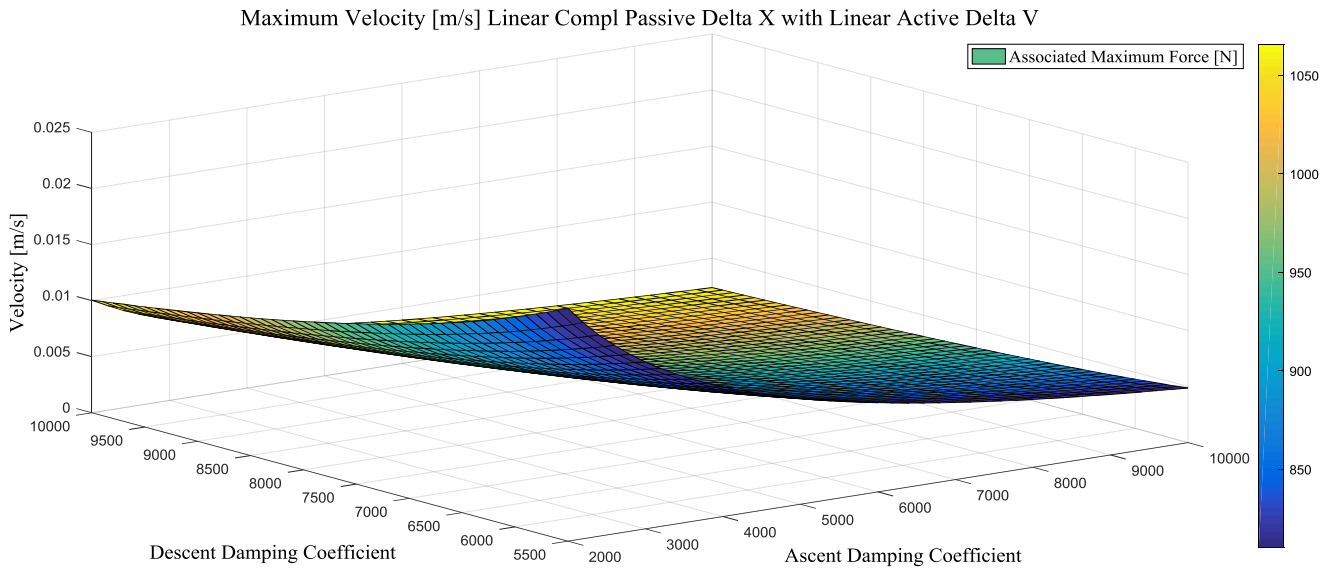

Figure 142

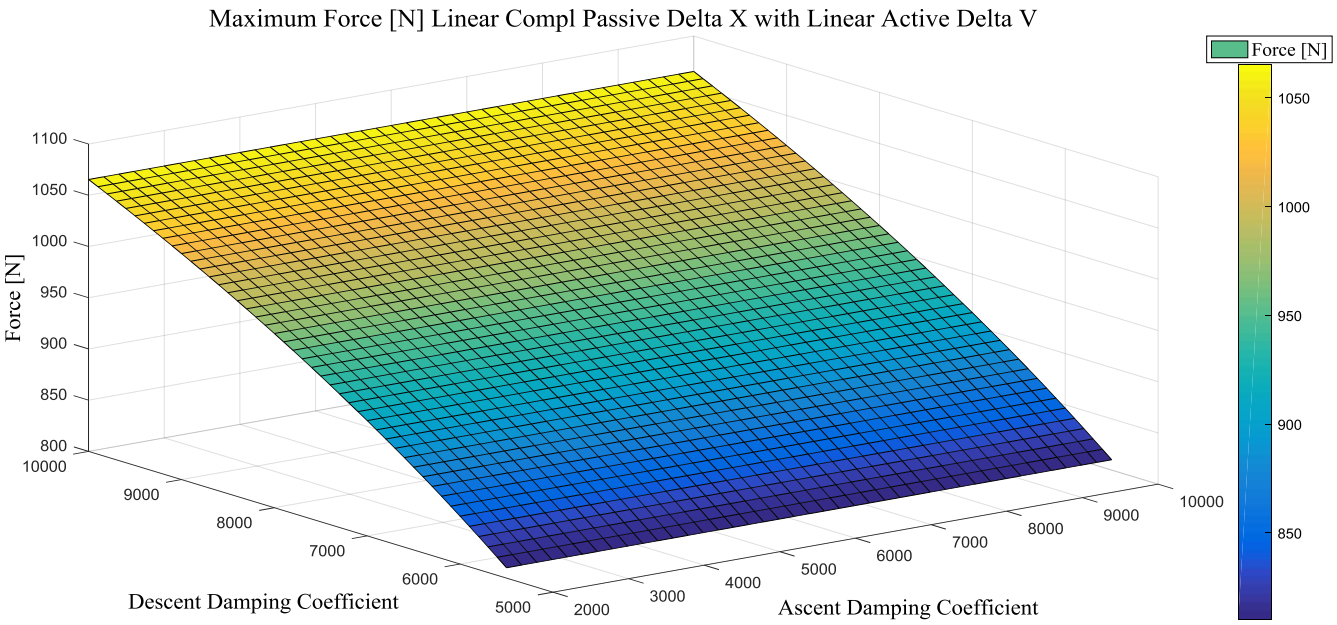

Figure 143

Linear Complementary Passive Delta V with Linear Active Delta V Force Law

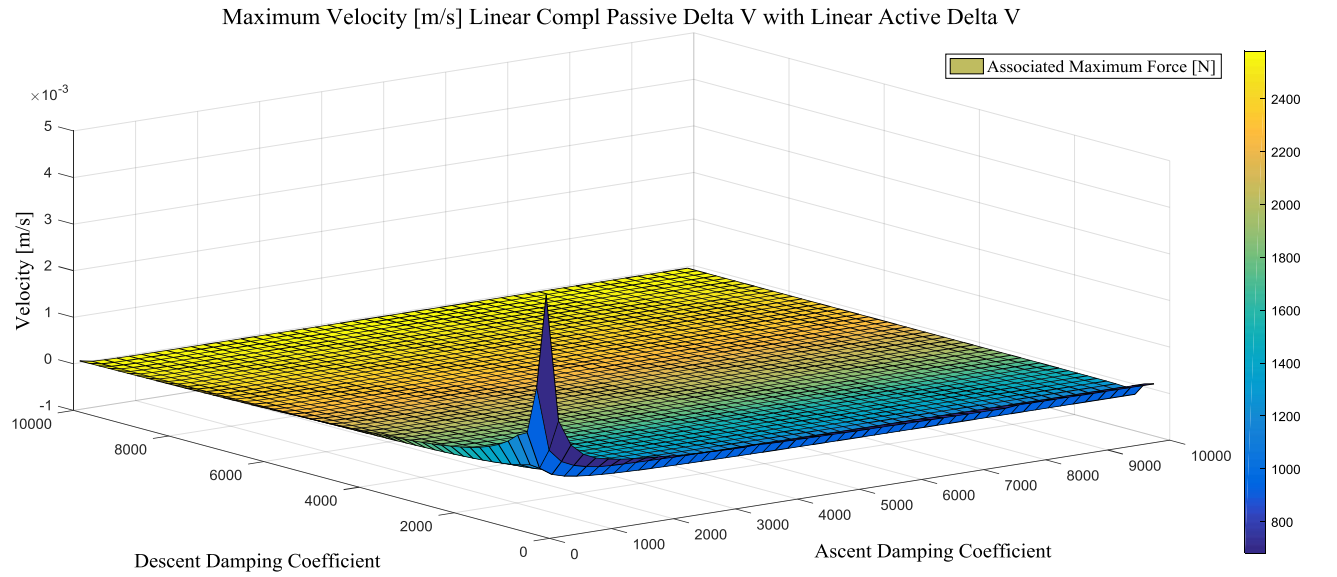

Figure 144

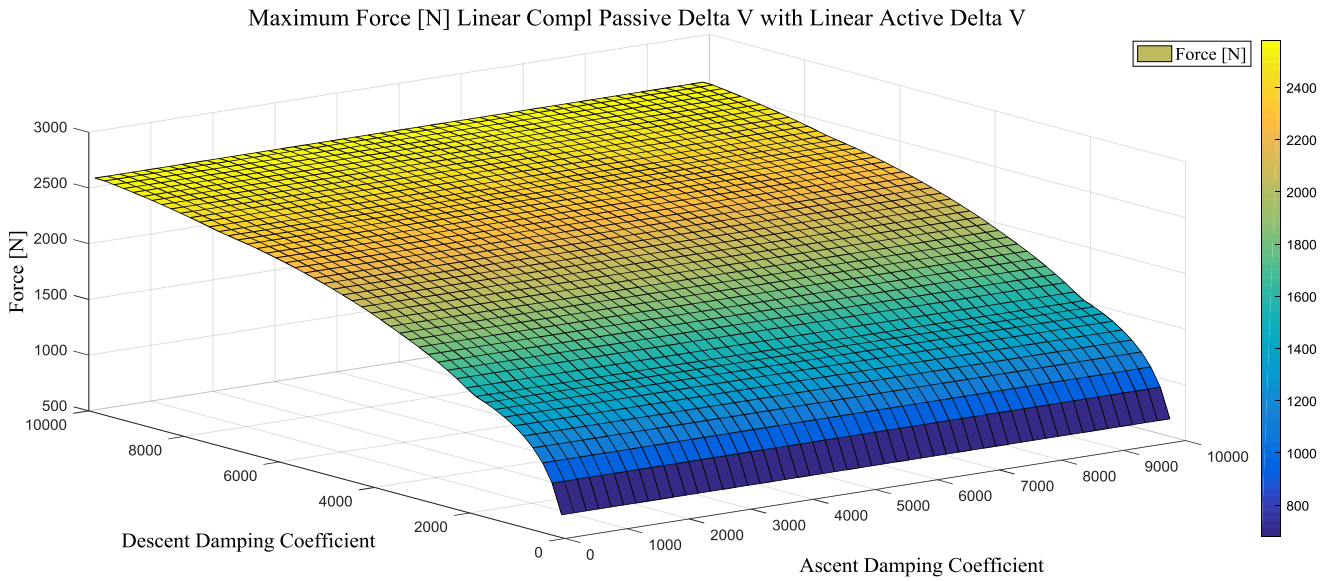

Figure 145

Optimal Results

Active Damper Calibration with 0.25 m Maximum Stroke						
	Maximum Velocity [m/s]	**Maximum Force [N]**	**Maximum Active Stroke [m]**	**Maximum Passive Stroke [m]**	**Active Work [J]**	**Passive Work [J]**
Linear Passive X and Active V	9,86E-04	635,96	0,2452	0,2502	107,82	135,89
Linear Compl Passive X and Active V	0,0049	810,08	0,2489	0,2502	85,72	157,95
Linear Passive V and Active V	2,03E-02	1657	0,1057	0,25	21,1	128,09
Linear Compl Passive V and Active V	1,76E-04	681,18	0,212	0,2502	94,65	149,13

Table 42

	Descent Damping Range	Ascent Damping Range	Optimal Descent Damping	Optimal Ascent Damping
Linear Passive X and Active V	6000_100_10000	100_200_10000	6000	9900
Linear Compl Passive X and Active V	5500_100_10000	2000_200_10000	5500	10000
Linear Passive V and Active V	4000_200_10000	100_200_10000	7800	9900
Linear Compl Passive V and Active V	200_200_10000	100_200_10000	200	9900

Table 43

Through these simulations, it was possible to verify that the active damper can be correctly calibrated according to the chosen polynomial for the granular model achieving interesting performances in terms of velocities and forces.

4.5.5 Active Damper Calibration with Short Stroke (0.125 m) – Results

The following results are related to the final configuration (maximum stroke 0.125 m for each actuator). In addition to the usual linear cases, the figures of "bell" and simple linear force law are given. Regarding the optimal data charts, some force-laws data are omitted. Indeed, some simulations weren't run because subjected to numerical issues (like the square root laws) while for the "bell" laws, the optimization of the coefficients were performed manually and not with an extensive parametric analysis as for other laws.

Linear Passive Delta X with Linear Active Delta V Force Law

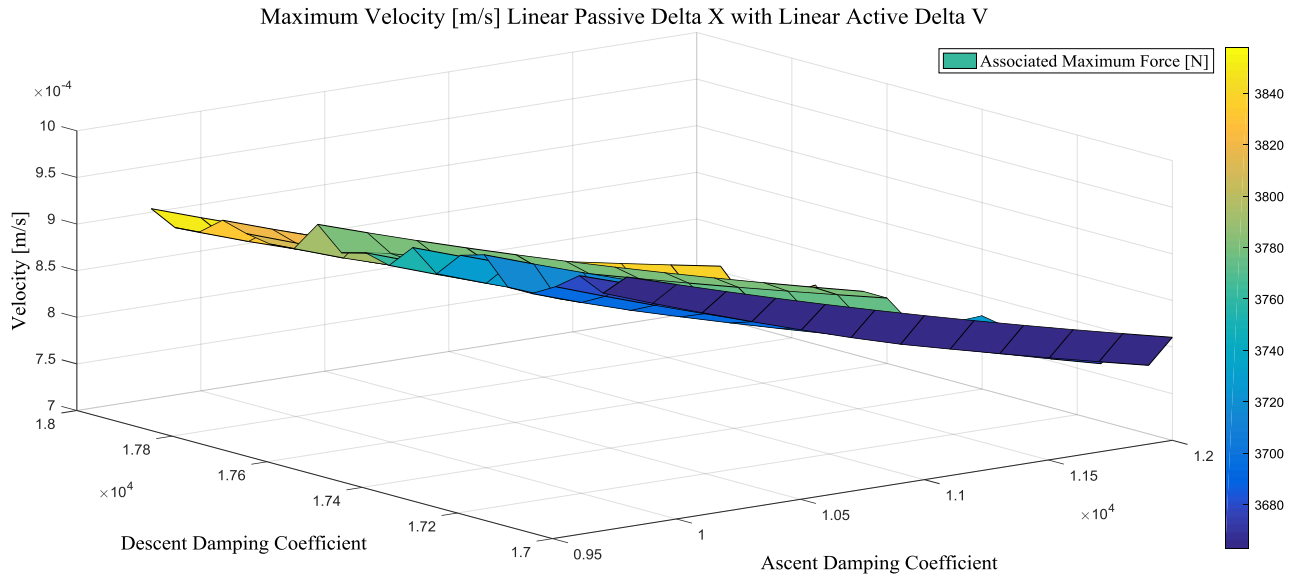

Figure 146

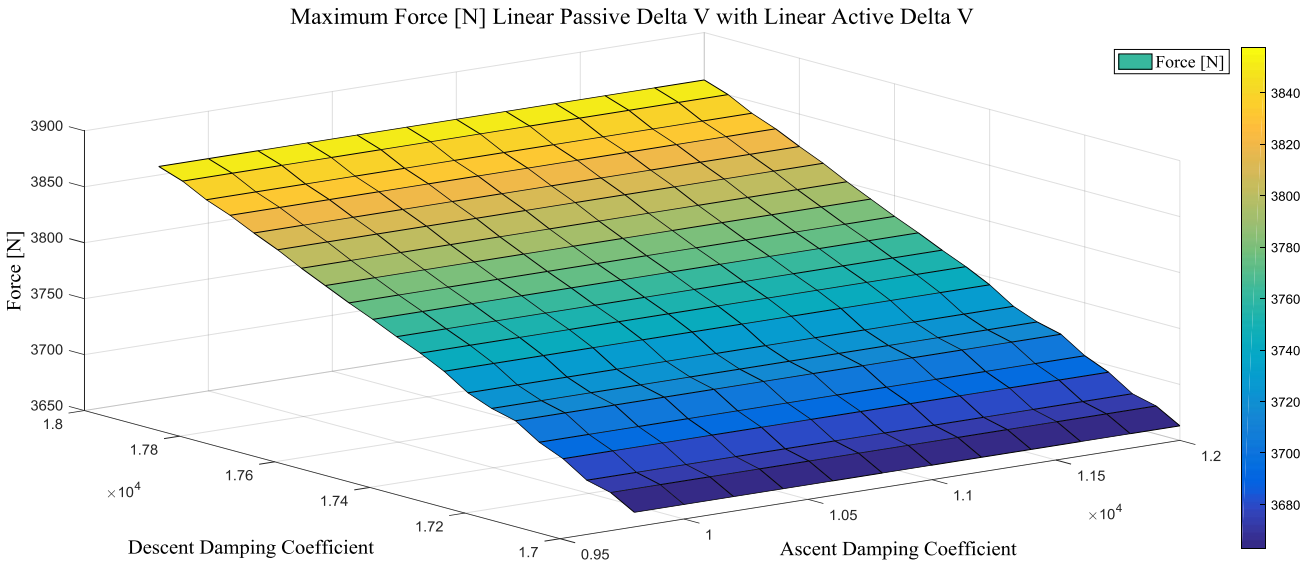

Figure 147

Linear Passive Delta V with Linear Active Delta V Force Law

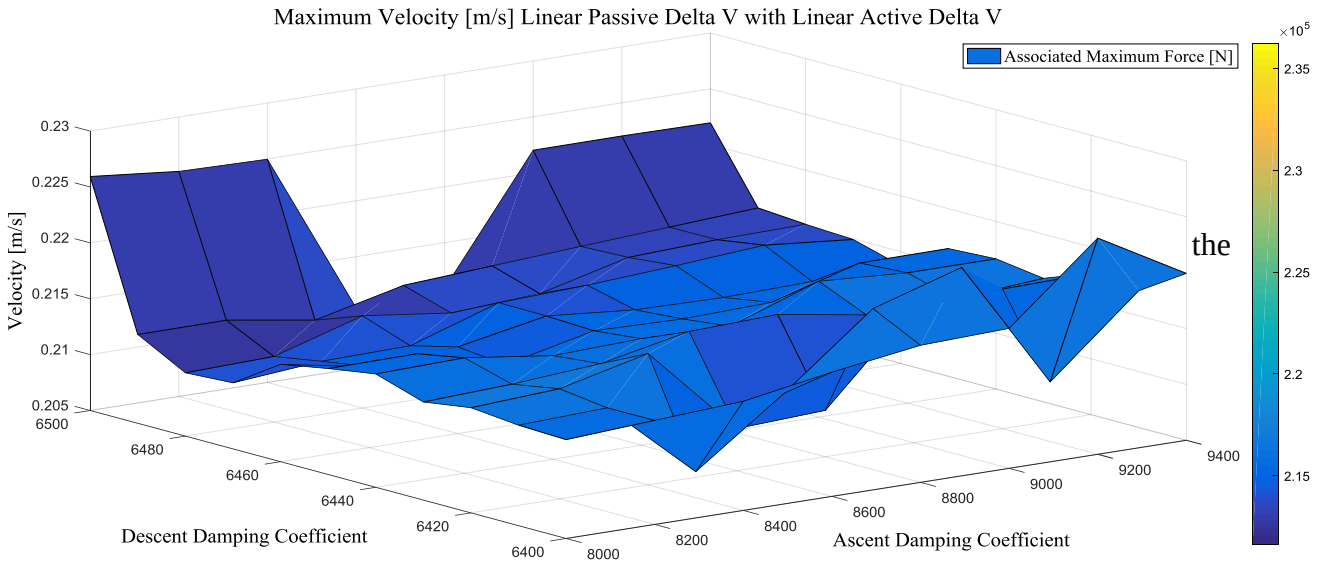

Figure 148

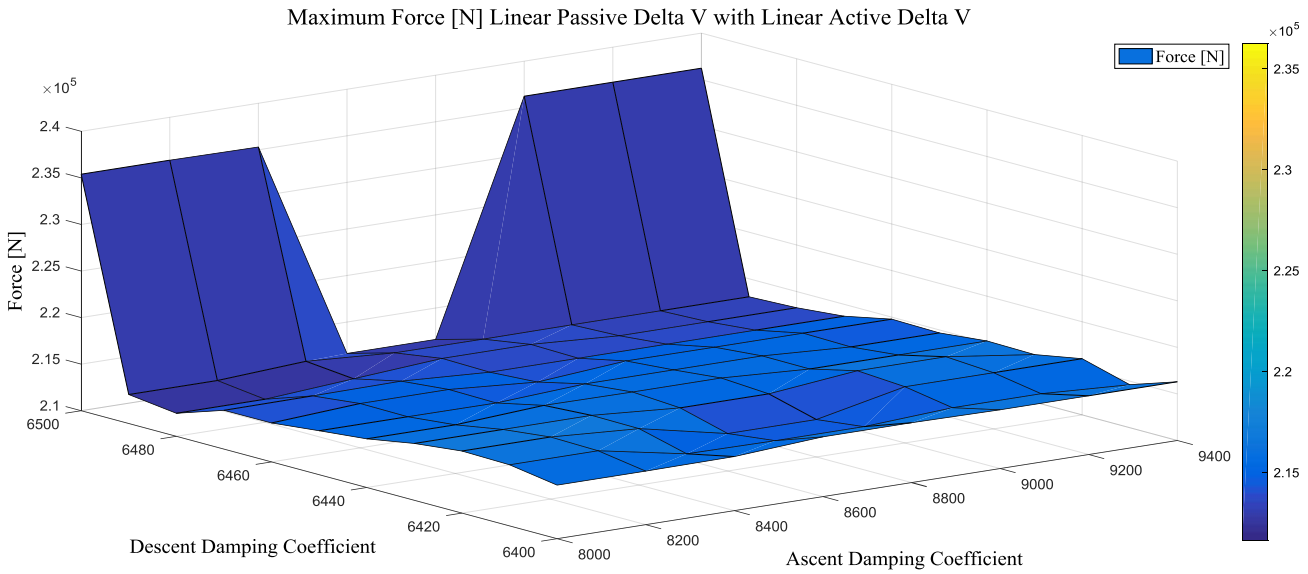

Figure 149

Linear Complementary Passive Delta X with Linear Active Delta V Force Law

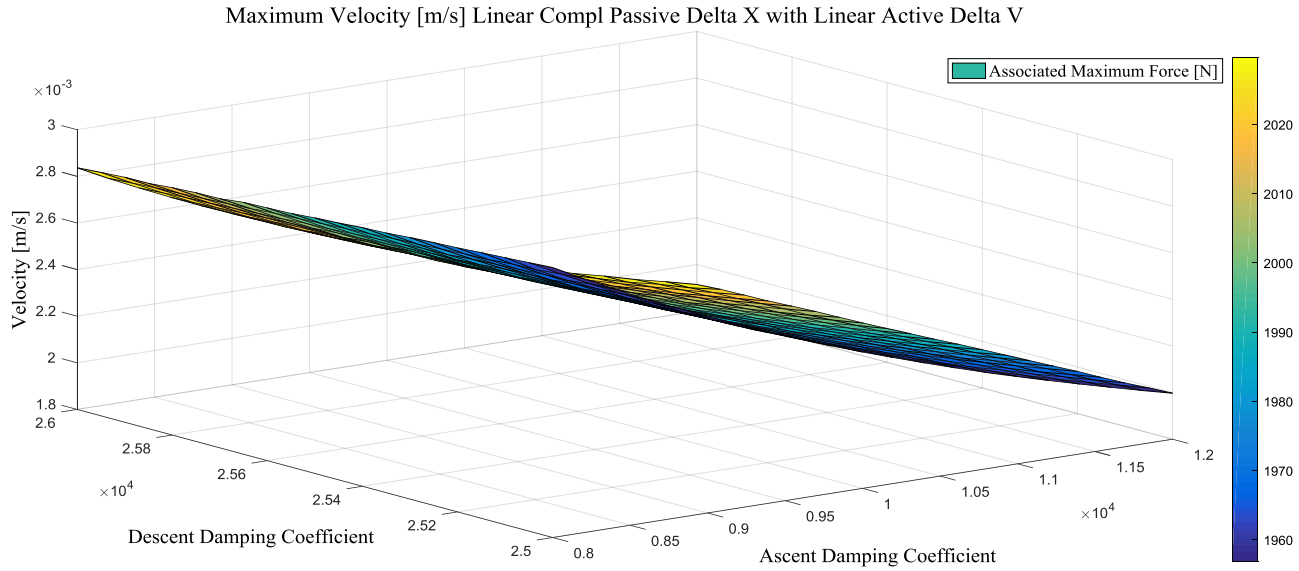

Figure 150

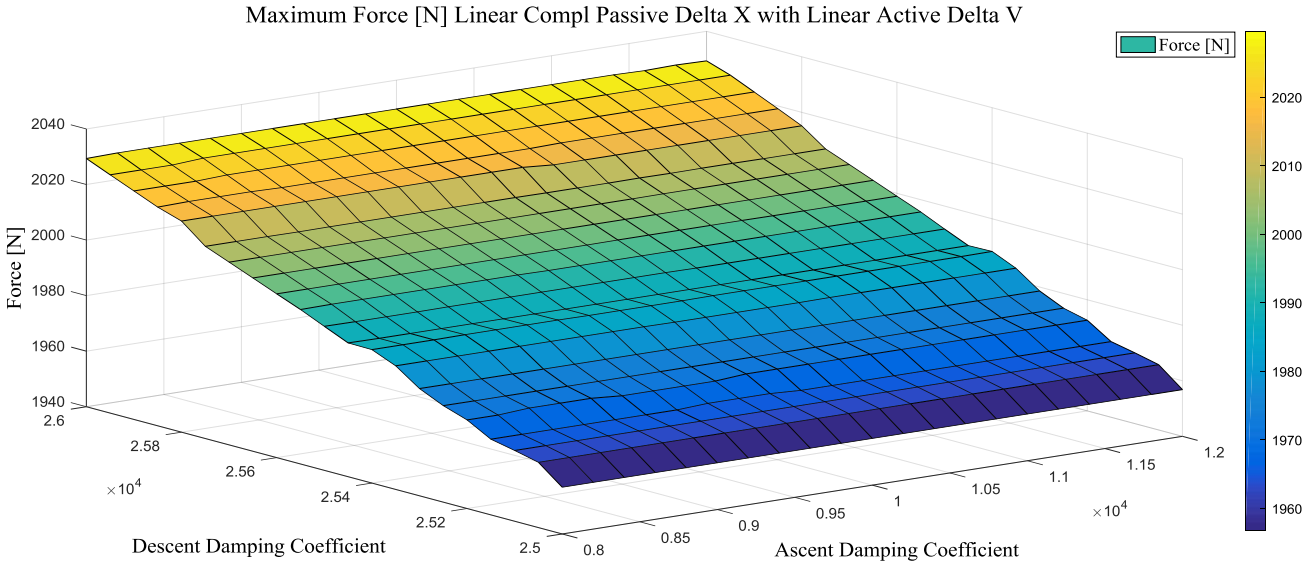

Figure 151

Linear Complementary Passive Delta V with Linear Active Delta V Force Law

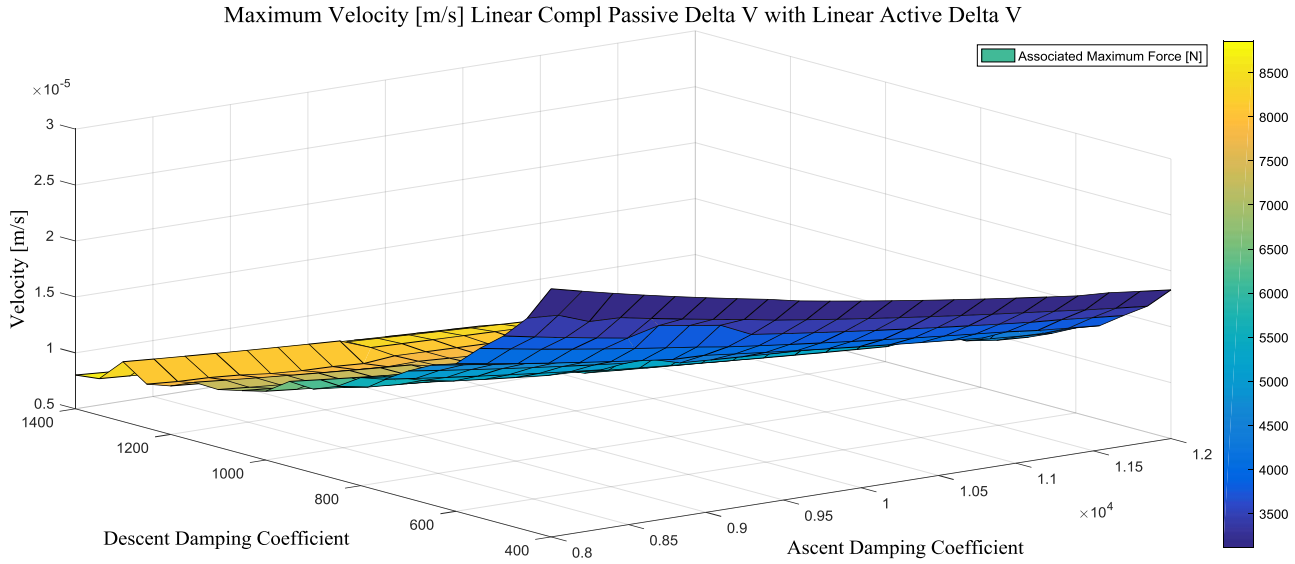

Figure 152

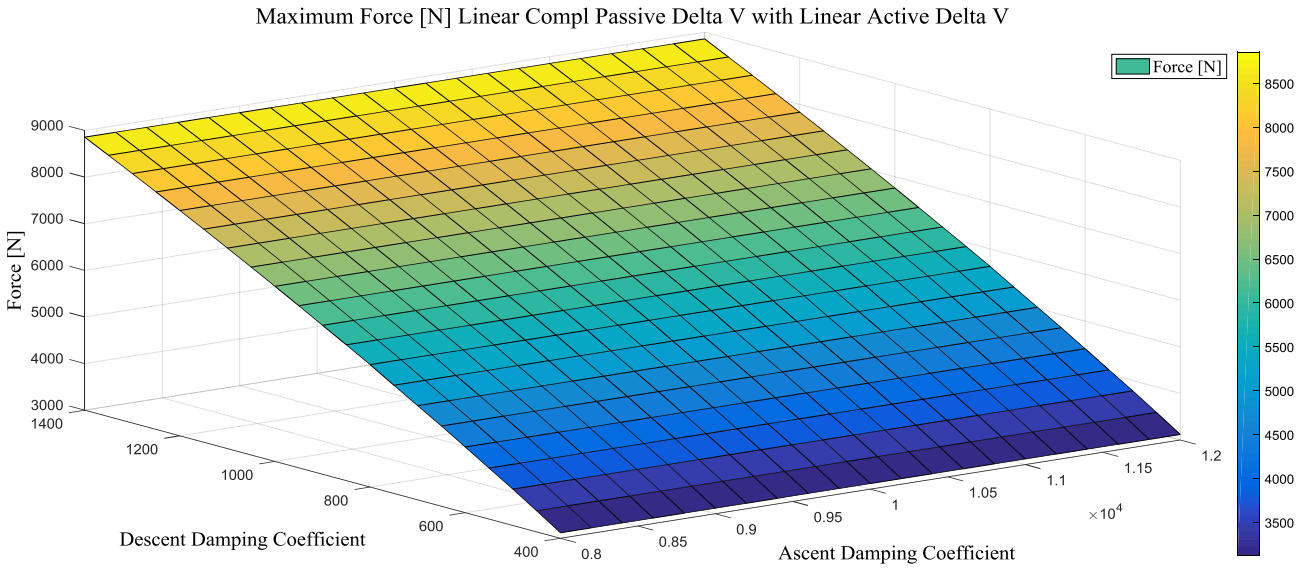

Figure 153

Simple Linear Active Delta V Force Law

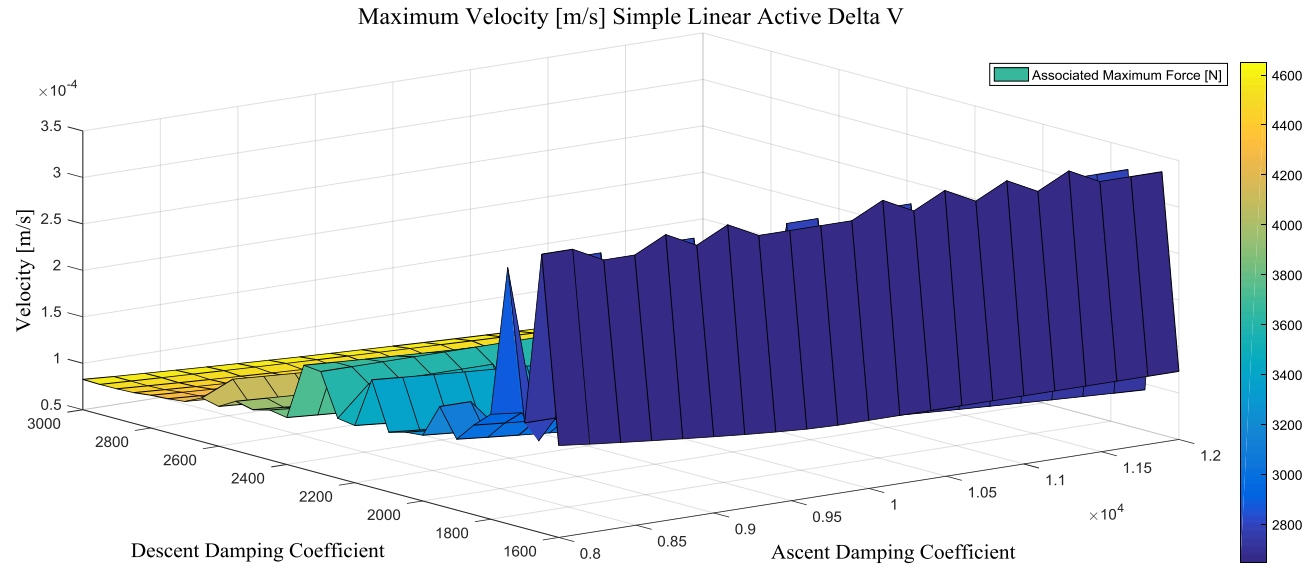

Figure 154

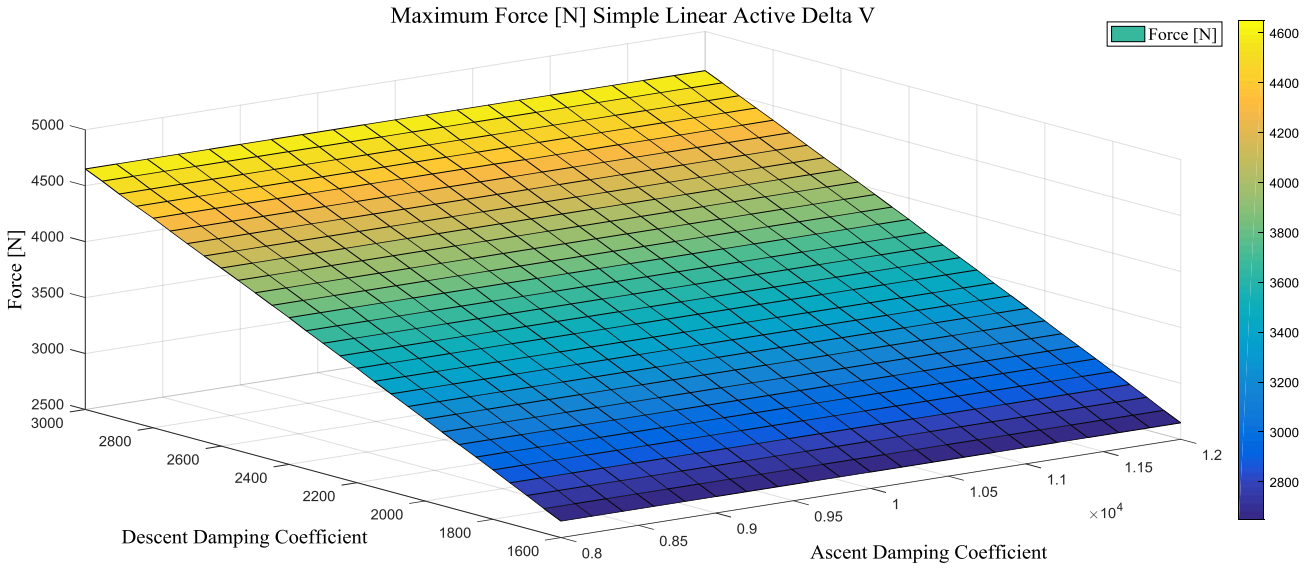

Figure 155

Up to now, it is observed that no one of the presented laws is able to ensure a maximum force far lower than the value (3800 N) obtained only with the passive case with a total

length of 0.25 m. The simple linear case was considered again in this phase of the work because it was interesting to check if the simplest solution could have a better behavior w.r.t more sophisticated laws considered up to now. However, as for others, the simple linear is not able drop the force value far below the value associated to the passive case.

Linear Complementary Passive Delta V with Bell Active Delta V Force Law

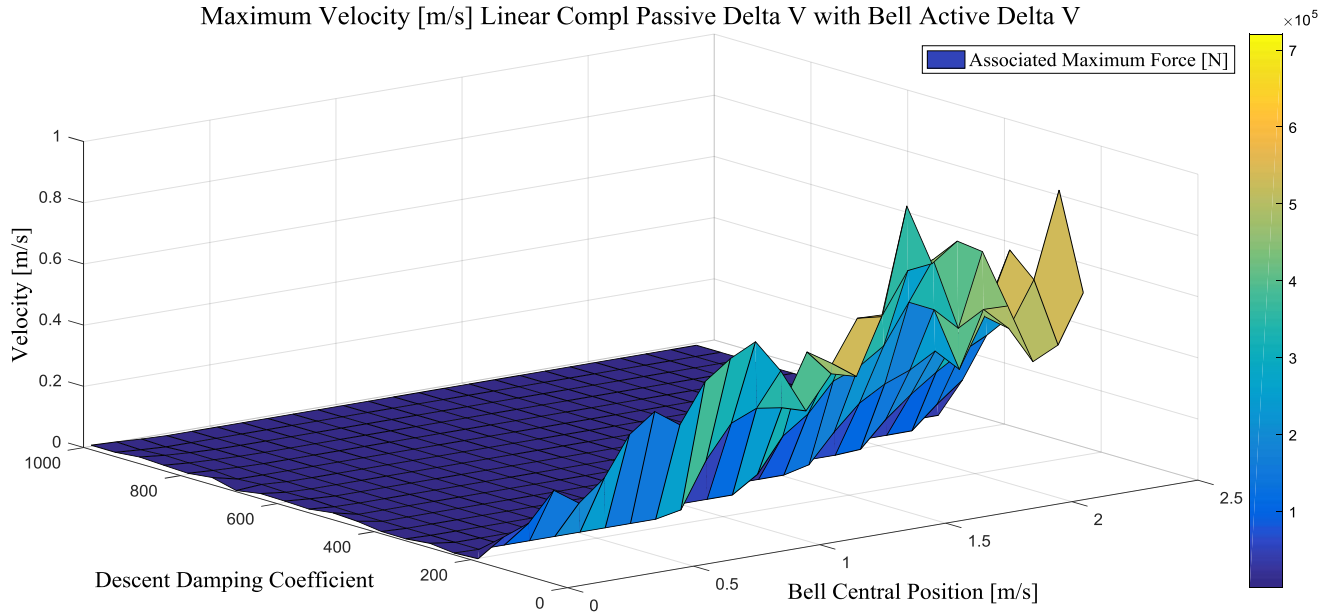

Figure 156

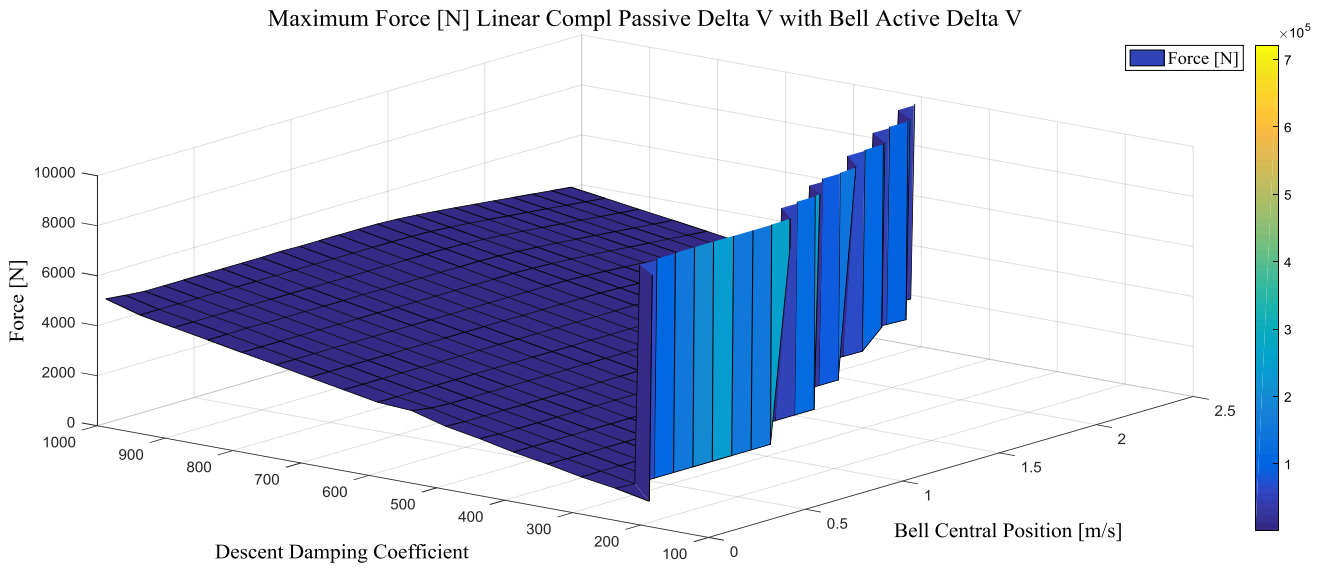

Figure 157

This force law, once calibrated, is able to ensure a quite low value of transmitted force (below 1 kN) with acceptable values of bouncing velocity. As it can be seen in the previous two figures, the parametric analysis for this law was done varying the descent damping coefficient and the central position of the "bell". The evident "knee" in the figures is related to the limit of the impact with the bottom of the actuator. It can be observed that the limit value of the damping coefficient can be decreased for lower values of central position. Indeed, lowering the central position, the slop of the force-velocity curve is increased and so doing also the dissipated power with the advantage of reducing the maximum force.

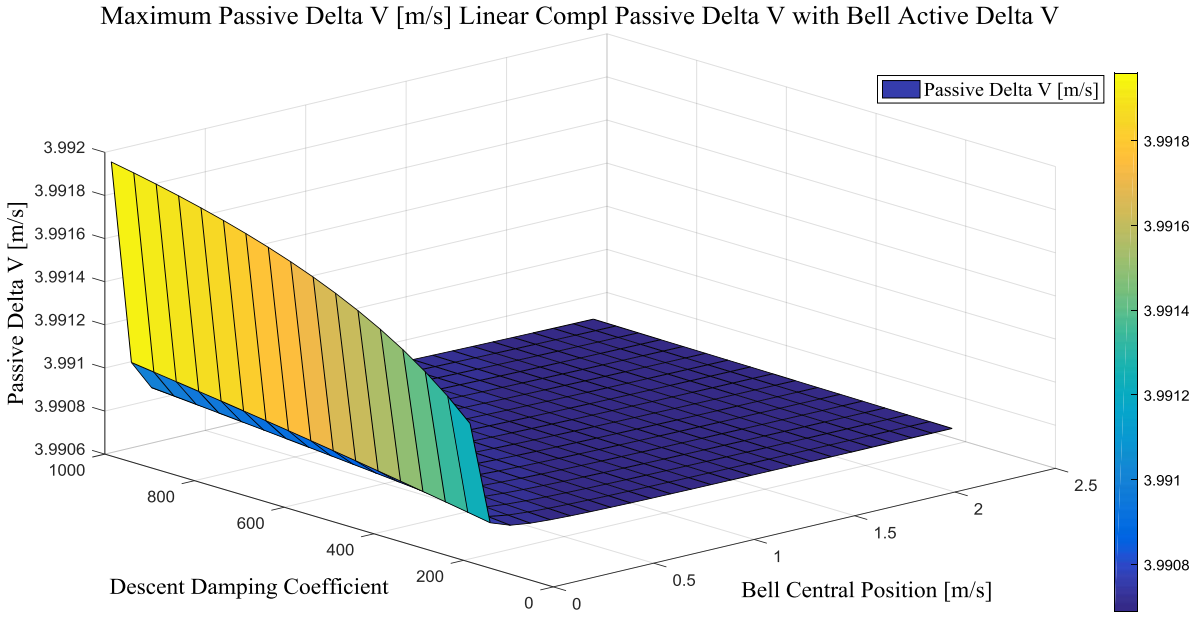

Figure 158

This last figure checks if the passive relative velocity doesn't exceed the allowed value ($2*V_{arrival}+1$) for the bell-law.

Optimal Results

Force Laws Linear with Active V and Passive X Dependent Coefficient						
	Maximum Velocity [m/s]	**Maximum Force [N]**	**Maximum Active Stroke [m]**	**Maximum Passive Stroke [m]**	**Active Work [J]**	**Passive Work [J]**
Linear	8,10E-04	3663	0,1156	0,125	115,01	128,82
Quadratic	7,53E-04	3708	0,1145	0,125	114,73	129,11
Cubic	7,88E-04	3708	0,1145	0,125	114,71	129,12
Logarithmic	8,60E-04	3463	0,1208	0,125	116,43	127,38
Square Root	3,14E-04	2997	0,1219	0,125	112,36	131,48

Table 44

	Descent Damping Range	**Ascent Damping Range**	**Optimal Descent Damping**	**Optimal Ascent Damping**
Linear	17000_50_18000	8000_200_12000	17000	12000
Quadratic	17000_50_18000	8000_200_12000	17000	12000
Cubic	17000_50_18000	8000_200_12000	17000	12000
Logarithmic	17000_50_18000	8000_200_12000	17000	12000
Square Root	5000_50_6000	8000_200_12000	5000	12000

Table 45

Force Laws Linear with Active V and Passive V Dependent Coefficient						
	Maximum Velocity [m/s]	**Maximum Force [N]**	**Maximum Active Stroke [m]**	**Maximum Passive Stroke [m]**	**Active Work [J]**	**Passive Work [J]**
Constant	1,23E-04	2647	0,1197	0,125	106,02	137,81
Linear	0,225	235300	0,125	0,125	44,06	192,79
Logarithmic	5,60E-01	230900	0,125	0,125	45,99	178,48

Table 46

Table 39	Descent Damping Range	Ascent Damping Range	Optimal Descent Damping	Optimal Ascent Damping
Constant	1600_50_3000	8000_200_12000	1600	1200
Linear	6400_10_6500	8000_200_9500	6500	8400
Logarithmic	6400_10_6500	8000_200_12000	6400	12000

Table 47

Force Laws Linear with Comp Passive V and Active V Dependent Coefficient						
	Maximum Velocity [m/s]	**Maximum Force [N]**	**Maximum Active Stroke [m]**	**Maximum Passive Stroke [m]**	**Active Work [J]**	**Passive Work [J]**
Linear	1,83E-05	3118	0,108	0,125	106,6	137,23
Quadratic	2,08E-05	3021	0,1229	0,125	111,65	132,15
Cubic	2,08E-05	3081	0,1224	0,125	111,56	132,24
Logarithmic	2,61E-05	2149	0,1207	0,125	110,37	133,43
Square Root	2,38E-04	1742	0,1129	0,125	108,06	135,68

Table 48

	Descent Damping Range	**Ascent Damping Range**	**Optimal Descent Damping**	**Optimal Ascent Damping**
Linear	400_50_1400	8000_200_12000	400	12000
Quadratic	330_50_1000	8000_200_12000	330	12000
Cubic	330_50_1000	8000_200_12000	330	12000
Logarithmic	450_50_1000	8000_200_12000	450	12000
Square Root	275_10_375	20_2_40	275	36

Table 49

Force Laws Linear with Passive X and Active V Dependent Coefficient						
	Maximum Velocity [m/s]	**Maximum Force [N]**	**Maximum Active Stroke [m]**	**Maximum Passive Stroke [m]**	**Active Work [J]**	**Passive Work [J]**
Quadratic	0,0233	14808,8812	0,1250	0,1250	118,7352	125,0360
Cubic	0,0347	21963,8838	0,1250	0,1250	118,8247	124,8779
Logarithmic	0,0314	19915,2587	0,1250	0,1250	118,4834	125,2154

Table 50

	Descent Damping Range	**Ascent Damping Range**	**Optimal Descent Damping**	**Optimal Ascent Damping**
Quadratic	14000_50_15000	20000_500_30000	14500	30000
Cubic	14000_50_15000	20000_500_30000	14500	30000
Logarithmic	19000_50_20000	20000_500_30000	19750	30000

Table 51

Force Laws Linear with Passive V and Active V Dependent Coefficient						
	Maximum Velocity [m/s]	**Maximum Force [N]**	**Maximum Active Stroke [m]**	**Maximum Passive Stroke [m]**	**Active Work [J]**	**Passive Work [J]**
Quadratic	0,0112	7239,6905	0,1250	0,1250	103,0099	140,7844
Cubic	0,0205	13226,1212	0,1250	0,1250	103,1780	140,6097
Logarithmic	0,0530	34496,1586	0,1250	0,1250	102,8312	140,7710

Table 52

	Descent Damping Range	**Ascent Damping Range**	**Optimal Descent Damping**	**Optimal Ascent Damping**
Quadratic	7000_50_8000	20000_500_30000	7550	30000
Cubic	7000_50_8000	20000_500_30000	7550	30000
Logarithmic	9000_50_10000	20000_500_30000	9750	30000

Table 53

Force Laws Linear with Comp Passive X and Active V Dependent Coefficient						
	Maximum Velocity [m/s]	**Maximum Force [N]**	**Maximum Active Stroke [m]**	**Maximum Passive Stroke [m]**	**Active Work [J]**	**Passive Work [J]**
Linear	0,0008	1922,2500	0,1248	0,1250	93,7238	150,0736
Quadratic	0,0693	43420,2422	0,1250	0,1250	95,3607	148,1392
Cubic	0,0347	21963,8838	0,1250	0,1250	118,8247	124,8779
Logarithmic	0,0008	1427,4263	0,1249	0,1250	92,9169	150,8898

Table 54

	Descent Damping Range	**Ascent Damping Range**	**Optimal Descent Damping**	**Optimal Ascent Damping**
Linear	24000_100_26000	20000_500_30000	24500	30000
Quadratic	22000_50_23000	20000_500_30000	22250	30000
Cubic	14000_100_16000	20000_500_30000	14500	30000
Logarithmic	30000_50_31000	20000_500_30000	30250	30000

Table 55

As it was explained in the dedicated section, the last force laws which were able to give acceptable values of forces were the Linear Complementary Passive Delta V with Bell Active Delta V and the Linear Passive Difference Positions with Bell Active Delta V laws. Hereafter, the force-stroke trends comparison between the bell laws and the only passive case are given (on the left side the figure for the bell with complementary of Delta V while on the right side for the bell with passive position difference are given).

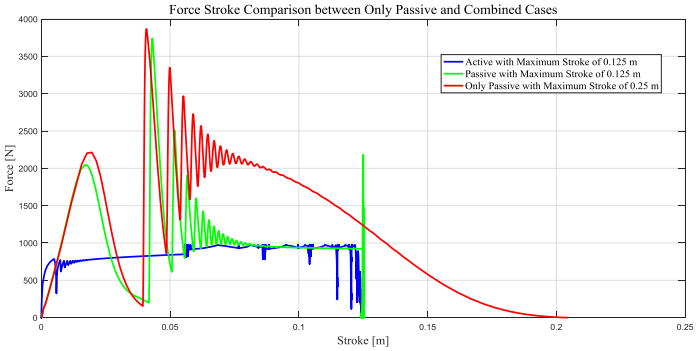

Figure 159

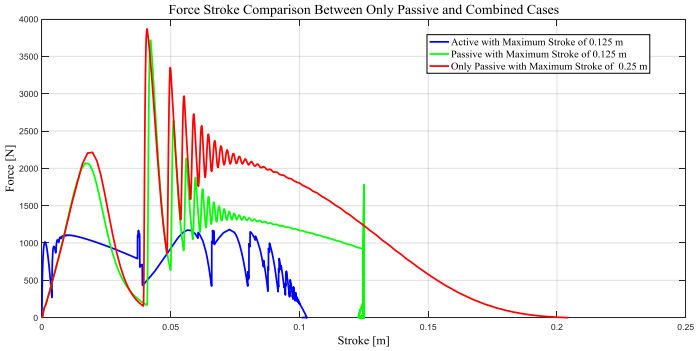

Figure 160

As it can be observed from these results, the force transmitted to the spacecraft when the active+passive system is applied, is far lower thant the force observed only with the passive device of the same equivalent length. This consideration put in evidence the advantage of the chosen configuration also in the nominal condition (-2m/s). The optimal coefficient values obtained through manual tuning for these last two laws are the following:

	Descent Central Position	**Descent Damping Coefficient**	**Ascent Central Position**	**Ascent Damping Coefficient**
Linear Passive Position Difference with Bell Active DeltaV	0.9	5740	2	20000
Linear Compl Passive Delta V with Bell Active Delta V	0.25	195	0.01	12000

Table 56

5. System Robustness Analysis and Final Sizing

This chapter is dedicated to the description of the strategy adopted for the final robustness analysis, the presentation of the related results and the illustration of dampers sizing process performed according to the obtained results. All the following considerations and data are given for the two previous best active damper laws which work in series with the characterized granular model.

5.1 Robustness Analysis of the definitive Models of Landing System

This analysis is conceptually equal to the one made for the precedent models, where the behaviour of the passive actuator wasn't still exactly characterized, the control law of active actuator wasn't still definitively identified and the strokes for both the actuators were 0.25 m for each one. The aim is to study robustness and sensitivity of the landing system with respect to the same factors of the previous analysis plus to some new elements, in order to make the system more suitable to work in a so harsh and uncertain environment. The models considered now are the final configuration of the system, where there are the passive actuator and the active one in series with stroke of each one of **0.125 m**, and the configuration with just the passive actuator with stroke **0.25 m**. Thanks to this comparison it will result that, with same total stroke, the active-passive system is better because, beyond having superior properties in nominal conditions, it

has a very robust behaviour against all the uncertainties that now are going to be presented. Since the parameters involved are a lot, isn't performed a multi-dimensional analysis, but two and three dimensional analysis with the attempt to verify the most possible dangerous cases. Run multi-body simulations varying all possible parameters at the same time would be very onerous by computational point of view, and the model behaviour would be further difficult to predict. First of all, it's verified which are the minimum level required of the control system in terms of minimum sampling frequency of control parameters (strokes and sliding velocities of both actuators), and maximum acceptable level of accelerometer noise, used to obtain strokes and sliding velocities by integrating its output. These two analyses are done for the best two control laws in order to study the robustness of the laws itself. In the model of this thesis, since it is built with Simulink, strokes and sliding velocities are directly obtained through Simulink tools, and therefore the real signal error that would be obtained integrating accelerometer output is directly included in the noise of stroke and sliding velocity signals. A Gaussian noise block is added in the model, with a variance different from zero and a mean value equal to zero, summing the noise to the mentioned signals.

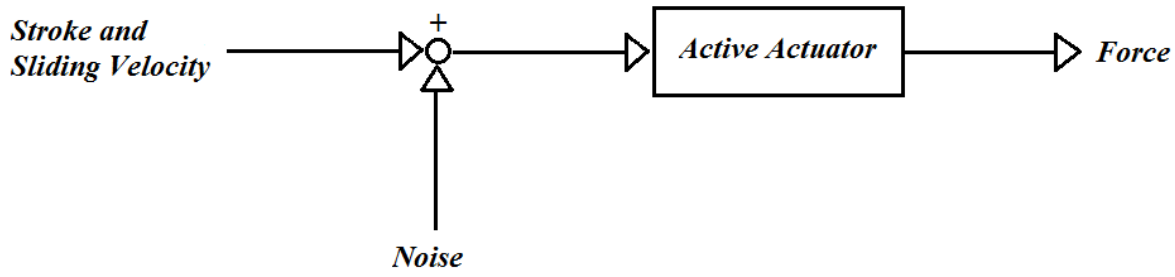

Figure 161 Schematic representation of active actuator block

The procedure adopted aims to find a maximum value of variance (to put in the Gaussian noise block) beyond that the active system isn't able anymore to braking properly the spacecraft. The tried variances go from 1e-04 to 1e-15, with a discretization step of one order of magnitude. All other parameters are kept nominal and the signal delay, element directly linked to the sampling frequency of the acquisition system, equal to zero. Once the maximum acceptable variance is found, three graphs are

plotted, with the variance vector along the abscissa axis and bouncing velocity, maximum force transmitted by satellite and maximum active actuator stroke along ordinate axis. Similar kinds of graphs are plotted, but along abscissa axis is put the noise density, a parameter that characterizes the accelerometers and allows to obtain the variance associated. The variance equation is the following:

$$\sigma_{xx}{}^2 = E[x(t)^2] - \mu_x(t)^2$$

Where the first term is the signal variance, the second is the mean square value and the third the mean value of the signal.

Since the noise considered is a Gaussian noise with the mean value $\mu_x(t)^2$ set to zero, the variance is equal to the mean square value. The root mean square (RMS), by definition, is the root square of the mean square value:

$$RMS = \sqrt{E[x(t)^2]}$$

Therefore, the variance is equal to the square of root mean square of the signal.

$$\sigma_{xx}{}^2 = RMS^2$$

Noise densities given by accelerometers datasheets are expressed in $\frac{\mu g}{\sqrt{Hz}}$ and have to be multiplied by the square root of the signal frequency to get the RMS. So, the variance is connectable with noise density of the accelerometer, making possible to choose properly the accelerometer knowing furthermore the bandwidth of the signal. The value of noise density goes from $\frac{\mu g}{\sqrt{Hz}}$ to $\frac{ng}{\sqrt{Hz}}$, where for the last one the associated variance is in the order of 1e-13. For what regard the acquisition system, the parameter analyzed is the sampling frequency, because lower it is, higher the delay of the applied force is. As before, all the parameters are kept nominal and the noise is zero. The delay considered passes from 1e-02 seconds to 1e-05 seconds, with a discretization step of an order of magnitude. A too big reduction would make no sense, since the interest is to verify

which is the maximum acceptable value and a too small delay value would slow too much the multibody simulations. The same graphs of before are plotted, but now once with along the abscissa axis the delay, and once with the sampling frequency, which is simply the inverse of the delay. The results obtained from the analysis of these two aspects will help to drive the final choice of the control law. But it won't be the unique aspect. The robustness of the system shall be characterized also against variations of arrival velocity and ground parameters as for the precedent models, but also of vehicle's mass and gravity field. Parameters and factors involved are a lot and so an accurate but not too computationally onerous strategy must be adopted. The idea is to have at least a plot representing the behaviour of the system, in terms of bouncing velocity, transmitted force (and so the acceleration experienced by the spacecraft during the landing), works carried out by both the actuators and active actuator force, with respect to the variation of all the mentioned factors. It's notable that active actuator force trends are plotted just for three legs system, because for one leg case it's pretty equal to force felt by the spacecraft and to highlight that with three legs every active actuator shall produce less force, and this is important because the tension available for the piezoelectric plates can't be too high. During all these multibody simulations, sampling frequency of acquisition system and signal noise are not taken into consideration since they were needed to help to identify the robustness of the control law in the nominal case. Therefore, are built four families of three-dimensions plots where is plotted system behaviour with respect to environment parameters variation (ground parameters and gravity field), four families of two-dimensions plot representing system behaviour with respect to arrival velocity and spacecraft mass variations, and one plot where are compared actuator force of only passive case and actuators forces of active-passive case. The last plot is built for both the best two control laws, whereas the first eight families are built for the best two laws of active-passive system and for the passive system with stroke of 0.25 m, in order to help the best law choice but also to highlight the better robustness of active-passive system with respect to just passive one. All these plots are built for models, both active-passive and passive, with one leg and three legs. Starting to explain the first four families, for every family are plotted four three-dimensions graphs where are represent the behaviour of bouncing velocity, force transmitted to the spacecraft, active actuator work and passive actuator work with

respect to gravity field and ground parameters. The gravity goes from a maximum value of 0.01 $\frac{m}{s^2}$ to a minimum of 1e-05 $\frac{m}{s^2}$, with a discretization step of 1e-04 $\frac{m}{s^2}$, while about ground parameters, they are unvaried with respect to the previous sensitivity analysis, in terms of tried values and ground model adopted. It's chosen to study the system behaviour with respect to environment parameters in this way because they are unpredictable and unknown during the design process. Families of three-dimensions plots differentiate one from the other by spacecraft mass and arrival velocity. The considered mass variation passes from a maximum increment of 10 kg (more than 10% of payload and structure containing it, with all what is needed to allow it to work) with respect to the nominal condition, to a maximum decrement of 4 kg (about 4% of payload and structure mass), with a discretization of 1 kg. Actuators and feet masses are kept constant, both in active-passive and only passive cases, and just payload-structure mass is changed. The meaning of analyze a mass variation is due to the fact that a different quantity of propellant could be consumed depending on manoeuvres performed. For arrival velocity, since in the previous sensitivity analysis a range with maximum of 4 $\frac{m}{s}$, minimum of 0.2 $\frac{m}{s}$ and a discretization of 0.2 $\frac{m}{s}$ was adopted, first three-dimensions plots family has maximum arrival velocity (4 $\frac{m}{s}$) and maximum mass (132 kg), second nominal arrival velocity (2 $\frac{m}{s}$) and nominal mass (122 kg), third minimum arrival velocity (0.2 $\frac{m}{s}$) and minimum mass (118 kg) and the last nominal arrival velocity and mass, but with the active system calibrated for 2.5 $\frac{m}{s}$. The mentioned cases are the most significant, being maximum, nominal and minimum kinetic energy to dissipate, with the last that aims to verify what happens landing at 2 $\frac{m}{s}$ but with the active system optimized for 2.5 $\frac{m}{s}$. The sense of this operation lies in the fact that when the detachment from the orbiter occurs, the control system sets up the parameters of active actuator for the actual velocity, but if there is an error and the landing velocity would be greater, it may be dangerous because the system is set up for a lower energy content. Observing and studying what happens in this case makes the landing system much more robust. Regarding the second group of four families, they are all two-dimensions plots, even if there are two sub-groups. First sub-group studies the behaviour of the usual quantity that characterized the landing system, bouncing

velocity, force transmitted to the spacecraft and so acceleration it is submitted to, and work of actuators, varying, according to ranges explained before, arrival velocity for one family and spacecraft mass for the other family, and keeping all other parameters constant (ground parameters, gravity and mass for one case and ground parameters, gravity and velocity for the other case). Second sub-group makes an analysis slightly more complex, where the aim is the same of the previous three-dimensions fourth family: studying the behaviour of the landing system with the active part set up for a precise value of arrival velocity and now also of mass, but the multibody simulations are performed with different values near the set ones. So, the first family of this sub-group keeps all parameters constant except velocity, that is set up for five values: 4 $\frac{m}{s}$, 3.5 $\frac{m}{s}$, 3 $\frac{m}{s}$, 2.5 $\frac{m}{s}$, 2 $\frac{m}{s}$, 1.5 $\frac{m}{s}$, 1 $\frac{m}{s}$. Once the active system is adjusted for the presented velocities, the multibody simulations are run varying the arrival velocity, with a range of 1 $\frac{m}{s}$ of decrement and a discretization step of about 0.05 $\frac{m}{s}$ for all the mentioned cases (the lower boundary for this last one is 0.2 $\frac{m}{s}$ as for the first sensitivity analysis). The idea is trying to cover all the prefixed arrival velocity range with an important variation respect to the active system calibrating velocity. The second family of the sub-group has the same idea of the velocity family but the changing parameter is the mass. Again, all is kept nominal, except mass, and three cases are considered: 106 kg, 101 kg, 96 kg, which are mass values the active coefficients are optimized to. The range for the first goes from 106 to 101 kg, for the second from 101 to 96 kg and for the third from 96 to 92 kg. The maximum and minimum value are the prefixed values of before. One more time, the goal is to analyze system behaviour through multibody simulations calibrated with certain mass values but run with others near the calibrating ones. The last built graph is simply a comparison between the force with respect to stroke of actuator of just passive case and forces respect their own strokes of actuators of active-passive case, where the meaning is to highlight that the force generated by the passive actuator is much more higher than the force produced by the active damper which is the force directly transmitted to the payload mass. An important point to underline again is that all these graphs are built for the landing system with just one leg made of a passive actuator, with just one leg made of an active-passive actuator with the control law proportional to sliding velocity of both actuators, with just one leg made of

an active-passive actuator with the control law proportional to active actuator sliding velocity and passive actuator scrolling, and then with the same combination in terms of active, passive and laws, but three legs instead that one. This process is needed to definitively choose the best control law, to highlight the higher robustness of active-passive system with respect to only passive one, to verify the capability of landing with just one leg (since the design is done from the beginning with only one leg in terms of braking force but three legs in terms of masses considered) and to observe the system performances improvement landing with three legs.

5.2 Delay and Noise Robustness Analysis – Results

5.2.1 Linear Complementary Passive Delta V with Passive Active Delta V Force Law

Delay Robustness

In the following figures, the trend of velocity and force w.r.t the sensor delay are given. They are plotted both w.r.t the time delay [s] and the sampling frequency [Hz].

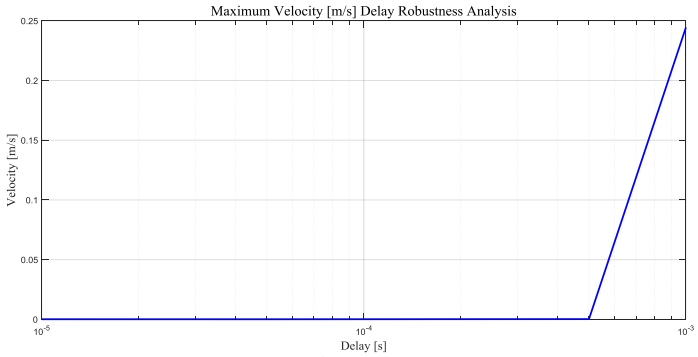

Figure 162

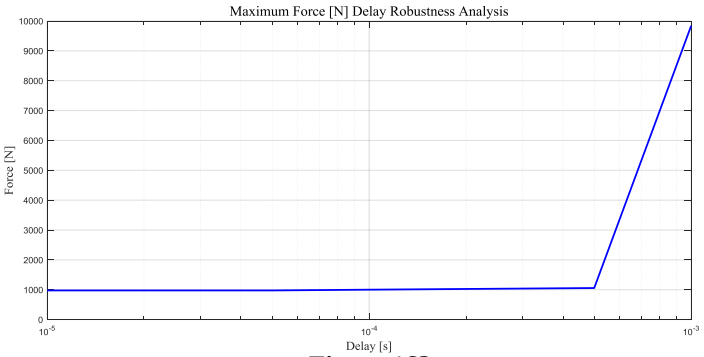

Figure 163

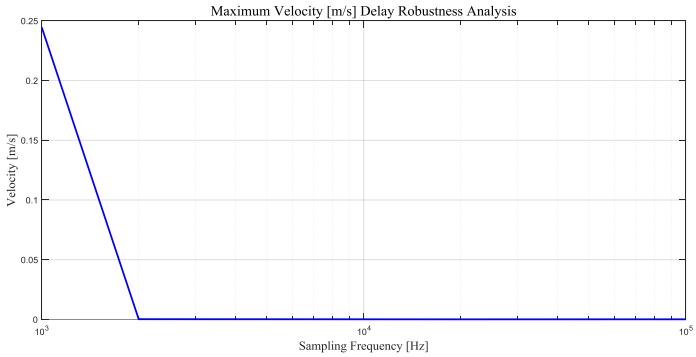

Figure 164

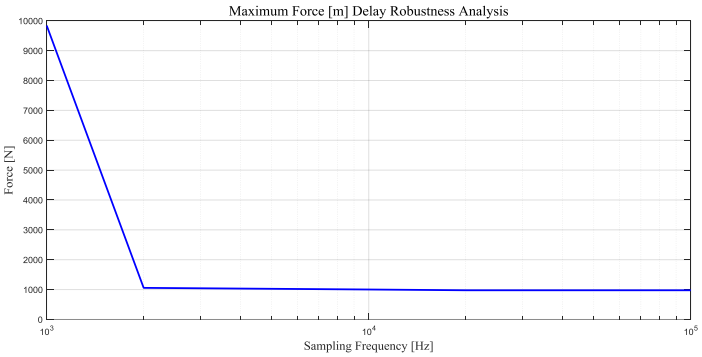

Figure 165

Noise Robustness

Velocity and force trends are plotted both w.r.t the noise variance and the equivalent noise density.

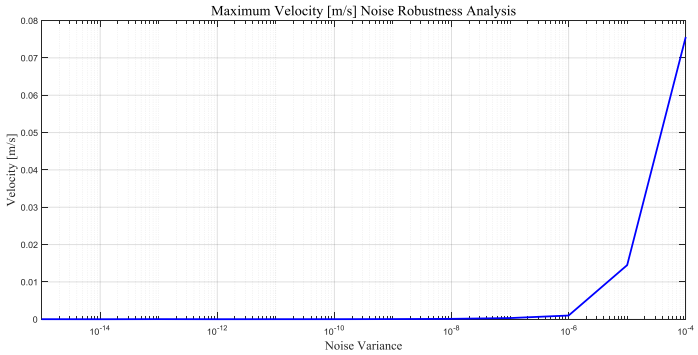

Figure 166

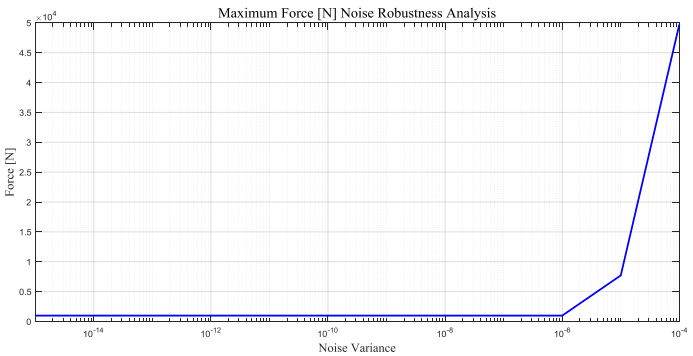

Figure 167

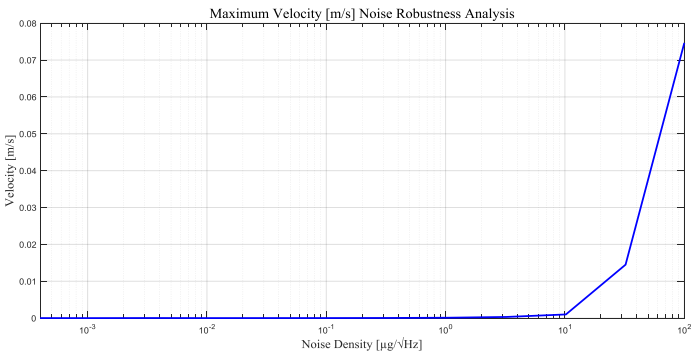

Figure 168

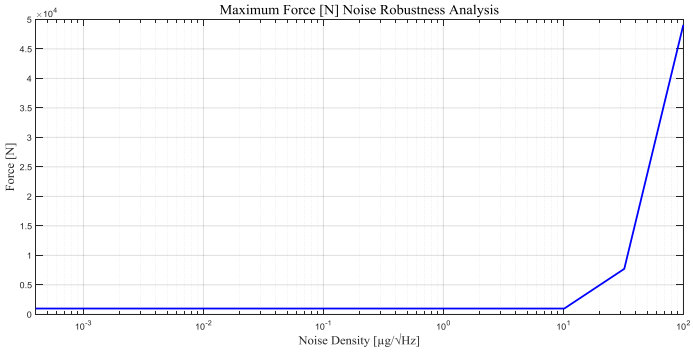

Figure 169

Noise Robustness with fixed Delay

In this case, the value of the delay was fixed to the highest acceptable value for this law and the velocity and force trends were plotted again w.r.t the noise variance and the noise density.

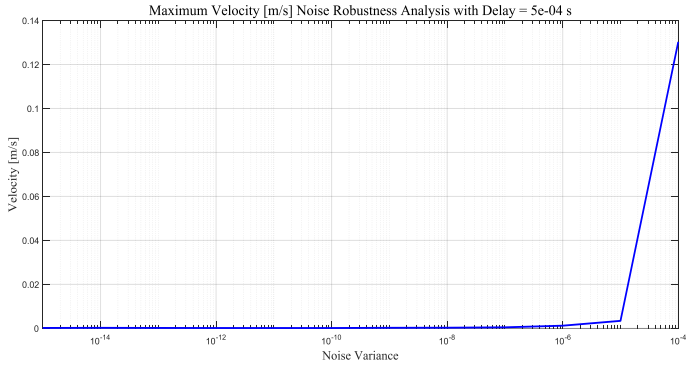

Figure 170

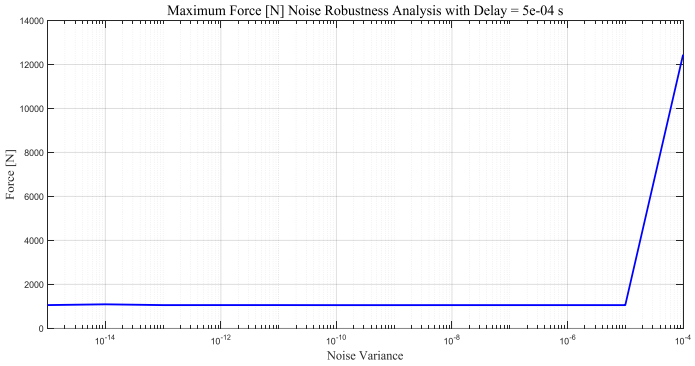

Figure 171

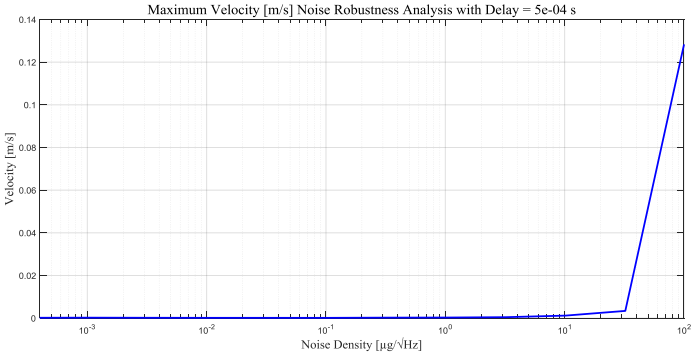

Figure 172

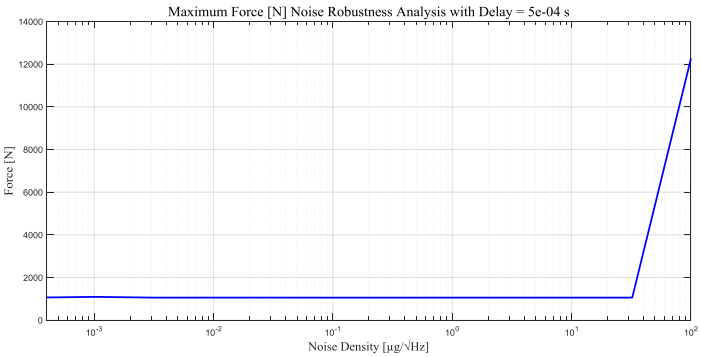

Figure 173

5.2.2 Linear Passive Positions Difference with Bell Active Delta V Force Law

Delay Robustness

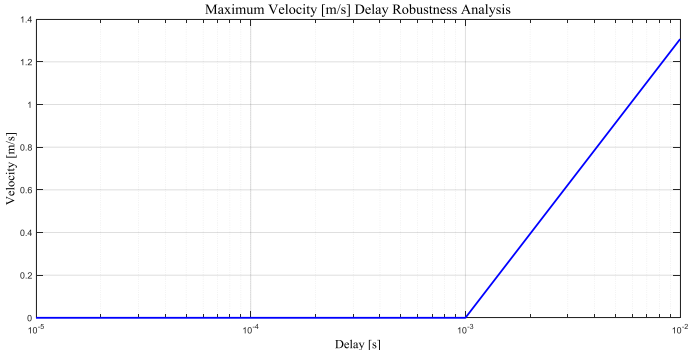

Figure 174

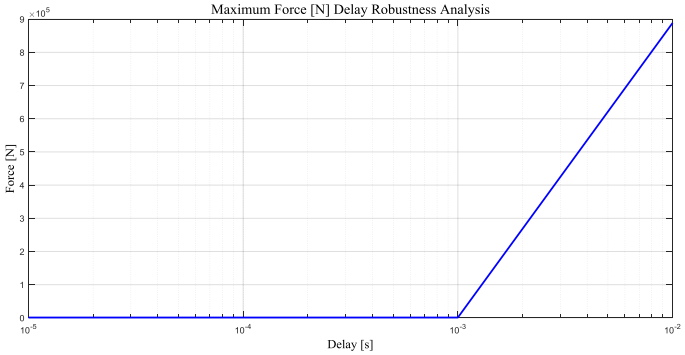

Figure 175

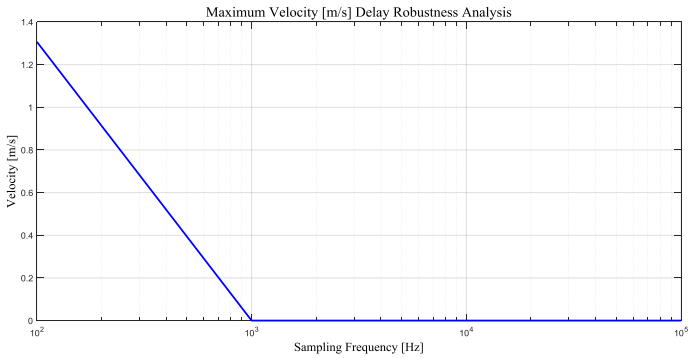

Figure 176

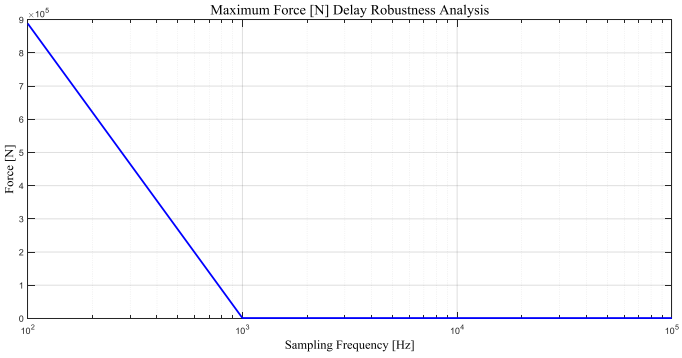

Figure 177

With this law the maximum acceptable delay reaches 1e-03 s which corresponds to 1 kHz of sampling frequency while in the previous law was 0.5e-04 s.

Noise Robustness

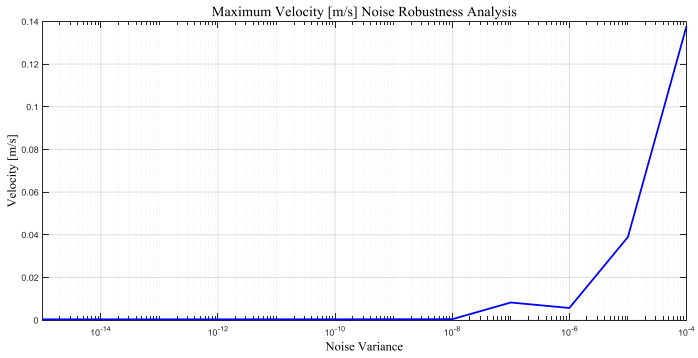

Figure 178

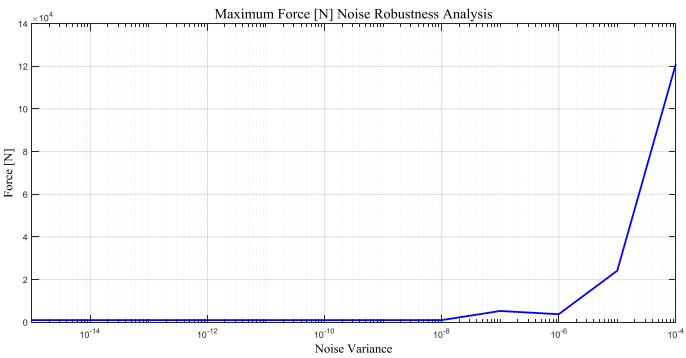

Figure 179

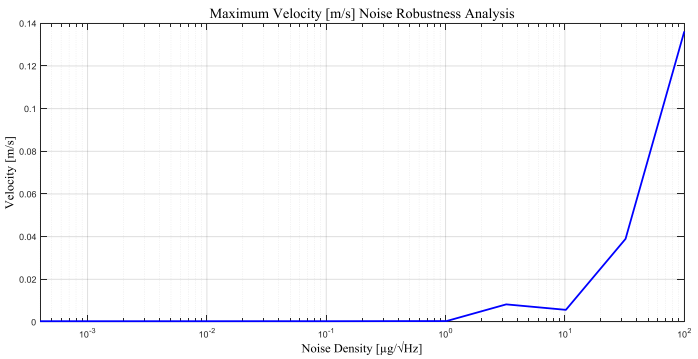

Figure 180

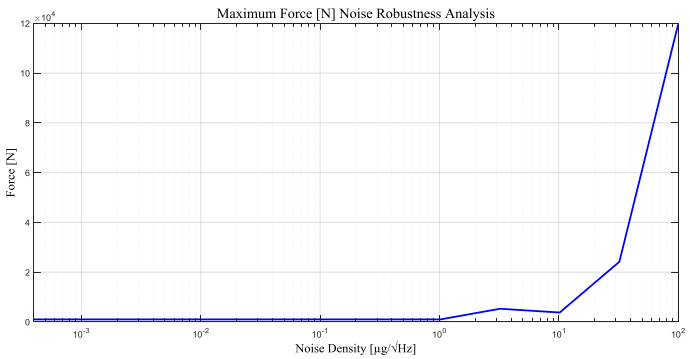

Figure 181

Noise Robustness with Fixed Delay

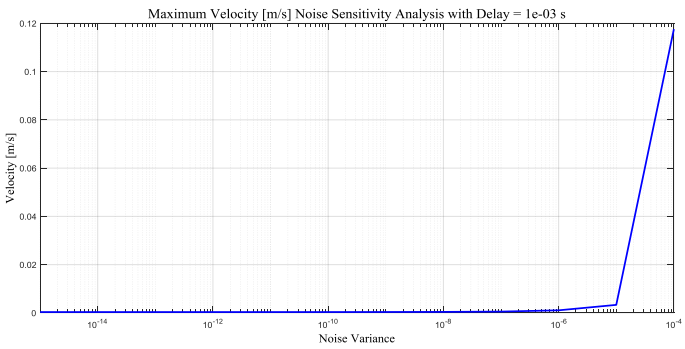

Figure 182

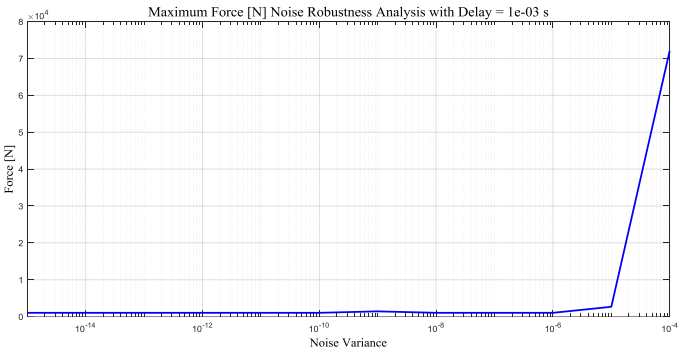

Figure 183

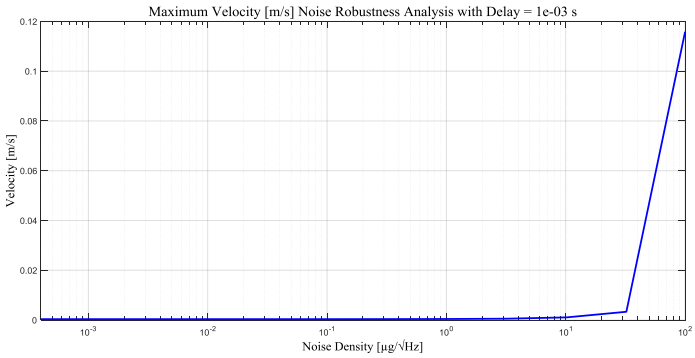

Figure 184

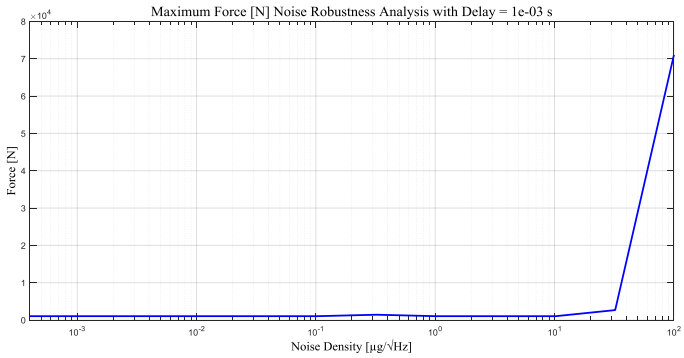

Figure 185

The limit value of the noise variance is around 1e-06 for both the considered laws.

5.3 Gravity and Ground Properties Robustness Analysis – 1 Leg – Results

Hereafter, the robustness analysis results only for the bell law which multiplies the passive position difference are given. Indeed, this law has the best behaviour in terms of delay-robustness. The same robustness analysis' were performed for the only-passive case in order to have a comparison term for the presented active laws.

5.3.1 Linear Passive Position Difference with Bell Active Delta V

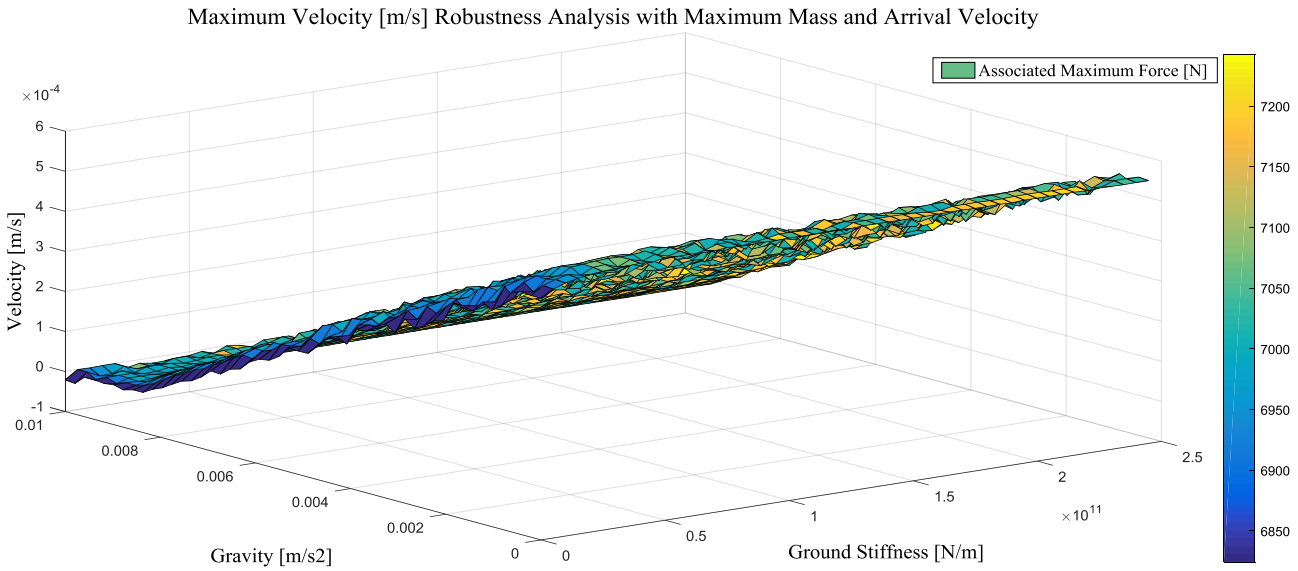

Figure 186

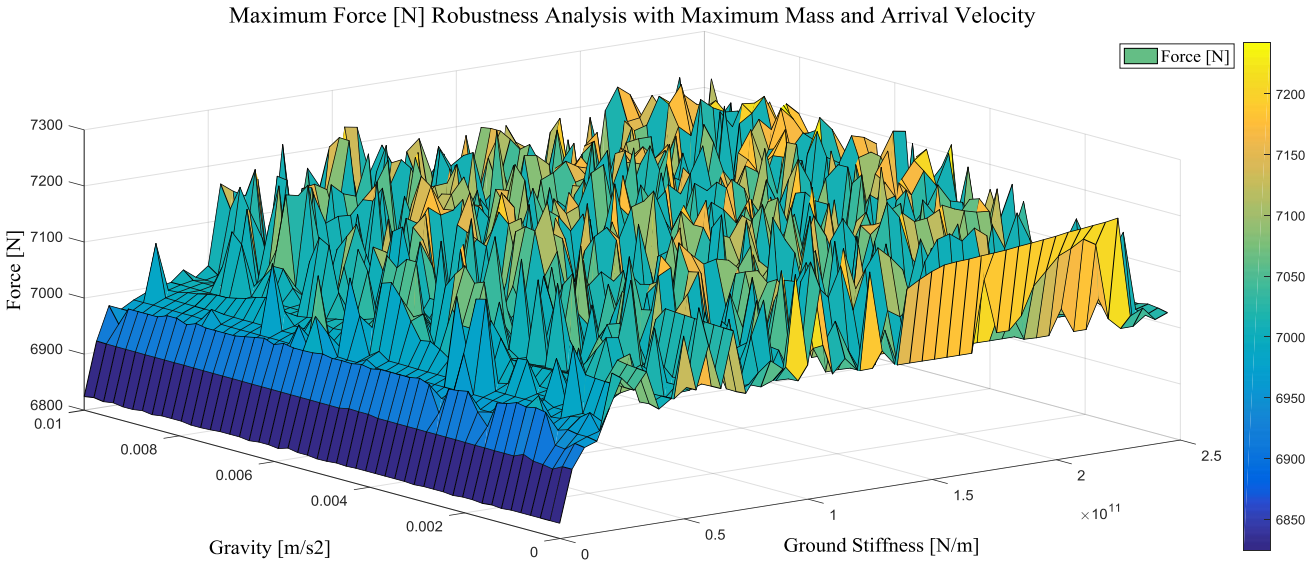

Figure 187

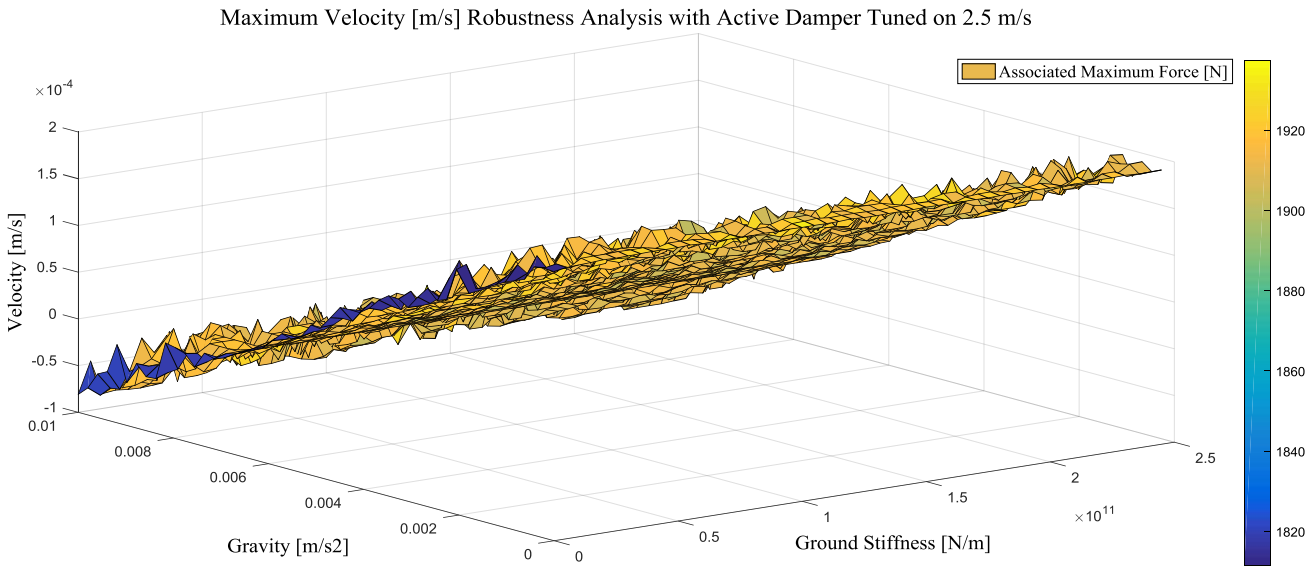

Figure 188

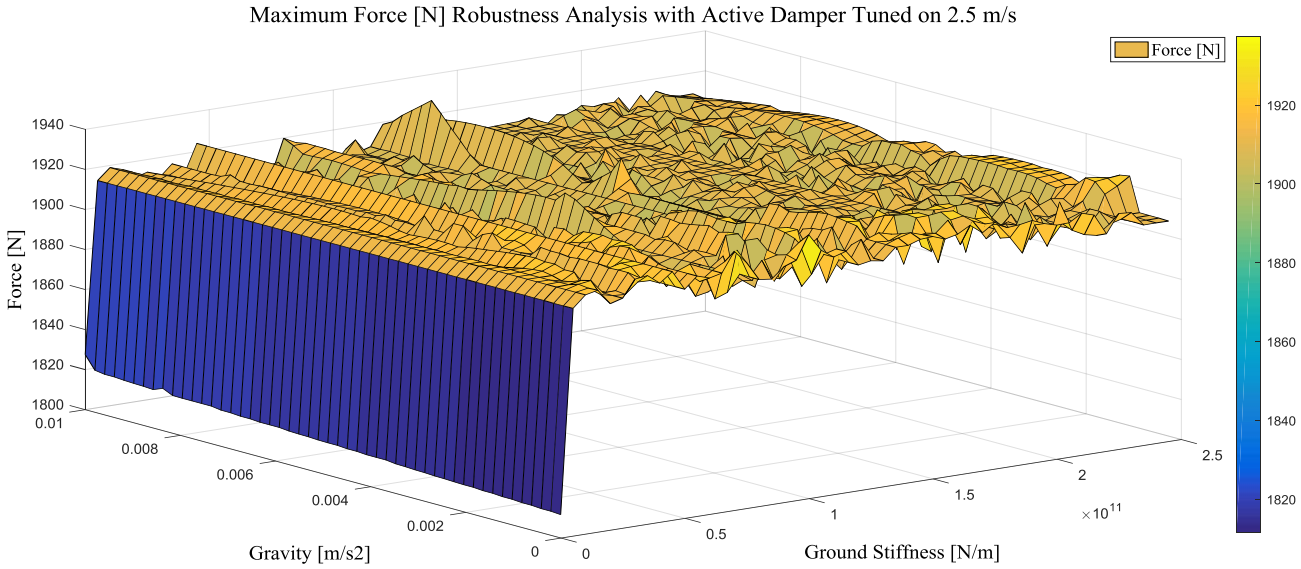

Figure 189

5.3.2 Granular Passive Case

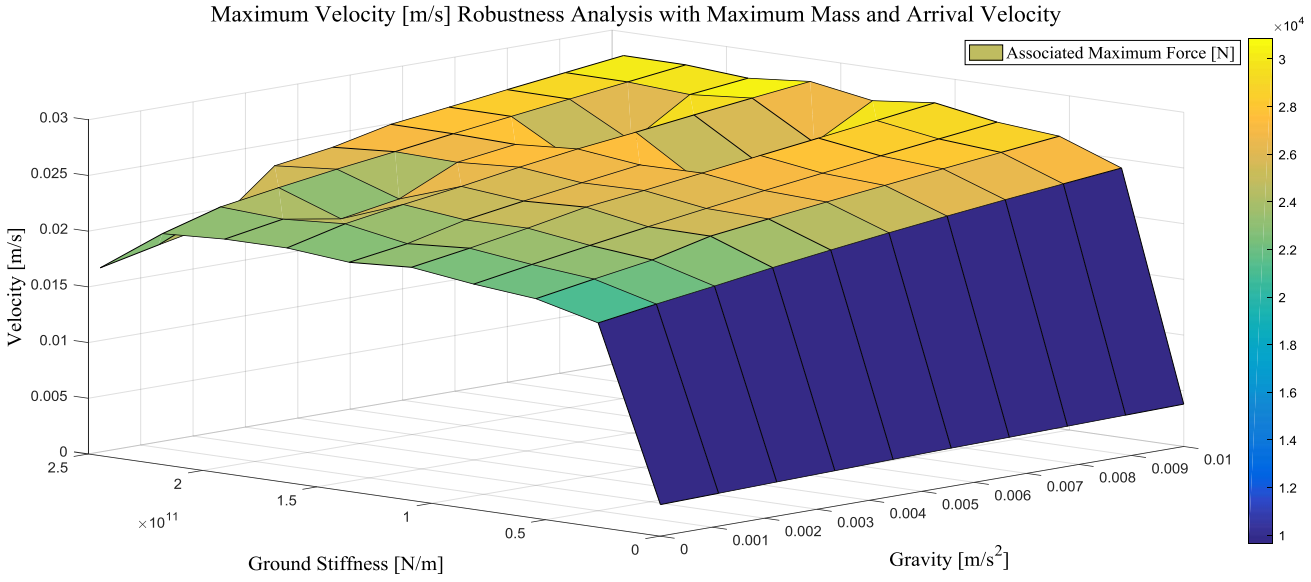

Figure 190

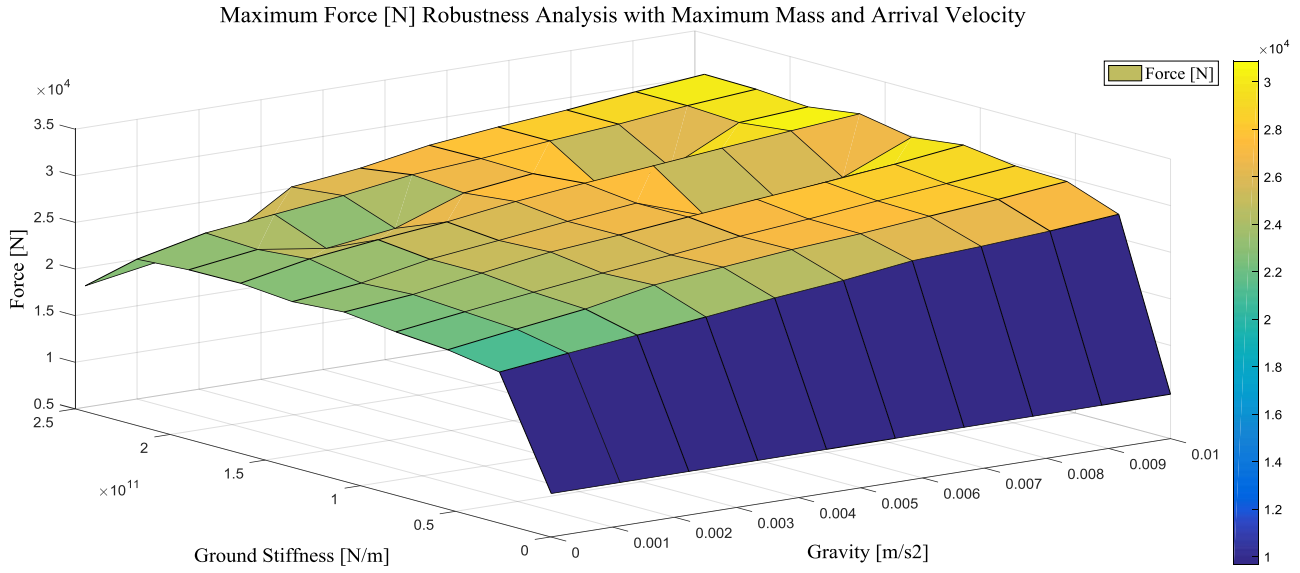

Figure 191

These results show that if the passive system is used alone, it is not able to guarantee the good performances in terms of velocity and force observed for the combined active and passive system when the gravity and the ground properties are varied.

5.3.3 Tables Gravity, Ground Properties, Arrival Velocity and Mass Robustness Analysis

In the following part, a table with the maximum force values obtained from the robustness analysis are presented. These values are used to check the structural resistance of the sized dampers. To each force a couple of gravity and ground properties (stiffness and damping) is associated. This table is reproduced for both the considered "bell" laws and for the system where only the passive damper with 0.25 m of stroke is employed.

Force Law Linear with Passive Positions Difference and Active V dependent Bell Coefficient					
		Force [N]	**Gravity [m/s2]**	**Ground Stiffness [N/m]**	**Ground Damping**
Maximum Velocity and Mass	**Maximum Active Force**	7,24E+03	7,757E-03	2,15E+11	3,25E+07
	Maximum Passive Force	5,99E+03	1,000E-02	1,85E+11	3,01E+07
	Maximum Ground Force	1,40E+08	5,107E-03	2,45E+11	3,48E+07
Nominal Case	**Maximum Active Force**	1,12E+03	4,495E-03	2,05E+11	3,17E+07
	Maximum Passive Force	1,39E+03	1,000E-02	1,90E+11	3,05E+07
	Maximum Ground Force	7,04E+07	4,903E-03	2,45E+11	3,48E+07

Minimum Velocity and Mass	**Maximum Active Force**	4,46E+01	9,184E-03	8,50E+10	1,64E+07
	Maximum Passive Force	5,24E+01	1,000E-02	2,45E+11	3,48E+07
	Maximum Ground Force	1,26E+07	9,796E-03	2,45E+11	3,48E+07
Nominal Case with Damper Tuned on 2.5 m/s	**Maximum Active Force**	1,94E+03	8,981E-03	1,20E+11	1,59E+07
	Maximum Passive Force	1,55E+03	1,000E-02	9,50E+10	1,36E+07
	Maximum Ground Force	7,04E+07	4,903E-03	2,45E+11	3,48E+07

Table 57

Force Law Linear with Compl Passive V and Active V dependent Bell Coefficient					
		Force [N]	**Gravity [m/s2]**	**Ground Stiffness [N/m]**	**Ground Damping**
Maximum Velocity and Mass	**Maximum Active Force**	5,08E+03	9,59E-03	1,80E+11	2,97E+07
	Maximum Passive Force	5,15E+03	1,00E-02	1,50E+11	2,63E+07
	Maximum Ground Force	1,35E+08	1,00E-02	2,45E+11	3,48E+07
Nominal Case	**Maximum Active Force**	1,07E+03	6,13E-03	1,01E+07	7,04E+04
	Maximum Passive Force	1,30E+03	1,00E-02	1,50E+11	2,63E+07

	Maximum Ground Force	6,82E+07	1,00E-02	2,45E+11	3,48E+07
Minimum Velocity and Mass	**Maximum Active Force**	5,25E+01	1,00E-02	1,01E+07	7,04E+04
	Maximum Passive Force	4,63E+01	1,00E-02	1,01E+07	7,04E+04
	Maximum Ground Force	1,26E+07	1,00E-02	2,45E+11	3,48E+07
Nominal Case with Damper Tuned on 2.5 m/s	**Maximum Active Force**	1,37E+03	1,00E-05	5,00E+10	1,32E+07
	Maximum Passive Force	1,42E+03	1,00E-02	1,50E+10	3,99E+06
	Maximum Ground Force	6,82E+07	1,00E-02	2,45E+11	3,48E+07

Table 58

Passive Granular Damper Sensitivity					
		Force [N]	**Gravity [m/s2]**	**Ground Stiffness [N/m]**	**Ground Damping**
Maximum Velocity and Mass	**Maximum Force on Sat**	9,77E+03	1,00E-02	1,01E+07	7,04E+04
	Maximum Ground Force	2,81E+05	1,00E-02	1,01E+07	7,04E+04
Nominal Case	**Maximum Force on Sat**	2,13E+03	1,00E-02	1,10E+11	1,26E+07
	Maximum Ground Force	6,82E+07	1,00E-02	2,45E+11	3,48E+07
Minimum Velocity	**Maximum**	9,66E+01	9,80E-03	3,50E+10	8,19E+06

and Mass	**Force on Sat**				
	Maximum Ground Force	1,25E+07	9,80E-03	2,45E+11	3,48E+07

Table 59

5.4 Arrival Velocity and Mass Robustness Analysis – 1 Leg – Results

5.4.1 Linear Passive Position Difference with Bell Active Delta V Force Law

5.4.1.1 Arrival Velocity Robustness Analysis

The following figures are obtained from simulations where the damper was tuned on the actual arrival velocity (adaptive behaviour).

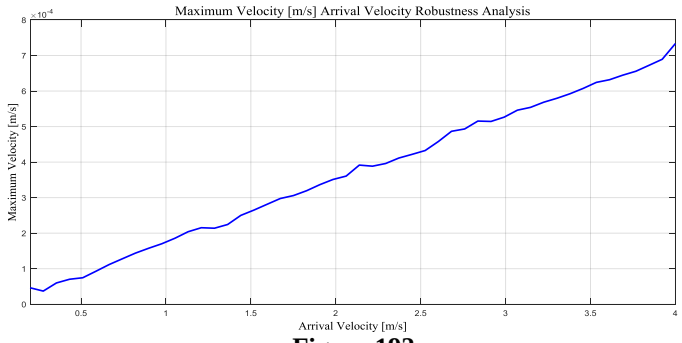

Figure 192

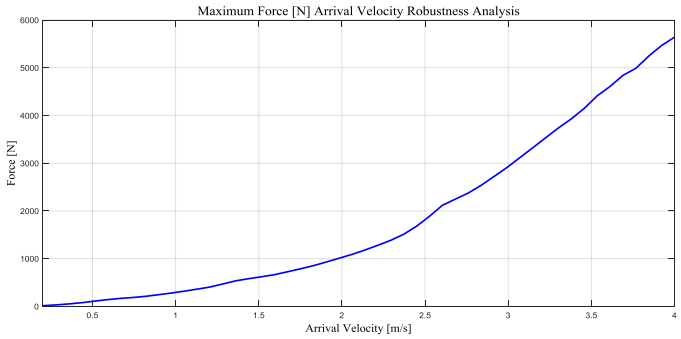

Figure 193

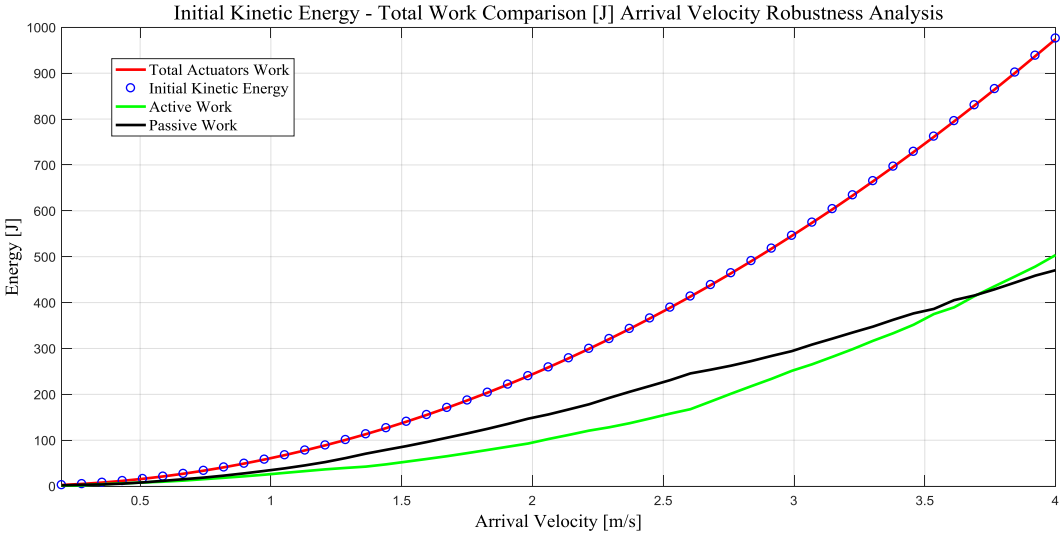

Figure 194

5.4.1.2 Arrival Velocity Robustness with fixed Coefficient

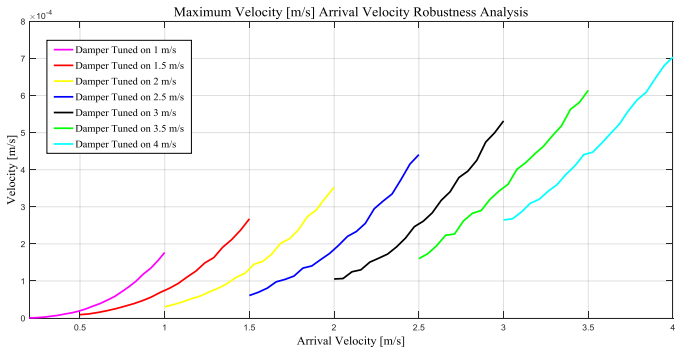

Figure 195

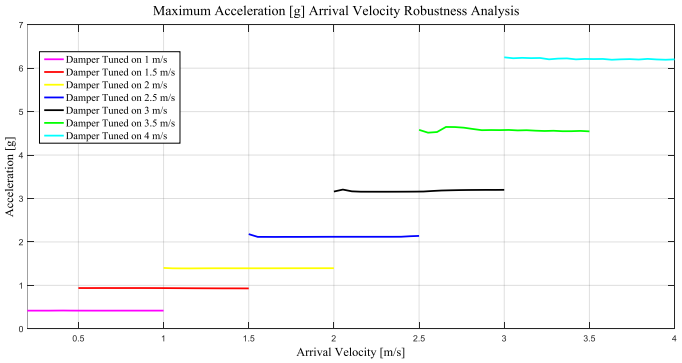

Figure 196

In order to give a more tangible idea of the phenomenon, the maximum force plot was substituted by the maximum deceleration plot.

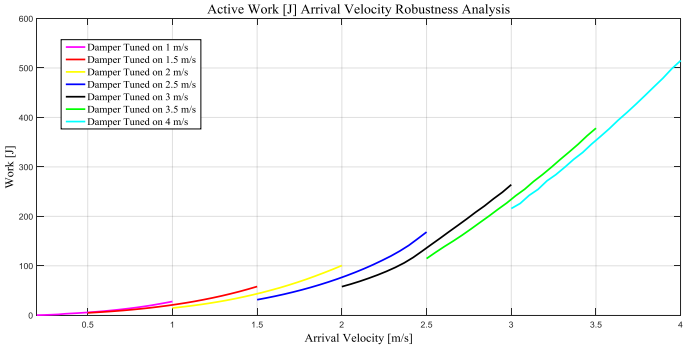

Figure 197

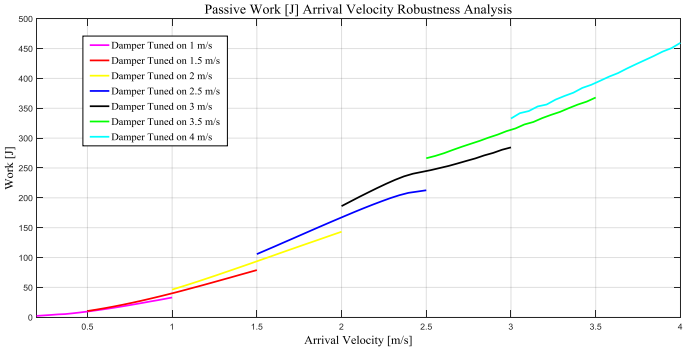

Figure 198

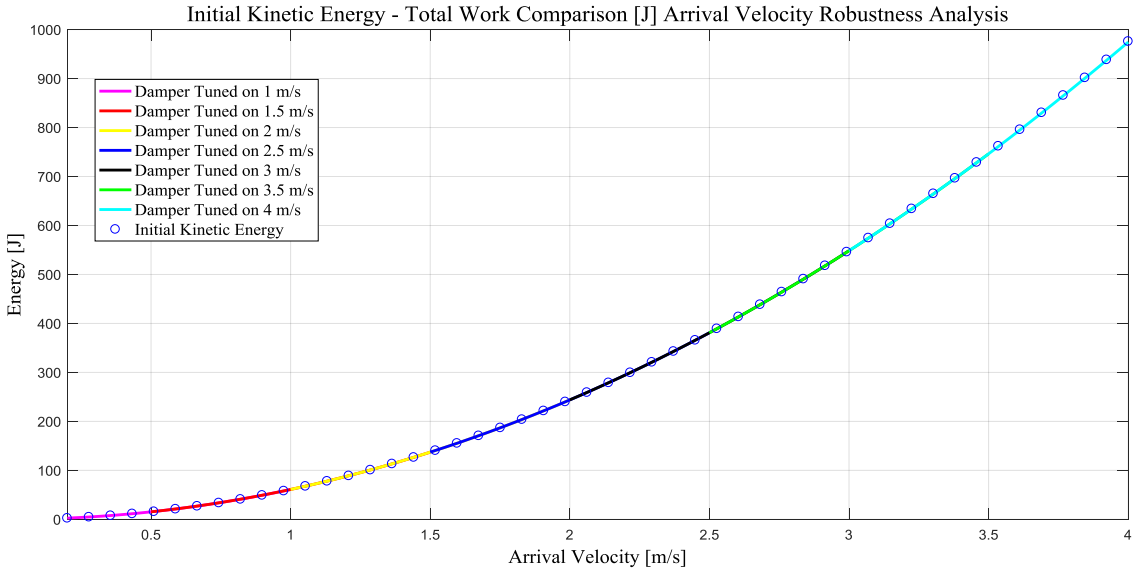

Figure 199

According to the presented results, in both the analysis' the maximum velocities and forces (and deceleration) remain acceptable and the damper is able to dissipate almost all the initial kinetic energy. From the active and passive work plots for the fixed coefficient-case, it can be observed that the active work is lower when it is not properly tuned on the actual arrival velocity and that this energy gap is somehow taken by the passive actuator.

5.4.1.3 Mass Robustness Analysis

The following figures are obtained from simulations where the damper was tuned on the actual mass of the satellite.

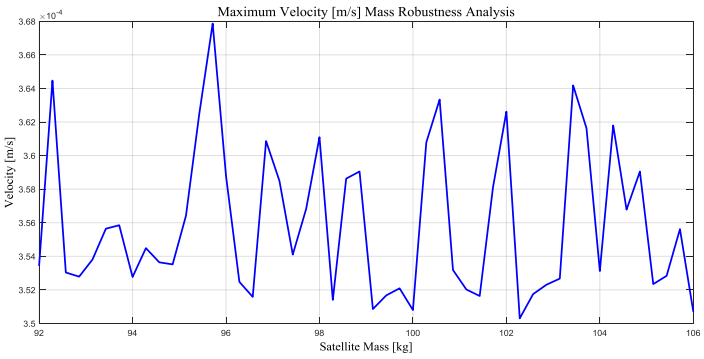

Figure 200

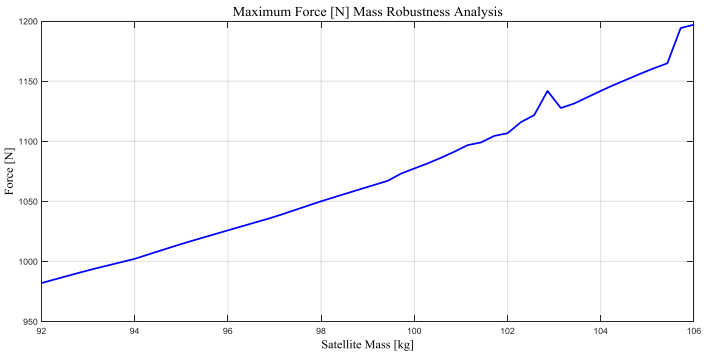

Figure 201

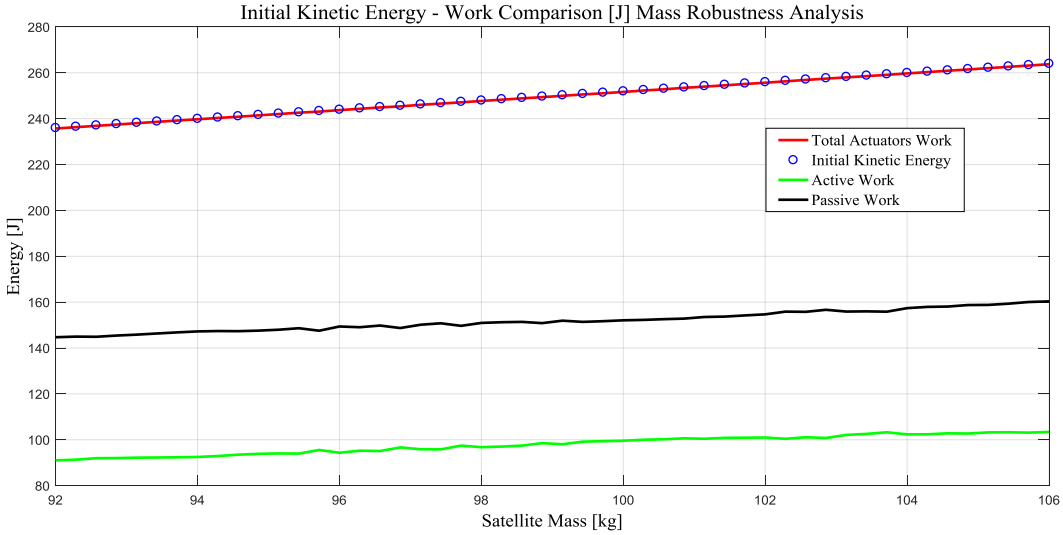

Figure 202

5.4.1.4 Mass Robustness Analysis with fixed Coefficient

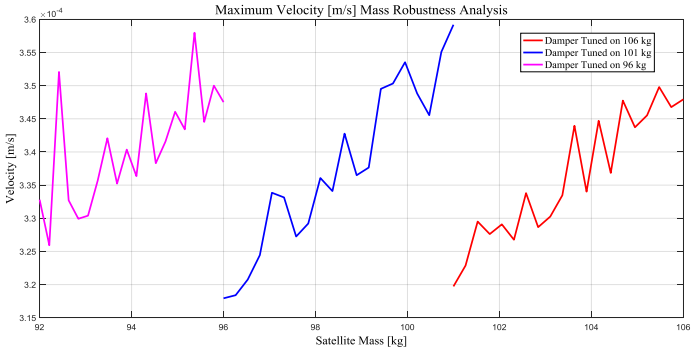

Figure 202

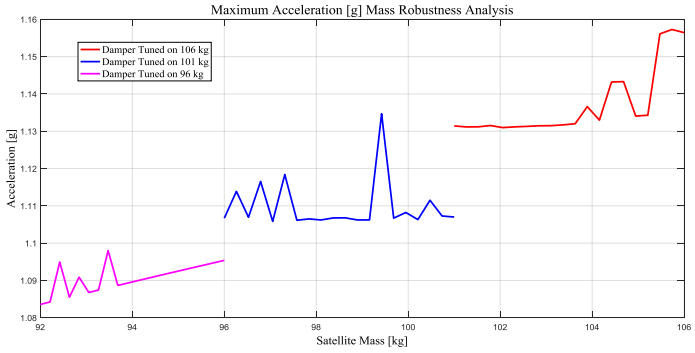

Figure 203

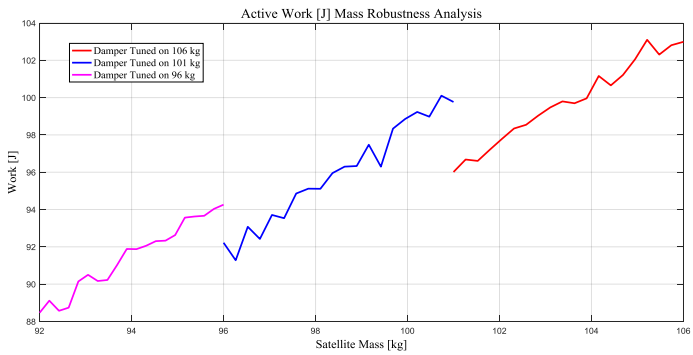

Figure 204

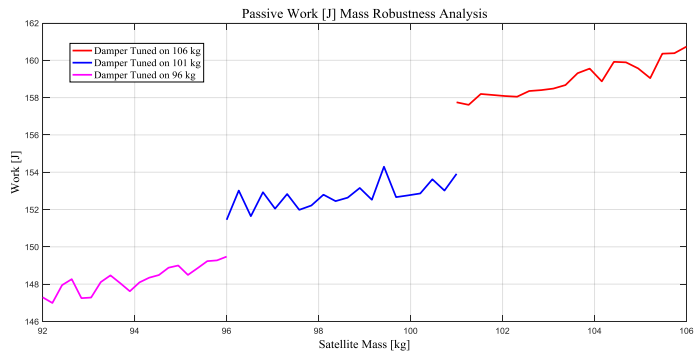

Figure 205

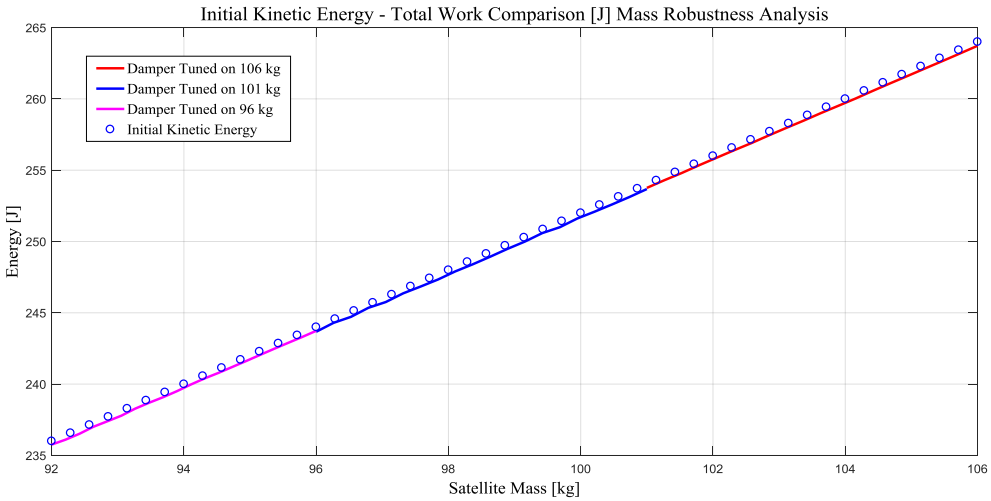

Figure 206

The same kind of analysis was performed in parallel for the bell-law with the complementary passive delta V term but only the most meaningful data are presented.

5.4.2 Linear Complementary Passive Delta V with Bell Active Delta V

5.4.2.1 Arrival Velocity Robustness Analysis

The following figures are obtained from simulations where the damper was tuned on the actual arrival velocity.

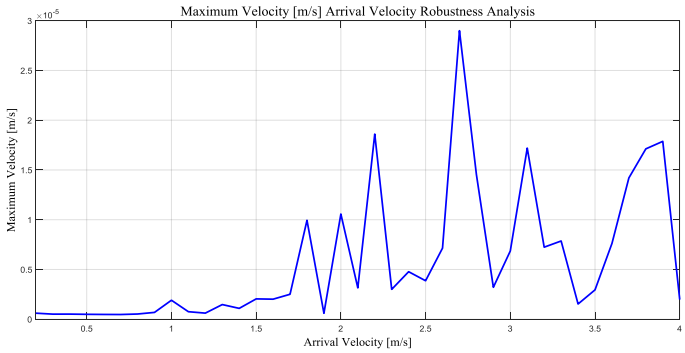

Figure 207

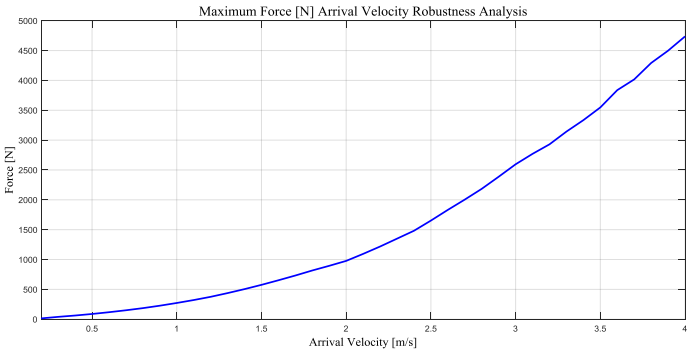

Figure 208

5.4.2.2 Arrival Velocity Robustness Analysis with fixed Coefficient

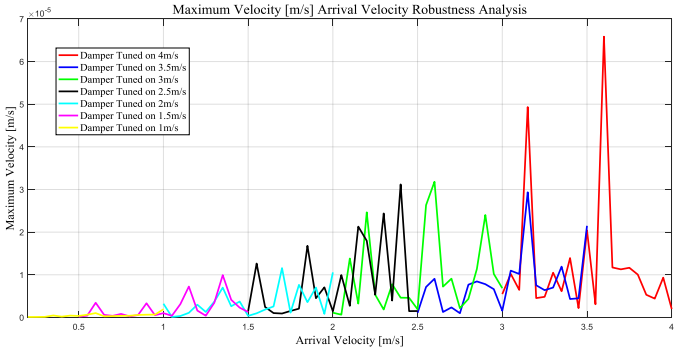

Figure 209

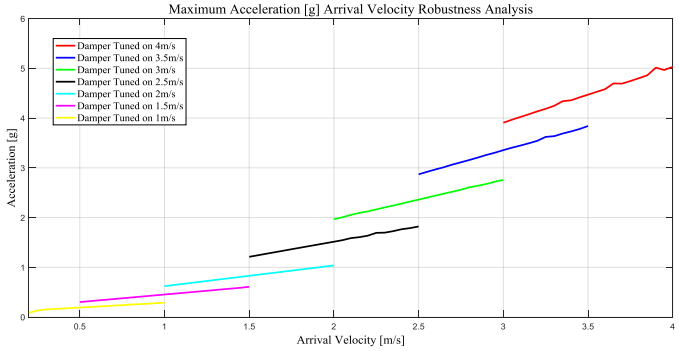

Figure 210

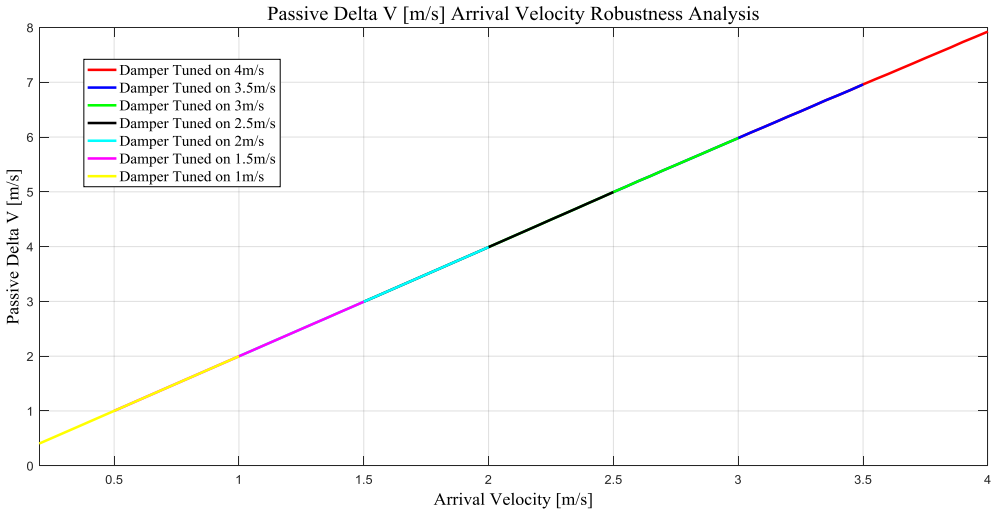

Figure 211

5.4.2.3 Mass Robustness Analysis

The following figures are obtained from simulations where the damper was tuned on the actual mass of the satellite.

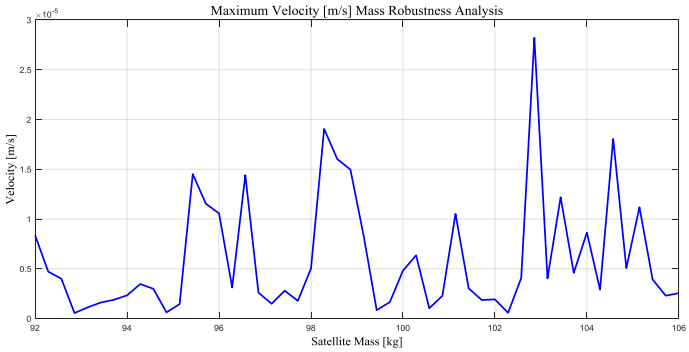

Figure 212

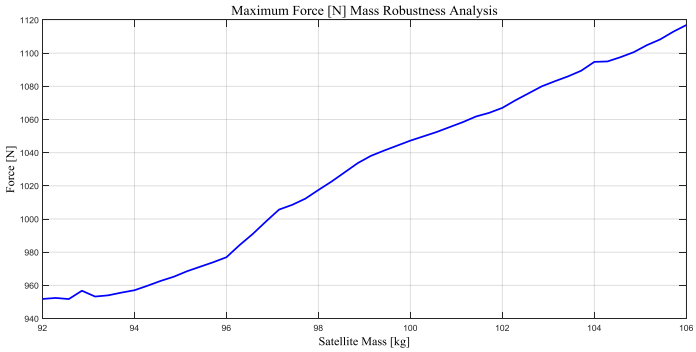

Figure 213

5.4.2.4 Mass Robustness Analysis with fixed Coefficient

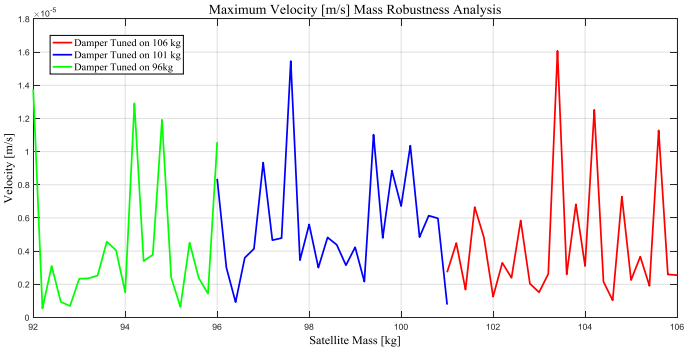

Figure 214

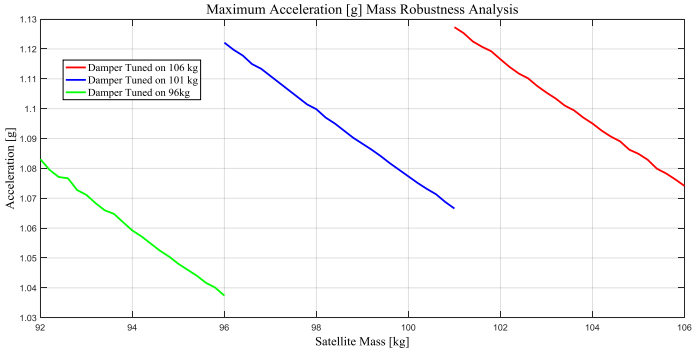

Figure 215

According to these results, the considered law, even if less robust against the sensor delay than the first bell-law, is able to generate lower forces (and accelerations) and velocities (around 1e-05 m/s) and able to dissipate almost all the initial kinetic energy for different mass and arrival velocities.

5.4.3 Granular Passive Case

5.4.3.1 Arrival Velocity Robustness Analysis

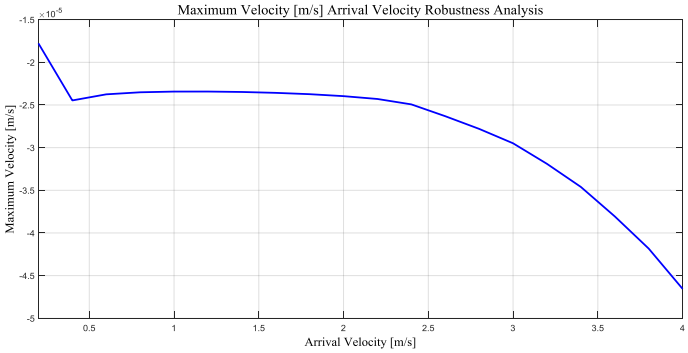

Figure 216

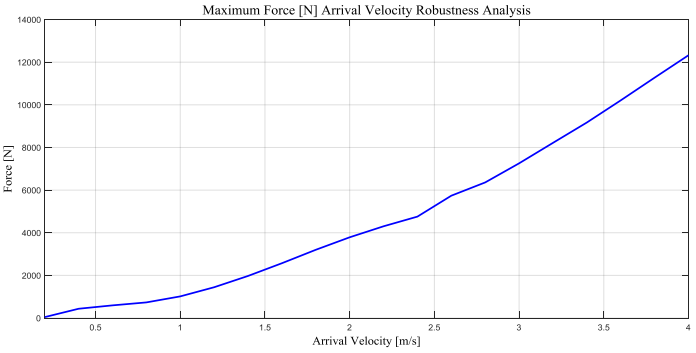

Figure 217

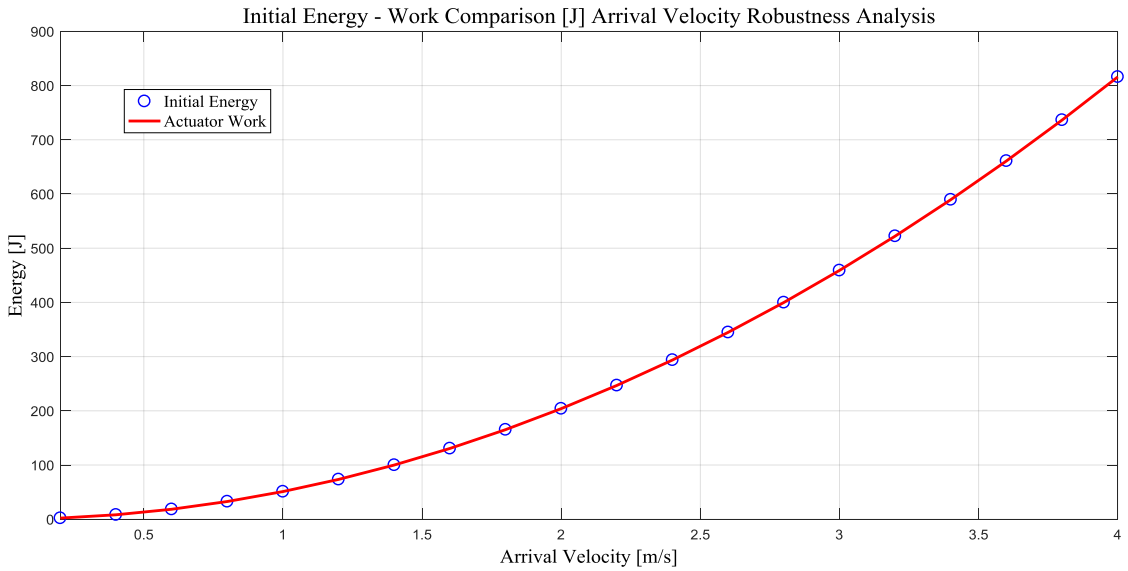

Figure 218

5.4.3.2 Mass Robustness Analysis

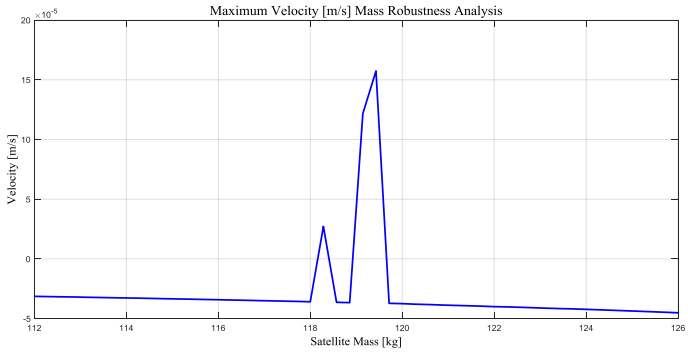

Figure 219

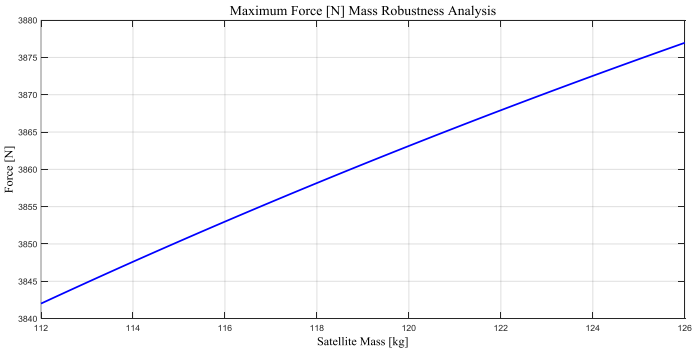

Figure 220

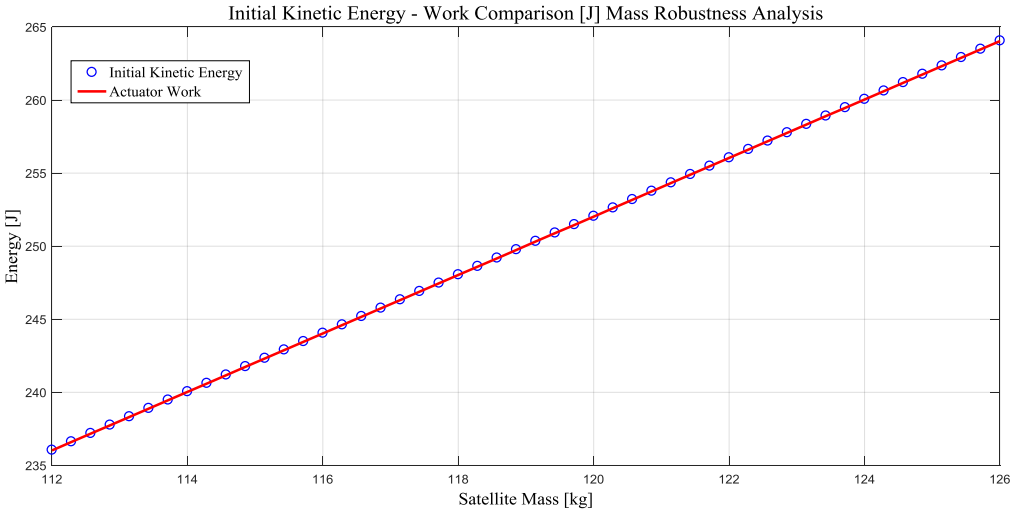

Figure 221

When the gravity and ground properties are kept fixed, the only passive system is able to ensure low velocities and it is able to dissipate almost all the initial kinetic energy. However, the generated forces especially when the arrival velocities are increased, reaches very high values which can be avoided only with the combined active-passive system.

5.5 Gravity and Ground Properties Robustness Analysis – 3 Legs – Results

The same type of robustness analysis was performed for the system with 3 Legs (3 active dampers and 3 passive dampers). In this case, the maximum active damper force plots are given, since the real objective of these simulations were to verify that the maximum force the active device must produce with multiple legs is far lower (more or less 3 times) than the force generated in the case with just 1 leg (which was the configuration that lead the sizing). The results are given only for the linear passive position difference with bell of active delta V force law, which shown the best performances in the 1-leg delay and noise robustness analysis.

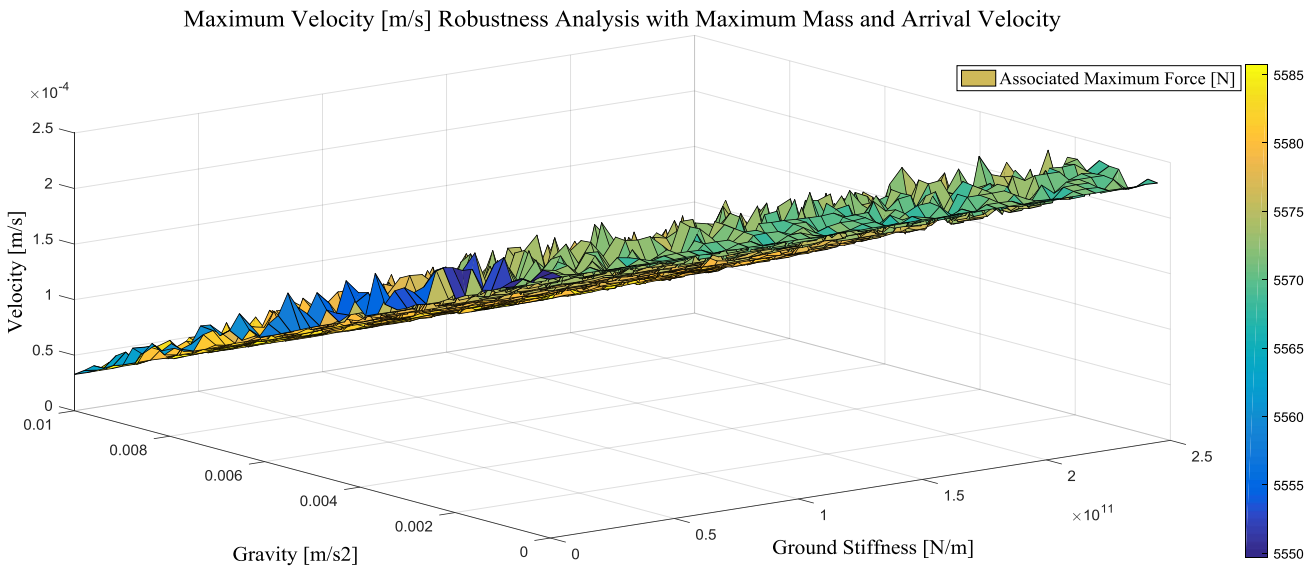

Figure 222

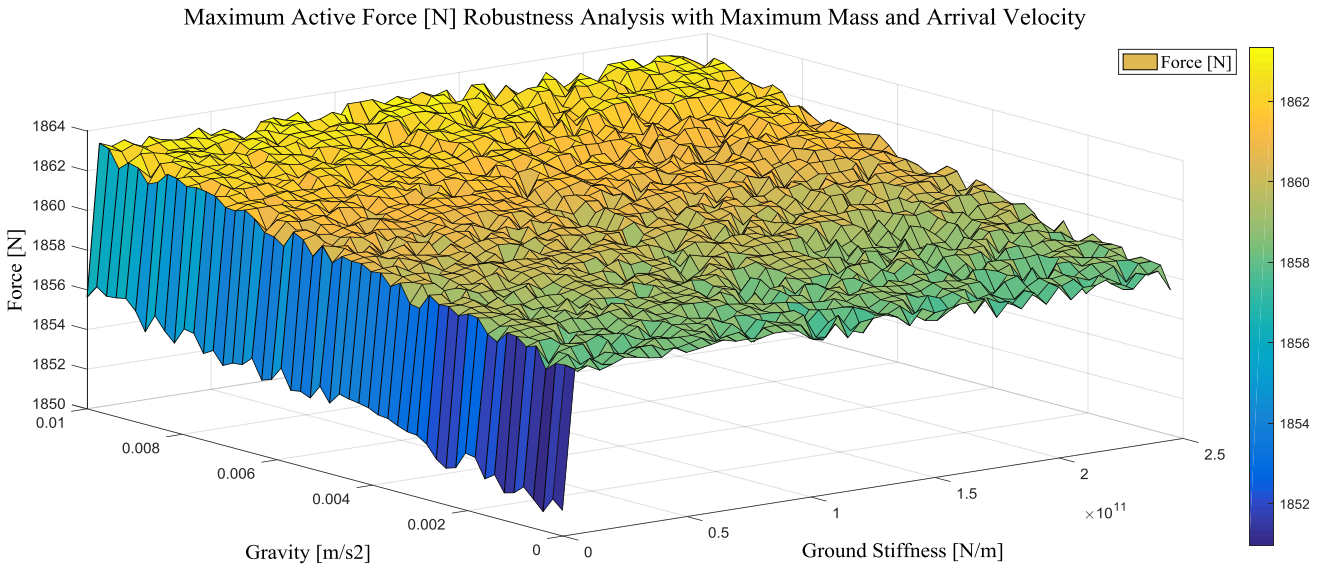

Figure 223

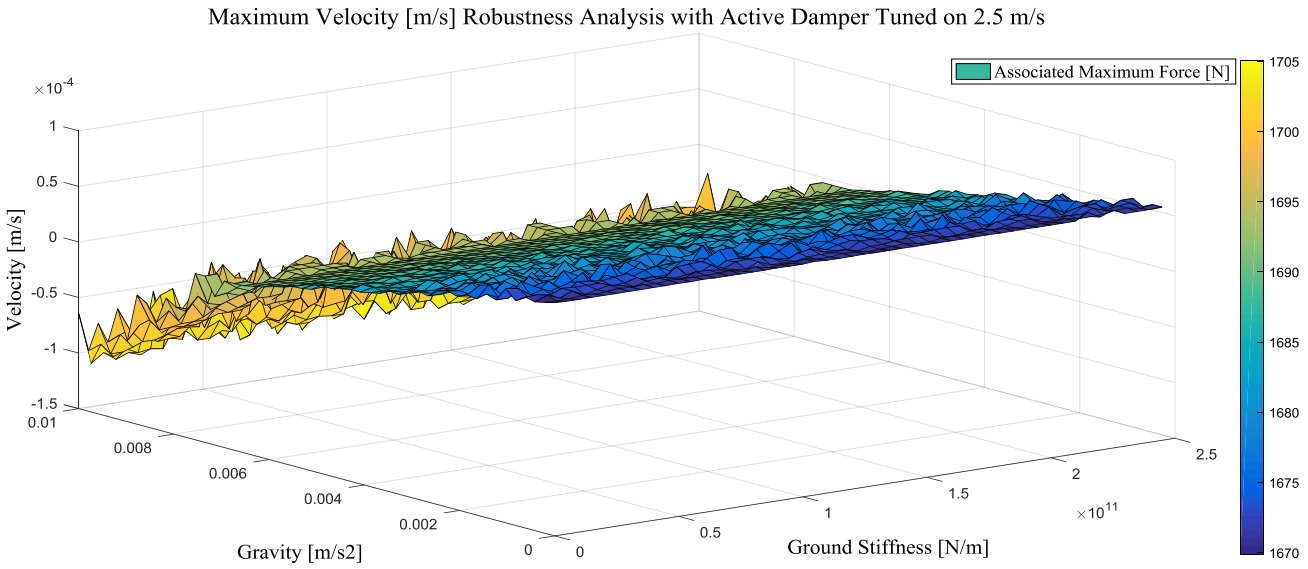

Figure 224

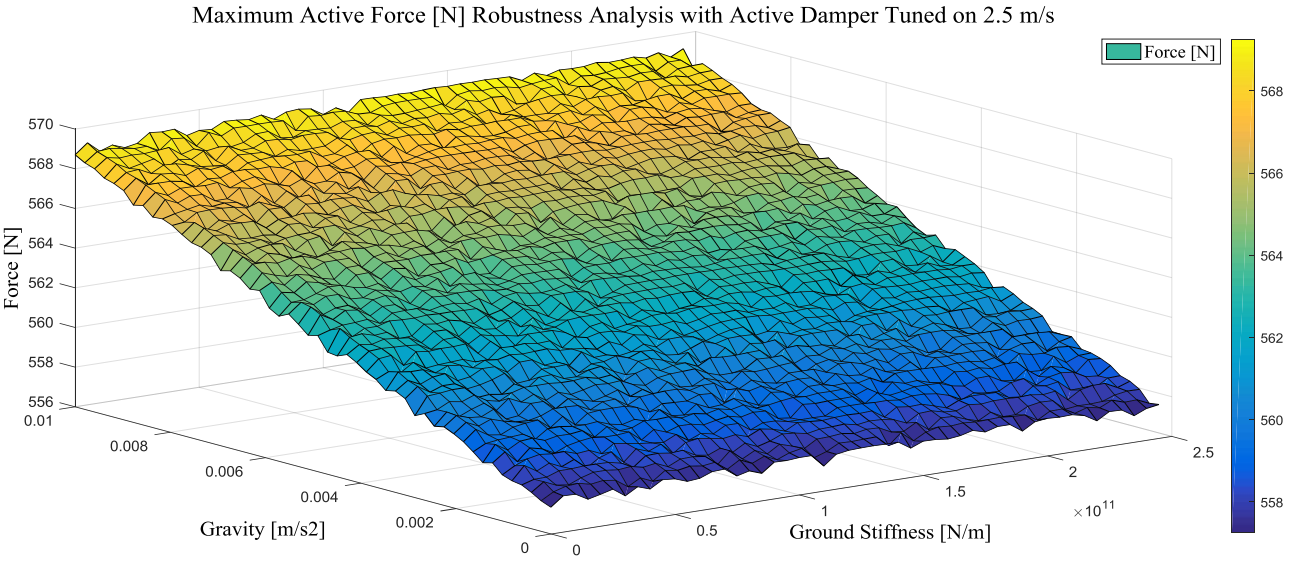

Figure 225

The maximum velocities remain acceptable also in the models with multiple legs and as it was predicted, the maximum force that the active device must generate is far lower than the single leg cases. Hereafter, a table with the maximum forces is presented. Differently from the previous ones, a row dedicated to the maximum active force is added. In the corresponding 1-Leg table, the active force was almost coincident with the maximum force on satellite (except for a small contribution given by the gravity).

		Force [N]	Gravity [m/s2]	Ground Stiffness [N/m]	Ground Damping
Maximum Velocity and Mass	**Maximum Force on Sat**	5,59E+03	1,00E-02	2,00E+10	5,04E+06
	Maximum Active Force	1,86E+03	1,00E-02	1,15E+11	1,43E+07
	Maximum Passive Force	2,95E+03	1,00E-02	6,00E+10	1,03E+07
	Maximum Ground Force	1,40E+08	5,11E-03	2,45E+11	3,48E+07
Nominal Case	**Maximum Force on Sat**	1,16E+03	9,80E-03	1,01E+07	7,04E+04
	Maximum Active Force	3,89E+02	1,00E-02	1,01E+07	7,04E+04
	Maximum Passive Force	6,60E+02	1,00E-02	1,50E+10	3,99E+06
	Maximum Ground Force	7,04E+07	4,90E-03	2,45E+11	3,48E+07
Minimum Velocity and Mass	**Maximum Force on Sat**	4,53E+01	9,59E-03	1,01E+07	7,04E+04
	Maximum Active Force	1,54E+01	1,00E-02	2,05E+11	3,17E+07
	Maximum Passive Force	3,20E+01	1,00E-02	1,05E+11	1,12E+07

	Maximum Ground Force	1,26E+07	1,00E-02	2,45E+11	3,48E+07
Nominal Case with Damper Tuned on 2.5 m/s	**Maximum Force on Sat**	1,71E+03	1,00E-02	5,00E+10	1,32E+07
	Maximum Active Force	5,69E+02	1,00E-02	1,45E+11	2,45E+07
	Maximum Passive Force	7,51E+02	1,00E-02	2,10E+11	3,21E+07
	Maximum Ground Force	7,04E+07	4,90E-03	2,45E+11	3,48E+07

Table 60

Also from this table, it can be noticed that the maximum force the satellite experiences can be reduced increasing the number of legs (maximum force of 7,24E+03 with one leg, maximum force of 5,59E+03 with three legs), and this is probably due to presence of more dissipative elements which work simultaneously.

5.6 Arrival Velocity and Mass Robustness Analysis – 3 Legs – Results

5.6.1 Arrival Velocity Robustness Analysis

The following figures are obtained from simulations where the damper was tuned on the actual arrival velocity.

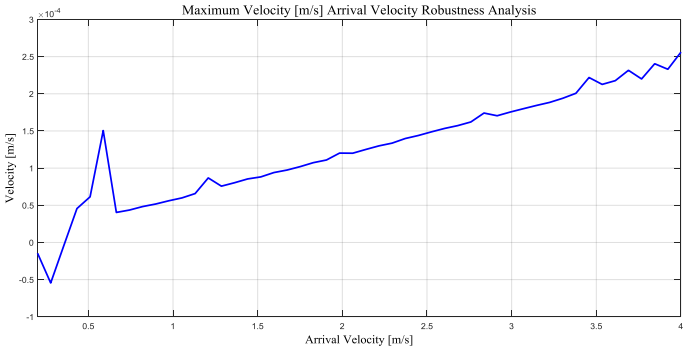

Figure 226

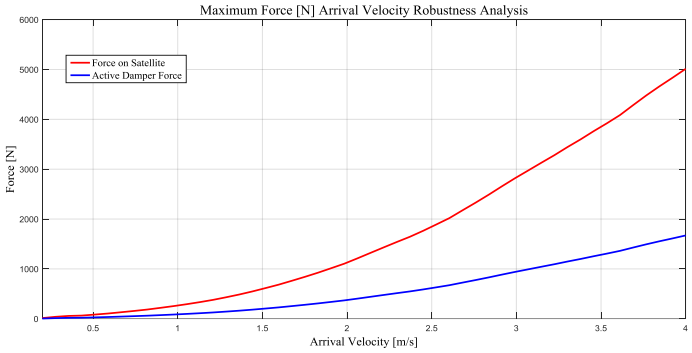

Figure 227

It is noticeable that the maximum force acting on the satellite is slight lower than the values observed in the 1 leg cases and coherently with the low values of the maximum velocities, the initial kinetic energy is almost completely dissipated as can be seen below.

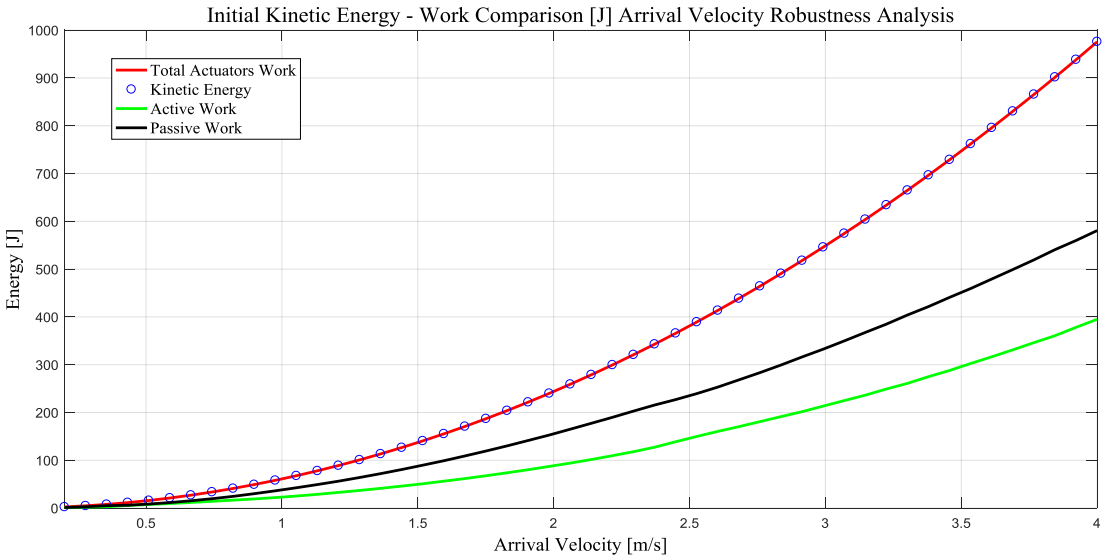

Figure 228

5.6.2 Arrival Velocity Robustness with fixed Coefficient

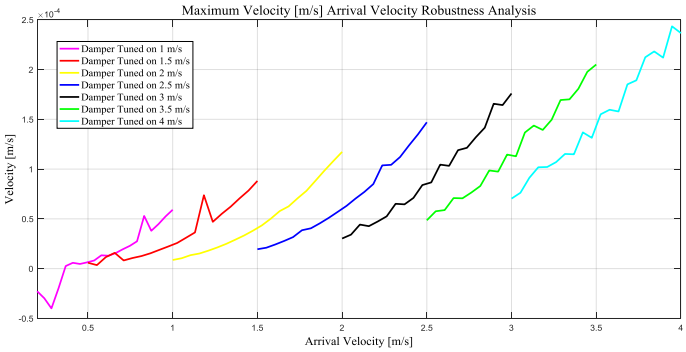

Figure 229

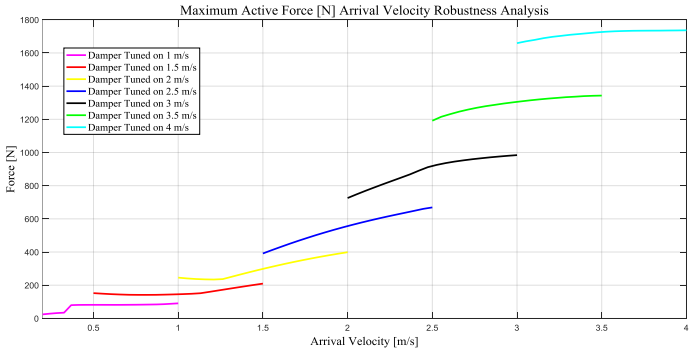

Figure 230

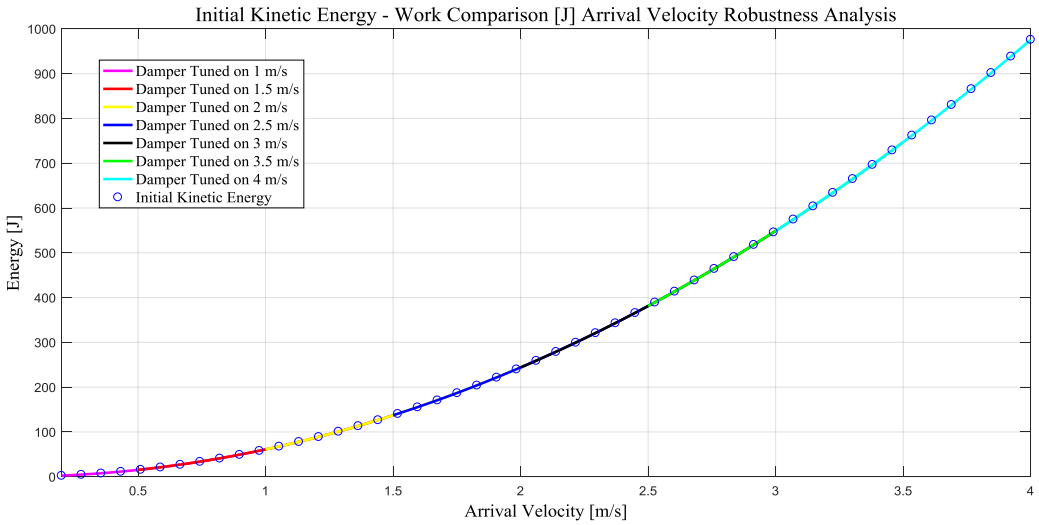

Figure 231

5.6.3 Mass Robustness Analysis

The following figures are obtained from simulations where the damper was tuned on the actual mass of the satellite.

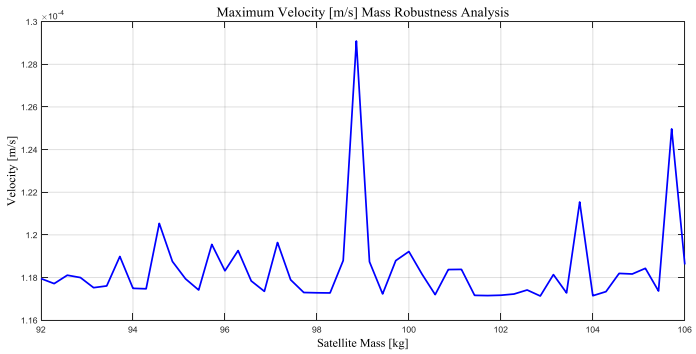

Figure 232

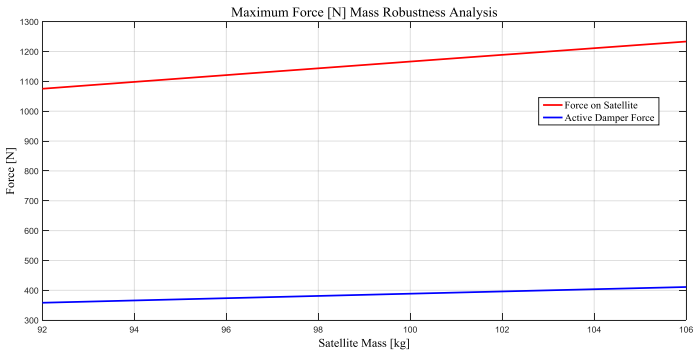

Figure 233

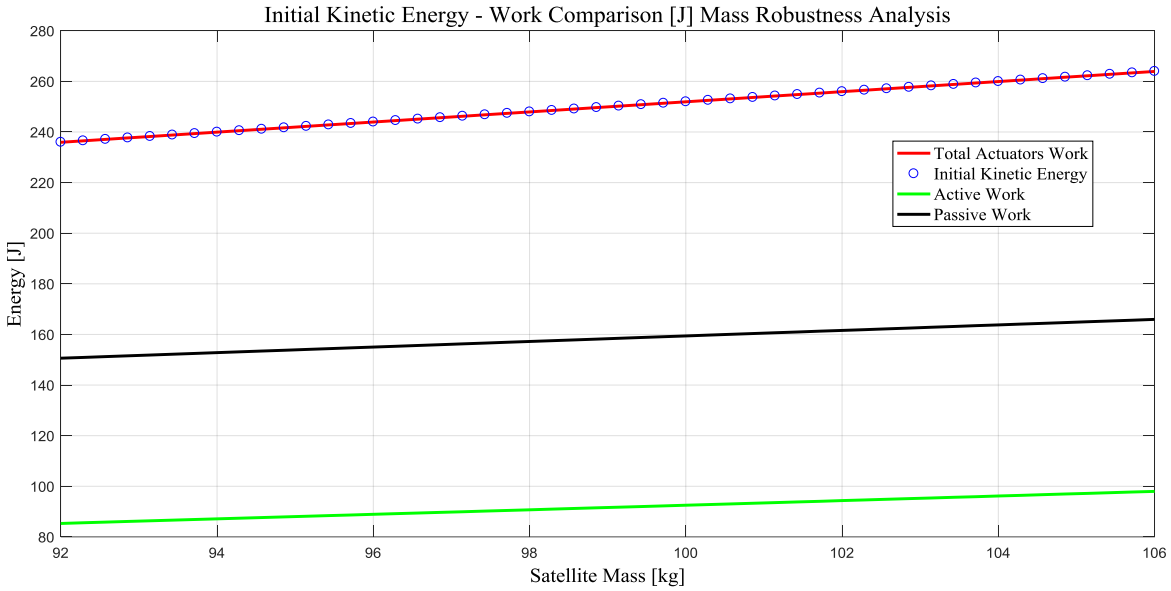

Figure 234

5.6.4 Mass Robustness Analysis with fixed Coefficient

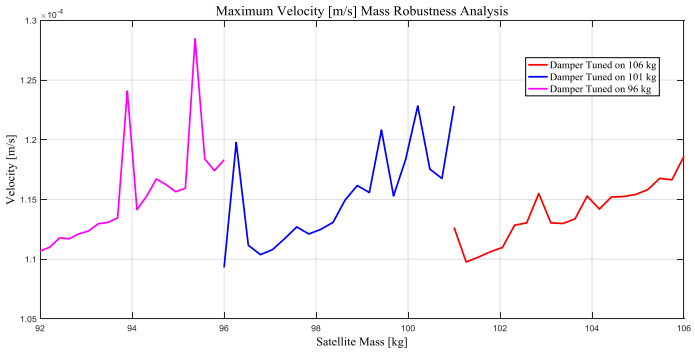

Figure 235

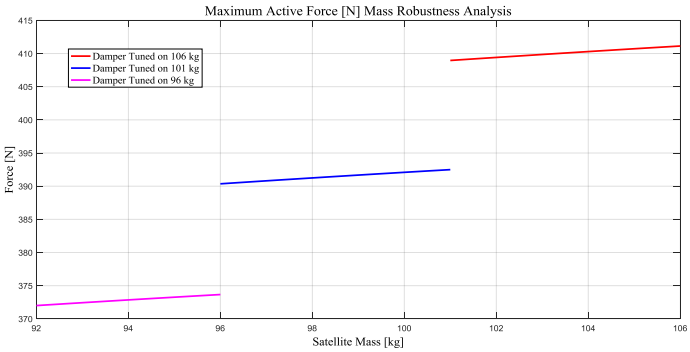

Figure 236

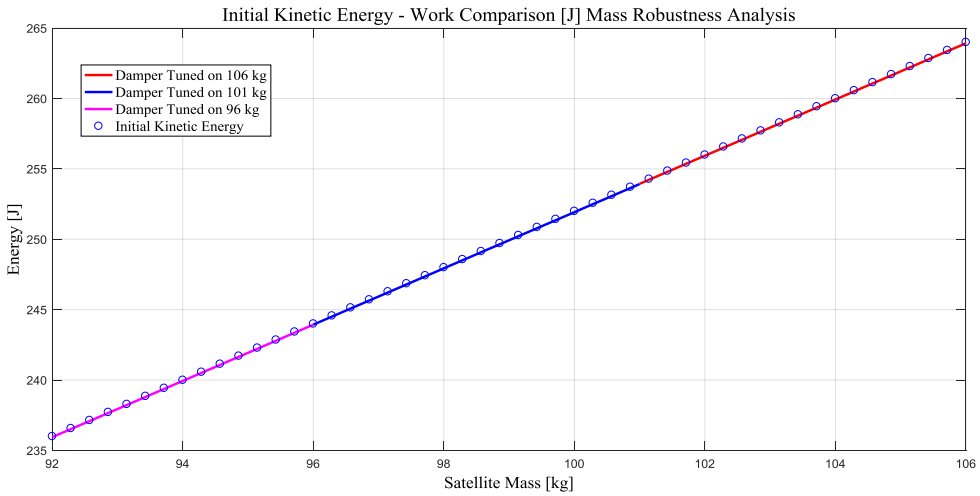

Figure 237

5.7 Final Sizing of the Landing Systems

5.7.1 Active-Passive Actuators combined Case

According to the results obtained from multibody and DEM simulations run in nominal conditions, it's performed the final design of actuators, in terms of masses, dimensions, configuration and power required. The design is done for both the possible configurations, active (piezoelectric actuator) and passive (granular actuator) combined together both with strokes of 0.125 m, and just passive (granular actuator) with a stroke of 0.25 m, in order to compare them and make possible to perform the final choice. In fact, although active-passive system gives better results than just passive one, in terms of force transmitted to the vehicle and bouncing velocity, the theme of feasibility isn't still dealt with. This refers to mass, dimensions and configuration, but especially to the possible power and voltage required by piezoelectric plates. So, sizing of both configurations is performed, with the goal to understand the building feasibility and to choose definitely the landing system configuration. The main driving design parameters are the force produced by active actuator, the force produced by passive actuator, the force that the landing pad is subjected to and the frequency content of active actuator force and input signals that it requires (active sliding velocity, passive scrolling and sliding velocity). Force coming from multibody simulation is doubled, in order to be more robust, and then they are utilized to size the various parts. Below are reported the mentioned driving design parameters for both the configurations.

Active-passive system with the best law (linear passive postion difference with bell active delta V):

- F_{active}: 1000 N
- $F_{passive}$: 3700 N
- F_{foot}**:** 50000 N
- f_{max}**:** 100 Hz

Passive system:

- $\boldsymbol{F_{passive}}$: 3870 N
- $\boldsymbol{F_{foot}}$: 48650 N

Starting from the combined active-passive system, it requires to dimension both active and passive system actuators, the junction between them and the landing pad. All these elements are considered made of Aluminium, since it is light and has good mechanical and environment resistant properties. The active actuator sizing starts taking into account its primary element, the piezoelectric plates. Available in the market there are cylindrical plates and prism-form plates, but a verification of cylindrical plates to generate the presented forces gives as result a required voltage of hundreds of volts, making discard the cylindrical piezoelectric plates and consider therefore the prism-form ones. But in order to use the prism-form plates, a perfectly cylindrical form of cylinder and piston can't be adopted, because otherwise the forms of the plates and the surface they are laid down wouldn't correspond. Therefore, prismatic cylinder and piston are considered, with three internal forms analyzed. The first is square-based piston, and so a square-internally shaped cylinder, then an octagon and finally a dodecagon. Below are reported the section of the cylinder for every form taken into consideration, and the associated piston section for each one.

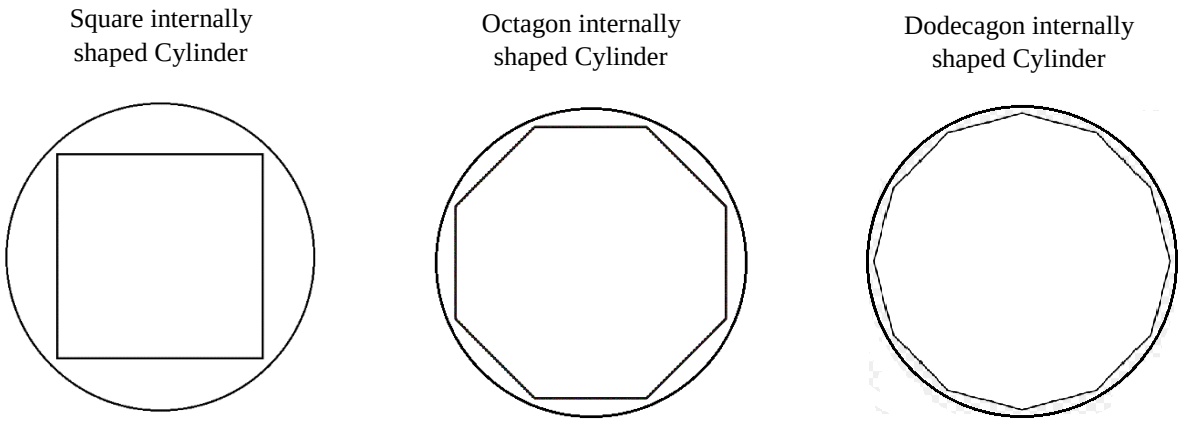

Figure 238 Section views of Active Actuator Cylinder

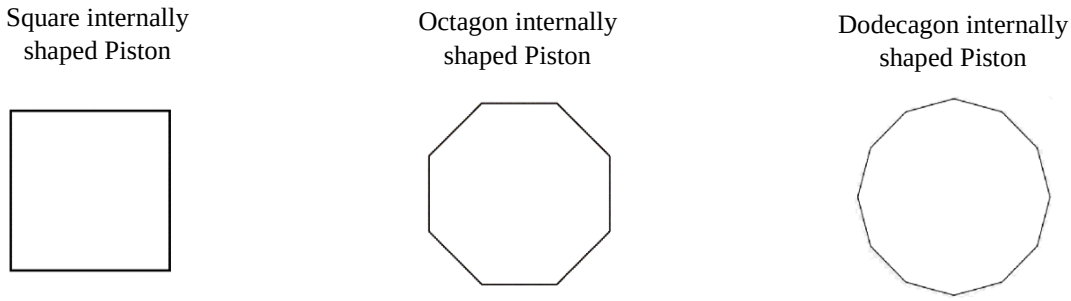

Figure 239 Section views of Active Actuator Piston

The idea is trying to increase the number of sides to attach the piezoelectric plates since so doing, it would tend to the circle, and so the area of piezoelectric plates would be maximized. The dodecagon form is chosen, since with this form, the area of piezoelectric plates is almost 99% of the circular case, while for square is about 91% and for octagon 97%. Obviously increasing to infinite, the number of sides a circle would be got, but for feasibility reason and the good result already obtained with twelve sides, dodecagon is chosen. The design of active actuator considers as maximum external radius cylinder 0.04 m, because it is a dimension similar of the one obtained from DEM simulations for passive actuator and it is a reasonable value for this active actuator. The cylinder so is externally circular, while internally it has the form of a dodecagon; the thickness chosen is 0.005 m, since it is much bigger than minimum value required to bear the internal pressure coming from piezoelectric plates and it is a reasonable value. The minimum thickness required is computed using the equation for the simple cylindrical pressured vessel even if in this case only the external form is circular, because this is considered more robust since 0.005 m is the minimum thickness in correspondence of dodecagon vertex (polygon inscribed into a circle of radius 0.035 m) while the apothem of the dodecagon is lower, and so there is more resistant mass in this configuration than in the simple cylinder case with same external radius. For the cylinder, it is also verified that the stress experienced doesn’t overcome the yielding value, and this is checked for axial compression, derived from the force coming by passive actuator, and for shear stress, exchanged with piezoelectric plates and coming from piston sliding. Cylinder internal height is 0.175 m because 0.125 m are necessary for the piston stroke while 0.05 m are used to attach to its internal wall all the piezoelectric plates. Piezoelectric plates considered are produced by PI Ceramic, and

each one is a multilayer plate obtained through the deposition of ten plates of 1 mm thickness and made of PIC 151. The chosen number of layers is ten because, since the force required is quite high, a total thickness of 0.01 m is retained suitable and more robust. As explained in the preliminary design of piezoelectric actuator, they can generate an axial force or a transverse one respect to the voltage direction; it's chosen to exploit the axial effect since it requires less voltage to generate the same force. Totally there are twelve piezoelectric plates, each one with a thickness of a 0.01 m, a width equal to the piston side (about 0.01 m) and a height of 0.05 m. The total force that the actuator shall generate is split among all the piezoelectric plates, and so each plate shall generate the total force coming from the multibody simulations divided by twelve and then divided by the friction coefficient between piezoelectric plates and piston. Between every plate and the piston is inserted a plate of Aluminium oxide, in built with piezoelectric plate and with the same width and height of it but smaller thickness, that for dodecagon case is 0.0045 m. Aluminium oxide plate thickness depends on the cylinder-piston geometry, because fixing the external cylinder radius at 0.04 m, piezoelectric plates thickness at 0.01 m and piston radius at 0.02 m (half of the cylinder one, which is considered a reasonable value for the piston), its thickness is simply the gap between all the mentioned fixed dimensions. The role of the Aluminium oxide plates is to increase the friction coefficient between piezoelectric plates and piston, in order to maximize the force exchanged. Aluminium oxide against Aluminium oxide in vacuum has a friction coefficient of 0.98, and so a plate made of this material is put between piezoelectric plate and piston. Also the piston is covered with a coating of 1 mm of Aluminium oxide, since the coefficient of 0.98 is for Aluminium oxide against Aluminium oxide. This material is robust against harsh environment, has good mechanical properties, has an important friction coefficient and is stable against space environment. Pure Aluminium is avoided because if it enters in contact with atomic oxygen, it oxidizes, changing its properties and so varying drastically the mode of operation respect to design conditions. Aluminium oxide is also a good electrical insulator, and this is important to not disperse electrical charges coming from electrodes and destined to piezoelectric plates, even if the piezoelectric plates are already produced with electrodes inserted and electrically insulated. Some considerations about the technological issues regarding the installation of the piezoelectric actuator with the

oxide contact and the cylinder must be done. A simple welding between the elements is actually unfeasible because of the high temperature required (the melting temperature of PZT and Aluminium oxide are respectively 1350°C and 2050 °C). Such a process could damage irreversibly the piezoelectric material and could melt the internal electrodes which are made of Silver (melting temperature 962°C). More sophisticated techniques like CVD and PVD allow to deposit the Aluminium oxide on a metallic substrate (Silver in this case) but because of the elevated temperature (in the traditional thermal CVD the substrate must be heated and temperature can increase up to 1900°C) and the low thickness of the coating (in the order of nm for both the techniques), make them unsuitable to deposit 4.5 mm thick layer of Aluminium oxide on the piezoelectric stack. The novel technique of Cold Spray allows to deposit ceramic material on metals and vice-versa without altering thermally the substrate (below the melting point of the common metallic materials). For soft and ductile coatings (like metals), this technique can reach thicknesses up to 50 mm while for hard materials (like ceramics), the achievable thicknesses are far lower (1e-05 m). However, it is observed that when the ceramic material is mixed with a ductile one (like Al-Al2O3 mixture), coatings with thicknesses higher than 1 mm can be deposited. In order to achieve the desired configuration, a solution could be an initial Cold Spray deposition of thin Aluminium oxide layer on both sides of the actuator to guarantee the electrical insulation (microns), subsequently an Al-Al2O3 mixed Cold Spray deposition on the internal side (toward the piston) of the actuator up to the desired thickness (almost 4.5 mm). Finally, only-Al2O3 based Cold Spray deposition should be applied on the external surface of the contact in order to obtain the correct frictional coefficient. The same procedure could be applied for the coating of the external surface of the piston. The issue related to the junction between the piezoactuator-oxide contact assembly and inner surface of the cylinder can be solved again through the Cold Spray technique which allows to deposit a layer of Aluminium alloy (of the same type of the cylinder) on the Al2O3 substrate (external insulator). This thin Aluminium layer can be sold with the cylinder without damaging any component since the melting temperature of the considered alloy is around 483 °C and below the melting points of other elements. It’s quite important to underline that the Curie temperature of the chosen piezoactuator is 250 °C and in the manufacturing of the damper a depolarization of the ceramic could occur. However, the actuator can be easily

re-polarized increasing its temperature above the Curie point and applying an external electric field in the correct direction. For both the piezoelectric and Aluminium oxide plates, as done for the cylinder, it is checked that the shear stress they experience doesn't exceed the yielding value. Since the kinetic energy of the spacecraft is dissipated by friction between piston and cylinder, a verification of the wear shall be performed, in order to understand if the piston could damage piezoelectric plates and if the wear process may create a gap between them, making invalid the hypothesis of piezoelectric plates perfectly constrained and no more able to use the concept, introduced in the preliminary design, of blocking force. The wear rate is very difficult to compute, since it is a very empiric process that should be performed experimentally. The computation so it is done thanks to a trend found in the literature (Koji Kato, Koshi Adachi, Tohoku University, 2001) which shows the variation of wear rate (expressed in $\frac{\mathrm{mm}^3}{\mathrm{m}}$) respect to the sliding velocity (expressed in $\frac{\mathrm{m}}{\mathrm{s}}$), with a considered normal load of 20 N. The total sizing force is 2000 N (the double of the active actuator value obtained from multibody simulations), and since the piezoelectric plates are twelve, the total force is split among all the plates, with a value for every one of about 170 N. Obviously, the trend found doesn't exactly correspond to the force case of this thesis, therefore to be robust, it's taken the wear rate corresponding to $4\ \frac{\mathrm{m}}{\mathrm{s}}$ and multiplied by one hundred, even if the nominal velocity is $2\ \frac{\mathrm{m}}{\mathrm{s}}$ and 170 N is about only ten times of the considered normal load of 20 N. However, the thickness of the material removed, computed using the selected wear rate and the active actuator stroke of 0.125 m, it's in the order of 1e-06 m, and so the hypothesis of perfectly constrained plates remains still valid. The obtained ware value is also compatible with the oxide coating which was mentioned before. A roughly evaluation is done to verify that plates temperatures, due to friction, doesn't increase too much making melt the plates. This is checked just for plates, since they are smaller and are the elements more subjected to friction. To be more robust, it's considered for every piezoelectric and Aluminium oxide plate that the total kinetic energy of the spacecraft is transformed in thermal energy, and then it's calculated the increment of temperature for each element. For plates of dodecagon case, the associated increment of temperature is about 67 K, and since in space the temperature is about 4 K, this doesn't represent in any case a problem. The blocking force is the force that a

piezoelectric material produces when it's perfectly constrained, and it's acquired giving an electrical potential to the piezoelectric plate, measuring the deformation it has experienced and applying a force to restore the material to its original length. So, undergoing the piezoelectric plates to an electrical potential and perfectly constraining them, they produce a value of blocking force depending on the entity of the electrical potential. The point is to verify if electrical potential and power required are admissible, because the power system can't provide too high voltages or currents. The piezoelectric plates are electrically linked in parallel, and so it's sufficient to verify the required electrical potential for one plate. Knowing the force every plate shall produce, and being it $\boldsymbol{F = K\Delta L}$ (where $\boldsymbol{K}$ is the equivalent stiffness of the plate and $\boldsymbol{\Delta L}$ is the deformation along the force axis), the electrical potential can be computed according to the following equation.

$$\boldsymbol{V = \frac{th * F}{E * A * N * d_{33}}}$$

Where ***th*** is the piezoelectric plate thickness, ***F*** is the force the single plate shall generate, ***E*** is the Young Modulus of piezoelectric material, ***A*** is the contact area between piston and every piezoelectric plate, ***N*** is the total number of layer of every piezoelectric plates and $\boldsymbol{d_{33}}$ is the associated coefficient of force and electrical voltage axially aligned (in this case is one third of data sheet value, since in cryogenic environment, R.P. Taylor, G. F. Nellis)..

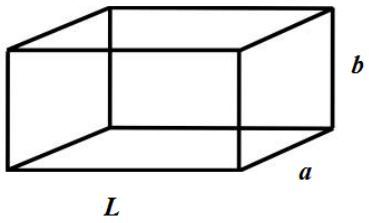

Figure 240 Example of a generic plate

$$\boldsymbol{K = \frac{EA}{L}}$$

Where ***E*** is the Young modulus and ***A*** is the area exchanging force $\boldsymbol{A = a*b}$.

The frequency content of the force that piezoelectric plates shall produce is about 100 Hz, and so this doesn't represent a problem since PIC 151 have a bandwidth of some KHz. Below it is reported the plot of the Fast Fourier Transform of the force signal.

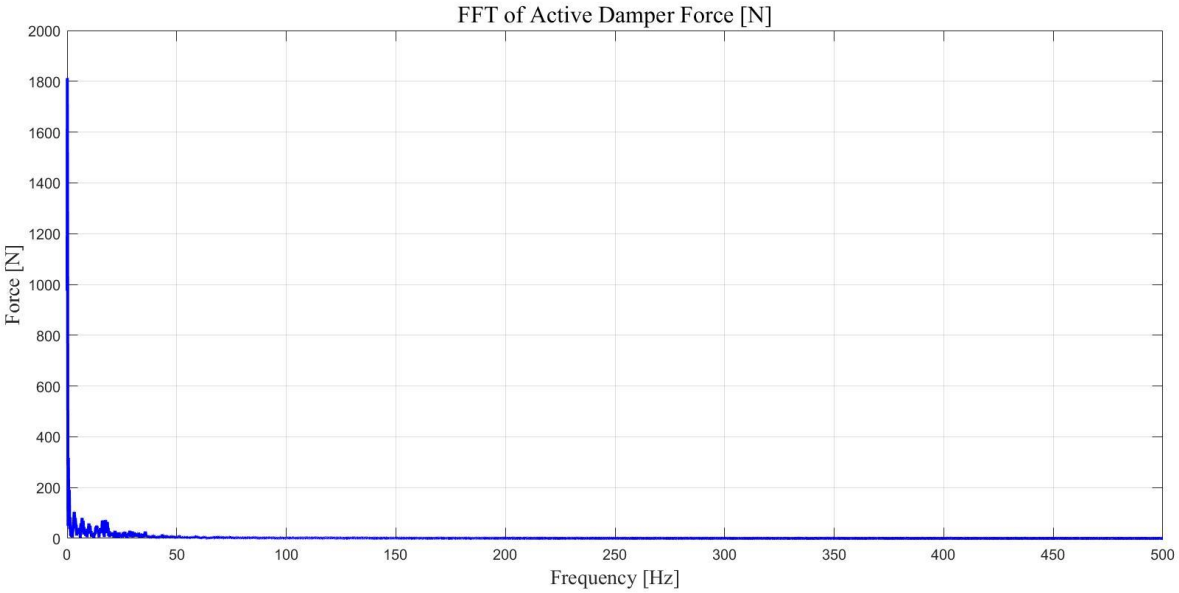

Figure 241

The power required by every piezoelectric plate is computed according to the following equation.

$$P = 2\,\pi\, f\, tan(\delta)\, C\, V^2$$

Where f is the maximum frequency of the signal force, $tan(\delta)$ is linked to the electrical dissipation of the piezoelectric material, C is the capacitance of the piezoelectric material, and V is the electrical potential.

$$C = \frac{N\,\varepsilon\,A}{th}$$

Where N is the number of layers that compose a multilayer piezoelectric plate, ε is the electrical permittivity of the piezoelectric material, A is the area exchanging force and th is the thickness of a single layer.

The powers obtained are very low, and for the dodecagon case it is in the order of 1e-04 W. Once the electric power for each piezoelectric plate is known the current can be got since $P = V\,I$, and for dodecagon case is the order of 1e-05 A. Regarding the sizing of the piston, obviously, its shape section is the same of the internal cylinder shape. Fixed, as said before, the radius of the circle at 0.02 m for all the considered geometries, what

changes from one configuration to the others is the radius of circle inscribed to the piston polygonal section, with maximum radius of 0.02 m. The radius of circle inscribed is used to verify the buckling of the piston and to check if, since it is axially compressed and exchanges shear force with the plates in solid with cylinder, the stress that it experiences doesn't exceed the compression and shear yielding values. The piston form isn't a perfectly cylinder form, but using as radius to verify buckling and compression the one of the circle inscribed, it is retained more robust since the real piston has more resistant mass than the equivalent cylindrical one with radius of circle inscribed. In the dodecagon case, for buckling, the minimum radius required is 0.0046 m, while the radius of the circle inscribed is 0.0193 m, more than four times of minimum value required. Total piston length is 0.18 m, chosen to allow piston to have an effective stroke of 0.125 m. A table with all dimensions, masses, admissible and experienced stresses, for all the considered geometries of the active actuator in the combined active-passive case, it is reported below.

	Square	**Octagon**	**Dodecagon**
Voltage Single Piezoelectric [V]	21,6461	19,9984	19,7128
Power Single Piezoelectric [W]	1,8000E-03	8,1739E-04	5,3715E-04
Current Single Piezoelectric [A]	8,1746E-05	4,0873E-05	2,7249E-05
Radius Circle Inscribed in Piston [m]	0,0141	0,0185	0,0193
Radius Minimum of Circle Inscribed in Piston for Instability [m]	0,0046	0,0046	0,0046
Piezoelectric/Al Oxide Contact Shear Stress [Pa]	1,2728E+06	1,1759E+06	1,1591E+06
Piezoelectric Yielding Shear Stress [Pa]	4,3879E+07	4,3879E+07	4,3879E+07
Actual Operating Piezoelectric Frequency [Hz]	100	100	100
Maximum Piezoelectric Operating Frequency [Hz]	1,E+03	1,E+03	1,E+03
Al Oxide Contact Yielding Shear Stress [Pa]	1,9053E+08	1,9053E+08	1,9053E+08

Aluminium Yielding Shear Stress [Pa]	5,4848E+07	5,4848E+07	5,4848E+07
Piston Axial Stress [Pa]	2,5E+06	1,7678E+06	1,6667E+06
Piston Yielding Axial Stress [Pa]	9,5E+07	9,5E+07	9,5E+07
Cylinder Axial Stress [Pa]	2,7944E+06	4,6102E+06	5,3272E+06
Cylinder Yielding Axial Stress [Pa]	9,5E+07	9,5E+07	9,5E+07
Increment of Temperature during the Landing of Al Oxide Contact [K]	180,9268	52,5615	66,7969
Increment of Temperature during the Landing of Piezoelectric [K]	13,0543	24,1212	35,6650
Wear Oxide Contact [mm]	3,5355E-06	6,5328E-06	9,6593E-06
External Radius Cylinder [m]	0,04	0,04	0,04
Minimum Cylinder Thickness [m]	0,005	0,005	0,005
Required Cylinder Thickness due to Pressure [m]	1,519E-04	1,403E-04	1,3834E-04
Section Area of the Actuator respect to Circumscribed Circle [%]	0,6366	0,9003	0,9549
Total Piezoelectrics Area exchanging Force [m2]	0,0057	0,0061	0,0062
Area exchanging Force respect to Circumscribed Cylinder one [%]	0,9072	0,9708	0,9868
Thickness Piezoelectric [m]	0,01	0,01	0,01
Thickness Al Oxide Contact [m]	6,066E-04	0,0039	0,0045
Piston Length [m]	0,18	0,18	0,18
Cylinder Internal Height [m]	0,175	0,175	0,175
Active Actuator Total Mass [Kg]	2,2977	2,0647	2,0161
Number of Active Actuators [n°]	3	3	3
Total Weight of Active Actuators [Kg]	6,8931	6,1941	6,0483

Table 62

Below it is reported a plot representing the link force-voltage of the active piezoelectric actuator.

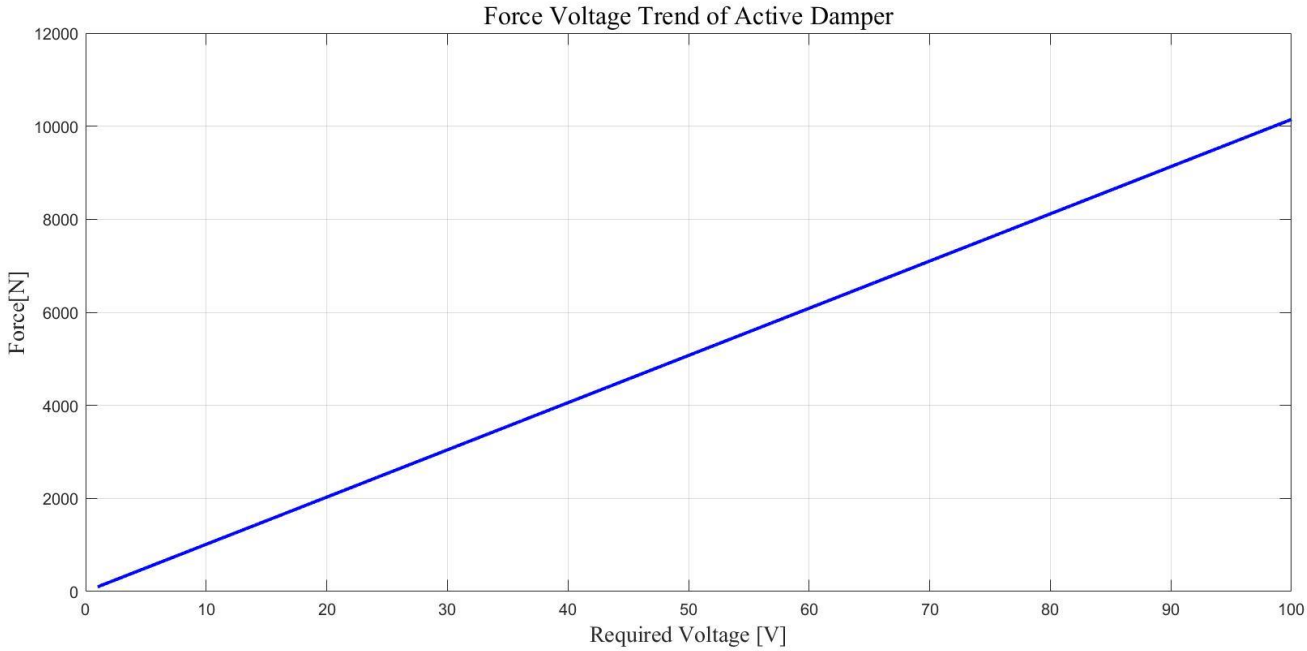

Figure 242

The active actuator shall be connected with the passive one, and so a junction between them must be sized. The material considered, for the usual reasons, is Aluminium, and it's a cylinder with the same radius of the external cylinder radius of active actuator and a height of 0.02 m, with attached below a truncated cone with major circular base of same radius of cylinder, minor base of same radius of passive actuator piston (0.013 m) and a height of 0.015 m. The idea is to have an element able to transfer properly the load from one actuator to the other and able to support the load itself. To verify that the base of the active cylinder doesn't bend under the concentrated load coming from the passive part, the following rough verification is performed. The cylindrical part is virtually replaced by twelve beams (since the chosen geometry is a dodecagon) of height 0.02 m, length equal to the apothem of the inscribed polygon to the circle of radius 0.04 m and width equal to the side of the inscribed polygon, and for each beam it is verified that the stress produced by the total force coming from passive actuator divided by twelve doesn't exceed the yielding value. This is a rough way to deal with the problem, but since the mass resistant to the force is bigger (all the circular section

has to be considered), and there is also the truncated cone which behaves the stress, this approximation is retained valid and robust. To compute the stress present in every beam is used De-Saint Venant equation: $\sigma_z = \frac{N}{A} + \frac{M_x}{I_x} y + \frac{M_y}{I_y} x$, where x is the horizontal axis, y is the vertical axis (along actuator axis), z is the beam axis, N is the axial load along beam axis, A is the resistant area along axial direction, M_x is the torque along x axis, M_y is the torque along y axis and σ_z is the axial stress experienced in the beam due to N, M_x and M_y. For both the truncated cone and cylindrical part of the junction it is verified also that the stress experienced along force direction doesn't exceed yielding value. A table with dimensions and masses of the junction linking active and passive actuator is reported below.

	Active Actuator - Passive Actuator Junction
Cylinder Radius [m]	0,04
Cylinder Height [m]	0,02
Truncated Cone Big Radius [m]	0,04
Truncated Cone Small Radius [m]	0,013
Truncated Cone Height [m]	0,015
Junction Total Weight [Kg]	0,03807
Number of Junction [n°]	3
Junctions Total Weight [Kg]	0,11421

Table 63

Regarding the passive actuator part, it is considered again as made of Aluminium and the dimensions are in part dictated by the ones set up by DEM simulations, especially for internal cylinder radius (0.05 m) and piston (head radius and head height are respectively 0.025 m and 0.05 m). The piston, also called intruder in the following

tables, is composed by one beam of 0.13 m and a head, always submerged in the cylinder, with the dimensions mentioned above. Just to remind, the stroke is the same of active part (0.125 m) and the piston beam is chosen properly to allow the piston to have the mentioned stroke. For the piston beam, it's verified which is the minimum radius required to avoid buckling (0.0064 m) utilizing the force produced by passive actuator, and its radius is taken as about the double of the minimum required value. Then, as done before, it's checked if the stress experienced by the material doesn't exceed the yielding value. For the cylinder are performed the same computations of the active one, but the forces used is obviously different. Here, as sizing forces, it is used the one produced by passive actuator to verify the minimum thickness necessary to resist the internal pressure, and the one coming from the landing pad for verify that the stress experienced in the cylinder doesn't overcome the yielding value. The minimum thickness required to behave pressure is in the order of 1e-05 m, and so it's chosen 0.005 m, a reasonable and feasible value bigger than the minimum required. The granular material is made of Aluminium, and it is put in the cylinder till a height of 0.125 m, in order to not enter in contact with the piston before the landing. It can be easily blocked in this position by using special foams, but this part isn't dealt with in this thesis since it is a very peculiar detail. The granular material is composed by balls made of Aluminium, with a diameter of 0.005 m and a friction coefficient of 0.3. This friction coefficient is considered between Aluminium against Aluminium since all parts (cylinder, piston and granular material) are made of Aluminium, and comes from the analysis performed in DEM simulations. Aluminium-Aluminium natural friction coefficient is not 0.3 but it's much higher (about 1). However, through surface treatments like PVD, CVD or electrochemical deposition it is possible to reduce its value. A table with dimensions, masses, admissible and experienced stresses for passive actuator in active-passive combined case it is reported below.

Intruder Total Length [m]	0,18
Beam Intruder Length [m]	0,13

Beam Intruder Radius [m]	0,013
Head Intruder Total Length [m]	0,05
Head Intruder Radius [m]	0,025
Cylindrical part of Intruder Head Length [m]	0,03
Conical part of Intruder Head Length [m]	0,02
Minimum Beam Intruder Radius required for Instability [m]	0,0064
Beam Intruder Axial Stress [Pa]	1,3938E+07
Beam Intruder Yielding Axial Stress [Pa]	9,5E+07
Intruder Total Weight [Kg]	0,2824
Cylinder Internal Radius [m]	0,05
Cylinder Internal Height [m]	0,175
Cylinder Thickness [m]	0,005
Cylinder Axial Stress [Pa]	6,063E+07
Cylinder Yielding Axial Stress [Pa]	9,5E+07
Minimum Cylinder Thickness required for Pressure [m]	9,9179E-05
Cylinder Weight [Kg]	1,0668
Aluminium Grain Radius [m]	0,0025
Aluminium Grains Total Number [n°]	6348
Grains Block Height [m]	0,0125
Aluminium Grains Total Weight [Kg]	1,1633
Friction Coefficient Grain - Grain	0,29
Friction Coefficient Grain - Cylinder/Intruder	0,29

Passive Actuator Total Weight [Kg]	2,5125
Number of Passive Actuators [n°]	3
Total Weight of Passive Actuators [Kg]	7,5375

Table 64

The last element that shall be designed is the foot (the landing pad of the leg, which enters directly in contact with the ground), and it is considered again as made of Aluminium. The sizing parameter used for its design is the force coming from the ground and, as the previous elements, obtained from multibody simulations run in nominal conditions. The landing pad shall not transmit to the passive actuator cylinder a force bigger than the one which would plastically deform the cylinder of the passive actuator, which is an element in contact with the foot. In order to guarantee that this fact doesn′t occur, the landing pad is sized as a composition of two parts, one full cylinder attached below the passive actuator cylinder with same external radius (0.055 m), height 0.01 m and put to make more robust, during the landing, the cylinder base since it has a thickness of just 0.005 m, and one hollow cylinder attached below the full one, with same external radius, internal radius of about 0.053 m and a height of 0.03 m. The aim of the hollow cylinder is to transmit a load to passive actuator cylinder smaller than the one that would plastically deform it. It is sized considering the force that would plastically deform the cylinder passive actuator, obtained knowing stress yielding value of Aluminium and the resistant area (the difference of areas of circles having external and internal radii of hollow cylinder, which is the thickness), and dividing it by two in order to be far from the limit value. Knowing the stress yielding value of hollow cylinder (which is the same of passive cylinder actuator since both are made of Aluminium) and its external radius (the same of the full cylinder), it′s possible to get the resistant area and so the internal hollow cylinder radius. For the hollow cylinder, it′s done the hypothesis of perfectly elasto-plastic behaviour. According to this hypothesis, the force the landing pad transmits when achieves plastic deformation does never exceed the maximum acceptable value for passive cylinder actuator, and since the total kinetic energy is equal to the force multiplied by the displacement, this last value is

checked and doesn't ever exceed the height of hollow cylinder. Transmitted force and plastic deformation it's verified also for every case analyzed in the sensitivity study. All the most demanding cases encountered in the sensitivity analysis are checked even for all the components (active actuator, passive actuator and the junction which links them) in order to guarantee that the landing system is able to land in different conditions but also to bear and physically resist in those conditions. Below it is reported a table with dimensions and masses of the landing pad.

	Foot
Upper Plate Height [m]	0.01
Hollow Cylinder External Radius [m]	0,055
Hollow Cylinder Internal Radius [m]	0,05256
Hollow Cylinder Height [m]	0.03
Total Foot Height [m]	0,04
Total Foot Weight [Kg]	0,3354
Number of Feet [n°]	3
Feet Total Weight [Kg]	1,0062

Table 65

The total landing system mass, considering three legs where each one is composed of one active actuator and one passive actuator both with a stroke of 0.125 m, a junction linking them and a landing pad, is about 14.71 kg. Below it is reported a schematic vertical-section representation of one leg in the combined active-passive case, which it isn't perfectly proportionate but it's useful to give a concrete idea of the system.

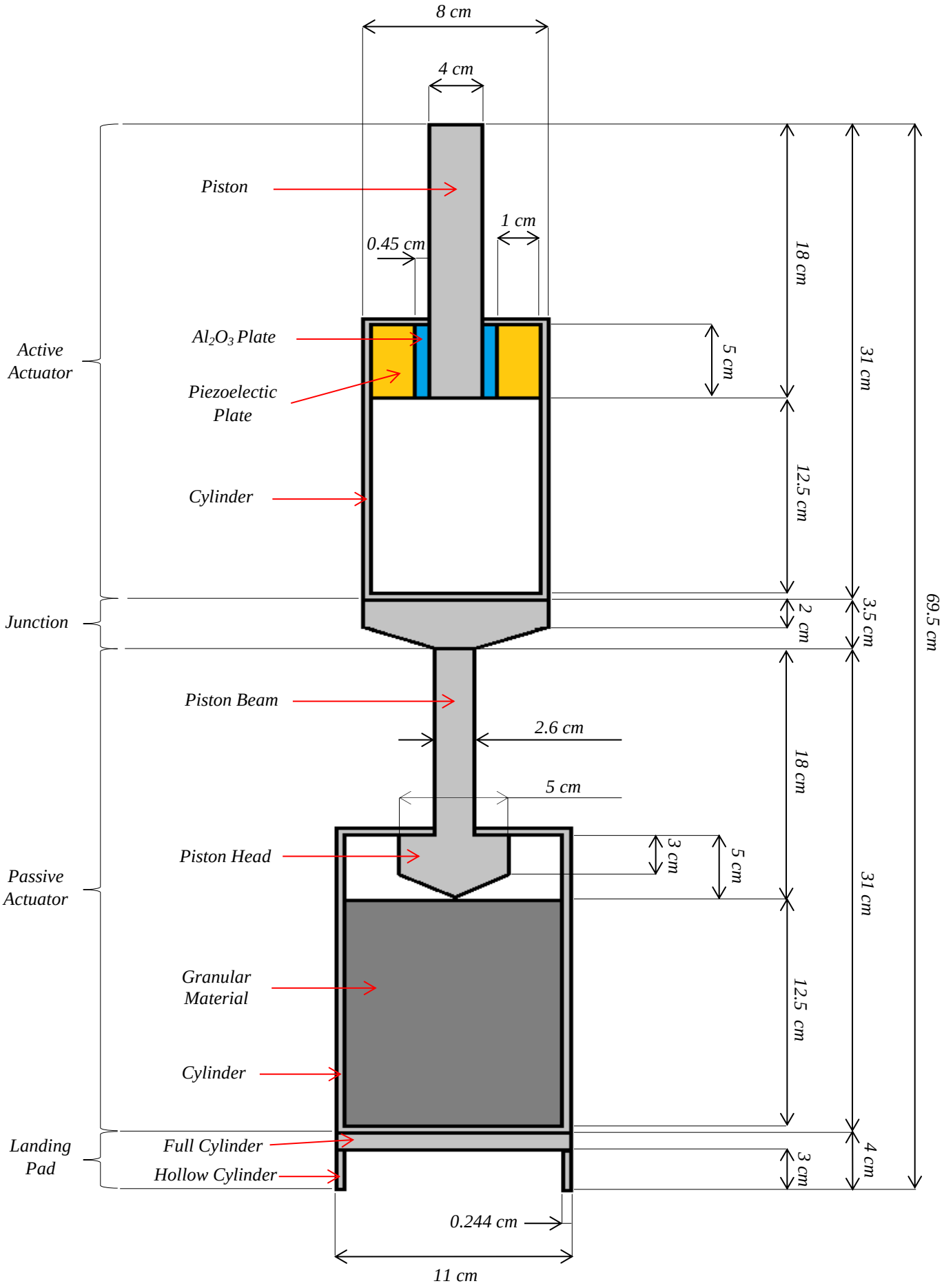

Figure 243 Schematic vertical-section representation of one leg in the combined Active-Passive case

5.7.2 Granular Passive Actuator Case

For what regard the only-passive case, the stroke of the actuator is the sum of actuators strokes of previous case, 0.25m. The driving sized parameters for this case are the ones mentioned at the beginning of the paragraph, which are the force produced by the passive actuator and the reaction force of the ground transmitted to the landing pad (respectively 3870 N and 48650 N), and again all is considered made of Aluminium. Starting from the actuator, the procedure is the same of the passive actuator for the combined active-passive case, where the only differences are just stroke and piston beam length (here 0.305 m). Since the piston beam length is bigger than previous case, a different minimum radius to avoid buckling is required, and being 0.0084 m, the beam piston radius is set 0.017 m, again about the double of the minimum required value to avoid buckling. The head of the piston is exactly the same of the previous case, since this is a parameter derived from DEM simulations. After having verified that the stress experienced by the piston beam doesn't exceed the yielding value, the same computations of previous case are done also for other elements. The quantity of granular material is considered the double since the volume it occupies is exactly the double, with the same properties of before keeping as how they come from DEM simulations. The internal radius cylinder dimension, being again a dimension coming from DEM simulations, is kept equal of previous case. Then is verified which is the minimum value of cylinder thickness to bear the internal pressure, and since it is in the order of 1e-05 m, the same thickness of passive cylinder in active-passive case is taken which is 0.005 m. To guarantee the stress experienced by the cylinder doesn't exceed the yielding value, it's adopted the same strategy used for passive actuator in the combined active-passive case. Since both thickness and material (Aluminium) are equal of combined case, the landing pad is considered perfectly equal of previous case, with same form, mass and dimensions. It's just verified that in each case considered in sensitivity analysis for only-passive case it plastically deforms, transmitting a force to the cylinder that doesn't induce it to plastically deform. Below it is reported a table with masses, dimensions, admissible and experienced stresses for the passive actuator in only passive case.

Intruder Total Length [m]	0,305
Beam Intruder Length [m]	0,255
Beam Intruder Radius [m]	0,017
Head Intruder Total Length [m]	0,05
Head Intruder Radius [m]	0,025
Cylindrical part of Intruder Head Length [m]	0,03
Conical part of Intruder Head Length [m]	0,02
Minimum Beam Intruder Radius required for Instability [m]	0,0084
Intruder Axial Stress [Pa]	1,5075E+07
Intruder Yielding Axial Stress [Pa]	9,5E+07
Intruder Total Weight [Kg]	0,7374
Cylinder Internal Radius [m]	0,05
Cylinder Internal Height [m]	0,3
Cylinder Thickness [m]	0,005
Cylinder Axial Stress [Pa]	6,063E+07
Cylinder Yielding Axial Stress [Pa]	9,5E+07
Minimum Cylinder Thickness required for Pressure [m]	5,1868E-05
Cylinder Weight [Kg]	1,6388
Aluminium Grain Radius [m]	0,0025
Aluminium Grains Total Number [n°]	12696
Grains Block Height [m]	0,025
Aluminium Grains Total Weight [Kg]	2,3266

Friction Coefficient Grain - Grain	0,29
Friction Coefficient Grain - Cylinder/Intruder	0,29
Passive Actuator Total Weight [Kg]	4,7028
Number of Passive Actuators [n°]	3
Total Weight of Passive Actuators [Kg]	14,1084

Table 66

The total landing system mass, considering three legs where each one is composed of one passive actuator with a stroke of 0.25 m and a landing pad, is about 15.11 kg. Below it is reported a schematic vertical-section representation of one leg in only-passive case, which isn’t perfectly proportionate but it’s useful to give a concrete idea of the system.

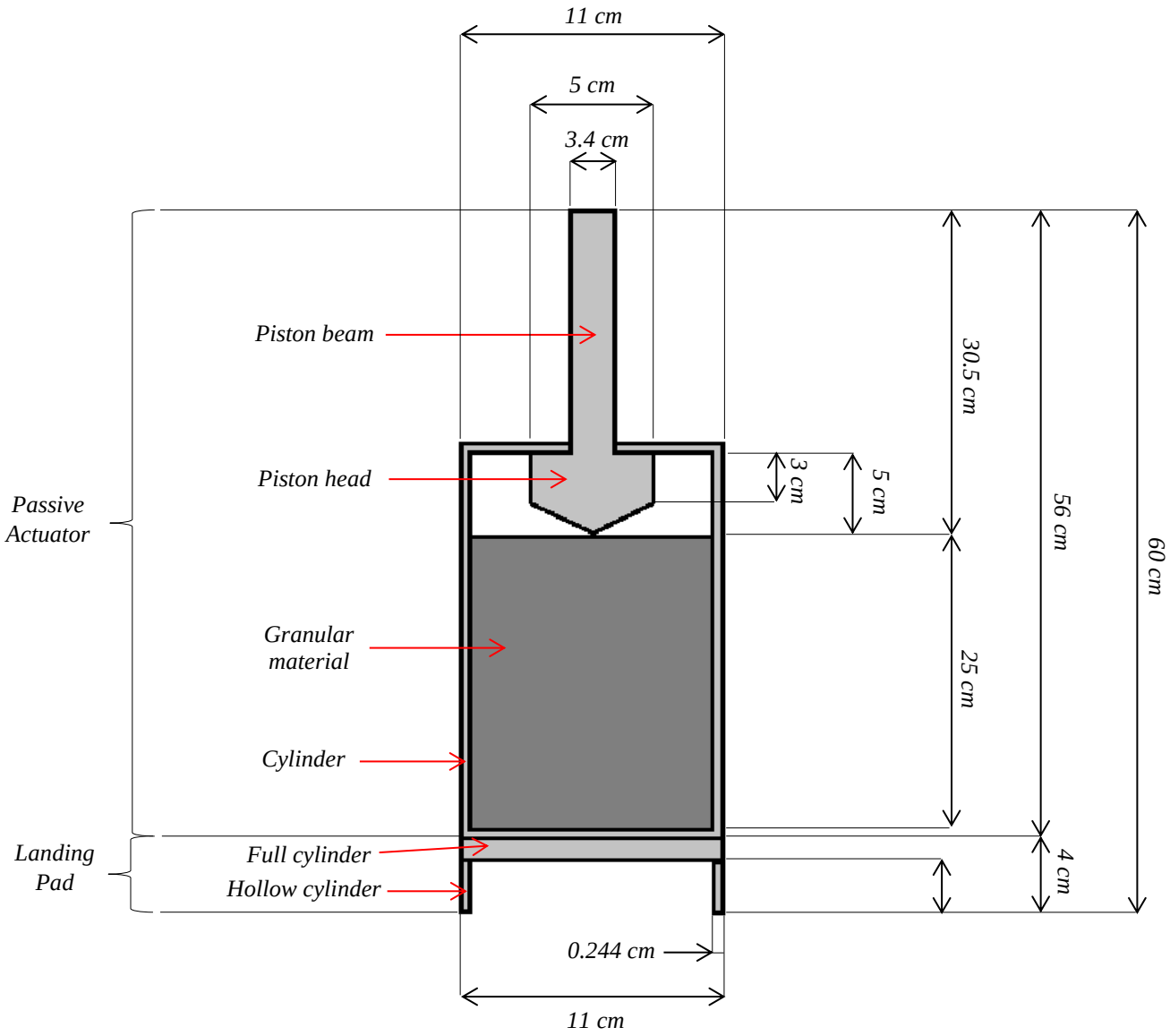

Figure 244 Schematic vertical-section representation of one leg in only-passive Granular case

5.7.3 Definitive Selection of Landing System Configuration

The results obtained from multibody and DEM simulations have shown as with both landing system configurations it is possible, in what have been defined nominal conditions (in terms of arrival velocity, vehicle mass, gravity field and ground parameters), to land on a celestial body with very low gravity, without bouncing away from it jeopardizing to reach the escape velocity and to transmit an excessive and

intolerable force to the vehicle and the payload contained inside it. Since in this kind of missions, the uncertainties about spacecraft dynamics and especially environmental conditions could be significant, a strong and extended analysis of the robustness has been performed for both the configurations in order to understand landing system behaviour not only in nominal conditions but also in different circumstances not too much distant from them. What has been resulted is that the combined active-passive case configuration is much more robust, in terms as bouncing velocity and transmitting force, of the only passive case, and this is the reason why the above-mentioned configuration has been taken into account. But before to perform a sizing, in order to understand masses, dimensions and power at stake, it wasn't certain if the results obtained through all the simulations could have been physically achieved. After having performed the sizing, what follows is that both configurations have acceptable masses and dimensions, even a lower mass than what was assigned before doing the first simulations. Since the combined active-passive landing system requires for the piezoelectric plates put in parallel a voltage of about 20 V, which was the most critical parameter of this configuration but it's easily achievable, and its mass is even lower of the only-passive configuration, the definitive selection is the active-passive landing system configuration, due to its superior performances and robustness against uncertainties.

6. Experimental Analysis of the Granular Damper

6.1 Motivations

As it was mentioned in the previous chapters, an experimental approach for the characterization of the granular damper cannot be considered suitable because of the impossibility to reproduce the absence of gravity. Moreover, the high number of parameters involved would have increased the complexity, the cost and the duration related to the preparation and the realization of such tests. These considerations led to the adoption of a numerical approach based on DEM which allowed to verify the feasibility and to determine the intruder and cylinder dimensions, the granular radius and the frictional coefficients able to ensure acceptable results. However, once the damper parameters are defined, it could be interesting to perform a single experimental test in order to validate the DEM model and to verify if the chosen configuration is able to ensure a good dissipation capability also in presence of the gravity. The validation of DEM model can be done through an experimental test which reproduces the scenario modelled with DEM where the container with the granular material was fixed to the ground. As term of comparison, DEM simulations should be performed with the similar characteristics of the experimental test but adding, of course, the contribution of the gravity. Even if the results in terms of force and stroke may not be satisfactory (because of the gravity and properties of the used material), a proper validation of DEM model could enhance the fidelity of the chosen approach and so the reliability of the sized damper.

6.2 Experimental Test Features

The experiment has the aim to reproduce the behaviour of a ground-fixed granular damper with a maximum available stroke of 0.25 m. Trying to test the shorter damper (0.125 m) could be erroneous since it is thought to be coupled with an active damper of the same stroke which is not considered in this test session. The choice of not testing also the active frictional damper is dictated by the fact that one of the purpose of this test is to validate DEM results, evaluating the passive damper performances when it's used alone. Moreover, it's quite obvious that an experimental verification shall be dedicated more to an unpredictable element like the granular damper instead of the active one. Anyway, the following part will be dedicated to the illustration of the configuration adopted for the test and description of the chosen material.

6.2.1 Test Configuration

A hollow cylinder made of Aluminium with the following dimensions (internal diameter 10 cm, thickness 0.5 cm and internal height 50 cm) is fixed to a cylindrical support with the same diameter of the internal diameter of the hollow cylinder and with a high of 1 cm. Inserting the lateral bolts between the hollow cylinder and the internal support, it is possible to constrain the first element to the second, which is clumped to the ground. The cylinder is filled with the granular material up to 0.25 cm of height and then covered with an upper cap with a hole which should allow the passage of the intruder. The upper cap could be made of a plastic material in order to facilitate the manufacturing and the bonding with the upper part of the cylinder. Differently from what was done in DEM model, where the intruder was composed by a head and a rod with different diameters, here the intruder is built as a one cylindrical piece of diameter 5 cm with a conical head of 2 cm, and it is rigidly attached to an upper mass which should simulate the mass associated to the spacecraft. A tolerance of 3 mm between the

hole and the intruder is adopted in order to be robust against misalignments during the fall. Thanks to the chosen configuration, since the spheres diameter is 5 mm, the leak of spheres from the container during the impact can be avoided. The height of the cylinder is chosen in order to give enough free space to the granular material, which should be allowed to move during the impact, without blocking the sliding of the intruder. Indeed, the volume occupied by the intruder in the granular mean when the maximum stroke is reached (0.25 m) is less than the initial free volume of the cylinder minus the space occupied by the half of the intruder. The length of the intruder (52 cm) is compatible with the internal height of the cylinder (50 cm) and the thickness of the upper cap. An additional cm is left in order to allow the intruder to reach to bottom of the cylinder without causing an impact between the upper mass and the cap of the cylinder. Since the mass associated to the intruder in this case is higher than the mass obtained in DEM models (because of the higher diameter and length of the rod), this mass increment must be compensated diminishing the upper mass in order to have a total mass equivalent to the mass used in DEM simulations. Instead of 105 kg, the experiment should be performed with an upper mass of 102.74 kg. Hereafter, a schematic view of the configuration adopted for the experimental test is given.

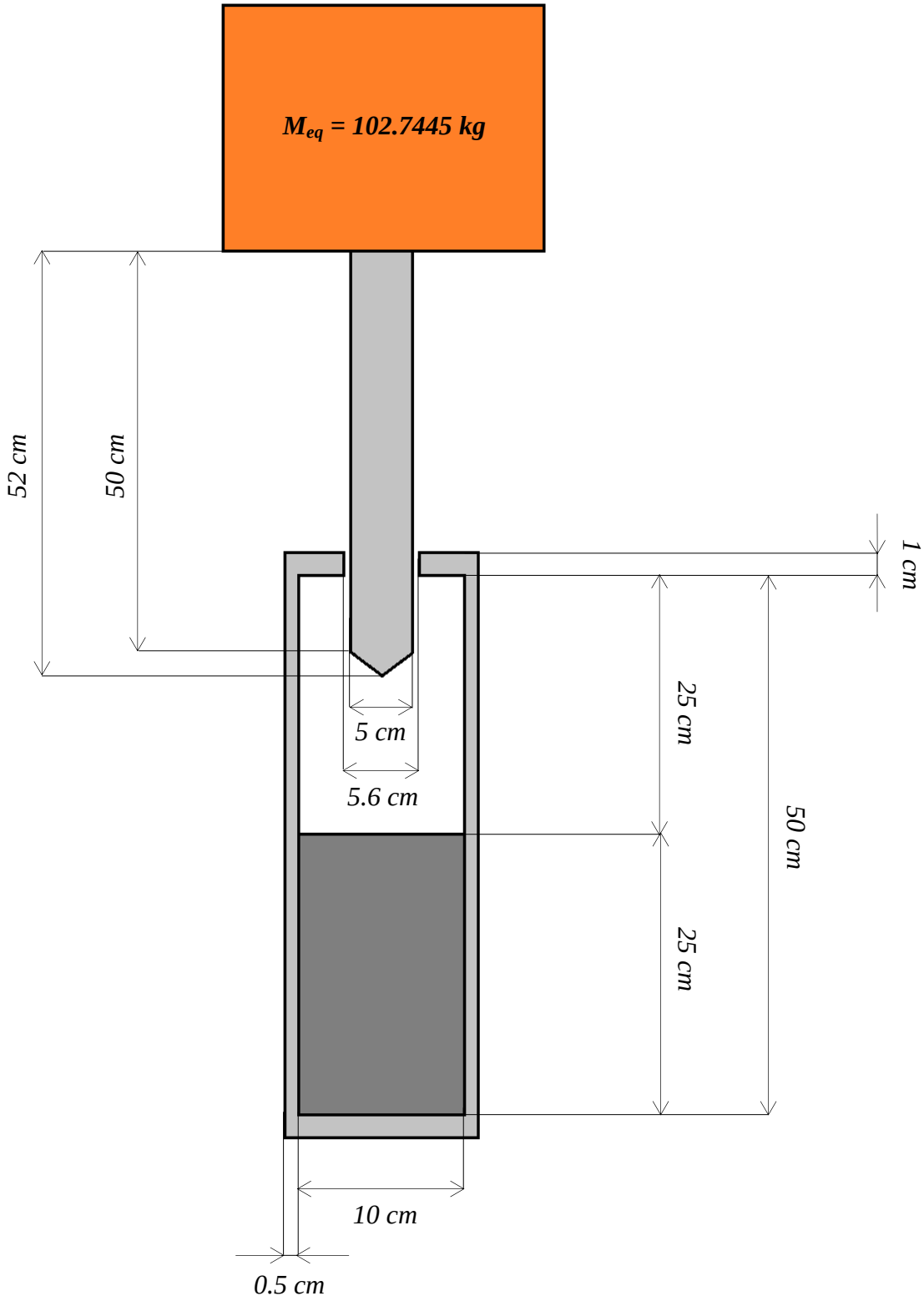

Figure 245 Schematic vertical-section representation of Granular Actuator used for the experimental analysis

6.2.2 Granular Material

Most of the commercially available spheres are employed in the production of ball bearings, valves or other safety components in the automotive and aerospace field, and are characterized by corrosion resistance, low ware rate and low frictional coefficients. They are available in different materials like metal alloys (Aluminium, Steel, Copper, Titianium, Nichel e.t.c), ceramics and polymers. In order to perform a correct validation of DEM analysis, it's necessary to adopt the same material used in the numerical simulations. At this point, it's important to remember that the material properties adopted in DEM (density, Young modulus and Poisson's coefficient) correspond to those of the Aluminium alloy (series 7075), while the frictional coefficient was fixed to 0.3, which is different from the values suggested by the literature. This assumption was based on the fact that there are techniques able to modify the frictional coefficient without changing the bulk properties of a material. Even if available, the application of such techniques would require long time and increase the cost up to unaffordable levels, making the experiment inconvenient. In order to conserve at least the similarities in the density, Young modulus and Poisson's coefficient, spheres of Aluminium alloy are adopted. According the literature, the frictional coefficient of the common Aluminium alloy in air is around 0.13 while other materials like the SiC or polymers can reach higher values. However, the application of these last two materials would make the experiment too different from DEM simulations in terms of bulk properties and would increase dramatically the cost (especially for SiC). Indeed, a different value of density could change significantly the way the momentum is exchanged between the spheres. Regarding the Aluminium alloy, such low friction value couldn't be enough to stop properly the falling mass in the available stroke, a fortiori when the gravity is applied. Even if the possibility to perform a test with the same frictional coefficient used in the previous DEM simulations is definitely abandoned, the test remains still meaningful because it can be used to validate DEM model, provided that new DEM simulations are run with the experimental frictional coefficient. It's worthy to notice that the exact value of the frictional coefficient of the adopted spheres is still unknown even if it cannot be too far from the value observed from the literature (0.13). Therefore, a proper

correlation could be done performing different DEM simulations with different values of frictional coefficients (around the literature value), trying to match the results obtained through the experiment. Thanks to this uncertainty and to the typical unpredictability of the granular behaviour, the possibility to stop in the available stroke the falling mass cannot be excluded until the experiment is performed. The diameter of the adopted spheres is **5 mm,** coherently with the values used in DEM simulations. It's important to underline that the definitive DEM solution was obtained using the gravity-deposited packing, which is similar to the random granular arrangement that will be used in the experiment. The number of spheres employed in the experimental test is around **20000** which is higher than the value predicted in DEM model. Indeed, in the last case, the packing was realized letting fall, under the gravity, an orthogonally packed sphere arrangement with the equivalent volume of the container. According to the data sheet of the manufacturer, the previously mentioned number is enough to fill a volume of **2 *l***, which is equivalent to the volume dedicated to the granular material. Because of its immediate availability and relatively low cost, spheres of Aluminium alloy of series 5000 will be used. This material has similar bulk properties of the alloy adopted in DEM simulations. Hereafter a table with the properties of the selected material for the spheres is given.

	Properties of AL 5050 (Al-Mg Alloy)
Density [kg/m3]	2690
Young Modulus [GPa]	72
Ultimate Strength [MPa]	120 – 160
Poisson's ratio	0.33
Hardness [HV0,5]	31 – 41
CTE [1E-6/°C]	22,8
Friction Coefficient	≈ 0.13

Table 67

6.2.3 The Test

The experiment will be performed at **LA.S.T.** (Laboratorio per la Sicurezza dei Trasporti) of Politecnico di Milano, using the equipment of a traditional drop test. The assembly of upper mass and intruder will be let fall into the granular mean from an equivalent altitude to reach the required velocity at the impact ($2\ \frac{m}{s}$). The altitude can be easily found knowing the impact velocity and the "equivalent" gravity. According to the indications of the laboratory, this last value is around $\mathbf{9.7\ \frac{m}{s^2}}$ instead of the $9.81\ \frac{m}{s^2}$ because it takes into account the frictional resistance of the guides during the sliding. The obtained value of the equivalent altitude is 0.21 m, which will be the initial distance between the inferior extremity of the intruder (cone) and the granular material. In order to evaluate the efficiency of the damper and to perform a proper correlation with the DEM simulations, information related to the force/acceleration, velocity and strokes are necessary. The maximum stroke can be easily measured just evaluating the difference between the initial and final position of the intruder/mass assembly, while all other information will be given by the measurements of an accelerometer which will be positioned on the falling mass. This sensor will measure the acceleration which the mass will be subjected to during the impact. From the acceleration-time trend, the maximum value will be valued and, through the numerical integration, the trends of velocity and stroke will be achieved in order to perform the correlation with the values observed in DEM simulations. The direct measurement of the displacement and the velocity would involve different and more sophisticated sensors (LVDT, laser e.t.c), complicating the experimental apparatus uselessly.

6.3 Correlation

There are different manners to correlate the experimental data with DEM results. Force/acceleration, velocity and stroke trends w.r.t time could be directly compared and/or a more meaningful force-stroke trend could be considered. The last one is more appropriate to put in evidence the dissipated energy and to compare the general behaviour of the damper. From the results of DEM simulations with the gravity updated to the terrestrial value, it can be observed that the force-stroke trend manifests a non-zero value from the beginning of the simulation. Having in mind that the acceleration (and so the force) was calculated as the derivative of the velocity w.r.t the time, the observed initial value corresponds to the weight of the falling mass. During the penetration, the force shows a sharp variation and reaches the peak value. In the remaining part, the force drops to zero, indicating that the equilibrium between the weight and the reaction of the granular mean and/or the bottom of the damper is reached. It's worthy to underline that if a piezoelectric accelerometer is used, since it is not able to measure the constant accelerations like those induced by the gravity, the experimental force-stroke trend could be slightly different from what is observed from the DEM simulations. According to this consideration, the measured force-stroke trend should be zero until the impact with the granular mean occurs. As it was said before, another way to correlate the data could be done comparing the trends of the velocity w.r.t the time obtained from the integration of the acceleration measured by the sensor (knowing the sampling frequency of the acquisition system) with the trend obtained by DEM simulation. If the accelerometer is able to measure also the constant acceleration, the velocity vs time trend should start from zero and reach the velocity of $-2\,\frac{m}{s}$ before the impact. Subsequently, it should tend to zero as it was observed from DEM simulations. However, if this is not case and piezoelectric sensors are used, the velocity trend obtained through the integration should have a zero value up to the impact with the granular mean and subsequently it should reach to value of $2\,\frac{m}{s}$. This unphysical trend could be easily corrected fixing the initial condition for the integration to $-2\,\frac{m}{s}$ and having in mind that the velocity trends obtained from simulations starts always

around this value. Anyway, comparing different trends of force-stroke and/or velocity-time found from DEM simulations with different frictional coefficient with those obtained from the experimental test, it will be possible to determine with good approximation the frictional coefficient of the used material and to verify the validity and the correctness of DEM model. Hereafter, some numerical results, which could be used in the correlation phase, are presented.

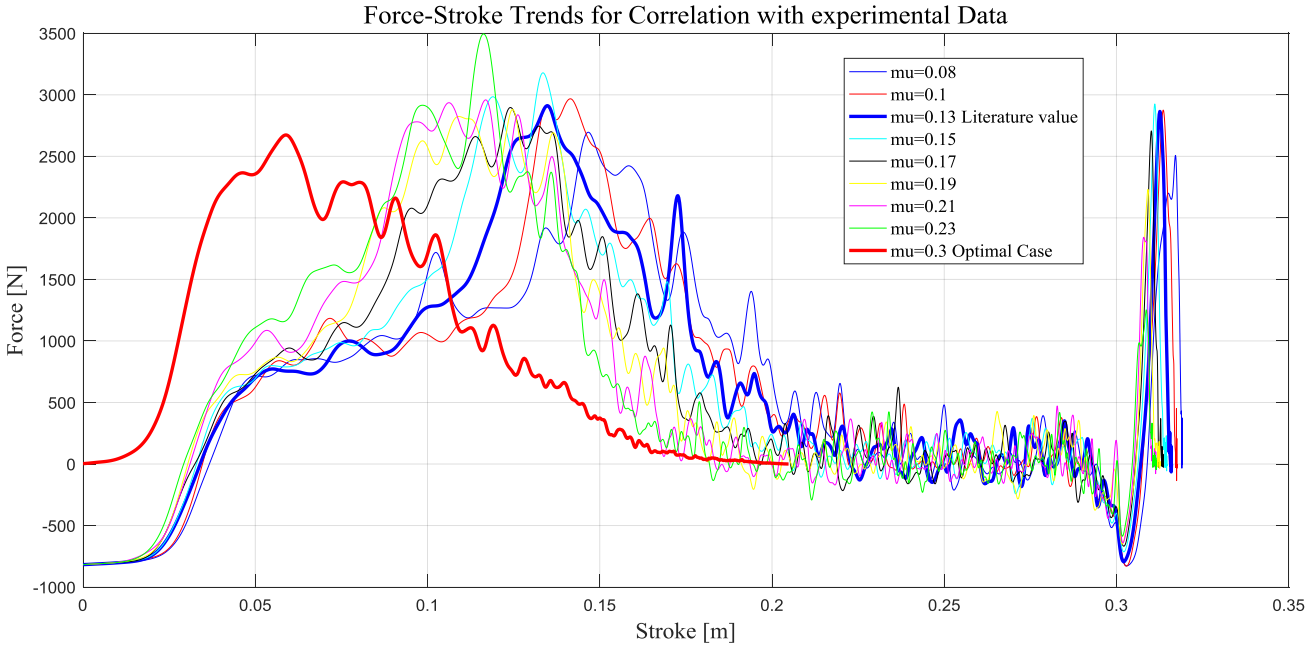

Figure 246

As it can be noticed, the force of the simulation where the gravity was included starts from a non-zero value, which corresponds to the weight of the falling mass. The low value of the frictional coefficient used in this last case is unsuitable to stop the mass properly within the allowed stroke (0.25 m). For sake of clarity, the optimal case corresponds to the simulations with almost zero gravity where the frictional coefficient was fixed to 0.3, while mu = 0.13 corresponds to the value of the frictional coefficient of Aluminium alloy in air found from the literature. The sharp decay of the force trend when the stroke reaches 0.3 m is due to the fact that the intruder head is completely out from the bottom of the container (which cannot interact with the polyhedron-made

intruder) and the entire falling mass assembly is pulled down by the gravity without meeting a significant resistance from the granular mean. The subsequent sharp increment is due to the interposition of the granular material between the container's bottom and box-made spacecraft.

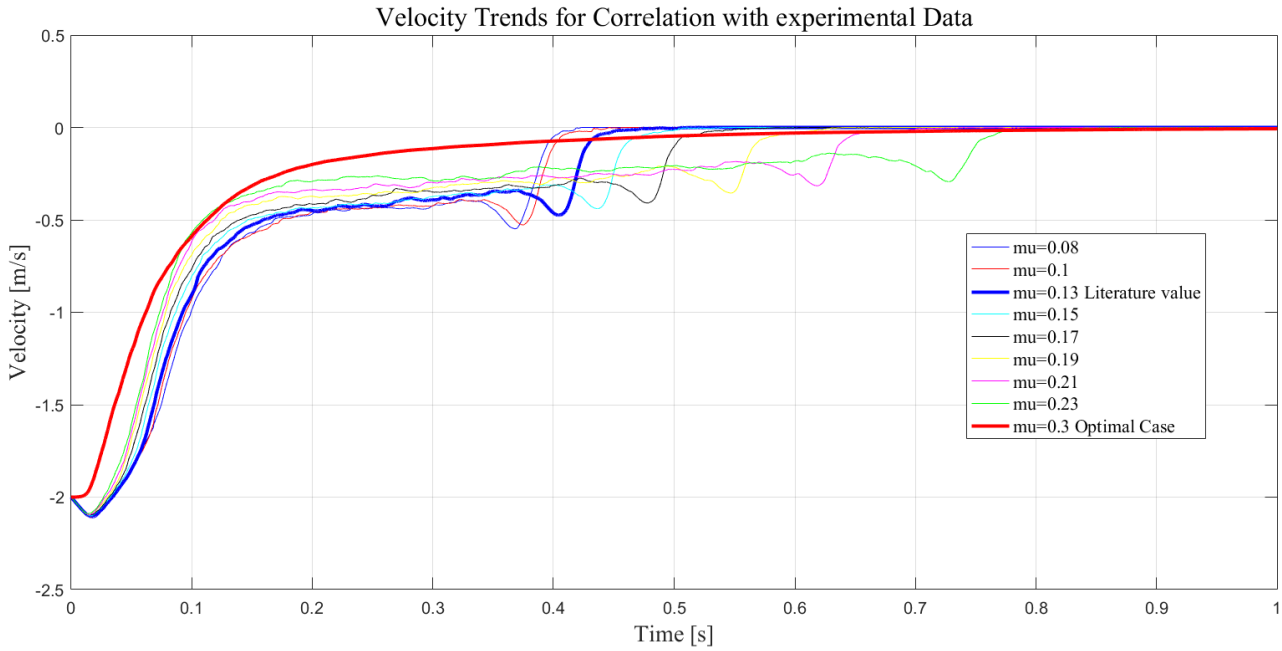

Figure 247

From the last figure, it can be observed that the velocity with gravity (blue) reaches values slightly lower than -2 $\frac{m}{s}$ before changing its trend toward higher values. This is caused by the presence of the gravity which accelerates the falling mass until the reaction of the granular material becomes consistent. Indeed, it's worthy to remember that a small gap between the intruder and the granules could be present in DEM model because of the irregular boundary of the gravity deposited packing. Because of the same reasons explained for the force-stroke trend, also the velocity shows a small decrement around 0.4 s (intruder head out from the container, acceleration caused by gravity) and a near-zero trend when the spacecraft mass is fully stopped by the already mentioned interposition of the granular material. Another equivalent plot that could be useful for the correlation is the velocity-stroke trend, where the unphysical DEM-data registered after 0.25 m of stroke can be easily (visually) excluded and only the data in the range

consistent to the experiment (0-0.25 m) can be considered for the comparison. Below, the mentioned plot is given.

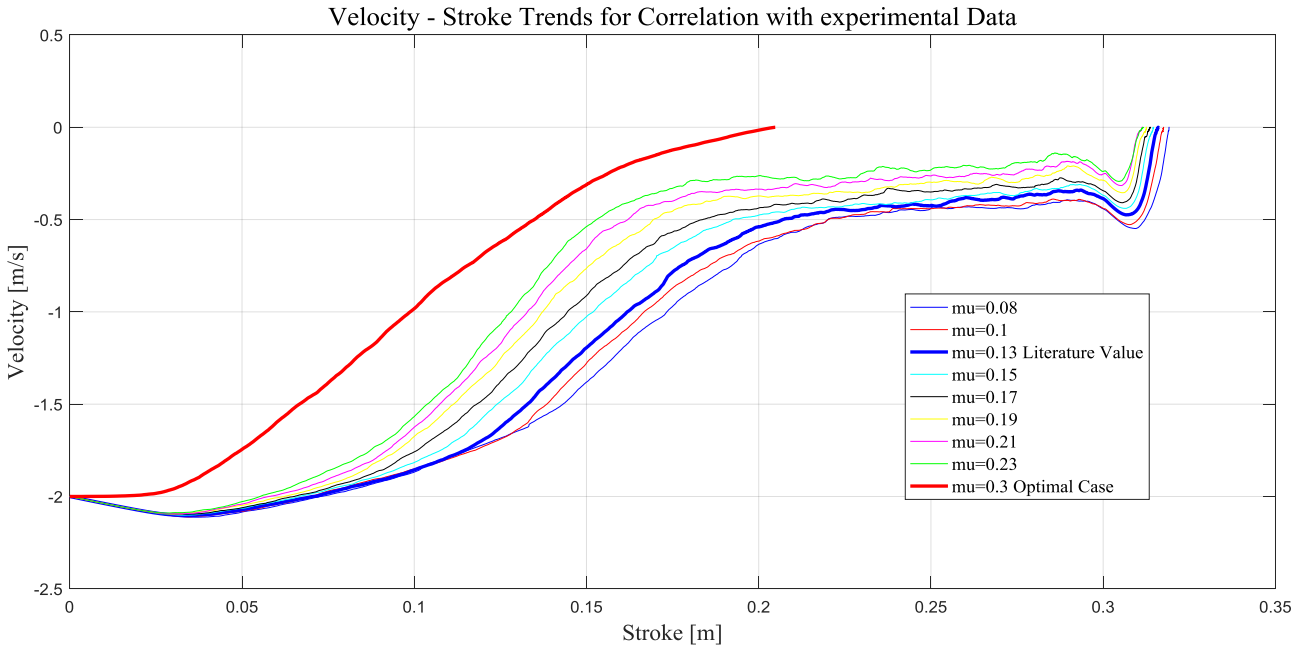

Figure 248

Conclusions

The conceptual line followed up to now had the aim of illustrating the rationale behind the performed work which brought to the selection of the final configuration. The research about the existing technologies, the environment and the preliminary sizing demonstrated that solutions like the piezoelectric and granular dampers are feasible, reliable and able to satisfy the requirements and so worthy of a further analysis. The elementary and the subsequent combined active and passive Multibody simulations gave the possibility to verify the correctness of the chosen approach and to investigate the general behaviour of the modelled systems. Notwithstanding the simplicity of the model adopted initially for the granular damper, the combined simulations demonstrated that the active force laws, which depend also on the parameters of the passive damper, can be harmonically coupled with the granular model, increasing effectively the performances of the entire system. The first sensitivity analysis put in evidence the inability of most of the optimized force laws to ensure an adequate dissipation capability at arrival velocities higher than 2 m/s and underlined the need of taking advantage of the adaptive capability of the chosen active damper. The simulations run with different active force laws for the ascent and the descent phases showed that it is possible to exploit better the available stroke, bringing a significative diminution of the transmitted forces, achieving at the same time low values of bouncing velocities. However, all these considerations and results would have remained quite inaccurate without a more realistic model obtained through DEM analysis. This numerical approach of the granular mechanics allowed to model and simulate the landing scenario evaluating the influence that could have the primary parameters, like the sphere radius, the packing and the friction coefficients, on the performances of granular damper. Anomalous and unpredicted trends of bouncing velocities were observed from this analysis and the will of deepening the issue brought to the conclusion that such anomalies can be avoided changing the packing and/or introducing an offset between the intruder and the granular arrangement. Moreover, it was possible to verify that, for

low values of the friction coefficients, the stroke can be better exploited and consequently, the transmitted force diminished. Because of their long duration, DEM simulations were performed for a discrete number of values of the mentioned parameters but the obtained results were enough to evaluate the model sensitivity to such parameters and to check the feasibility of this technology. The definitive characterization of the granular damper was performed running multiple DEM simulations with different arrival velocities and, subsequently, fitting the obtained data through a polynomial model. Thanks to this approach, it was possible to return to the Multibody simulations and calibrate the previous active force laws according to a more accurate granular model. Some force laws, like the "bell" shaped laws, revealed the possibility to keep the bouncing velocity in the order of 1e-05 m/s with a maximum deceleration of the spacecraft around 1 g, far below the value (4 g) that could be transmitted if only the passive actuator would be used. The advantages given by the combined active + passive model were again evident in the robustness simulations. Maximum forces and bouncing velocities can be maintained in their acceptable ranges also when the control system is affected by noise and delay. Good performances were observed also for different values of arrival velocity (up to 4m/s), spacecraft mass (up to 10% more than nominal mass), gravity and ground parameters. Moreover, the considered models revealed to be robust against uncertainties related to the determination of the actual touchdown velocity and spacecraft mass, guaranteeing satisfactory results also when the active damper is not perfectly adapted to these parameters. The final sizing, which was based on the results obtained from the mentioned simulations, demonstrated that is possible to ensure the observed damping capability, applying acceptable values of voltage (less than 20 V) to the piezoelectric actuators, and that the structural integrity of the entire system can be maintained also for the "extreme" conditions checked in the robustness analysis. Having in mind that all the proposed work was done considering only a single leg, it's quite obvious that the system was intentionally oversized and, thanks to the final simulations with multiple legs, it was possible to verify that the force each actuator should generate is far lower than the value which led the definitive sizing. As the Lector could realize from the proposed description, the approach adopted in this work is quite heuristic, like in most of the researches related to the application of new technologies. Because of the multiplicity of

the physical parameters and applicable control laws, a real fine “optimization” of the dampers was out of the purposes of this thesis, where the real objective was to verify the feasibility of the selected solutions. Indeed, a possible recommendation for a further analysis is to enlarge the ranges and the combinations of the mentioned variables (for example the frictional coefficients and the characteristics dimensions in DEM analysis) in order to determine a more accurate optimal set of the sizing parameters, preferably tailored to the number of legs of the lander.

Bibliography

[1] *"Critical Soft Landing Technology Issues for Future U.S. Space Missions",* J.M. Macha, D.W. Johnson, D.D. McBride (NASA), 1992.

[2] *"Magnetic Vibration Damper for Space Applications",* Tiffany Heyd, Benjamin Hensel, Jacob Norris, Thomas Sciotto (Rochester Institute of Technology), 2011.

[3] *"Current trends in Electro-magnetic Braking System: A review paper of the current scenario of the magnetic braking system"*, Umang S. Modi, Swapnil C. Bhavsar (Sal Institute of Technology & Engineering Research), 2015.

[4] *"Contactless Magnetic Brake for Automotive Applications"*, Sebastien Emmanuel Gay (Texas A&M University), 2005.

[5] *"Innovative Designs for Magneto-Rheological Dampers"*, James Poynor (Virginia Polytechnic Institute and State University), 2001.

[6] *"The Design of Eddy-Current Magnet Brakes",* Der-Ming Ma, Jaw-Kuen Shiau (Tamkang University), 2010.

[7] *"Shape Memory Actuators Improve Car Performance",* Dieter Stoeckel, 1992.

[8] *"Design and Analysis of a Shock Absorber",* Pinjarla.Poornamohan, Lakshmana Kishore.T (Godavari Institute of Engineering and Technology), 2012.

[9] *"SMA Hysteretic Shock Absorber",* Norman Munroe, Harold Hastings, Alexander Zuleta (Florida International University), 2013.

[10] *"Pressurized Metal Bellows Shock Absorber for Space Applications"*, John Trautwein (University of Central Florida), 2015.

[11] *"Shape Memory Actuators for Automotive Applications",* Dieter Stoeckel, 1990.

[12] *"Progetto di un assorbitore d'urto per monoposto di Formula SAE"*, Leonardo Bertini, Francesco Frendo, Stefano Cristofanelli (Università di Pisa), 2008.

[13] *"Radiation-Resistant Magnets",* R.L. Keizer, M. Mottier (CERN), 1982.

[14] *"Servomotori per Applicazioni Speciali",* Cyber Motors Datasheet.

[15] *"Impiego ed analisi dei motori a magneti permanenti nei sistemi per la mobilità",* Brenna Morris, Avigni Riccardo, D'Adda Fabio (Politecnico di Milano), 2011.

[16] *"Thermal Stability and Radiation Resistance of Sm-Co based Permanent Magnets",* Jinfang Liu, Payal Vora, Peter Dent, Michael Walmer (Electron Energy Corporation), Christina Chen (University of Dayton Research Institute), Joseph Talnagi (Ohio State University Research Reactor), Suxing Wu and Martin Harmer (Center for Advanced Materials and Nanotechnology, Lehigh University), 2007.

[17] *"Reliability & Lifetime of Multilayer Piezo Actuators",* PI Ceramic.

[18] *"Evaluation of Piezoelectric PVDF Polymers for Use in Space Environments. Effects of Atomic Oxygen and Vacuum UV Exposure",* Tim R. Dargaville, Mathew Celina, Jeffrey W. Martin (Sandia National Laboratories), Bruce A. Banks (NASA Glenn Research Center), 2005.

[19] *"Verification and Operation of Adaptive Materials in Space",* Mathias C. Celina, Tim R. Dargaville, Gary D. Jones, Julie M. Elliott (Sandia National Laboratories), 2006.

[20] *"Piezoelectric Actuators",* PI Ceramic Datasheet.

[21] *"Linee Guida per la Progettazione di Gallerie Paramassi",* Francesco Calvetti, Claudio Di Prisco (Politecnico di Milano), 2007.

[22] *"Metals and Ceramics",* Koji Kato, Koshi Adachi (Tohoku University), 2001.

[23] *"Durafosf Pus",* Pontoglio Vincenza Srl Datasheet.

[24] *"Aluminox",* Coelbo Srl Datasheet.

[25] *"Non-Linear Finite Element Analysis of a Shock Absorber Elastomer Piston Head",* Phillip Rodenbeck.

[26] *"Adaptive landing gear: Optimum control strategy and potential for improvement",* Grzegorz Mikułowski, Łukasz Jankowski (Institute of Fundamental Technological Research), 2008.

[27] *"Adaptive Impact Absorbtion Controlled Via Pyrotechnic Devices",* Marian Ostrowski, Jan Holnicki-Szulc (Institute of Fundamental Technological Research), 2008.

[28] *"A Novel Strategy for Asteroid Exploration with a Surface Robot"*, Kazuya Yoshida, Takeshi Maruki, Hajime Yano (Tohoku University), 2002.

[29] *"Adaptive Inflatable Structures for Impact Absorption"*, Cezary Graczykowski, Jan Holnicki-Szulc (Institute of Fundamental Technological Research), 2007.

[30] *"Adaptive Structures under Extreme Loads-Impact Detection, Self-Adaptation, Self-Repairing"*, Piotr Pawłowski, Jan Holnicki-Szulc (Institute of Fundamental Technological Research) 2004.

[31] *"Crashworthiness of Inflatable Thin-Walled Structures for Impact Absorption"*, Cezary Graczykowski, Jan Holnicki-Szulc (Institute of Fundamental Technological Research), 2015.

[32] *"Modeling and experiments on eddy current damping caused by a permanent magnet in a conductive tube"*, Jae-Sung Bae, Jai-Hyuk Hwang, Jung-Sam Park, Dong-Gi Kwag (Korea Aerospace University), 2009.

[33] *"On the modeling of dry friction dampers in vehicles suspensions",* Răzvan Andrei Oprea, Mihai Mihăilescu, 2015.

[34] *"Study on Damping Performances of New Link DeviceCusing Granular Materials"*, Toshiaki Makino, Michio Sebata, Muneo Furuse, Takeshi Kawasaki, Taichi Sat, 2014.

[35] *"Huygens Probe Impact Dynamics",* R.D. Lorenz (University of Kent), 1994.

[36] *"Study and Comparison on Linear Electromagnetic Shock Absorbers among other Available Intelligent Vibration Dampers"*, S. B. A.Kashem, M. A. Chowdhury, T. A. Choudhury, N. Shabrin, M. Ektesabi, R. Nagarajah, (International Journal of Science and Research), 2013.

[37] *"Design and Development of an Active Landing Gear System",* GMV Innovating Solutions, 2015.

[38] *"Design and Development of an Active Landing Gear System for Robotically Enhanced Surface Touchdown"*, Cristian Corneliu Chitu, Raluca Stefanescu, Paul Bajanaru (GMV-Romania), Julio Galipienzo, Cristina Ortega (AVS-UK), Tomasz Barciński, Tomasz Rybus, Karol Seweryn (CBK-PAN), Gianfranco Visentin (ESA/ESTEC), 2015.

[39] *"Lander Shock-Alleviation Techniques",* F. Doengi, S.T. Burnage, H. Cottard, R. Roumeas (ESA bulletin), 1998.

[40] *"Smart Technologies for Adaptive Impact Absorption"*, Cezary Graczykowski, Grzegorz Mikułowski, Arkadiusz Mróz, Piotr Krzysztof Pawlowski (Institute of Fundamental Technological Research), 2009.

[41] *"A feasibility study of a pneumatic adaptive impact absorber"*, Grzegorz MikuÃlowski (Institute of Fundamental Technological Research), 2008.

[42] *"Rebound of a confined granular material: combination of a bouncing ball and agranular damper"*, F. Pacheco-Vàzquez, S. Dorbolo (Universite´de Liège), 2013.

[43] *"Mechanics of Granular Materials: Constitutive Behavior and Pattern Transformation"*, Fatih Göncü (Delft Center for Computational Science and Engineering), 2012.

[44] *"Motors",* Sean DeHart, Smriti Chopra, Hannes Daepp, 2015.

[45] *"Design, Control, and Experimentation of Internally-Actuated Rovers for the Exploration of Low-Gravity Planetary Bodies",* B. Hockman, M. Pavone (NASA), A. Frick, I.A.D. Nesnas (Stanford University), 2016.

[46] *"Magnetorheological elastomers and their applications"*, W.H. Li, X.Z. Zhang, H. Du (University of Wollongong), 2013.

[47] *"Actively Controlled Landing Gear For Aircraft Vibration Reduction",* Lucas G. Horta, Robert H. Daugherty, Veloria J. Martinson (NASA), 1999.

[48] *"Dry-Frictional Shock Absorber",* NASA, 1970.

[49] *"Experimental Observation of High-rate Buckling of Thin Cylindrical Shape-memory Shells"*, Sia Nemat-Nasser, Jeom Yong Choi, Jon B. Isaacs, and David W. Lischer (University of California), 2005.

[50] *"NiTi Super Elastic Shape Memory Alloys for Energy Dissipation in Smart Systems for Aerospace Applications"*, Manjunatha Pattabi, G.N.Dayananda, (Mangalore University), 2008.

[51] *"Adaptive Crashworthiness of Front-End Structure of Motor Vehicles"*, Marian Ostrowski, Jan Holnicki-Szulc (Institute of Fundamental Technological Research), Paulius Griskevicius (Kaunas University of Technology), 2007.

[52] *"An innovative inflatable morphing body structure for crashworthiness of military and commercial vehicles"*, Dong Wook Lee, (University of Michigan), 2008.

[53] *"Electrical Properties and Power Considerations of a Piezoelectric Actuator"*, T. Jordan, J. Tripp, P. Tcheng (NASA), Z Ounaies (ICASE), 2000.

[54] *"Active buckling control of beams using piezoelectric actuators and strain gauge sensors"*, Q. S. Wang, S. C. Shrivastava (McGill University), 2009.

[55] *"Measurements of the material properties of a laminated piezoelectric stack at cryogenic temperatures"*, R.P. Taylor, G.F. Nellis, S.A. Klein, D.W.Hoch (University of Wisconsin), J. Feller, P. Roach (NASA), J.M. Park, Y. Gianchandani (University of Michigan), 2006.

[56] *"Characterization of a piezoelectric valve for an adaptive pneumatic shock absorber"*, Grzegorz Mikułowski, Rafał Wiszowaty and Jan Holnicki-Szulc, (Institute of Fundamental Technological Research), 2013.

[57] *"A new semi-active piezoelectric based friction damper"*, Memet Unsal, Christopher Niezrecki, Carl D. Crane III (University of Florida), 2002.

[58] *"Pneumatic Adaptive Absorber: Mathematical Modelling with Experimental Verification"*, Grzegorz Mikulowski and Rafal Wiszowaty (Institute of Fundamental Technological Research), 2015.

[59] *"Experimental Investigation on Energy Absorbing Pressurised Composite Tubes"*, T.Hou, B.G.Prusty, G.Pearce, D.Kelly (University of New South Wales), R. Thomson (Cooperative Research Centre for Advanced Composite Structures, Advanced Composite Structures Australia Pty Ltd), 2014.

[60] *"Instrumentation for Impact Test - Part 1 - Electronic Instrumentation",* SAE International, 2007.

[61] *"Feasibility study of an adaptive energy absorbing system for passenger vehicles",* Marian Ostrowski, Paulius Griškevičius, Jan Holnicki-Szulc (Institute of Fundamental Technological Research), 2005.

[62] *"Yade Documentation" ,* Václav Šmilauer, Emanuele Catalano, Bruno Chareyre, Sergei Dorofeenko, Jérôme Duriez, Nolan Dyck, Jan Eliáš, Burak Er, Alexander Eulitz, Anton Gladky, Ning Guo, Christian Jakob, François Kneib, Janek Kozicki, Donia Marzougui, Raphaël Maurin, Chiara Modenese, Luc Scholtès, Luc Sibille, Jan Stránský, Thomas Sweijen, Klaus Thoeni, Chao Yuan.

[63] *"Pyro-adaptive impact energy absorber",* Marian Ostrowski, Jan Holnicki-Szulc (Institute of Fundamental Technological Research), Paulius Griskevicius (Kaunas University of Technology), 2007.

[64] *"Experimental investigation of energy-absorption characteristics of components of sandwich structures",* S. Nemat-Nasser, W.J. Kang, J.D. McGee, W.-G. Guo, J.B. Isaacs (University of California), 2006.

[65] *"Semi-active linear vacuum packed particles damper"* Robert Zalewski, Paweł Chodkiewicz, (Warsaw University of Technology, Institute of Machine Design Fundamentals,) 2016.

[66] *"Vibration analysis for vehicle with vacuum packed particles suspension",* Michał Makowski, Robert Zalewski (Warsaw University of Technology, Faculty of Automotive and Construction Machinery Engineering), 2015.

[67] *"Simscape User's Guide",* The MathWorks, Inc.

[68] *"Damping force of a damper utilizing a spherical particle assemblage",* Yasushi Ido, Koichi Hayashi (Nagoya Institute of Technology), 2012.

[69] *"Rare earth permanent magnets for cryogenic space applications",* Silvia Scheithauer, Oliver Krause, Friedrich Muller, Stephan Birkmann, and Tobias Junginger (Max-Planck-Institut f¨ ur Astronomie), 2007.

[70] *"Investigation on zero-gravity behavior of particle dampers",* B. Yao, Q. Chen, (Journal of Vibration and Control), 2015.

[71] *"Journal of Vibration and Control 2015",* Hrishikesh Deo, Nam P. Suh, (Massachusetts Institute of Technology), 2006.

[72] *"Neutron and gamma radiation effects on MEMS structures",* P. Gkotsis, V. Kilchytska, U. Bhaskar, X. Tang, J.-P. Raskin, D. Flandre, L. A. Francis, O. Militaru (Université catholique de Louvain), ,C. Fragkiadakis, P.B. Kirby (Cranfield University), 2011.

[73] *"Effect of gas pressure and temperature on stereometric properties of al+al2o3 composite coatings deposited by lpcs method",* M. Winnicki, T. Piwowarczyk, A. Małachowska, A. Ambroziak (Wrocław University of Technology), 2014.

[74] *"Cold spray coating: review of material systems and future perspectives",* A. Moridi, S. M. Hassani-Gangaraj, M. Guagliano (Politecnico di Milano –

Massachusetts Institute of Technology), M. Dao (Massachusetts Institute of Technology), 2014.

[75] *"Plasma-Enhanced Chemical Vapor Deposition of Functional Coatings"*, L. Martinu, O. Zabeida, J.E. Klemberg-Sapieha (Ecole Polytechnique de Montreal), 2010.

[76] *"Temperature dependence of friction under cryogenic conditions in vacuum"*, J. C. Burton, P. Taborek, J. E. Rutledge (University of California), 2006.

[77] *"Frictional analysis of aerospace alloys and composite materials"*, Karthika Mohan (University of New South Wales), 2011.

[78] Website: *http://www.azom.com/article.aspx?ArticleID=6652* (Aluminium 7075)

[79] Website: *http://www.azom.com/properties.aspx?ArticleID=52* (Aluminium oxide)

[80] Website: *http://accuratus.com/alumox.html* (Aluminium oxide)

[81] Website: *https://en.wikipedia.org/wiki/Gas_dynamic_cold_spray* (Cold Spray Technique)

Acknowledgements

We are very thankful to Professor Massari and Professor Astori for the precious guidance and constant assistance that they have given us during the entire work.

I would like to thank deeply my parents Alessandro and Manuela for believing always in me and for the opportunity to study that they gave me, and my sister Valentina for her constant and loving support.

I would like to thank intensely my girlfriend Paola for her love and inestimable support that have encouraged me to overcome the difficult moments faced in these years.

I would like to express my authentic sense of gratitude to all my family, my grandmother, my aunts, my uncles and my cousins, for the encouragement that I have received from them.

I would like to thank my friends for the friendship and interest they have demonstrated to me through these years.

Finally, but not less important, I would like to thank my friend as well as coauthor of this work Jan, for the hard but gratifying period that I have shared with him.

Luciano

I would like to express a deep sence of gratitude to my family, who supported me during these years with their invaluable love and trust, and pushed me to do always my best, to my girlfriend who encouraged me in the difficulties, and to my friends who shared with me the academic experience. I would like to thank Luciano, coauthor and friend, with whom I had the pleasure of working together to reach this common objective.

Jan Guil